Simulating quantum dissipative and vibrational environments

From single qubits to many-body physics

Mattia Moroder

SIGILL: UNIVERSITAT: LUDOVIC: MAXIM:

München 2024

SIMULATING QUANTUM DISSIPATIVE AND VIBRATIONAL ENVIRONMENTS

FROM SINGLE QUBITS TO MANY-BODY PHYSICS

Mattia Moroder

Dissertation
an der Fakultät für Physik
der Ludwig-Maximilians-Universität
München

vorgelegt von
Mattia Moroder
aus Bozen, Italien

München, 21. August 2024

Erstgutacher: Prof. Dr. Ulrich Schollwöck

Zweitgutachter: Prof. Dr. Christian Mendl

Tag der mündlichen Prüfung: 13. November 2024

Zusammenfassung

Die Wechselwirkung von Quantensystemen mit einer Umgebung führt typischerweise zu einem Verlust der Quantenkohärenz und zu Dissipation von Energie. In dieser Dissertation, setzen wir effiziente Matrix-Produkt-Zustand-Methoden (MPS) ein, um die Auswirkungen von zunehmend komplexen Quantenumgebungen auf verschiedenste physikalische Systeme zu untersuchen, beginnend bei einfachen Zwei-Niveau-Systemen bis hin zu Quantenvielteilchensystemen.

Der einfachste Fall ist der von Markowschen (d. h. gedächtnislosen) Umgebungen, die schwach an ein System koppeln. Solche Umgebungen, welche implizit über die Lindblad-Gleichung beschrieben werden können, werden *dissipative Umgebungen* genannt. In diesem Rahmen hat das eigenartige Phänomen heißer Systeme die schneller abkühlen als Kalte (bekannt als Mpemba-Effekt) in letzter Zeit viel Aufmerksamkeit erregt. Hier definieren wir den Quanten-Mpemba-Effekt auf thermodynamisch konsistente Weise und zeigen, wie man die Thermalisierung beliebiger, gemischter Quantenzustände exponentiell beschleunigen kann.

Wenn System und Umgebung stark miteinander wechselwirken und/oder Langzeitgedächtniseffekte vorhanden sind, muss die Umgebung explizit berücksichtigt werden. Wichtige Beispiele für solche Umgebungen sind *Schwingungsumgebungen*, wenn sie durch eine niedrige Temperatur, eine nicht triviale Spektraldichte oder eine starke Kopplung gekennzeichnet sind. In der Physik der kondensierten Materie spielen quantisierte Gitterschwingungen, die als Phononen bezeichnet werden, eine entscheidende Rolle bei der Bestimmung verschiedener Eigenschaften von Festkörpern. In diesem Zusammenhang befasst sich eine neuen Klasse von Experimenten mit der optischen Anregung von Phononen und der Messung der elektronischen Antwort außerhalb des Gleichgewichts. Um die Auswirkungen von Phononanregungen auf die Elektronendynamik zu untersuchen, fügen wir die neuartige *Phononen Zustandstomographie (PST)* Methode ein. Wir wenden PST an, um ein Modell für ein eindimensionales Metall zu analysieren und finden bei niedrigen Phononenfrequenzen eine Verstärkung der Licht-induzierten langreichweitigen Elektronenkorrelationen.

Wir erforschen außerdem die Auswirkungen von kombinierten dissipativen Umgebungen und Schwingungsumgebungen auf elektronische Freiheitsgrade. Zuerst demonstrieren wir, dass Dissipation die numerische Beschreibung der Dynamik von Exzitonen in strukturierten Umgebungen vereinfachen kann. Anschließend wird gezeigt, dass die gebundenen Elektron-Phonon-Quasiteilchen im Hubbard-Holstein Modell unter Einwirkung starker Dissipation auf das Phononensystem lokalisiert werden, wobei sie jedoch nicht zerfallen.

Abstract

The interaction of quantum systems with an environment typically results in the loss of quantum coherence and energy dissipation. In this thesis, we employ state-of-the-art matrix-product state (MPS) methods to study the impact of quantum environments of increasing complexity on few-body and many-body systems.

The simplest case is that of Markovian (i.e. memoryless) environments that couple weakly to the system of interest. The effects of such environments can be accounted for implicitly via the Lindblad master equation, and we call them *dissipative environments*. In these setups, the peculiar phenomenon of "hot systems cooling faster than cold systems", known as the Mpemba effect, has recently attracted much attention. Here, we define the quantum Mpemba effect in a thermodynamically consistent way and show how to exponentially accelerate the thermalization of arbitrary mixed quantum states.

When the interaction with the system is strong and/or long memory effects are present, one must account for the environment explicitly. Important instances of such environments are *vibrational environments* when they are characterized by a low temperature, a non-trivial spectral density, or a strong coupling to the system of interest. In condensed matter physics, quantized lattice vibrations, known as phonons, play a crucial role in determining different properties of solids. In this context, an interesting recent class of experiments consists in optically exciting phonon modes and measuring the electronic response out of equilibrium. Here, we introduce a numerical method dubbed *phonon state tomography (PST)* as a novel tool for investigating the effect of phonon excitations on electron dynamics. Applying PST to study a model for a one-dimensional (1D) photo-excited metal at low phonon frequencies, we find an enhancement of light-induced long-range electron correlation.

We also explore the effect of joined dissipative and vibrational environments on electrons. Combining a Markovian-embedding method with a pure-state unraveling, we demonstrate that dissipation can facilitate the numerical description of exciton dynamics in structured environments. Moreover, we show that strong dissipation localizes the bound electron-phonon quasiparticles in the well-known Hubbard-Holstein model without altering their stability.

Publications

This thesis is based on the publications and preprints listed below.

1 **M. Moroder**, M. Grundner, F. Damanet, U. Schollwöck, S. Mardazad, S. Flannigan, T. Köhler and S. Paeckel:
'Stable bipolarons in open quantum systems',
in: *Phys. Rev. B* 107 (21 2023), p. 214310. doi: `10.1103/PhysRevB.107.214310`. url: `https://link.aps.org/doi/10.1103/PhysRevB.107.214310`.

2 **M. Moroder**, O. Culhane, K. Zawadzki and J. Goold:
'Thermodynamics of the Quantum Mpemba Effect',
in: *Phys. Rev. Lett.* 133 (14 2024), p. 140404. doi: `10.1103/PhysRevLett.133.140404`. url: `https://link.aps.org/doi/10.1103/PhysRevLett.133.140404`.

3 **M. Moroder**, M. Mitrano, U. Schollwöck, S. Paeckel and J. Sous:
'Phonon State Tomography of Electron Correlation Dynamics in Optically Excited Solids',
in: *Nano Letters* (2024). doi: `https://doi.org/10.1021/acs.nanolett.4c04314`.

4 Z. Xie, **M. Moroder**, U. Schollwöck and S. Paeckel:
'Photo-induced dynamics with continuous and discrete quantum baths',
in: *The Journal of Chemical Physics* 161.7 (Aug. 2024), p. 074109. issn: 0021-9606. doi: `10.1063/5.0221574`. url: `https://doi.org/10.1063/5.0221574`.

5 **M. Moroder**, M. Mitrano, S. Paeckel and J. Sous:
'Light-induced enhancement of long-ranged pairing coherence from slow phonons',
Manuscript in preparation. 2024.

My contributions to the different projects are shortly summarized below.

Ref. [1] I implemented and benchmarked Markovian and non-Markovian pure state methods combined with PP-MPS, performed the calculations, analyzed the data and contributed to the figures and the text of the manuscript.

Ref. [2] I analyzed the properties of Davies maps, introduced the Metropolis-based unitary transformation yielding exponential thermalization speedups, performed the calculations, analyzed the data and contributed to the figures and the text of the manuscript.

Ref. [3] I developed the PST method together with SP, performed the calculations, analyzed the data and contributed to the figures and the text of the manuscript.

Ref. [4] I implemented the Python package EVOS with which ZX performed the calculations, co-supervised the project, analyzed the data and contributed to the figures and the text of the manuscript.

Ref. [5] I performed the calculations, analyzed the data and I am contributing to the figures and text of the manuscript.

Contents

Zusammenfassung iii
Abstract iv
Publications v

Contents **vii**

1 Introduction **1**

I Theory and Methods **6**

2 Open quantum systems (OQSs) **8**
2.1 Brief introduction to open quantum system (OQS) 8
2.2 Vectorization 11
2.3 Quantum jumps (QJ) 13
2.4 Quantum state diffusion (QSD) 15
2.5 Hierarchy of pure states (HOPS) 17
2.6 Structured environments and the mesoscopic leads method 20
2.7 From global to local environments 22
2.8 The EVOS package 25

3 MPS-based methods for dissipative and vibrational environments **26**
3.1 MPS: basic concepts and applications to bosonic systems 26
3.2 MPS methods for OQS 31
3.3 Phonon state tomography (PST) 36

4 Comparing Markovian and Non-Markovian pure-state methods **40**
4.1 Exact diagonalization (ED) comparison 43
4.2 MPS comparison 48
4.3 Numerical complexity and stability 50
4.4 Summary 54

II Applications 55

5 The thermodynamics of the quantum Mpemba effect 58
5.1 The classical Mpemba effect 58
5.2 The quantum Mpemba effect 61
5.3 Exponential speedups via stochastic numerical optimization . . . 74
5.4 Summary and outlook 78

6 Photoexciting electrons: Exciton dynamics in structured vibrational environments 81
6.1 Overcoming current limitations in the simulations of exciton dynamics 82
6.2 A dissipative approach to singlet fission 84
6.3 Exciton transport in the Fenna-Matthews-Olson (FMO) complex at finite temperature 87
6.4 Summary and outlook 94

7 Photoexciting phonons: Analyzing light-induced phenomena with PST 95
7.1 Pulse shapes, phonon probes and electron correlations 97
7.2 Photo-induced enhancement of long-range electron correlation . 110
7.3 Summary and outlook 118

8 Dissipation-induced bipolaron localization 121
8.1 The Hubbard-Holstein model 121
8.2 Dissipation and double occupancy 124
8.3 Polarons and bipolarons 124
8.4 Bipolarons' stability and localization length 126
8.5 Summary and outlook 130

9 Conclusion and Outlook 132

Bibliography 136

Appendix 155
A Exact factorization of the Hubbard-Holstein time evolution operator 156
B Classical Liouvillians with detailed balance have real spectra 158
C Comparing Gaussian anharmonicities and dissipation 159

Glossary 161

List of Figures 164

Acknowledgements 167

Chapter 1

Introduction

A leading principle in the reductionism-based approach to physical modeling has always been selecting a few relevant degrees of freedom within a complex system and treating the remaining ones as an effective environment. As a simple example, consider the free fall of a soccer ball dropped from a high altitude. In addition to being pulled downwards by the Earth's gravitational force, the ball interacts with a huge number of nitrogen, oxygen, and other molecules at every instant. Describing the exact trajectories followed by the scattered molecules would make for a formidable computational task. However, if one does not care about the microscopic details, one can simply view the air as an environment into which the ball dissipates kinetic energy. This leads to an easily solvable equation of motion (assuming a constant air density) characterized by the onset of a constant limit velocity once the gravitational force and the air drag balance each other out. If one repeats the experiment in a vacuum chamber, one will find that the ball's (negative) velocity will increase linearly, obeying $v(t) = v(0) - gt$, where g is the constant gravitational acceleration. The interaction of the ball with the few remaining air molecules in the vacuum chamber, with light and cosmic radiation, will not cause any significant deviation from the simple equation above. This exemplifies the very successful concept of an isolated system in classical physics, in which weak interactions with environments can safely be neglected.

In quantum systems, the situation changes dramatically. Consider a huge vacuum box isolated as best as possible from its surroundings. If one places a free quantum particle initially described by a narrow Gaussian wave packet in the center of the box, the Schrödinger equation tells us that the wave packet should coherently spread out. However, in practice, the few remaining air molecules within the box, thermal photons, and even microwave background radiation will quickly measure the quantum particle's position by scattering off the wave packet. This will lead to an exponential decay in the particle's coherence length; after a short time, it will be indistinguishable from a classical particle whose position is described by an incoherent probability distribution [6]. This phenomenon is known as environmental scattering-induced decoherence, or simply *decoherence*. Thus, for quantum particles, the picture of an isolated system is typically valid only for short timescales. In the context of a more famous thought experiment, we could say that after a short time, Schrödinger's cat will be dead *or* alive without needing anyone to open its box. The main difference to the classical case is that the interaction of a quantum system with its environment typically leads to the formation of an *entangled* state, meaning that in some sense, the system cannot be described as an independent, local object anymore [6]. Instead, in the classical example, while the presence of the air molecules alters the ball's velocity, the ball and the air molecules maintain their individual properties.

In a much-simplified picture, decoherence can be understood as follows. Imagine a two-level system prepared at an initial time in the superposition $|\psi\rangle = c_0 |0\rangle + c_1 |1\rangle$ and a two-level environment which finds itself in some state $|E_0\rangle$ at the initial time. After interacting, the total system-environment state may evolve into the entangled state $|\Psi\rangle = (c_0 |0\rangle + c_1 |1\rangle) \otimes |E_0\rangle \rightarrow c_0 |0\rangle \otimes |E_0\rangle + c_1 |1\rangle \otimes |E_1\rangle$. The information that we can obtain if we can measure only the system is contained in the reduced density matrix $\hat{\rho}_s \equiv \mathrm{Tr}_E |\Psi\rangle\langle\Psi|$ which, if $|E_0\rangle$ and $|E_1\rangle$ are orthogonal to one another (indicating that the interaction with the system has significantly changed the environment), is given by $\hat{\rho}_s = |c_0|^2 |0\rangle\langle 0| + |c_1|^2 |1\rangle\langle 1|$. Thus, if we can access the system only, the interaction with the environment appears to have destroyed the coherences of the system's state. In contrast to the classical case, for quantum systems, the weak interaction with an environment can usually not be ignored as a minor perturbation but, on the contrary, lies at the center of fundamental debates concerning the measurement problem and the very foundations of quantum mechanics [7].

In this thesis, much more modestly, we improve upon existing numerical methods in order to be able to address challenging open problems regarding dissipative quantum systems. First, we must define what we mean by a dissipative quantum system. Consider two weakly-coupled quantum systems, A and B. When B is characterized by a fast relaxation time compared to A, one can use the so-called Markovian (or memoryless) approximation and derive an equation of motion for A only, which accounts implicitly for the influence of B (we will formulate these ideas more precisely in Chapter 2). Thus, when we can avoid the explicit description of B and consider only its effects on A, typically the loss of quantum coherence and energy dissipation, we call B a dissipative environment for A or simply A a dissipative system. Studying the dynamics of dissipative quantum systems employing so-called master equations is the main subject of the field of open quantum systems (OQSs). Master equations were employed as early as 1927 by Landau for describing the interaction of a radiation field with electrical charges and in 1936 by Fermi for modeling neutron scattering [8]. It was only in 1976, however, that Gorini, Kossakowski, and Sudarshan [9] and independently Lindblad [10] formulated the general expression for the generator of the quantum dynamical semigroup, putting the field of OQS on firm theoretical grounds. The complete positivity of the generator, essential to describe a physical evolution of entangled states, had until then been ignored [8].

Since then, the field of OQS has investigated fascinating topics, ranging from irreversibility [11] to the emergence of classicality in large systems [12] and stochastic quantum trajectories [13]. Despite these remarkable developments, OQS played a relatively marginal role in physics for many decades following the seminal papers [9, 10]. The recent surge of quantum technologies, ranging from digital [14] and analog [15] computation to secure communication [16] and metrology [17], and the associated compelling need to shield quantum systems from environmental decoherence and dissipation, completely changed the scenario, elevating OQS to an integral part of quantum mechanics. This boosted the methodological research in OQS, leading, for instance, to the development of efficient pure-state unraveling schemes [18] and novel approaches for mesoscopic environments [19]. In the last two decades, in the context of many-body quantum systems, MPS algorithms [20, 21], based on the efficient compressions and the local manipulations of wave functions, have established themselves as very effective numerical methods for simulating the dynamics of stronly-correlated low-dimensional systems. While initially developed for isolated systems, in the past ten years MPS methods have been successfully applied to compute dissipative dynamics [22–24] or to directly target the non-equilibrium steady states of dissipative systems via a variational approach [25] (see Chapter 3).

Let us come back to our definition of a dissipative quantum system. It is clearly very restrictive, as A and B can exhibit strong coupling and similar relaxation timescales in many physically relevant cases. Then, to calculate B's dynamical impact on A, one typically needs to evolve the joint system explicitly, i.e. solve the Schrödinger equation for AB and then compute A's reduced state by tracing out B. For specific systems, non-Markovian methods have been developed, which allow to treat both a strong coupling between A and B and strong memory effects in B [26]. However, non-Markovian equations of motion are typically much more complex to solve than their Markovian counterparts, and their numerical cost can become comparable to that of evolving AB unitarily. Thus, in Chapter 4, we perform a systematic comparison of different approaches for studying strongly-coupled, non-Markovian environments. We underline the strengths and weaknesses of all considered methods, outlining the parameter regimes in which they perform best.

Throughout this thesis, we will study scenarios of increasing methodological complexity. In quantum thermodynamics, a topic that has attracted massive attention in 2024 [27] is the exponential acceleration of thermalization processes in dissipative quantum systems. In 2020, the controversial Mpemba effect, colloquially indicating the phenomenon of "hot water freezing faster than cold water," was unambiguously measured in colloidal systems [28]. Shortly after, the effect started being explored in quantum dissipative systems [29]. In Chapter 5, considering single-and few-qubit Markovian setups, we study the interplay between initial quantum coherences and dissipation and devise an exact unitary transformation that reveals a genuine Mpemba effect in dissipative quantum systems.

Vibrational systems constitute some of the most relevant environments for electrons. In the context of quantum chemistry, molecular vibrational degrees of freedom can be investigated with infrared or Raman spectroscopy [30] and are essential in describing photo-induced exciton dynamics in molecular crystals [31]. Even in biological systems, the exciton dynamics in light-harvesting complexes involved in the early stages of photosynthesis [32, 33] are strongly affected by protein vibrations. These environments are often characterized by long memory effects, which cannot be described by a Markovian dissipative master equation but must be accounted for explicitly. Usually, they are modeled as collections of quantum harmonic oscillators. Bosonic degrees of freedom, such as quantum harmonic oscillators, are very challenging to describe numerically due to the formally infinite dimensionality of their Hilbert spaces. In the context of MPS, however, crucial recent advances in their representation [34, 35] and time-evolution [36, 37] have enabled the exact numerical description of large vibrational environments. In Chapter 6, we combine these methods with an OQS Markovian-embedding approach [38] to study the dynamics of a single electronic excitation in a structured vibrational environment. Directly comparing our approach to a unitary evolution, we demonstrate that in this context, we can use weak dissipation as a valuable computational resource.

Furthermore, vibrational environments also play a crucial role in condensed matter physics, where phonons (quantized lattice vibrations) are instrumental in determining different equilibrium properties of solids, such as their specific heat and thermal conductivity [39]. Notably, at low temperatures, phonons can mediate an effective electron-electron attraction leading to superconductivity, as Barden, Cooper, and Schrieffer described in their seminal paper in 1957 [40]. A more recent class of exciting experiments concerns probing the electronic response of a system following the optical pumping of infrared-active phonon modes. The most notable example in this field is the observation of light-induced superconducting-like electronic states out of equilibrium [41, 42]. Despite significant efforts [43–46], the modeling and interpretation of these experiments remains challenging. In Chapter 7, we study the electron dynamics following a coherent photo-excitation of the phonon modes in a 1D metal. We introduce a new numerical method dubbed phonon state tomography (PST), which allows us to study the impact of different pulse shapes and phonon frequencies. We find that small phonon frequencies enable long-range electron correlation to dominate over phonon-induced disorder.

While representing vibrational environments via collections of quantum harmonic oscillators has proven very successful across different scientific fields, more accurate descriptions are desirable in some cases. In the context of phonons, extensions accounting for anharmonicities [47, 48] and dispersive behaviour [49, 50] have been proposed. In Chapter 8, we take a different approach and consider dissipative phonons. This represents a first step in going beyond the coherent, isolated phonons paradigm and implicitly accounting for effects such as phonon-impurity and phonon-phonon scattering, which can be present in real materials. Specifically, by studying the famous Hubbard-Holstein model, we show that strong dissipation dramatically suppresses the mobility of the bipolaronic quasiparticles.

Part I

Theory and Methods

In the first part of this thesis, we focus on the theory and numerical methods for quantum dissipative and vibrational systems.

We start by giving a brief overview of the vast field of open quantum system (OQS) in Chapter 2. Two crucial numerical tools for the description of OQS are vectorization and pure-state unravelings. The former is essential for investigating spectral properties, while the latter is better suited for dealing with the dynamics of large systems. We also present methods for non-Markovian OQS and their link to Markovian descriptions via Markovian embedding. We conclude our analysis of OQS considering structured vibrational environments and why the widespread practice of replacing a global environment with a local environment for each degree of freedom of the system of interest can be justified.

In Chapter 3, we introduce the tensor network methods used for most applications presented in this thesis. We summarize some basic concepts about MPS and mention two recent developments that have greatly enhanced the size of the vibrational systems that one can describe numerically, namely projected purification (PP) and local subspace expansion time-dependent variational principle (LSE-TDVP). Then, we consider the description of large-scale OQS dynamics with MPS, pointing out some subtle issues regarding the numerical implementations. Moreover, we introduce a novel method dubbed phonon state tomography (PST), which is a valuable tool for analyzing the impact of phonon excitations on electron dynamics.

Finally, in Chapter 4, we compare the accuracy and efficiency of a non-Markovian and a Markovian-embedded description of a many-body, dissipative electron-phonon system. Surprisingly, the two methods are very similar in complexity but excel in accuracy in complementary parameter regimes.

We collected many of the methods discussed in this thesis in the Python package EVOS. The package contains NumPy-based ED solvers for OQS dynamics and serves as an interface with SyTen [51, 52] for dissipative MPS calculations.

Chapter 2

Open quantum systems (OQSs)

This chapter provides an overview of open quantum systems (OQSs) from a numerical perspective. In Section 2.1, we give a short introduction to OQS, sketching the main steps of the derivation of the Lindblad equation and outlining the difference between Markovian and non-Markovian systems. Then, in Section 2.2, we present vectorization, a valuable tool for solving the Lindblad equation, which will be essential to study the quantum Mpemba effect in Chapter 5. In a complementary approach to vectorization, the equations of motion for large dissipative systems can be efficiently solved using pure-state unraveling methods for both Markovian (Sections 2.3 and 2.4) and non-Markovian systems (Section 2.5). We also consider structured vibrational environments in Section 2.6, which can be captured by non-Markovian or Markovian-embedded methods. In conclusion, we discuss the approximations implied when transitioning from global to local environments in Section 2.7 and mention the main features of the Python package EVOS, in which we collected many time evolution methods for OQS. This chapter is partially based on Refs. [1, 4].

2.1 Brief introduction to OQS

The field of open quantum systems (OQSs) studies the influence of quantum environments on a system of interest. While OQS approaches had already been used for a long time for instance in quantum optics [9], its theoretical foundations were laid in 1976 by the pioneering work of Gorini, Kossakowski, and Sudarshan [9] and independently Lindblad [10]. The two seminal papers provided the most general linear equation of motion for density matrices under the assumption of Markovianity (we will define Markovianity shortly). This equation is known as the Gorini-Kossakowski-Sudarshan-Lindblad equation or simply the Lindblad equation for short. Here, we will not include the complete derivation of the Lindblad equation but sketch some of the most relevant implied approximations. We will follow closely [53], to which we refer for a detailed yet accessible presentation.

Consider an arbitrary quantum system whose total Hamiltonian is partitioned as

$$\hat{H} = \hat{H}_S + \hat{H}_E + \lambda \hat{H}_I \,, \tag{2.1}$$

where $\hat{H}_S$ and $\hat{H}_E$ are the system and environment Hamiltonians, respectively, and $\hat{H}_I$ represents the interaction between the two. In the interaction picture, the density matrix $\hat{\rho}$ for the combined state of the system and the environment obeys the Liouville-von Neumann equation

$$\frac{\mathrm{d}\hat{\rho}(t)}{\mathrm{d}t} = -i\lambda [\hat{H}_I(t), \hat{\rho}(t)] \,, \tag{2.2}$$

where $\hat{H}_I(t) = e^{i(\hat{H}_S+\hat{H}_E)t} \hat{H}_I e^{-i(\hat{H}_S+\hat{H}_E)t}$. Now, we perform the weak coupling approximation, also known as the Born approximation, i.e., we consider $\lambda \ll 1$. Then, when expanding Eq. (2.2) as a Dyson series

$$\frac{\mathrm{d}\hat{\rho}(t)}{\mathrm{d}t} = -i\lambda [\hat{H}_I(t), \hat{\rho}(0)] - \lambda^2 \int_0^t \mathrm{d}s [\hat{H}_I(t), [\hat{H}_I(s), \hat{\rho}(t)]] \quad (+\mathcal{O}(\lambda^3)) \tag{2.3}$$

we can discard the contributions of order λ^3 and higher. Next, we define the reduced density matrix $\hat{\rho}_s$ for the system's degrees of freedom as the partial trace of $\hat{\rho}$ over the environment $\hat{\rho}_s(t) = \mathrm{Tr}_E\,(\hat{\rho}(t))$ obtaining

$$\frac{\mathrm{d}\hat{\rho}_s(t)}{\mathrm{d}t} = -i\lambda \, \mathrm{Tr}_E\left([\hat{H}_I(t), \hat{\rho}(0)]\right) - \lambda^2 \int_0^t \mathrm{d}s \, \mathrm{Tr}_E\left([\hat{H}_I(t), [\hat{H}_I(s), \hat{\rho}(t)]]\right) . \tag{2.4}$$

It can be shown that if we assume that at the initial time, the total state factorizes as $\hat{\rho}(0) = \hat{\rho}_s(0) \otimes \hat{\rho}_E^{\beta}(0)$, where $\hat{\rho}_E^{\beta}(0)$ denotes the thermal state $\exp\left(-\beta\hat{H}_E\right)/\,\mathrm{Tr}\left((\exp\left(-\beta\hat{H}_E\right))\right)$, the first term in Eq. (2.4) vanishes [53]. To make progress, we need to perform the important Markovian[1] (or memoryless) approximation, i.e. we assume that the environment's relaxation and correlation times are much shorter than the system's characteristic timescale. This allows us to make two substantial simplifications. First, in the weak-coupling regime, we can assume that at any time the total state is $\hat{\rho}(t) = \hat{\rho}_s(t) \otimes \hat{\rho}_E(0)$. Second, we can extend the integration limit in Eq. (2.4) to ∞, since only terms where s is close to t will give nonzero contributions. Then, performing the variable change $s \to t - s$ we get

$$\frac{\mathrm{d}\hat{\rho}_s(t)}{\mathrm{d}t} = -\lambda^2 \int_0^\infty \mathrm{d}s \, \mathrm{Tr}_E\left([\hat{H}_I(t), [\hat{H}_I(t-s), \hat{\rho}_s(t) \otimes \hat{\rho}_E(0)]]\right) . \tag{2.5}$$

---

[1] It is named after the Russian mathematician Andrey Markov, who made important contributions to the field of stochastic processes and initiated the study of what became known as Markov chains.

Eq. (2.5), known as the Redfield equation, is Markovian but does not in general preserve the positivity of $\hat{\rho}_s(t)$.

To arrive at the Lindblad equation, one has to perform the rotating wave approximation, which consists of expanding $\hat{H}_I$ and neglecting the fast oscillating terms. Unlike the Born and Markov approximations, the rotating wave approximation is not a restrictive requirement from a physical point of view. However, it implies a long sequence of non-trivial algebraic steps for which we refer to [53] and mention the final result here. After transforming back from the interaction to the Schrödinger picture one obtains

$$\frac{\mathrm{d}\hat{\rho}_s(t)}{\mathrm{d}t} = -i[\hat{H}_S + \hat{H}_\mathrm{L}, \hat{\rho}_s] + \overbrace{\sum_l \hat{L}_l \hat{\rho}_s \hat{L}_l^\dagger - \frac{1}{2}\{\hat{L}_l^\dagger \hat{L}_l, \hat{\rho}_s\}}^{\mathscr{D}(\hat{\rho}(t))} \equiv \mathscr{L}\hat{\rho}(t)\,. \tag{2.6}$$

This is the celebrated Lindblad equation, which is as central to OQS as the Schrödinger equation to isolated systems. On the r.h.s. of Eq. (2.6) we have introduced the *Lindbladian* superoperator $\mathscr{L}$. The operators $\hat{L}_l$ are referred to as *jump operators* and are closely related to the interaction Hamiltonian $\hat{H}_I$. The non-Hermitian part of Eq. (2.6) denotes the effective interaction with the environment and is called *dissipator* $\mathscr{D}$. $\hat{H}_\mathrm{L}$, known as the Lamb shift Hamiltonian, commutes with $\hat{H}_S$ and describes the environment-induced renormalization of the energy levels of the system.

The derivation of Eq. (2.6) sketched above is referred to as microscopic derivation or physical derivation because one can use it to obtain a specific Lindblad equation starting from a particular system of interest Eq. (2.1). However, to show that Eq. (2.6) represent the most general linear, Markovian equation of motion for density matrices, one can follow a so-called mathematical derivation which, in the spirit of the original papers [9] and [10] does not start by assuming a microscopic model Eq. (2.1). For a very accessible presentation of the mathematical derivation of the Lindblad equation, we refer to [54].

The Lindbladian superoperator $\mathscr{L}$ is known as the Markovian completely positive trace-preserving (CPT) generator. While the trace-preserving property simply ensures that the state is normalized at every time, complete positivity is a less trivial concept worth discussing. A map Φ between matrices (i.e., a superoperator) is said to be positive if it maps positive matrices to positive matrices, i.e., $\Phi : \mathscr{M}^N \to \mathscr{M}^N$, where $\mathscr{M}^N$ denotes the set of N-dimensional positive matrices. Φ is called completely positive if its composition with the identity $\mathbb{1}^d$ is positive $\forall d$, i.e. $\Phi \otimes \mathbb{1}^d : \mathscr{M}^{Nd} \to \mathscr{M}^{Nd}$. Complete positivity is crucial for guaranteeing a physical evolution since positive *but not completely positive* maps can turn positive, multipartite, entangled states into non-positive ones. The most famous example of such a map is partial transposition, obtained by composing the positive map T (which switches the row and column indices of a matrix) with an identity map. For a two-qubit system, $\Phi \equiv T \otimes \mathbb{1}^2$ maps the Bell state $\hat{\rho}^{(B)} = |\psi^{(B)}\rangle \langle\psi^{(B)}|$ with $|\psi^{(B)}\rangle = 1/\sqrt{2}(|00\rangle + |11\rangle)$ to

$$\Phi\left(\hat{\rho}^{(B)}\right) = \frac{1}{2}\begin{pmatrix} 1 & 0 & 0 & 0 \\ 0 & 0 & 1 & 0 \\ 0 & 1 & 0 & 0 \\ 0 & 0 & 0 & 1 \end{pmatrix} , \tag{2.7}$$

which is non-positive since it has spectrum $1/2(1, 1, 1, -1)$. Partial transposition can also be used as an entanglement witness for low-dimensional, bipartite, mixed states [55].

The Lindblad equation Eq. (2.6) tells us that the state of the system at time $\hat{\rho}(t')$ depends only on the state of the system at an infinitesimally earlier time $\hat{\rho}(t' - \delta t')$. This directly followed from imposing the Markovian approximation, which allowed us to obtain Eq. (2.5). The Markovian approximation is typically justified when the weakly-coupled environment is at a high temperature and interacts with many system frequencies with equal strength. However, in a general setup, $\hat{\rho}_s(t')$ can depend on the whole dynamical history of $\hat{\rho}_s$, i.e. on $\hat{\rho}_s(t)\ \forall t < t'$. This can be described by a non-Markovian CPT generator $\mathscr{K}(t)$, yielding [6]

$$\frac{\mathrm{d}}{\mathrm{d}t}\hat{\rho}_s(t) = \mathscr{K}(t)\hat{\rho}_s(t) . \tag{2.8}$$

In 2010, Laine, Piilo, and Breuer introduced a simple approach for characterizing the non-Markovianity of a general (CPT) map $\Phi_t \equiv \exp(\mathscr{K}(t)t)$ [56]. They studied the trace distance between two states $D(\hat{\rho}_1, \hat{\rho}_2) \equiv 1/2\,\mathrm{Tr}\Big(\sqrt{(\hat{\rho}_1 - \hat{\rho}_2)^\dagger(\hat{\rho}_1 - \hat{\rho}_2)}\Big)$. D is invariant under unitary transformation. Moreover, since in a Markovian evolution there is only flow from the system to the environment, the rate of change of D,

$$\sigma(t, \hat{\rho}_{1,2}) \equiv \frac{\mathrm{d}}{\mathrm{d}t}D(\Phi_t(\hat{\rho}_1), \Phi_t(\hat{\rho}_2)) , \tag{2.9}$$

will always be negative for a Markovian process described by $\Phi_t = e^{\mathscr{L}t}$, denoting a steady equilibration with the environment. Thus, a positive σ, indicating the flow of information from the environment to the system, can be taken as a witness of non-Markovianity.

Non-Markovian dynamics are, in general, very challenging to describe. However, we will discuss in Section 2.5 that efficient non-Markovian descriptions have been introduced for an important class of systems.

2.2 Vectorization

One of the most useful tools for studying OQS is *vectorization* [57, 58]. When applied to a matrix, it simply consists in reshaping it into a vector by stacking its columns and is usually denoted as vec():

$$\mathrm{vec}\begin{pmatrix} a & b \\ c & d \end{pmatrix} \to \begin{pmatrix} a \\ b \\ c \\ d \end{pmatrix} . \tag{2.10}$$

A vectorized matrix, as for instance the density matrix $\hat{\rho}_s$, is typically represented with a double bracket: $\mathrm{vec}(\hat{\rho}_s) \equiv |\rho_s\rangle\rangle$. Most importantly, vectorization can also be used to recast a superoperator into an operator. For the Lindbladian superoperator $\mathscr{L}$, this can be achieved by using a general property of vectorization, namely that three matrices $\hat{M}_1$, $\hat{M}_2$ and $\hat{M}_3$ satisfy

$$\mathrm{vec}(\hat{M}_1\hat{M}_2\hat{M}_3) = (\hat{M}_3^T \otimes \hat{M}_1)\mathrm{vec}(\hat{M}_2) . \tag{2.11}$$

With this, the Lindbladian Eq. (2.6) can be written in vectorized form as [57]

$$\begin{aligned} \hat{\mathscr{L}} &= -i\hat{H}_S \otimes \hat{\mathbb{1}} + i\hat{\mathbb{1}} \otimes \hat{H}_S^T + \\ \sum_l \hat{L}_l &\otimes \left(\hat{L}_l^\dagger\right)^T - \frac{1}{2}\hat{L}_l^\dagger \hat{L}_l \otimes \hat{\mathbb{1}} - \frac{1}{2}\hat{\mathbb{1}} \otimes \left(\hat{L}_l^\dagger \hat{L}_l\right)^T . \end{aligned} \tag{2.12}$$

The normalization condition for a density matrix $\hat{\rho}_s$ can be obtained by observing that the Hilbert Schmidt inner product reduces to the regular inner product in the vectorized framework $\mathrm{Tr}\left(\hat{M}_1^\dagger \hat{M}_2\right) = \langle\langle M_1 || M_2 \rangle\rangle$ [57] and thus a physical state needs to obey

$$\langle\langle \mathbb{1} || \rho_s \rangle\rangle = 1 , \tag{2.13}$$

where $|\mathbb{1}\rangle\rangle$ is the vectorized identity matrix. Then, using the relation $\langle\langle O| = \langle\langle \mathbb{1}|(\mathbb{1} \otimes \hat{O})$, the expectation value of an observable $\hat{O}$ can be written as

$$\langle \hat{O} \rangle = \frac{\mathrm{Tr}\left(\hat{\rho}_s \hat{O}\right)}{\mathrm{Tr}\left(\hat{\rho}_s\right)} = \frac{\langle\langle \mathbb{1}|\mathbb{1} \otimes \hat{O}|\rho_s\rangle\rangle}{\langle\langle \mathbb{1}|\rho_s\rangle\rangle} . \tag{2.14}$$

Vectorization presents several useful features. First, it allows us to recast the Lindblad equation into an imaginary-time Schrödinger equation with a non-Hermitian Hamiltonian

$$\frac{\mathrm{d}}{\mathrm{d}t}|\rho_s\rangle\rangle = \hat{\mathscr{L}}|\rho_s\rangle\rangle , \tag{2.15}$$

which can be solved with standard numerical techniques (for instance, by computing the exponential $\exp\left(\hat{\mathscr{L}} t\right)$ with exact diagonalization (ED)). Second, it gives us access to the Lindbladian spectrum, which, analogously to the Hamiltonian spectrum for isolated systems, holds crucial information about the energy spacing of the excited states and the slow-decaying system modes (which will be central to the study of the Mpemba effect in Chapter 5). In the typical case of a Lindbladian with a unique steady state, the spectrum of $\hat{\mathscr{L}}$ will have a zero eigenvalue with multiplicity 1 corresponding to it. The remaining eigenvalues have a non-positive real part and come in complex conjugate pairs due to the Hermiticity-preserving property of the Lindbladian [59]. Thus, vectorization offers a simple way to compute the steady state of the system, which is the eigenvector of the Lindbladian relative to the zero eigenvalue. Finally, we anticipate that vectorization can be used to compute the dynamics of Markovian and non-Markovian OQS with MPS methods (see Section 3.2.1).

2.3 Quantum jumps (QJ)

While vectorization gives an in principle simple prescription for solving the Lindblad equation (i.e. exponentiating $\hat{\mathscr{L}}$), it is in practice not very efficient for large systems, because vectorized mixed states have dimension D^2, where D is the dimension of the system's Hamiltonian. A solution scheme based on the propagation of D-dimensional pure states would thus be highly desirable. To this end, following closely Daley's review [18], here we present a version of quantum jumps (QJ), a pure-state unraveling method that allows us to obtain the dissipative dynamics of a mixed state by averaging over an ensemble of stochastic pure-states dynamics.

The first step of QJ consists in introducing an effective, non-Hermitian Hamiltonian

$$\hat{H}_{\text{eff}} \equiv \hat{H}_S - \frac{i}{2} \sum_l \hat{L}_l^\dagger \hat{L}_l \, . \tag{2.16}$$

This enables us to express the Lindblad equation Eq. (2.6) as

$$\partial_t \hat{\rho}_s = -i(\hat{H}_{\text{eff}} \hat{\rho}_s - \hat{\rho}_s \hat{H}_{\text{eff}}^\dagger) + \sum_l \hat{L}_l \hat{\rho}_s \hat{L}_l^\dagger \, . \tag{2.17}$$

When dealing with pure states, we introduce a stochastic process $\mathcal{Q}$ to obtain the time evolution of the density matrix through averaging over N realizations:

$$\frac{1}{N} \sum_{q=1}^{N} |\Psi(t)_{\text{q}}\rangle \langle \Psi(t)_{\text{q}}| \equiv \mathscr{E}_N[|\Psi(t)_{\text{q}}\rangle \langle \Psi(t)_{\text{q}}|] = \hat{\rho}_{sN}(t) \, . \tag{2.18}$$

Here, $q \in \mathcal{Q}$ represents a set of pseudo-random numbers that characterizes a so-called trajectory. Formally, this will converge to the exact Lindblad-evolved density matrix for an infinite number of trajectories $\hat{\rho}_{sN}(t) \xrightarrow{N\to\infty} \hat{\rho}_s(t)$. Instead of constructing the density matrix directly, it is numerically more efficient to calculate the observables of interest for each trajectory and subsequently compute their averages:

$$\langle \hat{O} \rangle_N(t) = \mathscr{E}_N[\langle \Psi(t)_{\text{q}}| \hat{O} |\Psi(t)_{\text{q}}\rangle] \, . \tag{2.19}$$

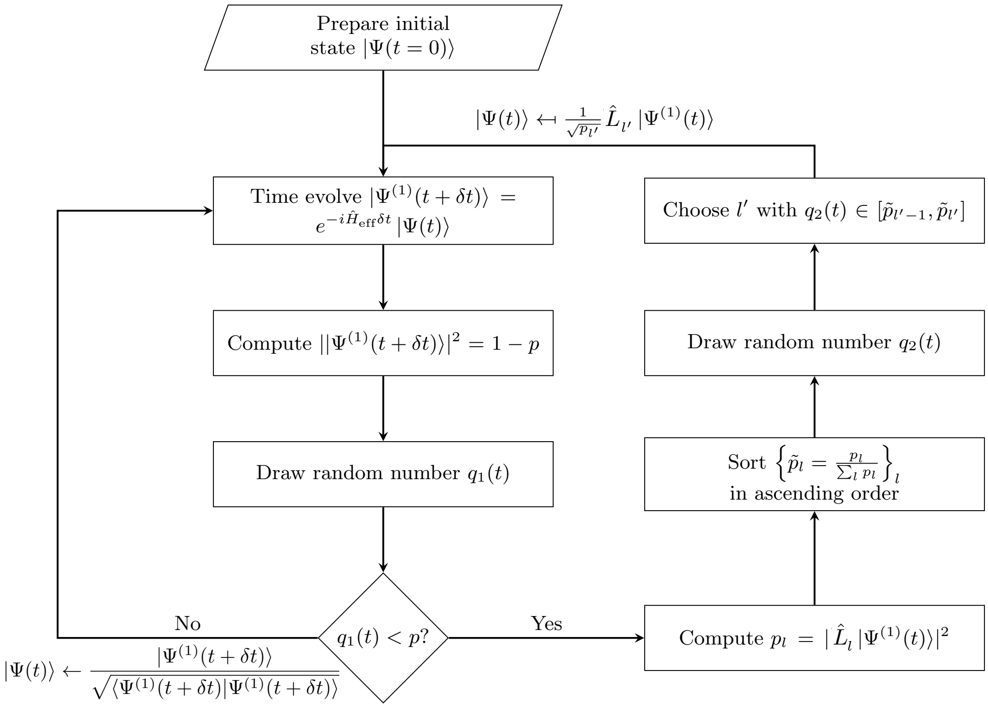

Figure 2.1: Algorithmic sketch of the quantum jumps (QJ) method.

For a trajectory specified by two collections of random numbers $q = (q_1(t), q_2(t))$ uniformly distributed between 0 and 1, the algorithm for computing one step of the time evolution of $|\Psi(t)\rangle_{\mathrm{q}}$ is shown in Fig. 2.1. The central idea is to expand the time-evolved state to first order and break down the change in its norm, which serves as a measure for the magnitude of the non-Hermitian (i.e. dissipative) component:

$$||\Psi^{(1)}(t+\delta t)\rangle|^2 = 1 - p \approx 1 - \delta t \sum_l \langle\Psi(t)|\,\hat{L}_l^\dagger \hat{L}_l\,|\Psi(t)\rangle \equiv 1 - \sum_l p_l\,. \tag{2.20}$$

Subsequently, we select the random number $q_1(t)$ and compare it to the overall norm change p to determine whether a jump should occur or not. If a jump is required, the second random number $q_2(t)$ is chosen to select the specific jump operator, based on the various jump probabilities $\delta t\,\langle\Psi(t)|\,\hat{L}_l^\dagger \hat{L}_l\,|\Psi(t)\rangle$. When the algorithm mentioned above is applied for each trajectory q, the averaging over the projectors in the limit $N \to \infty$ leads to

$$\begin{aligned}
\hat{\rho}_s(t+\delta t) &= \mathscr{E}_\infty[|\Psi(t)_\mathrm{q}\rangle\langle\Psi(t)_\mathrm{q}|] \\
&= (1-p)\frac{|\Psi^{(1)}(t+\delta t)\rangle}{\sqrt{1-p}}\frac{\langle\Psi^{(1)}(t+\delta t)|}{\sqrt{1-p}} + \sum_l \frac{p_l}{p}\frac{\hat{L}_l|\Psi(t)\rangle}{\sqrt{p_l/\delta t}}\frac{\langle\Psi(t)|\hat{L}_l^\dagger}{\sqrt{p_l/\delta t}} \\
&= \hat{\rho}_s(t) - i\delta t(\hat{H}_\mathrm{eff}\hat{\rho}_s - \hat{\rho}_s\hat{H}_\mathrm{eff}^\dagger) + \delta t\sum_l \hat{L}_l\hat{\rho}_s\hat{L}_l^\dagger\,.
\end{aligned} \tag{2.21}$$

This expression precisely converges to the Lindblad equation in the limit $\delta t \to 0$.

Using the independence of different trajectories, one can estimate the statistical error ϵ_{O_N} for the expectation value of an observable $\hat{O}$ as [18]

$$\epsilon_{O_N} = \frac{\sqrt{\langle\hat{O}^2\rangle_N - \langle\hat{O}\rangle_N^2}}{N}\,, \tag{2.22}$$

i.e. as the estimated standard deviation computed for N trajectories divided by $\sqrt{N}$. In this thesis, when plotting a quantity obtained with a pure-state unraveling method, we will always set the error bars equal to Eq. (2.22). The number of trajectories needed to obtain statistically converged observables can depend on the model, the parameters, and the system size. In practice, for the models analyzed here, we found that we usually needed to compute between $N = 100$ and $N = 1000$ trajectories. The other crucial convergence parameter for QJ is the time step δt. Since at most one jump per time step is allowed by construction, when the coupling between the system and the environment is strong, δt needs to be chosen small enough not to underestimate the environment's effect.

2.4 Quantum state diffusion (QSD)

An alternative method for unraveling the Lindblad master equation Eq. (2.6) is known as the linear quantum state diffusion (lQSD) method [60]. The main difference to the QJ approach is that the stochastic component is not an external process encoded in strong jumps happening only at certain time steps but rather an intrinsic part of the effective Hamiltonian. For clarity, it is now convenient to explicitly write down the system-environment coupling c_l relative to the l-th jump operator (which we had absorbed in $\hat{L}_l$ in Eq. (2.6)), i.e. consider $\hat{L}_l \to \sqrt{c_l}\hat{L}_l$. For each trajectory, the time evolution is generated by a non-Hermitian Hamiltonian, as outlined in [61]:

$$\hat{H}^z_\mathrm{eff}(t) = \hat{H}_S + i\sum_l\left[z_l(t)\hat{L}_l - \frac{c_l}{2}\hat{L}_l^\dagger\hat{L}_l\right]\,, \tag{2.23}$$

where $\hat{H}_\mathrm{s}$ represents the system Hamiltonian, $\hat{L}_l$ is a jump operator, and $z_l(t)$ is a random number drawn from a real-valued Gaussian distribution with a mean of zero and a standard deviation σ, which corresponds the square root of the coupling parameter c_l divided by the time step δt. With this, the time evolution for one trajectory $|\Psi_z(t)\rangle$ is given by

$$\partial_t |\Psi_z(t)\rangle = -i\hat{H}^z_\mathrm{eff}(t) |\Psi_z(t)\rangle \ . \tag{2.24}$$

To demonstrate the first-order equivalence between the Lindblad and the lQSD evolution, we perform a first-order expansion of the state $|\Psi_z(t)\rangle$ using the effective Hamiltonian Eq. (2.23). For clarity, we will consider the case involving only one jump operator $\hat{L}$ and drop the z subscript for the wavefunction:

$$|\Psi(t+\delta t)\rangle \approx \big[1 + \delta t\big(-i\hat{H}_s + \hat{L}z(t) - \frac{c}{2}\hat{L}^\dagger \hat{L}\big)\big] |\Psi(t)\rangle \ . \tag{2.25}$$

To first order in δt, keeping in mind that z^2 is of $\mathcal{O}(\delta t^{-1})$, the outer product of Eq. (2.25) with its Hermitian conjugate is

$$\begin{aligned} |\Psi(t+\delta t)\rangle \langle \Psi(t+\delta t)| \approx{}& |\Psi(t)\rangle \langle\Psi(t)| + \delta t\big(-i\hat{H}_s + \hat{L}z(t) - \frac{C}{2}\hat{L}^\dagger\hat{L}\big) |\Psi(t)\rangle\langle\Psi(t)| \\ &+ |\Psi(t)\rangle\langle\Psi(t)| \, \delta t\big(+i\hat{H}_s + \hat{L}^\dagger z(t) - \frac{C}{2}\hat{L}^\dagger\hat{L}\big) \\ &+ \delta t^2 z^2(t)\hat{L} |\Psi(t)\rangle\langle\Psi(t)| \hat{L}^\dagger \ . \end{aligned} \tag{2.26}$$

By utilizing the mean and variance of z, which are $\mathscr{E}_\infty[z(t)] = 0$ and $\mathscr{E}_\infty[z^2(t)] = \frac{c}{\delta t}$, we proceed to calculate the ensemble average over the projectors

$$\begin{aligned} \mathscr{E}_\infty[|\Psi(t+\delta t)\rangle\langle\Psi(t+\delta t)|] = \hat{\rho}_s(t+\delta t) &\approx \hat{\rho}_s(t) + \delta t(-i\hat{H}_s - \frac{c}{2}\hat{L}^\dagger\hat{L})\hat{\rho}_s(t) \\ &+ \hat{\rho}_s(t)\delta t(+i\hat{H}_s - \frac{c}{2}\hat{L}^\dagger\hat{L}) + \delta t^2\frac{c}{\delta t}\hat{L}\hat{\rho}_s(t)\hat{L}^\dagger \\ &= \hat{\rho}_s(t) + \delta t\big(-i[\hat{H}_s, \hat{\rho}_s(t)] - \frac{c}{2}\{\hat{L}^\dagger\hat{L}, \hat{\rho}_s(t)\} + c\hat{L}\hat{\rho}_s(t)\hat{L}^\dagger\big) \ . \end{aligned}$$

In the limit where δt approaches zero, the expression obtained converges to the Lindblad equation.

To potentially reduce the required number of trajectories for achieving observable convergence in this pure-state method, one can employ a modification of Eq. (2.23) known as non-linear quantum state diffusion (nlQSD) Hamiltonian [60, 61]

$$\hat{H}^z_\mathrm{eff}(t) = \hat{H}_S + i\sum_l \big[z_l(t)\hat{L}_l - \frac{c_l}{2}\hat{L}_l^\dagger\hat{L}_l + c_l\langle\Psi(t)|(\hat{L}_l^\dagger + \hat{L}_l)|\Psi(t)\rangle\,\hat{L}_l\big] \ . \tag{2.27}$$

The nonlinear dynamics generated by the Hamiltonian given in Eq. (2.27) can be linearized by computing the expectation value using the state $|\Psi(t-\delta t)\rangle$. This approximation is reasonable if the time step δt is small.

2.5 Hierarchy of pure states (HOPS)

The Lindblad equation Eq. (2.6), which describes explicitly only the dynamics of a system of interest, represents a huge simplification compared to the Schrödinger equation for the combined system and environment. Its derivation, starting from a microscopic model for the combined system and environment, requires stringent assumptions (weak system-environment coupling, memoryless environment, rotating wave approximation), which strongly limit its range of applicability. Loosely speaking, it is unreasonable to assume that for arbitrary setups, accounting only effectively for the environment will yield a good description of the system's dynamics. Nonetheless, an exact open quantum system approach can be formulated for certain classes of systems without any assumption on the coupling strengths or the separations of timescales. Moreover, equally importantly, these descriptions can be formulated as pure-state unravelings.

Let us consider the usual Hamiltonian partitioning

$$\hat{H} = \hat{H}_S + \hat{H}_E + \hat{H}_I \ , \tag{2.28}$$

where $\hat{H}_S$ and $\hat{H}_E$ are the system and environment Hamiltonians, respectively, and $\hat{H}_I$ represents the interaction between the two. While the system Hamiltonian can be an arbitrary Hermitian operator, the bosonic environment Hamiltonian needs to be a collection of harmonic oscillators[2]

$$\hat{H}_E = \sum_p \omega_p \hat{a}_p^\dagger \hat{a}_p \ . \tag{2.29}$$

Here $\hat{a}_p^\dagger$ ($\hat{a}_p$) creates (annihilates) a vibrational mode with frequency ω_p. Moreover, we require the interaction Hamiltonian to take the linear form

$$\hat{H}_\mathrm{I} = \sum_{j,p} g_{jp} \hat{L}_j \hat{a}_{jp}^\dagger + g_{jp}^* \hat{L}_j^\dagger \hat{a}_{jp} \ , \tag{2.30}$$

where $\hat{L}_j$ is an arbitrary operator acting on the system's degrees of freedom. This interaction form is used to model a broad class of phenomena, ranging from electron transport in solids [63] to exciton dynamics in molecules [64, 65] and comprises central toy models like the spin-boson model.

For the sake of simplicity (and anticipating Chapters 4 and 8) in the following we will consider a constant vibrational frequency ω for the environment and, for every system site, one harmonic oscillator locally coupled to it with strength g, so that $\hat{H}_\mathrm{I} = g \sum_j \left(\hat{L}_j \hat{a}_j^\dagger + \hat{L}_j^\dagger \hat{a}_j \right)$. In analogy to the Markovian quantum state diffusion (QSD) introduced in the previous section, the trajectory-unraveled dynamics of the subsystem is described by the non-Markovian quantum state diffusion

---

[2] For fermionic environments, which were not considered in this thesis, we refer the reader to [62].

(NMQSD) equation [60]

$$\partial_t |\psi(t)\rangle = -i\hat{H}_s |\psi(t)\rangle + g \sum_j \hat{L}_j z_j^*(t) |\psi(t)\rangle - g \sum_j \hat{L}_j^\dagger \int_0^t \mathrm{d}s\, \alpha^*(t-s) \frac{\delta |\psi(t)\rangle}{\delta z_j^*(s)} \ . \tag{2.31}$$

Here, $\alpha(t)$ denotes the environment correlation function, $z_j(t)$ is a noise term for site j, and $\delta/\delta z_j^*(s)$ represents the functional derivative with respect to z_j^* at time s. At zero temperature, $\alpha(t)$ can be expressed as the Fourier transform of the spectral density $J(\omega)$:

$$\alpha(t-t') \equiv \langle \hat{a}(t)\hat{a}^\dagger(t')\rangle = \frac{1}{\sqrt{2}} \int_{-\infty}^{+\infty} \mathrm{d}\omega\, J(\omega) e^{-i\omega(t-t')} \ . \tag{2.32}$$

Instead, at finite temperature, the relationship between the environment correlation function and the spectral density is given by:

$$\alpha(t-t') = \frac{1}{\pi} \int_0^\infty \mathrm{d}\omega\, J(\omega)\big[\coth\big(\frac{\beta\omega}{2}\big)\cos\big(\omega(t-t')\big) - i \sin\big(\omega(t-t')\big)\big] \ . \tag{2.33}$$

Here, β represents the inverse temperature. In the subsequent discussions, we consider $T = 0$ and refer to [66] for the finite-temperature case (which amounts to modifying the effective Hamiltonian). Moreover, we impose that the environment correlation function is described by a single complex exponential, i.e., $\alpha(t-t') = e^{-\kappa|t-t'|-i\omega(t-t')}$. We will relax this condition on $\alpha(t)$ at the end of this section when we consider a more general interaction Hamiltonian Eq. (2.30). The colored noise $z_j(t)$ satisfies $\mathscr{E}_\infty\big[z_j(t) z_{j'}^*(t')\big] = \alpha(t-t')\delta_{j,j'}$. It can be generated in practice following methods such as [67, 68].

The observables for the electronic system are obtained by averaging the outcomes of Eq. (2.31) over multiple trajectories, as explained for QJ in Section 2.3.

Directly solving Eq. (2.31) is impracticable due to the last term on the right-hand side, which exhibits non-locality in time [66]. To circumvent this problem, Süß, Eisfeld, and Strunz introduced the hierarchy of pure states (HOPS) method [26]. The starting point for HOPS is to define

$$|\psi^{(1,j)}(t)\rangle \equiv D_j(t) |\psi(t)\rangle \equiv \int_0^t \mathrm{d}s\, \alpha^*(t-s) \frac{\delta |\psi(t)\rangle}{\delta z_j^*(s)} \ , \tag{2.34}$$

which is referred to as the *first auxiliary state* relative to site j. The *k-th auxiliary state* is defined recursively as

$$|\psi^{(k,j)}(t)\rangle = [D_j(t)]^k |\psi(t)\rangle \ . \tag{2.35}$$

For improving the numerical stability of this method (as we will show in Fig. 4.9), it is crucial to rescale the auxiliary states as [69]

$$|\psi^{(k,j)}(t)\rangle \to \frac{1}{\sqrt{\alpha(0)^k k!}} |\psi^{(k,j)}(t)\rangle \ . \tag{2.36}$$

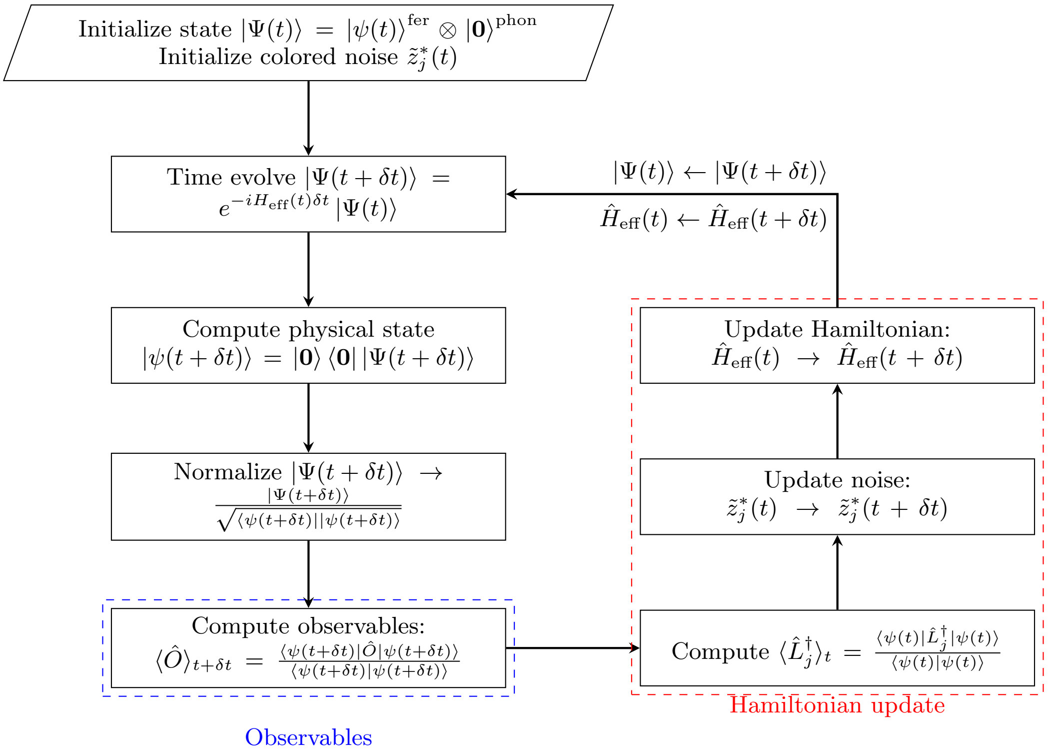

Figure 2.2: Algorithmic sketch of the hierarchy of pure states method.

This effectively reduces the norm of the relative auxiliary state, widely improving the numerical stability of the HOPS method and allowing the study of highly excited baths.

By utilizing Eq. (2.34) and Eq. (2.36), we can substitute Eq. (2.31) with a hierarchy of time-local equations. Following [67], it is advantageous to define a state in the combined system and (bosonic) environment Hilbert space as

$$|\Psi(t)\rangle = \sum_{\mathbf{k}} C_{\mathbf{k}}(t)\,|\psi^{(\mathbf{k})}(t)\rangle \otimes |\mathbf{k}\rangle^{\text{bos}} . \tag{2.37}$$

Here, $|\mathbf{k}\rangle^{\text{bos}} \equiv \otimes_j |k\rangle_j^{\text{bos}}$ denotes the bosonic mode associated with the k-th auxiliary state and $C_{\mathbf{k}}(t)$ is a time-dependent coefficient. Consequently, the hierarchy adopts the form of a straightforward Schrödinger equation for the state in the combined fermionic and bosonic Hilbert space:

$$\partial_t |\Psi(t)\rangle = -i\hat{H}^z_{\text{eff}}(t)\,|\Psi(t)\rangle \ , \tag{2.38}$$

with the effective non-Hermitian Hamiltonian defined as [26, 67]

$$\hat{H}^z_{\text{eff}}(t) = \hat{H}_S + \sum_j i\Big(\tilde{z}^*_j(t) g\hat{L}_j - (\kappa + i\omega)\hat{K}_j + g\hat{L}_j \otimes \hat{K}_j^{1/2}\hat{b}_j^\dagger - g\big(\hat{L}_j^\dagger - \langle\hat{L}_j^\dagger\rangle_t\big) \otimes \hat{b}_j\hat{K}_j^{1/2}\Big) . \tag{2.39}$$

In this context, $\hat{K}_j$ represents the bosonic number operator on site j, while $\hat{b}_j^\dagger$ and $\hat{b}_j$ are the *bare* creation and annihilation operators, respectively, acting on the bosonic modes as

$$\begin{aligned} \hat{b}^\dagger \left|k\right\rangle &= \left|k+1\right\rangle \\ \hat{b} \left|k\right\rangle &= \left|k-1\right\rangle \ . \end{aligned} \tag{2.40}$$

Moreover, the colored noise is modified as

$$\tilde{z}_j^*(t) = z_j^*(t) + g \int_0^t \mathrm{d}s \, \alpha^*(t-s) \langle \hat{L}_j^\dagger \rangle_s \ .$$

As for nlQSD (see Section 2.4), Eq. (2.38) is linearized by evaluating the non-linear term $\langle \hat{L}_j^\dagger \rangle_t$ with $|\psi(t-\delta t)\rangle$. This is a reasonable approximation, provided that the time step δt is sufficiently small. To compute the electronic observables, the entire state must be projected onto the physical state at each time step

$$|\Psi(t)\rangle \rightarrow |\psi(t)\rangle = \left|\mathbf{0}^{\mathrm{bos}}\right\rangle \left\langle \mathbf{0}^{\mathrm{bos}}\right| |\Psi(t)\rangle \,, \tag{2.41}$$

with $\left|\mathbf{0}^{\mathrm{bos}}\right\rangle \equiv \otimes_j \left|0^{\mathrm{bos}}\right\rangle_j$ being the bosonic vacuum. In Fig. 2.2, we provide an overview of the HOPS algorithm. In practical applications, the Schrödinger equation 2.38 is time-evolved using the initial condition $|\Psi(t=0)\rangle = |\psi^{(\mathbf{0})}(t=0)\rangle \otimes \left|\mathbf{0}^{\mathrm{bos}}\right\rangle$. Here, all the auxiliary states are initially set to zero and are subsequently populated as time progresses. Moreover, the formally-infinite hierarchy depth $k_{\max}$ must be truncated. In Section 3.1, we will illustrate how the projected purification (PP) method facilitates an optimal and automated choice of $k_{\max}$.

2.6 Structured environments and the mesoscopic leads method

In Section 2.5, we have considered the simple case in which the environment correlation function $\alpha(t)$ is a complex exponential, which corresponds to a spectral density $J(\omega) = \pi/2 \sum_k |g_{jk}|^2 \delta(\omega - \omega_k)$ being a Lorentzian function. In many situations though, this approach is not valid, as $J(\omega)$ can assume more complicated forms (see Chapter 6). In these cases, the HOPS method needs to be generalized by increasing the bath for every system site j from a single harmonic oscillator to a set of P_j harmonic oscillators. The idea behind this approach relies on the fact that since complex exponentials form a complete orthonormal set in L^2, we can approximate any (square-integrable) environment correlation function as

$$\alpha_j(t-t') \approx \sum_{p=1}^{P_j} g_{jp} e^{-\kappa_{jp}|t-t'| - i\omega_{jp}(t-t')} \ . \tag{2.42}$$

This decomposition, which can be computed using, for instance, the Laplace-Padé method [70], provides a set of parameters denoted as ω_p, g_p, and κ_p for every site j, which specify the environment Hamiltonian Eq. (2.29), the interaction Hamiltonian Eq. (2.30) and the damping strength of the environment modes, respectively. Detailed analyses of structured baths ($P > 1$) can be found in [66, 69].

A different approach for studying structured environments is to consider a Markovian embedding (see Chapter 4), i.e. to enlarge the physical system to include the bosonic modes. In this way, the dissipation on the bosonic modes can be described exactly via jump operators in the Lindblad equation Eq. (2.6). Differently from HOPS, in this case, one works in the frequency domain and approximates the spectral density for the physical site j as a sum of P^j Lorentzians

$$J_j(\omega) = \sum_{p=1}^{P^j} \frac{\kappa_{jp} \left| g_{jp} \right|^2}{(\omega - \omega_{jp})^2 + (\kappa_{jp}/2)^2} \,, \tag{2.43}$$

where the width of the Lorentzian is equal to the (possibly non-uniform) frequency spacing $\kappa_{jp} = \omega_{jp+1} - \omega_{jp}$. Every harmonic oscillator is coupled to its own Markovian thermal bath at inverse temperature β with coupling strength κ_{jp}, which is described by the Lindblad dissipator

$$\mathscr{D}_{jp}(\hat{\rho}) = \kappa_{jp} \left[f_{jp} \mathscr{D}(\hat{\rho}, \hat{a}_{jp}^{\dagger}) + (1 + f_{jp}) \mathscr{D}(\hat{\rho}, \hat{a}_{jp}) \right] \,, \tag{2.44}$$

where $f_{jp} = 1/(\exp\big(\beta\omega_{jp}\big) - 1)$ is the Bose-Einstein distribution function and $\mathscr{D}(\hat{\rho}, \hat{L}) = \hat{L}\hat{\rho}\hat{L}^{\dagger} - \frac{1}{2}\{\hat{L}^{\dagger}\hat{L}, \hat{\rho}\}$. The combined system $\hat{\rho}$ thus obeys the Lindblad equation

$$\frac{\mathrm{d}\hat{\rho}}{\mathrm{d}t} = \mathscr{L}(\hat{\rho}) = -i\big[\hat{H}, \hat{\rho}\big] + \sum_{j,p} \mathscr{D}_{jp}(\hat{\rho}) \,. \tag{2.45}$$

This approach is known under different names [19, 38, 71–75]. In the following, we will refer to it as the *mesoscopic leads* method. Note that in the continuous limit $P_j \to \infty$ the bosonic modes decouple from their thermal baths as $\kappa_{jp} \to 0$ and thus Eq. (2.45) reduces to a Schrödinger equation. However, we will always consider a finite P_j in practical numerical calculations. Importantly, as we will show in Chapter 6, given a Hamiltonian of the type Eq. (2.28), Eq. (2.45) allows to accurately describe the dynamics of the system's reduced density matrix $\hat{\rho}_S$ by using a significantly smaller number of bosonic modes P_j than required when evolving Eq. (2.28) unitarily. Moreover, the damping of the bosonic modes suppresses their occupation and the buildup of entanglement in the system, further simplifying the dynamics.

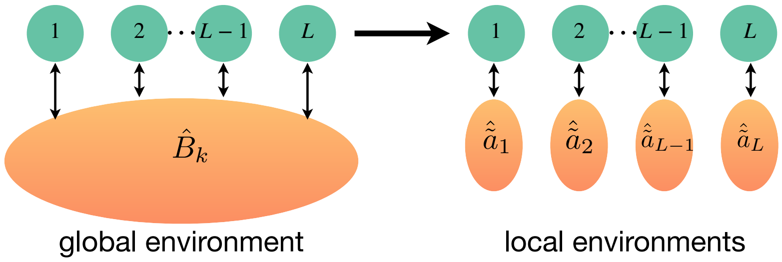

Figure 2.3: Schematic representation of the transition from a global to local environments. For simplicity, we consider a one-dimensional physical system with L sites, which could represent, for instance, fermionic or excitonic degrees of freedom. On the left panel, every system site is coupled to a shared environment, while on the right panel, each site is linked to its own local environment.

2.7 From global to local environments

Realistic physical systems are typically surrounded by a global environment. Take electrons in a material as an example; they interact with crystal atoms, which collectively vibrate through excited phonon modes. Here, we sketch the necessary physical approximations for the transition from a system coupled globally to a continuum of environmental energy modes to the models analyzed in Chapters 6 to 8 in which each lattice site is linked locally to one or multiple independent modes, whose effective correlation functions decay exponentially over time.

We first assume a linear form of interaction between the system and the global environment (see Fig. 2.3)

$$\hat{H}_{\mathrm{I}} = \sum_{j,k} g_{j,k} \hat{L}_j \hat{B}_k^\dagger + g_{j,k}^* \hat{L}_j^\dagger \hat{B}_k \,, \tag{2.46}$$

Here, $\hat{L}_j$ operates on system site j, $\hat{B}_k$ annihilates an excitation in environment mode k, and the $g_{j,k}$ represents a complex coefficient characterizing the coupling strength. These coefficients are generally dependent on the momentum k and might also exhibit spatial inhomogeneity. Next, we introduce *effective* environmental modes

$$\begin{aligned} \hat{\hat{a}}_j &= \sum_k g_{j,k}^* \hat{B}_k \\ \hat{\hat{a}}_j^\dagger &= \sum_k g_{j,k} \hat{B}_k^\dagger \,, \end{aligned} \tag{2.47}$$

which enable us to express the interaction Hamiltonian as

$$\hat{H}_{\mathrm{I}} = \sum_j \hat{L}_j \hat{\hat{a}}_j^\dagger + \hat{L}_j^\dagger \hat{\hat{a}}_j \,. \tag{2.48}$$

This form now resembles the systen-environment coupling discussed in Section 2.5. Nonetheless, we must also take into account the correlations among distinct effective environmental modes, which are in general not independent from one another:

$$\begin{aligned}
\langle \hat{\tilde{a}}_{j'}(t')\hat{\tilde{a}}_j^\dagger(t)\rangle &= \sum_{k,k'} g_{j,k} g^*_{j',k'} \langle \hat{B}_{k'}(t')\hat{B}_k^\dagger(t)\rangle \\
&= \sum_{k,k'} g_{j,k} g^*_{j',k'} e^{-i\omega_k t + i\omega_{k'} t'} \langle \hat{B}_{k'}\hat{B}_k^\dagger\rangle \\
&= \sum_{k,k'} g_{j,k} g^*_{j',k'} e^{-i\omega_k t + i\omega_{k'} t'} \delta_{k,k'} \\
&= \sum_{k} g_{j,k} g^*_{j',k} e^{-i\omega(t-t')} \ .
\end{aligned} \tag{2.49}$$

In the penultimate line, we have employed the relationship (at zero temperature) $\langle \hat{B}_{k'}\hat{B}_k^\dagger\rangle = \delta_{k,k'}$. This holds when the environment consists of non-interacting bosons Eq. (2.29).

Moving forward, we make the assumption that the magnitudes of the coupling coefficients are uniform, but we allow for a possible phase factor:

$$g_{j,k} = g_k e^{-ikja} \ , \tag{2.50}$$

where a is the lattice constant. Consequently, we get the correlation functions

$$\langle \tilde{a}_{j'}(t')\tilde{a}_j^\dagger(t)\rangle = \sum_k |g_k|^2 e^{-ika(j-j')} e^{-i\omega(t-t')} \ . \tag{2.51}$$

Next, we consider strong lattice confinement in accordance with [76]. In this regime, the localized basis for the fermions can be approximated by the eigenstates of the harmonic oscillator. Thus, the coupling coefficients between these fermionic states and a continuous bosonic excitation within the environment, described as a plane wave, can be expressed as

$$g_k^{\alpha,\beta} \propto \int \mathrm{d}z\, \Phi^{\alpha *}(z)\Phi^{\beta}(z) e^{-ikz} \ , \tag{2.52}$$

where $\Phi^\alpha(z)$ corresponds to the α-th eigenstate of the harmonic oscillator:

$$\Phi^\alpha(z) = \frac{1}{\sqrt{2^\alpha n!}} (\pi a^2)^{-1/4} e^{\frac{z^2}{2a_z}} H^\alpha\left(\frac{z}{a_z}\right) \ . \tag{2.53}$$

Here, $a_z = \sqrt{1/m\omega_z}$ and H^α denote the Hermite polynomials. Under the assumption that only the ground state $\Phi^0(z)$ is occupied, we can compute the coupling coefficients exactly:

$$g_k = g e^{-k^2 a^2/2} \ . \tag{2.54}$$

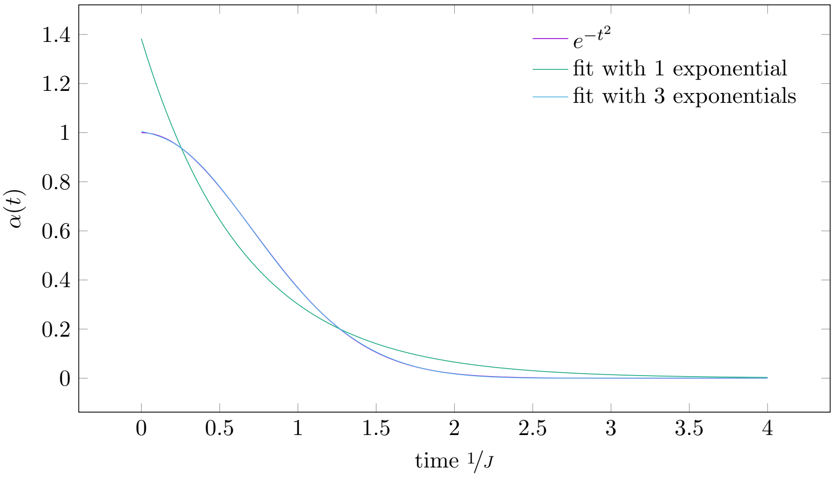

Figure 2.4: Bath correlation function Eq. (2.55) approximated with one and three complex exponentials via the Laplace-Pade method for $c = g = a$. Note that the purple and the blue lines overlap almost perfectly and minor discrepancies can bee seen mainly at time $t \sim 0$.

Here, we have assumed a momentum-independent prefactor denoted by g.

We proceed by incorporating the linear dispersion relation $\omega = ck$ and substituting the expression for g_k into Eq. (2.51). When $ka \gg 1$, the sum for $j \neq j'$ introduces a large oscillating component that results in an vanishing correlation. This scenario is commonly referred to as the large wavevector limit. It is valid when the characteristic wavelength of excitations within the environment, denoted as λ_{eff}, is notably smaller than the interspace between lattice sites within the system. By approximating the sum as an integral when $j = j'$, we get

$$\begin{aligned}\langle \hat{\tilde{a}}_{j'}(t')\hat{\tilde{a}}_j^\dagger(t)\rangle &= \sum_k |g_k|^2 e^{-i\omega(t-t')} \approx \int_0^\infty \mathrm{d}k\, |g_k|^2 e^{-ick(t-t')} \approx \int_0^\infty \mathrm{d}k\, g^2 e^{-k^2a^2-ick(t-t')} \\ &= \sqrt{\frac{\pi}{a^2}} g^2 e^{-c^2/4a^2(t-t')^2} \equiv \alpha(t-t') \,. \end{aligned} \tag{2.55}$$

Approximating this correlation function with a single complex exponential leads to the situation sketched on the r.h.s. of Fig. 2.3, i.e., each system site is coupled to one environmental mode. As we show in Fig. 2.4 (green line), this is quite a crude approximation. However, three exponentials (and thus three modes for system site j) suffice to accurately reproduce Eq. (2.55) (blue line). This paves the way for linking the models considered in our work to a broader range of realistic physical systems.

2.8 The EVOS package

Many of the methods discussed in this chapter were collected in the Python package EVOS (Evolving Open Systems). The primary goal of EVOS is to compute the dynamics of large-scale dissipative quantum systems. It works both for ED representation using NumPy arrays and for MPS representation, for which it employs SYTEN [51, 52] as a backend. One of the most useful features of EVOS is that the syntax for ED and MPS calculations is basically the same. Thus, one can use ED for small system tests and then almost effortlessly switch to MPS for large-scale computations. The main classes in EVOS are the following:

- **lattice**: Specify the lattice of interest, indicating which sites correspond to which type of particles, such as spinless and spinful fermions, spin-1/2 particles, bosons ...
- **method**: Select whether to propagate a density matrix directly via the Lindblad equation, adopt a pure state unraveling, or solve the Schrödinger equation for an isolated system.
- **observables**: Define which local or global observables should be computed at every time step. This class conveniently computes averages and statistical errors for pure state unraveling methods and automatically discards failed trajectories.

To investigate the Mpemba effect [2] (Chapter 5), we needed the full spectrum of the Lindbladian superoperator and thus we used EVOS's ED solver. Instead, to compute the impact of dissipation on bipolarons in the Hubbard-Holstein model [1] (Chapter 8) and to compute exciton dynamics in structured environments together with Zhaoxuan Xie [4] (Chapter 6) we used EVOS as a convenient interface to SYTEN. Moreover, Master's students Réka Schwengelbeck, Tobias Kiermeyer, and Yudong Sun used the package for research projects.

EVOS is hosted on the LMU Gitlab, which is not publicly accessible, but it is available upon request. It is still a work in progress, and I will keep debugging, improving, and expanding it over the next few years.

Chapter 3

MPS-based methods for dissipative and vibrational environments

This chapter provides an overview of efficient matrix-product state (MPS) methods for computing the dynamics of quantum many-body systems interacting with dissipative and vibrational environments. It will hopefully serve as a helpful guide for those who want to use existing MPS toolkits for large-scale open quantum system (OQS) simulations. In Section 3.1, we summarize some basic concepts about MPS and examine the representation and time evolution of bosonic systems. Then, in Section 3.2, we discuss the computation of OQS dynamics with MPS either by directly propagating a density matrix $\hat{\rho}(t)$ or by adopting pure-state unraveling methods. The latter option will be our method of choice for almost all the results presented in this thesis. Finally, we present the main original contribution in this chapter in Section 3.3, where we introduce phonon state tomography (PST). PST, which was developed together with Sebastian Paeckel, allows for disentangling the impact of different excitations in the vibrational bath on electronic degrees of freedom and will be used extensively in Chapter 7 to study the effect of photo-excited phonons on the non-equilibrium properties of 1D electronic systems. This chapter is partially based on Refs. [1, 3].

3.1 MPS: basic concepts and applications to bosonic systems

The field of tensor network algorithms for quantum systems was initiated by Steve White's *density-matrix renormalization group (DMRG)*, a groundbreaking method for computing groundstates of 1D strongly-interacting many-body quantum systems [20]. His idea, inspired by Wilson's numerical renormalization group, was to discard the states with the smallest spectral weight rather than those with the highest energy. A comprehensive presentation of DMRG in its

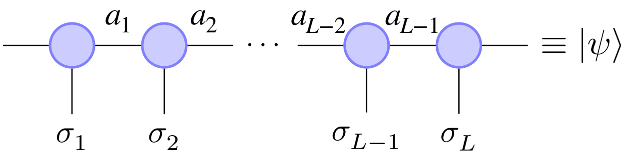

Figure 3.1: Graphical representation of a matrix-product state (MPS) (see Eq. (3.2)). On each site, vertical legs represent the physical indices, while horizontal legs represent bond indices, also called auxiliary indices.

original formulation can be found in [77]. In 1995, only three years after White's seminal paper, Ostlund and Rommer began reformulating DMRG in terms of matrix-product states (MPSs) [78], laying the foundation for many of today's tensor-network-based algorithms. In the following, we will briefly review some basic concepts about MPS.

Consider a 1D quantum system on a lattice of length L, where each site j is a d-level system described by the states $\sigma = 1, 2, \dots d$. The total Hilbert space corresponds to the tensor product of the local Hilbert spaces $\mathscr{H} = \bigotimes_{j=1}^{L} \mathscr{H}_j$, and every pure state is a linear combination of the basis states $|\sigma_1, \sigma_2, \dots \sigma_L\rangle$:

$$|\psi\rangle = \sum_{\sigma_1, \sigma_2, \dots \sigma_L} c^{\sigma_1 \sigma_2 \dots \sigma_L} |\sigma_1, \sigma_2, \dots \sigma_L\rangle \ . \tag{3.1}$$

The coefficients $c^{\sigma_1 \sigma_2 \dots \sigma_L}$ can be viewed as forming a rank-L tensor with d^L entries. The main idea of MPS is to decompose the coefficient tensor into a product of rank-3 tensors

$$|\psi\rangle = \sum_{\substack{\sigma_1, \sigma_2, \dots \sigma_L \\ a_1, a_2, \dots a_{L-1}}} M^{\sigma_1}_{1,a_1} M^{\sigma_2}_{a_1,a_2} \dots M^{\sigma_L}_{a_{L-1},1} |\sigma_1, \sigma_2, \dots \sigma_L\rangle \ . \tag{3.2}$$

At site j, the two lower indices of $M^{\sigma_j}_{a_{j-1},a_j}$ run from 1 to some integer m_{j-1} and m_j, respectively. These are called *bond dimension* or auxiliary dimension to differentiate them from the physical dimension d_j, which determines the range of the physical index σ_j. Note that the MPS representation is not unique, since introducing an identity $\hat{\mathbb{1}} = \hat{X}\hat{X}^{-1}$ between two sites in Eq. (3.2) (known as gauge transformation) does not change $|\psi\rangle$. To visualize tensors and their manipulation, it is useful to introduce a graphical notation, in which each index is represented by a leg sticking out from a geometric shape. For MPS, physical indices correspond to vertical legs and bond indices to horizontal ones, as depicted in Fig. 3.1. If one allows for a sufficiently large bond dimension, one can represent any pure state *exactly* as an MPS by performing a series of singular value decompositions (SVDs) [79].

A SVD consists of decomposing a matrix $\hat{M}$ as $\hat{M} = \hat{U}\hat{\Lambda}\hat{V}^\dagger$, where $\hat{U}$ and $\hat{V}$ are unitary and $\hat{\Lambda}$ is a diagonal matrix whose entries, which are all non-negative,

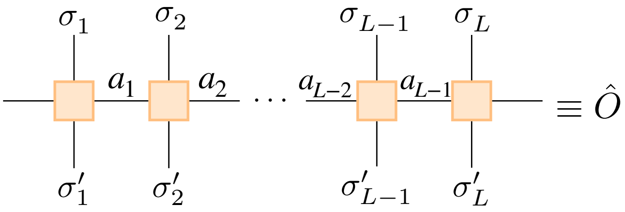

Figure 3.2: Graphical representation of a matrix-product operator (MPO) (see Eq. (3.3)). On each site, the two vertical legs represent the physical indices while the horizontal legs represent bond indices, also called auxiliary indices.

are arranged in descending order and are known as singular values. SVDs have many applications in linear algebra and also in quantum information theory (as they allow to bring a pure state into Schmidt form [14]). In the context of MPS algorithms, one of the most important features of SVDs is that given a matrix $\hat{M}$ of rank r, the best low-rank approximation of $\hat{M}$, i.e. the matrix $\hat{M}'$ with rank $r' < r$, which has the minimal distance to $\hat{M}$ w.r.t. the Frobenius norm, is obtained by setting the smallest $r - r'$ singular values of $\hat{M}$ to zero. Thus, successively truncating all site tensors of an MPS by performing local SVDs allows us to find an efficient global compression of a quantum state. The truncation is usually controlled by the so-called discarded weight $\delta = \sum_{i=r'}^{r} \Lambda_i^2$, i.e. the sum over the squared singular values discarded on every site.

Similarly to what we just discussed for quantum states, an operator $\hat{O}$ can be decomposed in rank-4 tensors with two physical and two auxiliary legs

$$\hat{O} = \sum_{\substack{\sigma_1,\sigma_2,\ldots\sigma_L \\ \sigma'_1,\sigma_2,\ldots\sigma'_L \\ b_1,b_2,\ldots b_{L-1}}} W^{\sigma_1\sigma'_1}_{1,b_1} W^{\sigma_2\sigma'_2}_{b_1,b_2} \ldots W^{\sigma_L\sigma'_L}_{b_{L-1},1} \left|\sigma_1,\sigma_2,\ldots\sigma_L\right\rangle \left\langle\sigma'_1,\sigma'_2,\ldots\sigma'_L\right| \ , \tag{3.3}$$

as depicted in Fig. 3.2. Applying a matrix-product operator (MPO) to an MPS results in a new MPS where on every site the new rank-3 tensor reads $N^{\sigma_j}_{(b_{j-1},a_{j-1}),(b_j,a_j)} = \sum_{\sigma'_j} W^{\sigma_j\sigma'_j}_{b_{j-1},b_j} M^{\sigma'_j}_{a_{j-1},a_j}$. Thus, the application of an MPO with bond dimension m_o to an MPS having bond dimension m_s (see Fig. 3.3) results in an MPS with $m_o m_s$ and typically needs to be truncated.

While in principle every pure state can be represented exactly as an MPS, the bond dimension m_j grows exponentially with the von Neumann entropy relative to the bipartition of $|\psi\rangle$ at the bond j [79]. Thus, the MPS representation of many-body states can quickly become impractical in the presence of long-range correlation. Luckily, in 1D, ground states of gapped Hamiltonians with local interactions obey area laws [80] and can therefore be efficiently described as MPS. The situation is different for non-equilibrium states, which typically have finite overlaps with many high-energy states of the Hamiltonian generating the dynamics and generally obey a volume-law. The problem is particularly severe for global

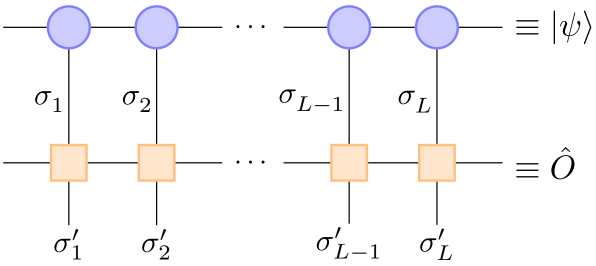

Figure 3.3: Application of an MPO to an MPS.

quenches, corresponding, for instance, to a sudden change in a global Hamiltonian parameter, where in the worst case, the spreading of quasiparticles and the associated linear increase in the von Neumann entropy results in an exponential increase of the required bond dimension in time [21]. This severely limits the simulation times one can reach with MPS algorithms.

Remarkably though, in the last decade, sophisticated versions of the time-dependent variational principle (TDVP) formulated for MPS [36, 81–83] have enabled simulating time evolutions of large systems following global quenches up to relatively long times. The main idea of the TDVP method is to exploit the gauge freedom of MPS to construct projectors that yield a Lie-Trotter decomposition of the Hamiltonian. Such decomposition allows one to approximate the Schrödinger equation for the full MPS with local Schrödinger equations evolving single-site tensors and bond tensors (for the so-called single-site time-dependent variational principle (1TDVP) method), which one can efficiently solve with Krylov subspace methods [82]. However, the drawback of 1TDVP is that it cannot increase the bond dimension of a state and thus fails to capture the spread of correlations during a time evolution correctly. Thus, typically, one resorts to the two-site time-dependent variational principle (2TDVP), in which two neighboring sites are updated simultaneously. Nonetheless, adopting a two-site scheme comes at the cost of increased algorithmic complexity, with the most expensive computational steps scaling with d^3, whereas it is proportional to d^2 for 1TDVP [82]. This constitutes a big obstacle for bosonic systems (such as vibrational environments), where highly excited baths can require local dimensions $d \sim \mathcal{O}(10)$ to $\mathcal{O}(10^2)$ for an accurate description [1, 3, 4, 37, 84].

To tackle this issue, in 2020, Yang and White [36] proposed to combine 1TDVP with subspace expansions, which had previously been employed for ground-state DMRG calculations [85]. The Global subspace expansion time-dependent variational principle (GSE-TDVP) proved to be both accurate and numerically less expensive than 2TDVP. However, GSE-TDVP relies on global Krylov vectors for growing the state's bond dimension during the time evolution, and the computation of such vectors can become very expensive at long simulation times. One can overcome this difficulty by replacing the global subspace expansion with a much faster local scheme [37, 85, 86], called local subspace expansion time-dependent variational principle (LSE-TDVP). The only drawback of LSE-TDVP is that being an entirely local method, it can suffer from a significant projection error (see [82]) when evolving a state with small bond dimension, as is also the case for 1TDVP and 2TDVP. Thus, when time-evolving a product state (or heuristically a state with $m < d$), we find it convenient to compute the first few steps with the slower but more accurate GSE-TDVP and then switch to the faster LSE-TDVP.

Apart from their high dimensionality, another issue that one encounters when dealing with the MPS description of vibrational environments is that the number of bosonic particles is usually not conserved: i.e., the typical local interaction term

$$\hat{H}_j^{\mathrm{I}} \propto \hat{c}_j^\dagger \hat{c}_j (\hat{a}_j + \hat{a}_j^\dagger) \tag{3.4}$$

creates and annihilates vibrational excitations. The fact that Eq. (3.4) is not $U(1)$-symmetric w.r.t. the bosonic particle number represents a significant challenge numerically, since the presence of global $U(1)$ symmetries and the consequent block-diagonal structure of site tensors hugely simplifies MPS calculations [87]. This problem was addressed by Köhler, Stolpp, and Paeckel in 2021 when they introduced the projected purification (PP) method [35, 88]. The starting point of PP is to double the bosonic Hilbert space $\mathscr{H} \to \mathscr{H} \otimes \mathscr{H}$ by introducing an auxiliary site $B;j$ for every physical bosonic site $P;j$. Then, one considers only the subspace spanned by the states that obey the gauge constraint

$$n_j = n_{P;j} + n_{B;j} = d - 1 \ , \tag{3.5}$$

i.e., one projects the total enlarged Hilbert space to the subspace where on each pair of physical-auxiliary sites the total occupation is equal to the local dimension d minus one: $\mathscr{H} \otimes \mathscr{H} \to \mathscr{P}(\mathscr{H} \otimes \mathscr{H}) \equiv \tilde{\mathscr{H}}$. This restores the global particle conservation and, thus, the corresponding $U(1)$ symmetry. Note that $\tilde{\mathscr{H}} \cong \mathscr{H}$, which means that the PP mapping does not increase the computational complexity of the problem[1], as is the case for instance, for thermal purification [89]. In practice, the projection $\mathscr{P}$ onto the subspace satisfying the gauge constraint Eq. (3.5) is implemented by transforming the bosonic creation and annihilation operators as

$$\begin{aligned} \hat{a}_j^\dagger &\to \hat{a}_{P;j}^\dagger \otimes \hat{b}_{B;j} \\ \hat{a}_j &\to \hat{a}_{P;j} \otimes \hat{b}_{B;j}^\dagger \ , \end{aligned} \tag{3.6}$$

where $\hat{b}$, $\hat{b}^\dagger$ are called *balancing* operators and are equivalent to the bare operators introduced for the HOPS method in Eq. (2.40). From Eq. (3.6), the meaning of the PP-auxiliary sites becomes immediately apparent: they act as particle sources and drains, ensuring the global particle number conservation, as sketched in Fig. 3.4.

---

[1] In practical calculations, in the most straightforward cases where d is very small, the PP-doubling of the sites can slow down calculations.

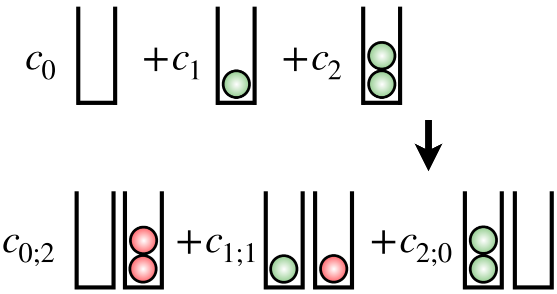

$$|\psi\rangle = \sum_{n=0}^{d-1} c_n |n\rangle$$

$$|\psi\rangle_{PP} = \sum_{n_P=0}^{d-1} c_{n_P;d-1-n_P} |n_P\rangle |d-1-n_P\rangle$$

Figure 3.4: The projected purification (PP) mapping. For simplicity, we depict a single three-level, truncated bosonic site (upper sketch). Within the PP mapping (lower sketch), the auxiliary sites ensure that the total particle number is conserved. In general, for a many-body state, mapping the local bosonic operators according to Eq. (3.6) ensures the global particle number conservation for the bosonic system.

In addition to restoring the global $U(1)$ symmetry relative to the bosonic particle conservation, the second useful feature of PP is that it naturally introduces an efficient truncation scheme for the physical dimension d of the bosonic sites. Consider the diagonal matrix $\hat{\Lambda}^{n_{p;j}}$ containing the singular values relative to the block with $n_{p;j}$ particles for a physical bosonic site j. It can be shown [35] that the diagonal entry of the single-site reduced density-matrix (1RDM) on site j, corresponding to the occupation n_p, satisfies

$$\rho_{n_{p;j},n_{p;j}} = \sum_l \left(\Lambda_l^{n_{p;j}}\right)^2 , \tag{3.7}$$

where the sum runs over all singular values. Thus, by discarding all blocks $n_{p;j}$ for which the sum of the squared singular values is smaller than a fixed threshold, one can truncate the physical dimension d in precisely the same fashion as the bond dimension in standard DMRG calculations. In practical calculations, we typically set the same discarded weight of $\delta = 10^{-10}$ for the truncation of the physical and the bond dimensions. Moreover Eq. (3.7) devises an efficient method for computing bosonic 1RDMs, which we will make use of in Section 3.3 and Chapter 7.

3.2 MPS methods for OQS

This section discusses the simulation of the dynamics of many-body dissipative quantum systems with MPS. While here we focus on the difficult aspects of such simulations, we want to note that, in general, dissipation can simplify MPS calculations by suppressing the spread of correlations, as we will discuss in Chapter 6.

3.2.1 Direct propagation of the density matrix vs. pure state unravelings

One strategy for computing the dynamics of a dissipative quantum system using MPS is to use the vectorization method that we outlined in Section 2.2. While in the ED framework, it is sufficient to view the vectorization of a matrix as the stacking of the matrix's columns (Eq. (2.10)), when utilizing MPS, it is helpful to adopt a slightly different angle. For a mixed state $\hat{\rho} = \sum_{ij} \rho_{ij} |i\rangle \langle j|$ the vectorization procedure corresponds to applying the Choi-Jamiolkowski isomorphism for every element $|i\rangle \langle j| \rightarrow |j\rangle \otimes |i\rangle$ [57]. Thus, vectorizing the MPO representation (see Fig. 3.2) of a many-body mixed state yields

$$\begin{aligned}
\hat{\rho} &= \sum_{\substack{\sigma_1\sigma_2\ldots\sigma_L \\ \sigma_1'\sigma_2'\ldots\sigma_L'}} \rho_{\sigma_1\sigma_2\ldots\sigma_L\sigma_1'\sigma_2'\ldots\sigma_L'} |\sigma_1\sigma_2\ldots\sigma_L\rangle \langle\sigma_1'\sigma_2'\ldots\sigma_L'| \rightarrow \\
|\rho\rangle\rangle &= \sum_{\substack{\sigma_1\sigma_2\ldots\sigma_L \\ \sigma_1'\sigma_2'\ldots\sigma_L'}} \rho_{\sigma_1\sigma_2\ldots\sigma_L\sigma_1'\sigma_2'\ldots\sigma_L'} |\sigma_1'\sigma_2'\ldots\sigma_L'\sigma_1\sigma_2\ldots\sigma_L\rangle \ ,
\end{aligned} \tag{3.8}$$

i.e. an MPS with $2L$ physical sites. Note that we are using the shorthand notation $|\sigma_1\sigma_2\ldots\sigma_L\rangle = |\sigma_1\rangle \otimes |\sigma_2\rangle \cdots \otimes |\sigma_L\rangle$. Due to the doubling of the Hilbert space, this procedure is often referred to as *purification* [23].

When doubling the lattice, one is confronted with the choice of how to arrange the auxiliary sites. In [90] Casagrande, Poletti, and Landi argue that in the Markovian case it is convenient to alternate physical and auxiliary sites

$$|\rho\rangle\rangle = \sum_{\substack{\sigma_1\sigma_2\ldots\sigma_L \\ \sigma_1'\sigma_2'\ldots\sigma_L'}} \rho_{\sigma_1\sigma_1'\ldots\sigma_2\sigma_2'\sigma_L\ldots\sigma_L'} |\sigma_1\sigma_1'\sigma_2\sigma_2'\ldots\sigma_L\sigma_L'\rangle \ , \tag{3.9}$$

because this best preserves the locality of $\hat{L}_l \otimes (\hat{L}_l^\dagger)^T$ in the dissipator. Besides the state $\hat{\rho}$, we also need to vectorize the generator $\mathscr{L}$, which is the Lindbaldian for Markovian systems, while for non-Markovian systems, it could be, for instance, the hierarchy of equations of motion (HEOM)-generator [91]. The superoperator $\mathscr{L}$ can be recast into an operator $\hat{\mathscr{L}}$ following the rule outlined in Section 2.2, yielding for the Lindbladian

$$\begin{aligned}
\hat{\mathscr{L}} =& - i\hat{H} \otimes \hat{\mathbb{1}} + i\hat{\mathbb{1}} \otimes \hat{H}^T \\
&+ \sum_l \hat{L}_l \otimes \left(\hat{L}_l^\dagger\right)^T - \frac{1}{2}\hat{L}_l^\dagger \hat{L}_l \otimes \hat{\mathbb{1}} - \frac{1}{2}\hat{\mathbb{1}} \otimes \left(\hat{L}_l^\dagger \hat{L}_l\right)^T \ .
\end{aligned} \tag{3.10}$$

Propagating the vectorized state in time then amounts to solving an imaginary-time Schrödinger equation with a non-Hermitian Hamiltonian

$$\frac{\mathrm{d}}{\mathrm{d}t}|\rho\rangle\rangle = \hat{\mathscr{L}}|\rho\rangle\rangle \ , \tag{3.11}$$

which can be solved using for instance TDVP or time-evolving block decimation (TEBD) [82]. In Section 3.2.2, we will outline how to deal with TDVP for non-Hermitian Hamiltonians.

The expectation value of an operator $\hat{O}$ in the vectorized framework can be calculated as (see Section 2.2) [23]

$$\langle \hat{O} \rangle = \frac{\mathrm{Tr}\left(\hat{\rho}\hat{O}\right)}{\mathrm{Tr}\left(\hat{\rho}\right)} = \frac{\langle\!\langle \mathbb{1} | \hat{O} | \rho \rangle\!\rangle}{\langle\!\langle \mathbb{1} | \hat{\rho} \rangle\!\rangle} , \tag{3.12}$$

where $\hat{O}$ acts on one or multiple physical degrees of freedom $\sigma_1, \sigma_2, \dots \sigma_L$. The (non-unique) purification of the identity can be obtained by taking the tensor product of a maximally entangled states on every couple of physical-auxiliary site $|\mathbb{1}\rangle\!\rangle = \bigotimes_{j=1}^{L} \sum_{\sigma_j=1}^{d} |\sigma_j \sigma_j'\rangle\!\rangle$, where d is the physical local dimension on site j. The vectorization scheme discussed here presents some computational drawbacks. First, doubling the lattice sites corresponds to a (at worse) quadratic increase in the dimensionality of the Hilbert space. This constitutes a severe limitation, especially when considering many-body bosonic systems with large local physical dimensions, and is the main reason we will use pure-state unraveling methods instead of vectorization. Second, since truncated SVDs do not preserve the positivity of a matrix, one has to be careful when solving Eq. (3.11), as states compressions can lead to the appearance of negative or imaginary diagonal elements in the diagonal part of $\hat{\rho}(t)$. Even worse, for many-body systems, one cannot determine whether a truncated SVD yields an unphysical state since positivity is a global quantity that cannot be efficiently tested locally [92]. A way to circumvent this problem was put forward by Werner et al. [93], who proposed a TEBD algorithm based on the decomposition $\hat{\rho} = \hat{X}\hat{X}^{\dagger}$, which is positive by construction.

A vectorization approach can be advantageous compared to pure-state unravelings when one is interested in the density matrix or the Wigner function rather than in observables. However, in our opinion, vectorization is truly beneficial only in the direct calculation of the steady state in scenarios in which the dissipative dynamics (e.g., the decoherence or thermalization timescales) are not of interest. In such cases, Cui, Cirac and Bañuls [25] proposed to construct the positive MPO $\hat{\mathscr{L}}^{\dagger}\hat{\mathscr{L}}$. For systems with a unique steady state $|\rho_{\mathrm{ss}}\rangle\!\rangle$, the lowest-energy eigenstate corresponding to the eigenvalue $\lambda = 0$ is (up to normalization) $|\rho_{\mathrm{ss}}\rangle\!\rangle$. Thus one can compute $|\rho_{\mathrm{ss}}\rangle\!\rangle$ using a standard DMRG groundstate search for the Hermitian operator $\hat{\mathscr{L}}^{\dagger}\hat{\mathscr{L}}$. For practical calculations though, one needs to bear in mind that if the MPO representing $\hat{\mathscr{L}}$ has bond dimension m, $\hat{\mathscr{L}}^{\dagger}\hat{\mathscr{L}}$ has in general bond dimension of m^2 and is highly non-local.

As anticipated in the introduction to this chapter, our preferred strategy for computing dissipative dynamics of quantum many-body systems with MPS is to use pure state unravelings (see Sections 2.3 to 2.5). These methods offer up to quadratically better dimensional scaling than vectorization methods. Moreover, from a practical point of view, they do not require any adjustment w.r.t. unitary MPS-dynamics, with the sole exception of having to deal with a non-Hermitian Hamiltonian, which we will discuss in Section 3.2.2. The price one has to pay is that the stochastic Schrödinger equation

$$\frac{\mathrm{d}}{\mathrm{d}t} |\Psi_q\rangle = -i\hat{H}_{\mathrm{eff}} |\Psi_q\rangle \ , \tag{3.13}$$

has to be solved for many different noise realizations or trajectories q which, however, can all be computed independently[2]. Moreover, for HOPS and QSD, the effective Hamiltonian $\hat{H}_{\mathrm{eff}}$ is time-dependent, and thus a part of the MPO needs to be constructed at every time step. However, one can construct MPOs efficiently (for example, with a finite-states machine (FSM) [94]) so that this computational step is never a bottleneck for the calculations. One more drawback of pure-states unravelings is that they typically require small time steps. For QJ, this stems from the fact that only one jump per time step can occur, and thus, when the coupling between system and environment is strong, a large time step leads to underestimating the effect of the environment. This requirement can be mitigated by adopting an adaptive time step variant of QJ [95] or, in some cases, by directly reducing the number of quantum jumps via a suitable unitary transformation of the Hamiltonian (see Section 6.3).

As a speculative concluding remark for this section, we want to point out that, to the best of our knowledge, currently, there is no pure-state unraveling method that allows us to compute the steady-state directly, in analogy to the calculation of the zero-energy eigenstate of the vectorized Liouvillian $\hat{\mathscr{L}}$ in the vectorized framework. It would be interesting to investigate whether such a scheme, avoiding the computation of the time evolution, could be found, as it would represent a significant methodological advancement. More precisely: Given a vectorized Lindbladian $\hat{\mathscr{L}}$ with dimension $D^2 \times D^2$ possessing a unique steady state, is there a set of Hamiltonians $\hat{H}^q_{\mathrm{eff}}$ with dimension $D \times D$, such that averaging over their groundstates $|\Phi^0\rangle_q$, which can be computed with DMRG, yields the steady state $\hat{\rho}_{\mathrm{ss}} = \mathscr{E}\left[|\Phi^0\rangle_q \langle\Phi^0|_q\right]$? Maybe a first more modest step would be to consider the deterministic $\hat{H}_{\mathrm{eff}}$ from QJ (see Eq. (2.16)) and try to incorporate the complicated term $\hat{L}_l \otimes (\hat{L}_l^\dagger)^T$ perturbatively.

3.2.2 TDVP with non-Hermitian Hamiltonians

When evolving open systems, one encounters the difficulty of dealing with non-Hermitian Hamiltonians. This issue arises both when propagating the density matrix directly and when adopting a pure-state unraveling. In the context

---

[2] We discuss how to account for initially mixed states with QJ in Section 6.3

of TDVP [81], let us first consider the case of a Hermitian Hamiltonian $\hat{H}$. At every time step, after the projection on a single-site subspace (or on a two-site subspace for 2TDVP), local Schrödinger equations are solved by exponentiating an effective, local, Hermitian Hamiltonian $\hat{\hat{H}}_j$ in a Krylov subspace [82]. Given the effective site-reduced state $|\tilde{\psi}_j\rangle$, the Krylov subspace $\mathcal{K}_N(\hat{\hat{H}}_j, |\tilde{\psi}_j\rangle)$ is obtained by repeatedly applying $\hat{\hat{H}}_j$ on $|\tilde{\psi}_j\rangle$:

$$\mathcal{K}_N(\hat{\hat{H}}_j, |\tilde{\psi}_j\rangle) = \text{span}\left(|\tilde{\psi}_j\rangle, \hat{\hat{H}}_j|\tilde{\psi}_j\rangle, \dots \hat{\hat{H}}_j^{N-1}|\tilde{\psi}_j\rangle\right) \equiv \text{span}\left(|\tilde{v}_j^0\rangle, |\tilde{v}_j^1\rangle, \dots |\tilde{v}_j^{N-1}\rangle\right) . \tag{3.14}$$

The Krylov vectors $(|v_j^0\rangle, |v_j^1\rangle, \dots |v_j^{N-1}\rangle)$ are generated by orthogonalizing the vectors $(|\tilde{v}_j^0\rangle, |\tilde{v}_j^1\rangle, \dots |\tilde{v}_j^{N-1}\rangle)$ against one another. We now collect the Krylov vectors in a rectangular matrix $\hat{Q} = (|v_j^0\rangle, |v_j^1\rangle, \dots |v_j^{N-1}\rangle)$, which satisfies the right-orthogonality condition $\hat{Q}\hat{Q}^\dagger = \hat{\mathbb{1}}$. Q can be used to obtain the tridiagonal matrix $\hat{T} = \hat{Q}^\dagger \hat{\hat{H}}_j \hat{Q}$. Then, the exponential of the tridiagonal matrix, which can be efficiently computed numerically [82], can be written as

$$e^{-i\delta t\hat{T}} = \sum_{m=0}^{\infty} \frac{\left(-i\delta t\hat{Q}^\dagger \hat{\hat{H}}\hat{Q}\right)^m}{m!} = \hat{Q}^\dagger \sum_{m=0}^{\infty} \frac{\left(-i\delta t\hat{\hat{H}}\right)^m}{m!}\hat{Q} = \hat{Q}^\dagger e^{-i\delta t\hat{\hat{H}}}\hat{Q} . \tag{3.15}$$

Thus, the application of the exponential of the Hamiltonian on the state $|\tilde{\psi}_j\rangle$ can be efficiently obtained as:

$$e^{-i\delta t\hat{\hat{H}}_j}|\tilde{\psi}_j\rangle = \hat{Q}e^{-i\delta t\hat{T}}\hat{Q}^\dagger|\tilde{\psi}_j\rangle . \tag{3.16}$$

Instead, when the Hamiltonian (and thus also the TDVP effective, single-site reduced Hamiltonian) is non-Hermitian $\hat{\hat{H}}_j \neq \hat{\hat{H}}_j^\dagger$, as is the case when considering for instance QJ (Section 2.3), QSD (Section 2.4), HOPS (Section 2.5) or the vectorized Lindbladian (Section 2.2) , one has to construct two Krylov subspaces $\mathcal{K}_N(\hat{\hat{H}}_j, |\tilde{\psi}_j\rangle)$ and $\mathcal{K}'_N(\hat{\hat{H}}_j^\dagger, |\tilde{\psi}_j\rangle)$ [96]. From the vectors of these two subspaces we obtain two matrices $\hat{Q} = (|v_j^0\rangle, |v_j^1\rangle, \dots |v_j^{N-1}\rangle)$ and $\hat{P} = (|v_j^{0'}\rangle, |v_j^{1'}\rangle, \dots |v_j^{N-1'}\rangle)$, which again satisfy $\hat{Q}\hat{Q}^\dagger = \hat{\mathbb{1}}$ and $\hat{P}\hat{P}^\dagger = \hat{\mathbb{1}}$. However, in general, we have that $\hat{Q}\hat{P}^\dagger \neq \hat{\mathbb{1}}$ and thus we cannot obtain the exact (within the Krylov subspace) expression of $e^{-i\delta t\hat{\hat{H}}_j}$ simply by exponentiating the tridiagonal matrix $\hat{T} = \hat{P}^\dagger\hat{\hat{H}}_j\hat{Q}$, as we did for the Hermitian case (see Eqs. (3.15) and (3.16)). Thus, for a non-Hermitian $\hat{\hat{H}}_j \neq \hat{\hat{H}}_j^\dagger$ we resort to a brute-force Taylor expansion and compute

$$e^{-i\delta t\hat{\hat{H}}_j}|\tilde{\psi}_j\rangle \approx \sum_{m=0}^{M} \frac{\left(-i\delta t\hat{\hat{H}}_j\right)^m}{m!}|\tilde{\psi}_j\rangle , \tag{3.17}$$

by applying the Hamiltonian on the state M times [96]. One can perform this operation efficiently as long the Krylov subspace is low-dimensional.

If one does not want to modify the TDVP algorithm as outlined above or worries about the convergence of the Taylor expansion Eq. (3.17), there is another simple alternative for dealing with non-Hermitian Hamiltonians. One can split every non-Hermitian operator into a Hermitian and an anti-Hermitian part

$$\hat{\tilde{H}}_j = \frac{1}{2}(\hat{\tilde{H}}_j + \hat{\tilde{H}}_j^\dagger) + \frac{1}{2}(\hat{\tilde{H}}_j - \hat{\tilde{H}}_j^\dagger) \equiv \hat{S}_j + \hat{A}_j \,. \tag{3.18}$$

A first-order Trotter decomposition then yields

$$e^{-i\delta t \hat{\tilde{H}}_j} \approx e^{-i\delta t \hat{S}_j} e^{-i\delta t \hat{A}_j} \equiv e^{-i\delta t \hat{S}_j} e^{-\delta t \hat{S}'_j} \,, \tag{3.19}$$

where we have introduced the Hermitian operator $\hat{S}'_j \equiv i\hat{A}_j$. Eq. (3.19) tells us that we can approximate a non-Hermitian time evolution by an alternating real- and -imaginary time evolution with two Hermitian Hamiltonians $\hat{S}_j$ and $\hat{S}'_j$. The Trotter error of order $\mathcal{O}(\delta t^2)$ is typically not an issue for pure-state unraveling methods, which require a small time step. When using TDVP to propagate the density matrix $\hat{\rho}$ with the vectorized Lindbladian, which allows applying a relatively large δt, one can substitute Eq. (3.19) with a higher-order Trotter decomposition if needed [82].

3.3 Phonon state tomography (PST)

The control of femtosecond laser pulses has opened new possibilities for investigating non-equilibrium properties of solids [97, 98]. A particularly intriguing class of experiments are pump-probe setups that involve the excitation of optical phonon branches by an infrared pump pulse, followed by the probing of the electronic system with a second pulse [99, 100]. These have enabled the investigation of, for instance, non-equilibrium light-induced transient superconductivity [41, 101, 102].

The exponentially large Hilbert space of a solid's phonon subsystem renders the theoretical modeling of such experiments extremely challenging. In 1D systems, it is feasible to use MPS to numerically calculate quantities like the average total number of phonon excitations $\langle \hat{N}^{\mathrm{ph}} \rangle$ or even phonon correlation functions. However, the global phonon distribution function $\mathscr{P}(N^{\mathrm{ph}})$, describing the probability of finding a total of N^{ph} phonon excitations in the system, remains out of reach of such methods due to the exponential scaling of the number of phonon configurations with the system size. This is problematic since $\mathscr{P}(N^{\mathrm{ph}})$ plays a prominent role in the analysis of the pump-probe experiments, as it is directly connected to the pump pulse's shape, which can significantly influence electronic dynamics [42]. Here, we will show that having access to $\mathscr{P}(N^{\mathrm{ph}})$ allows us to determine the dependence of electron correlation functions on the pump strengths from a single simulation (i.e., only one value of the pump strength). Inspired by snapshot-based sampling methods, which are well-established in the context of ultracold atoms [103–109], we introduce PST as a solution to address these computational challenges.

We investigate a lattice system comprising electronic and phononic degrees of freedom, described by the total Hilbert space $\mathscr{H} = \mathscr{H}^{\mathrm{el}} \otimes \mathscr{H}^{\mathrm{ph}}$. We assume a tensor-product structure for the phononic Hilbert space $\mathscr{H}^{\mathrm{ph}} = \bigotimes_{j=0}^{L^{\mathrm{ph}}-1} \mathscr{H}_j^{\mathrm{ph}}$, where j denotes the L^{ph} distinct phononic degrees of freedom. For example, $\mathscr{H}_j^{\mathrm{ph}}$ could represent the Hilbert space of a local Holstein phonon. Still, we do not impose any specific constraints on the type of phonons considered in the following. Introducing the vector $\mathbf{n}^{\mathrm{ph}} = \left(n_0^{\mathrm{ph}}, n_1^{\mathrm{ph}}, \dots, n_{L^{\mathrm{ph}}-1}^{\mathrm{ph}}\right)$ to label a possible configuration of the total phonon system, any state $|\Psi\rangle \in \mathscr{H}$ in the total Hilbert space can be expanded as

$$|\Psi\rangle = \sum_{\{\mathbf{n}^{\mathrm{ph}}\}} \varphi(\mathbf{n}^{\mathrm{ph}})\, |\psi^{\mathrm{el}}(\mathbf{n}^{\mathrm{ph}})\rangle \otimes |\mathbf{n}^{\mathrm{ph}}\rangle \ , \tag{3.20}$$

where $|\psi^{\mathrm{el}}(\mathbf{n}^{\mathrm{ph}})\rangle \in \mathscr{H}^{\mathrm{el}}$ represents a normalized electronic wave function, and the sum runs over all possible configurations $\mathbf{n}^{\mathrm{ph}}$ of the phononic system. Here, $|\varphi(\mathbf{n}^{\mathrm{ph}})|^2 \equiv p(\mathbf{n}^{\mathrm{ph}})$ is the probability of measuring the phonon configuration $\mathbf{n}^{\mathrm{ph}}$. We can calculate the global phonon distribution function $\mathscr{P}(N^{\mathrm{ph}})$ by summing $p(\mathbf{n}^{\mathrm{ph}})$ over all configurations $\mathbf{n}^{\mathrm{ph}}$ with N^{ph} phonons. To emphasize the practical significance of $p(\mathbf{n}^{\mathrm{ph}})$ and $\mathscr{P}(N^{\mathrm{ph}})$, let us examine an observable $\hat{O}$ that acts exclusively on the electronic subsystem $\mathscr{H}^{\mathrm{el}}$. The expectation value can be expressed as

$$\langle \hat{O} \rangle = \sum_{\{\mathbf{n}^{\mathrm{ph}}\}} p(\mathbf{n}^{\mathrm{ph}}) O^{\mathrm{el}}(\mathbf{n}^{\mathrm{ph}}) \tag{3.21}$$

$$= \sum_{N^{\mathrm{ph}}} \mathscr{P}(N^{\mathrm{ph}}) \sum_{\mathbf{n}^{\mathrm{ph}} \in \Omega_{N^{\mathrm{ph}}}} \frac{p(\mathbf{n}^{\mathrm{ph}})}{\mathscr{P}(N^{\mathrm{ph}})} O^{\mathrm{el}}(\mathbf{n}^{\mathrm{ph}}) \ , \tag{3.22}$$

where $O^{\mathrm{el}}(\mathbf{n}^{\mathrm{ph}}) = \langle \psi^{\mathrm{el}}(\mathbf{n}^{\mathrm{ph}}) | \hat{O} | \psi^{\mathrm{el}}(\mathbf{n}^{\mathrm{ph}}) \rangle$. In the final line, we can recognize the conditional probability $\frac{p(\mathbf{n}^{\mathrm{ph}})}{\mathscr{P}(N^{\mathrm{ph}})}$, which represents the probability of measuring a phonon configuration $\mathbf{n}^{\mathrm{ph}}$ given that there are N^{ph} phonons in total.

Since there are exponentially many configurations $\mathbf{n}^{\mathrm{ph}}$, we suggest to approximate Eq. (3.21) as

$$\langle \hat{O} \rangle \approx \frac{1}{|\Omega|} \sum_{\mathbf{n}^{ph} \in \Omega} O^{\mathrm{el}}(\mathbf{n}^{\mathrm{ph}}) \ , \tag{3.23}$$

i.e. by drawing a finite number of samples $|\Omega|$ according to $p(\mathbf{n}^{\mathrm{ph}})$. To achieve this, we extend the perfect sampling approach previously introduced for MPS in the context of ultracold atoms [110]. The starting point is to decompose the joint probability distribution function of a phonon configuration $\mathbf{n}^{\mathrm{ph}}$ into a product of conditional probabilities as

$$p(\mathbf{n}^{\mathrm{ph}}) = p(n_0^{\mathrm{ph}})p(n_1^{\mathrm{ph}}|n_0^{\mathrm{ph}}) \cdots p(n_{L-1}^{\mathrm{ph}}|n_{L-2}^{\mathrm{ph}}, \dots, n_0^{\mathrm{ph}}) \, . \tag{3.24}$$

The importance of Eq. (3.24) lies in the fact that the local probability distributions $p(n_j^{\mathrm{ph}}|n_{j-1}^{\mathrm{ph}}, \dots, n_0^{\mathrm{ph}})$ correspond to the diagonal part of the phononic 1RDM which, as we will show, can be computed efficiently with PP. $p(\mathbf{n}^{\mathrm{ph}})$ can then be estimated by simulating repeated projective measurements of the phononic system and counting how often a particular configuration $\mathbf{n}^{\mathrm{ph}}$ is observed. One complete projective measurement can, for instance, be implemented as a sweep from left to right (i.e., initializing $j = 0$) as follows:

1. On site j, compute the phononic 1RDM $\hat{\rho}_j^{\mathrm{ph}} \equiv \mathrm{tr}_{\mathrm{el}}\, \mathrm{tr}_{\mathrm{ph}_{\setminus j}} |\Psi\rangle \langle\Psi|$ and identify its diagonal part with $p(n_j^{\mathrm{ph}})$. Here $\setminus j$ indicates that we are tracing out all phononic sites except site j.
2. Draw the projector $|n_j^{\mathrm{ph}}\rangle \langle n_j^{\mathrm{ph}}|$ according to the probablilty distribution $p(n_j^{\mathrm{ph}})$ and apply it to $|\Psi\rangle$.
3. Move one site to the right by increasing j by 1 and repeat steps 1. and 2., until the last site has been reached.

Note that in 1. and 2. $p(n_j^{\mathrm{ph}})$ indicate a conditional probability for all $j > 0$ (see Eq. (3.24)), but we have omitted the second part of the argument for simplicity.

After having generated a sufficient number of measurements (or samples) $\mathbf{n}^{\mathrm{ph}}$, an arbitrary electron observable $\langle\hat{O}\rangle$ can be reconstructed using Eq. (3.23). We will show in Chapter 7 that PST-decomposed electronic observables converge to the exact results much faster than $\mathscr{P}(N^{\mathrm{ph}})$. Here, we need to stress an important point: Averaging over the samples first and using the resulting state to compute an expectation value is equivalent to computing the expectation value for every sample individually and then averaging the results. This is due to the fact that, because of the orthogonality of the phonon configurations in the decomposition Eq. (3.20), the interference terms vanish. Being able to compute the expectation values for the individual samples has the crucial advantage that by categorizing the samples based on the total phonon number, denoted as $N^{\mathrm{ph}} = \sum_{j=0}^{L-1} n_j^{\mathrm{ph}}$, we obtain the decomposition of an electron observable $\langle\hat{O}(N^{\mathrm{ph}})\rangle$ into contributions from the different phonon sectors N^{ph}. We summarize the main features of PST in Fig. 7.3.

We represent the combined electron-phonon system as an MPS and utilize the PP method, as described in Section 3.1, to efficiently handle the large local Hilbert

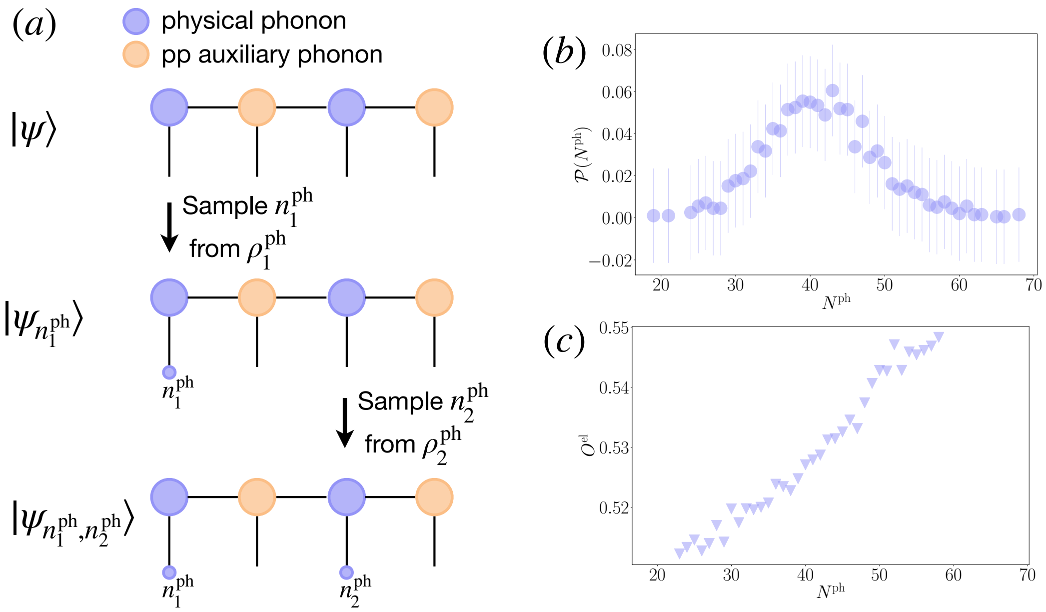

Figure 3.5: Depiction of the phonon state tomography (PST) method. (a): A sample $\mathbf{n}^{\mathrm{ph}}$ for a system with $L = 2$ sites is drawn by performing a projective measurement on the phononic system. (b): For a 1D electron-phonon system with $L = 20$ sites (see Fig. 7.1), the phonon distribution function $\mathscr{P}(N^{\mathrm{ph}})$ is computed by categorizing the samples $\mathbf{n}^{\mathrm{ph}}$ based on the total phonon number N^{ph}. (c): A electron observable O^{el} is decomposed into contributions from the different phonon sectors N^{ph}. The data for panels (b) and (c) is extracted from Fig. 7.3.

space dimensions of the phononic degrees of freedom. A standard computation of the conditional probabilities $p(n_j^{\mathrm{ph}}|n_{j-1}^{\mathrm{ph}}, \dots, n_0^{\mathrm{ph}})$ would require tracing out the electronic system and all phononic sites except for site j to obtain the 1RDM $\hat{\rho}_j^{\mathrm{ph}}$, which is numerically costly. PP allows substituting the challenging computation of the 1RDM with a SVD of every block n_j^{ph} of the tensor on the physical phononic site j (see Eq. (3.7) in Section 3.1). It is worth noting that the computational cost of this operation remains independent of the system size L.

Chapter 4

Comparing Markovian and Non-Markovian pure-state methods

This chapter compares non-Markovian open quantum system (OQS) methods to Markovian-embedding ones. The latter consist in enlarging the physical subsystem considered explicitly in the dynamics so that the impact of the (reduced) environment can be captured exactly by the Lindblad equation. To explore the numerical properties of the methods described in Chapter 2, we study the dissipative dynamics of the Hubbard-Holstein model [111] that describes electrons linearly coupled to dispersionless phonons. Despite being numerically very challenging, it offers a conceptually simple way of understanding the Markovian-embedding procedure. The rich physics captured by the model and, in particular, the impact of the dissipative environment on the bipolaronic quasi-particles will be discussed in Chapter 8.

In 1D, the Hubbard-Holstein Hamiltonian reads

$$\begin{aligned}\hat{H}_{\text{HH}} = &-J\sum_{j=1}^{L}\sum_{\sigma=\uparrow,\downarrow}\left(\hat{c}^{\dagger}_{j,\sigma}\hat{c}_{j+1,\sigma}+\text{h.c.}\right)+U\sum_{j=1}^{L}\hat{n}_{j,\uparrow}\hat{n}_{j,\downarrow}\\ &+\omega\sum_{j=1}^{L}\hat{a}^{\dagger}_{j}\hat{a}_{j}+g\sum_{j=1}^{L}\left(\hat{a}_{j}+\hat{a}^{\dagger}_{j}\right)\hat{n}_{j}\,. \end{aligned} \tag{4.1}$$

Here U represents the on-site electron-electron interaction, ω stands for the phonon frequency, and g denotes the electron-phonon coupling. The operator $\hat{c}^{\dagger}_{j,\sigma}$ ($\hat{c}_{j+1,\sigma}$) creates (annihilates) a fermionic particle with spin σ on site j while $\hat{a}^{\dagger}_{j}$ ($\hat{a}_{j}$) creates (annihilates) a phonon on site j. In the following, we set J to represent the energy unit and J^{-1} to denote the unit of time.

A sketch for a 1D electron-phonon system is shown in Fig. 4.1. The right panel depicts one possible system-environment bipartition: the electrons represent the system and the dissipative phonons represent the environment. In this case, the

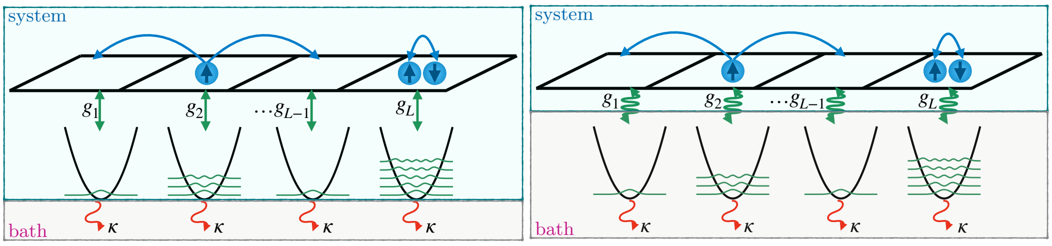

Figure 4.1: Two possible system-environment partitionings for dissipative electron-phonon models. Markovian embedding (left panel): In this approach, we consider both electrons and phonons as the system, whereas the dissipation acting on the phonons is modeled as a Markovian environment. Non-Markovian approach (right panel): In this case, only the electrons are treated as the system, while the dissipative phonon modes form a non-Markovian environment.

environment is non-Markovian, as the electrons strongly influence the dynamics of the phonons. Attempting to describe this scenario with a Markovian master equation for only the electronic degrees of freedom yields wrong results, as we will explicitly show in Fig. 4.4. The other possible bipartition is the so-called Markovian-embedding approach [112], represented in the left panel of Fig. 4.1: the electrons and the phonons are both treated as the system, and dissipation models the environment. In this setup, we are confronted with a Markovian system, as the system's state does not alter the dissipative environment.

In the following benchmark, our primary methods of choice will be quantum jumps (QJ) for the Markovian case and the hierarchy of pure states (HOPS) for the non-Markovian one. Despite HOPS and QJ being well-established tools for describing open quantum systems, we integrate these methods with a tensor-network representation, which introduces its own set of approximations. Furthermore, we must take into account the truncation within the phononic Hilbert space generated by the projected purification (PP) mapping (see Section 3.1). It is, therefore, crucial to grasp the impact of additional numerical approximations, particularly when we can control numerical precision within each method by adjusting typical control parameters like the bond dimension or the discarded weight [21, 82].

We initialize the system in a product state between the electronic and the phononic systems, corresponding to a highly-excited state of Eq. (4.1). One noteworthy aspect of the post-quench dynamics is the potentially very large occupation of the bosonic, local degrees of freedom. This occurrence is primarily driven by the excess energy of the electronic system, and it competes with the influence of dissipation. In certain parameter regimes, describing the dynamics of the overall system requires a large local Hilbert space dimension $\sim 10-60$ for the bosonic system. Capturing these competing effects correctly is one of the most important

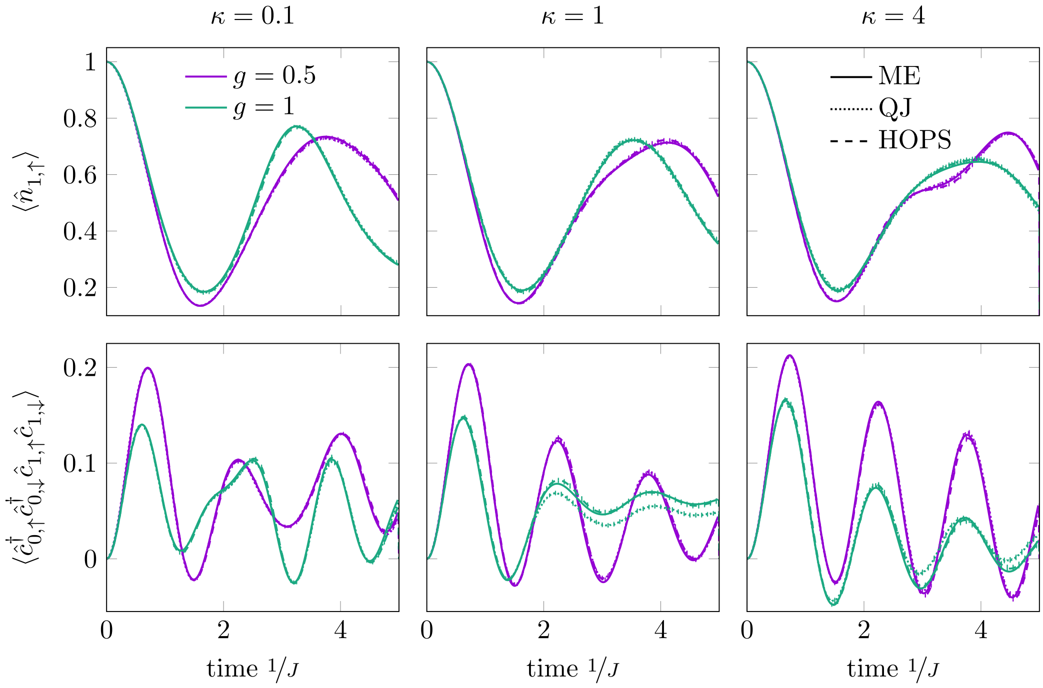

Figure 4.2: Comparison of HOPS and QJ to the exact master equation (ME). All curves were computed using ED for a system consisting of two fermionic and two phononic sites. For all panels, we set the Hamiltonian parameters to $U = J$, $\omega = 2\,J$, and employed 500 trajectories with a time step of $dt = 0.005\,J^{-1}$. Both HOPS and QJ closely align with the exact ME results. Only QJ, in scenarios involving intermediate and strong dissipation combined with a large electron-phonon interaction ($\kappa = 1, 4J$, $g = J$), displays small deviations at later times $t > 2J^{-1}$.

points in practice since we will show that small, uncontrolled approximations already modify the short-time dynamics of correlation functions drastically. It is worth noting that a substantial amount of energy is injected into the system when quenching from a product state. In this sense, our analysis represents an extreme test case. In practical scenarios, for near-equilibrium (or local) quenches, we anticipate that both methods will perform reasonably well, even in the regime that complements the optimal one described in the following sections.

An intriguing aspect lies in the dependence on the strength of dissipation, as both approaches are fundamentally complementary: For HOPS, the environment becomes Markovian as $\kappa \to \infty$, while for QJ, the non-unitary component of the dynamics within the extended system becomes negligible as $\kappa \to 0$. This chapter is based on Ref. [1].

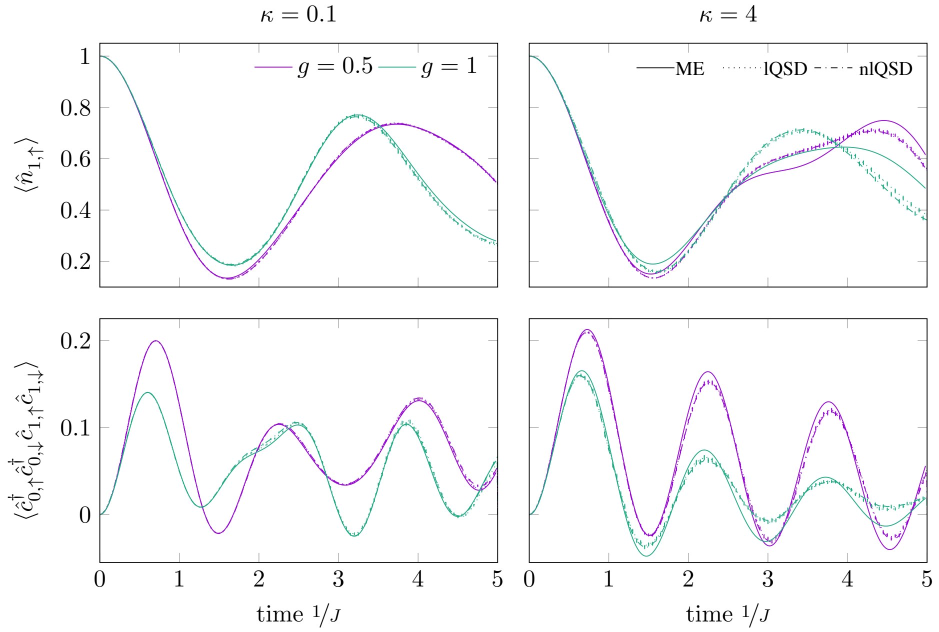

Figure 4.3: Comparing the linear and nonlinear QSD to the exact Master Equation (ME). All results were computed using ED for a system consisting of two fermionic and two phononic sites. In all panels, the Hamiltonian parameters were set to $U = J$, $\omega = 2J$, with 500 trajectories and a time step of $dt = 0.005J^{-1}$. For the two left panels, the dissipation strength is $\kappa = 0.1J$, while in the two right panels we used $\kappa = 4J$. Across all analyzed parameters, the linear and nonlinear methods yield almost the exact same results. While both methods reasonably agree with the exact results under low dissipation strength, deviations become substantial as the dissipation grows stronger. This issue becomes more pronounced in the presence of a large electron-phonon coupling.

4.1 ED comparison

The dynamics of the smallest meaningful Hubbard-Holstein model, consisting of two electronic and two phononic sites, can be described by the exact Lindblad master equation (Eq. (2.6)) via ED[1]. We employ this as an exact reference point to evaluate both the accuracy and computational costs of the QJ, quantum state diffusion (QSD), and HOPS methods before applying them to larger systems. We set $U = J$ and $\omega = 2J$, and vary the electron-phonon coupling g and the dissipation strength κ. We initiate the time evolution with the Neel state for the fermions

---

[1] Due to the large local Hilbert space dimension required for the phonons, this system is already quite challenging to simulate exactly. For instance, in a model with a 10-level harmonic oscillator, the total Hilbert space dimension for the density matrix of the two-electron and two-phonon system is $\approx 2.6 \times 10^6$. In some cases where we perform matrix product state (MPS) calculations, we need to consider up to 60 phononic states, leading to a total Hilbert space dimension of approximately 3.3×10^9 for a two-site system.

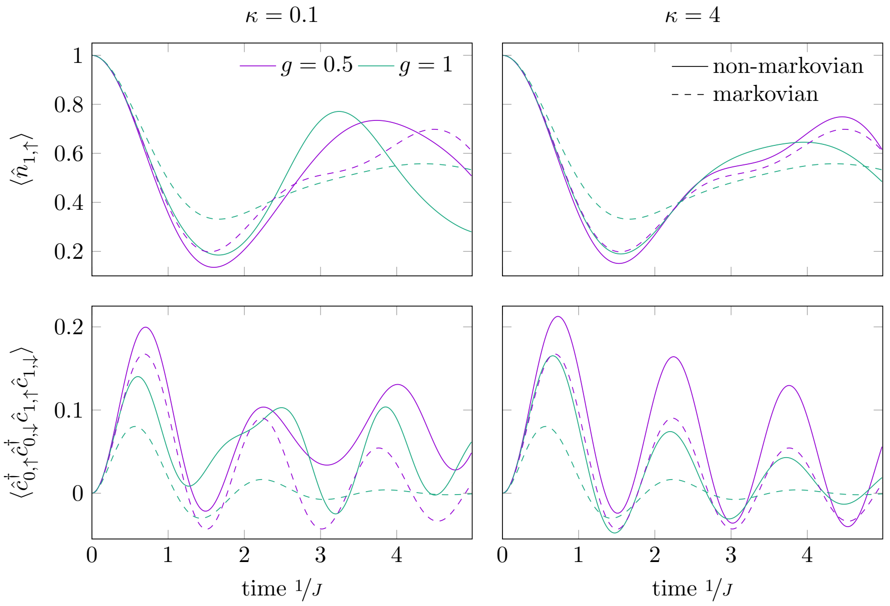

Figure 4.4: Comparison between a master equation for the "electron + phonon" system and a master equation for the electron system alone. For all panels, the Hamiltonian parameters were set to $U = J$ and $\omega = 2J$. Additionally, the dissipation strength was set to $\kappa = 0.1\,J$ for the left panels and to $\kappa = 4\,J$ for the right panels. The results obtained with the two methods exhibit significant discrepancies, highlighting that the electron dynamics of the systems under consideration cannot be adequately described by the simple Lindblad master equation of the form shown in Eq. (4.3).

and the vacuum state for the phonons

$$|\Psi\rangle^{\text{init}} = |\uparrow\rangle_1^{\text{fer}} |\downarrow\rangle_2^{\text{fer}} |0\rangle_1^{\text{bos}} |0\rangle_2^{\text{bos}} \ ,$$

and perform a global quench both in the electronic and in the phononic system. We study a single and a two-site observable: the number of spin-up fermions on site one $\langle \hat{n}_1^{\uparrow} \rangle$, and the pairing correlation between the two fermionic sites $\langle \hat{c}^\dagger_{0,\uparrow}\ \hat{c}^\dagger_{0,\downarrow}\ \hat{c}_{1,\downarrow}\ \hat{c}_{1,\uparrow} \rangle$. We opt to compare the two methods for very weak ($\kappa = 0.1\,J$), intermediate ($\kappa = J$), and very strong ($\kappa = 4\,J$) dissipation, considering both medium and strong electron-phonon couplings, specifically $g = 0.5\,J$ and $g = J$.

4.1.1 Comparing QJ and HOPS

We start investigating the performance of the HOPS and the QJ methods by considering the quench protocol described above in Section 4.1. In the QJ approach, the dissipative dynamics are simulated by unraveling the Lindblad equation 2.6 where $\hat{H}_s$ is the Hubbard-Holstein Hamiltonian Eq. (4.1) and one jump operator $\hat{L}_j = \sqrt{\kappa}\hat{a}_j$ acts on every site j. Instead, for HOPS the effective Hamilto-

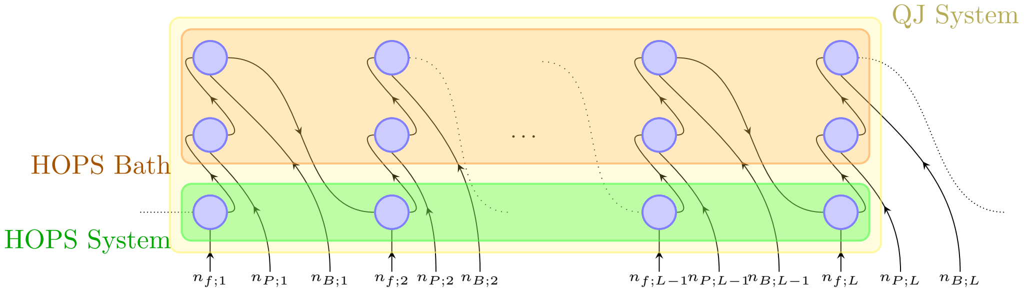

Figure 4.5: MPS for a 1D electron-phonon system with the PP mapping (see Section 3.1). Each column represents a full lattice site, made up of one electronic site (n_f), one physical bosonic site (n_P), and one PP-auxiliary bosonic site (n_B). The bosonic sites constitute the non-Markovian environment for the HOPS method, while in the Markovian-embedded QJ scheme they are part of the system.

nian Eq. (2.39) is constructed setting $\hat{H}_s$ equal to the Hubbard Hamiltonian (i.e. the upper line in Eq. (4.1)) and again $\hat{L}_j = \sqrt{\kappa}\hat{a}_j$. We summarize our findings in Fig. 4.2. In general, we notice an excellent agreement between both HOPS and QJ with the master equation (ME) outcomes during short time intervals $t \leq 2\,J^{-1}$. The sole noteworthy deviation arises in the QJ outcomes for the two-site observable at late times, specifically in instances of strong electron-phonon coupling ($g = 1J$) and moderate or strong dissipation ($\kappa \geq 1J$). We believe that reducing the time step while increasing the number of trajectories (or adopting a QJ algorithm with an adaptive time step [95]) would enhance the agreement with the exact outcome. Nevertheless, one has to be cautious when employing MPS methods, as an overly tiny time step may result in the accumulation of truncation errors. Hence, we propose that, especially in scenarios involving a global quench from a product state and falling within the aforementioned parameter range, HOPS should be the preferred choice over QJ.

4.1.2 QSD comparison

We continue the numerical benchmark by presenting an ED comparison of the linear and nonlinear QSD methods introduced in Section 2.4 with the exact ME results. In Fig. 4.3, we study the spin-up electron density and the pairing correlation function, using the same parameters as those in Fig. 4.2. Both the linear and nonlinear homodyne detection methods perform well when the dissipation is small. However, they fail to yield correct results for single-site and two-site observables in cases of large dissipation. These results suggest that the QJ method is more suitable than QSD for a comparison with HOPS.

For the dissipative Hubbard-Holstein model that we considered here, the

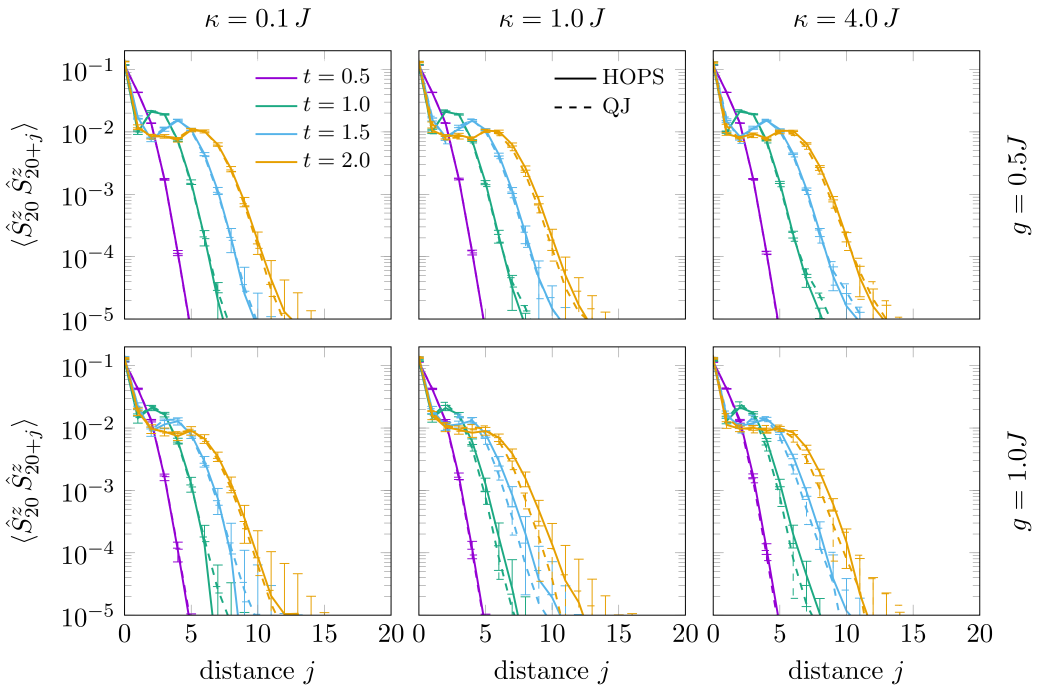

Figure 4.6: Spin-density correlations $\langle \hat{\sigma}^z_{20}\,\hat{\sigma}^z_{20+j}\rangle$ computed for a system consisting of $L = 40$ sites at half-filling, following a quench from a Neel state. The correlations are evaluated using both HOPS and QJ for two distinct values of g (columns) and across three different values of κ (rows). Both methods exhibit excellent agreement, even in the context of long-range correlations. Minor discrepancies between HOPS and QJ are observed primarily in cases of strong electron-phonon coupling ($g = J$) and intermediate to strong dissipation ($\kappa = 1\,J,\ 4\,J$). We used a time step of $\delta t = 0.005\,J^{-1}$ for QJ and $\delta t = 0.01\,J^{-1}$ for HOPS to account for the lower sensitivity of the latter method to the time step.

lQSD effective Hamiltonian is given by

$$\hat{H}^z_{\text{eff}} = \hat{H}_{\text{HH}} + i\sum_{j=1}^{L}\left[Z_j(t)\hat{a}_j - \frac{\kappa}{2}\hat{a}_j^\dagger\hat{a}_j\right]. \tag{4.2}$$

In Appendix A, we show that for the effective Hamiltonian Eq. (4.2), an exact decomposition of the time evolution operator can be obtained. It consists of a simple non-Hermitian term (for which we derive the exact MPO representation) and an involved Hermitian one, opening the possibility of alternating an MPO-MPS application for the non-Hermitian part with a conventional time evolution scheme for Hermitian Hamiltonians like TDVP. We discussed how to adapt the TDVP algorithm to treat general non-Hermitian Hamiltonians in Section 3.2.2.

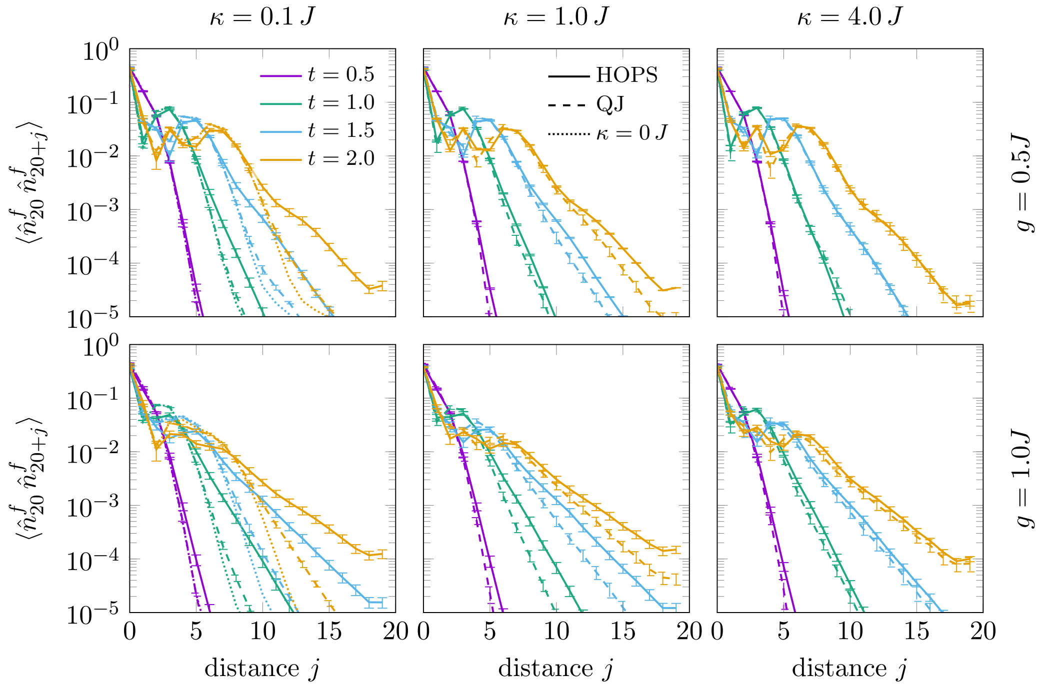

Figure 4.7: Charge-density correlations $\langle \hat{n}^{\mathrm{f}}_{20}\,\hat{n}^{\mathrm{f}}_{20+j}\rangle$ computed using both HOPS and QJ for the same quench scenario as depicted in Figure 4.6. A discrepancy becomes apparent in the results at long times and for large spatial separations. In the two left panels, at each time, we have added a dotted line that represents the case without dissipation, i.e. a unitary evolution with the Hubbard-Holstein Hamiltonian. This suggests that when dissipation is very weak, QJ provides a more accurate description of long-range correlations compared to HOPS.

4.1.3 Failure of the Markovian description

The non-Markovian method described in Section 2.3 and the Markovian approach for the enlarged physical system (comprising electrons and phonons) discussed in Section 2.5 pose significant numerical challenges. As a result, one might question whether a much simpler Markovian master equation for the electronic system alone could adequately capture the dissipative dynamics. Such an equation was obtained following the standard microscopic derivation of the Lindblad equation (see Section 2.1) in Ref. [67] and reads

$$\partial_t \hat{\rho}_s = -i[\hat{H}_S, \hat{\rho}_s] + g^2\Big(\sum_{j=1}^{L} \hat{n}_j \hat{\rho}_s \hat{n}_j - \frac{1}{2}\{(\hat{n}_j)^2, \hat{\rho}_s\}\Big)\,. \tag{4.3}$$

Here, $\hat{H}_S$ represents the Hubbard Hamiltonian, g is the electron-phonon coupling, and $\hat{n}_j$ is the number operator acting on the j-th fermionic site. The non-Hermitian part in Eq. (4.3) is known as a dephasing environment. The exact diagonalization comparison between the master equation for the enlarged system and the master equation for the electronic system only (Eq. (4.3)) is illustrated in Fig. 4.4. This comparison reveals that the latter is inadequate for describing the non-Markovian vibrational environment, especially for large electron-phonon coupling g. This is in agreement with the fact that the Lindblad equation Eq. (4.3) has been derived via the Markovian and the Born (i.e. weak coupling) approximation.

4.2 MPS comparison

We now move to many-body dynamics and enlarge the system size to $L = 40$. These system sizes are out of reach for both ED techniques and, to the best of our knowledge, even to density operator-based MPS time-evolution approaches, especially when dealing with a substantial number of phononic modes (in our case ≤ 60) per site. Each lattice site, i.e., each column in Fig. 4.5, is made up of an electronic site, a physical bosonic site, and a PP-auxiliary bosonic site (see Section 3.1). We systematically vary all pertinent parameters during the benchmark calculations to ensure numerical convergence. In Table 4.1, we show the configurations we identified as yielding accurate and well-converged outcomes. For all calculations, we choose a time step of $\delta t = 0.01\ J^{-1}$ for HOPS and $dt = 0.005\ J^{-1}$ for QJ. Additionally, we usually set the maximum allowed hierarchy depth k_{max} (for HOPS) and the local Hilbert space dimension of the phonons b_{max} (for QJ) to $k_{\text{max}} = b_{\text{max}} = 40$. We observe that these values are adequate for characterizing the dynamics, and as a result, the actually used local dimensions never reach their respective maximum limits. Given that the initial state is a product state, we initiate the time-evolution using the global Krylov [82] method and subsequently switch to the two-site time-dependent variational principle (2TDVP) method. To

	d-surface Figs. 4.8, 4.10	**QJ, HOPS** Figs. 4.6, 4.7 4.11	**double occupations** Fig. 8.2	**bipolaron metallicity** Figs. 8.3, 8.4
δ	10^{-10}	10^{-10}	10^{-10}	10^{-10}
m_{max}	6000	6000	500	2000
d_{max}	60	40	40	40
L	10	40	20	20
N	5	200	50	200

Table 4.1: Summary of the most relevant simulation parameters: the max. allowed discarded weight δ, the max. allowed MPS bond dimension m_{max}, the max. allowed local dimension d_{max}, the number of sites L, and the overall number of trajectories N.

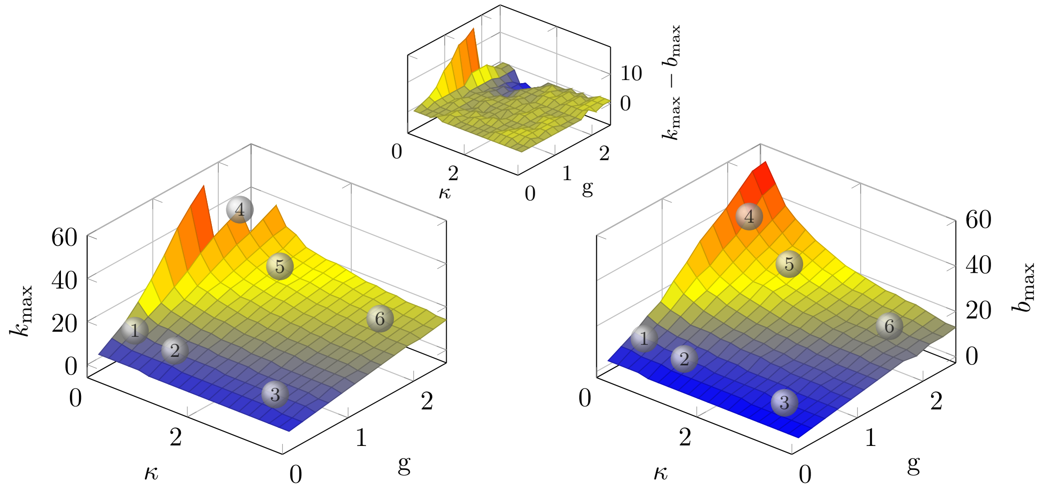

Figure 4.8: Left: Hierarchy depth k_{max} for HOPS as a function of g and κ. Right: Local physical dimension of the phonons $\mathrm{b}_{\mathrm{max}}$ for QJ as a function of g and κ. Center: The difference between k_{max} and $\mathrm{b}_{\mathrm{max}}$. The truncation is automatically determined using the PP method with a fixed discarded weight $\delta = 10^{-10}$. For all calculations, we use the model parameters $N_{\mathrm{sites}} = 10, U = J$, and $\omega = 2\,J$. The time evolution was performed up to $T_{\mathrm{max}} = 2\,J^{-1}$, and we computed 10 trajectories for each data point. For the six points marked by a sphere, the convergence analysis of an observable is provided in Fig. 4.10 and discussed in the main text. Note that in the region of very large g and very small κ (i.e., the top-left area in the left panel), HOPS exhibits instability issues, which are discussed in the main text.

achieve converged results, it is necessary to perform at least approximately 50 Krylov time-evolution steps, with all other numerical configurations remaining unchanged[2]. Our comparative analysis seeks to identify the parameter regions in which QJ and HOPS excel in capturing the post-quench dynamics of many-body systems.

Given that the dynamics involve the propagation of correlations on various time scales, we study the dynamics of spin-density and charge-density correlation functions with respect to the central site. It is worth noting that both methods demonstrated comparable performance throughout our investigations when describing simpler local observables, which we do not show here. As demonstrated in Fig. 4.6, there is a remarkable agreement in the spin-density correlations between the two methods. Nevertheless, when examining the charge-density correlations as presented in Fig. 4.7, we observe discrepancies in the long-distance behavior, particularly in cases of very weak dissipation. An additional feature becomes evident in the tails of the correlation functions at times $t > 1\,J^{-1}$ in the

---

[2] When working on [1], LSE-TDVP and GSE-TDVP had not been implemented SyTen yet. As we discuss in Section 3.1, the global Krylov time-evolution can be replaced by the more efficient GSE-TDVP.

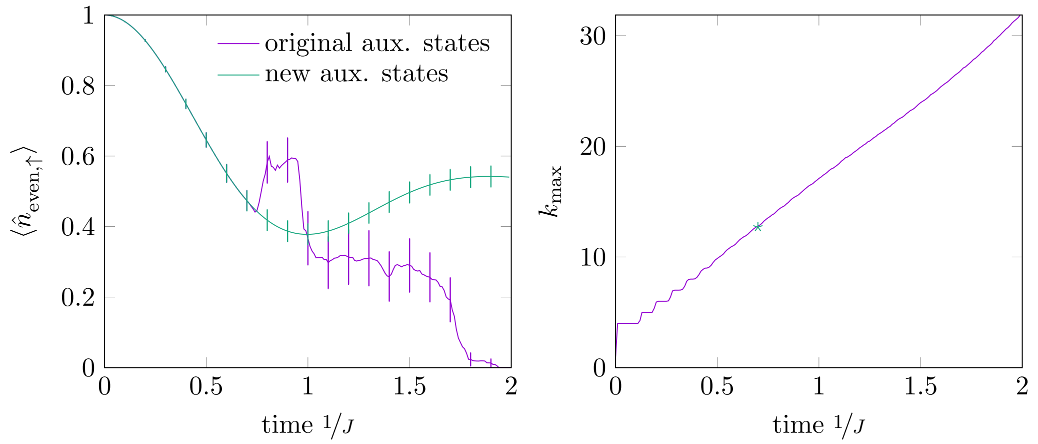

Figure 4.9: HOPS's stability is improved by employing auxiliary states transformed according to Eq. (2.36). In the strongly non-Markovian regime, as depicted in the right panel, numerous phononic modes become populated. Under the original HOPS formulation, in such cases, the norm of the auxiliary states grows significantly, leading to a pronounced instability when computing observables with the normalized physical state, as illustrated in the left panel. These calculations were conducted for a system with 20 sites and averaged over 100 trajectories, with parameters set to $g = J$ and $\kappa = 0.1\,J$. All other parameters align with those used in Figs. 4.6 and 4.7.

dynamics generated by HOPS. This characteristic corresponds to an enhanced propagation of density correlations in the HOPS results, as compared to QJ. It is worth noting that we have verified that reducing the time step of HOPS does not lead to an improvement in the results. We considered quench dynamics without dissipation to determine which method provides more trustworthy results in this regime. As illustrated in the upper-left panel of Fig. 4.7 by the dotted curves, we observe that QJ exhibits a smooth connection with the non-dissipative case. We interpret this observation as indicating that QJ is more precise, particularly in scenarios with low dissipation strengths.

4.3 Numerical complexity and stability

Clarifying whether the methods can be implemented within the identified optimal parameter ranges is crucial for practical calculations. Here, we first compare the hierarchy depth $k_{\text{max}} \equiv d_{\text{max}}$ for HOPS with the local Hilbert space dimension of the phonons $b_{\text{max}} \equiv d_{\text{max}}$ for QJ across various values of g and κ. When utilizing 2TDVP as the time evolution method, the most computationally intensive operations scale as $\mathcal{O}(m_{\text{max}}^3 d_{\text{max}}^2 \delta_{\text{max}})$ and $\mathcal{O}(m_{\text{max}}^2 d_{\text{max}}^3 \delta_{\text{max}}^2)$ [82]. For very large local dimensions where $d_{\text{max}} > 10$, the numerical cost of the latter operations can become predominant, and the feasibility of employing QJ and HOPS hinges on the requirements of their respective local Hilbert space dimensions.

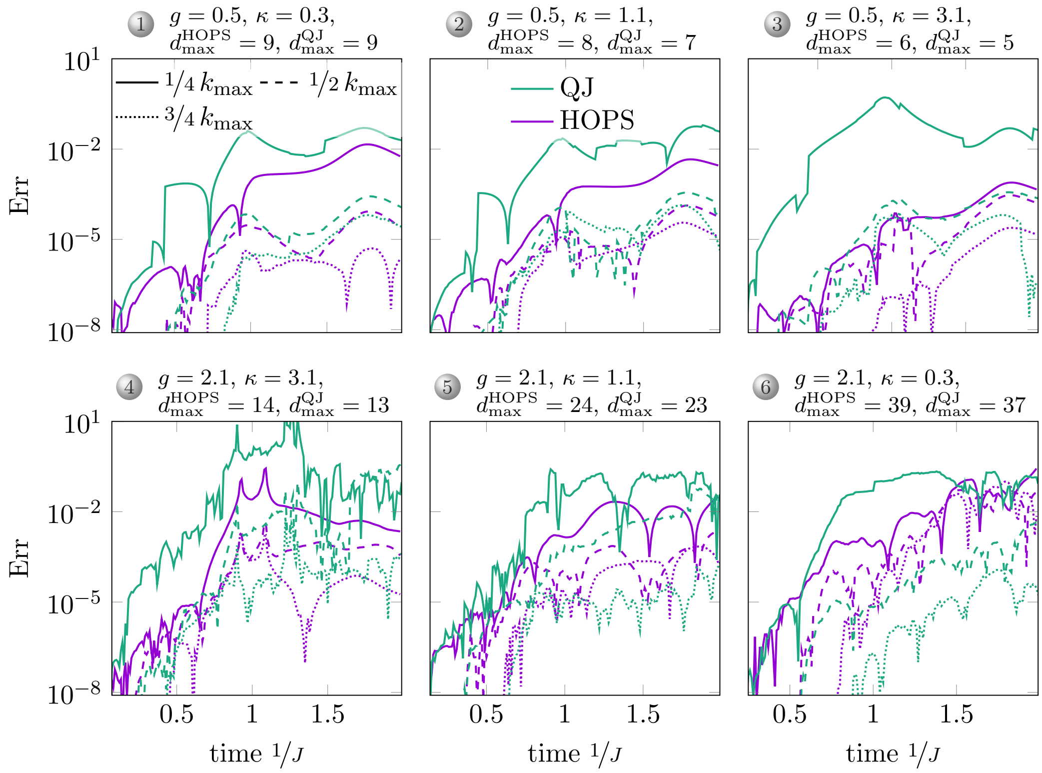

Figure 4.10: Convergence analysis of the nearest neighbor pairing correlation Eq. (4.4) with respect to the local Hilbert space dimension $d_{\max}$. We consider six specific parameter sets (g, κ) as indicated on the numbered spheres in Fig. 4.8. At each time step, we calculate the relative error by comparing the results obtained with the chosen local dimension $d_{\max}$ to a reference time evolution carried out with the optimal local dimension. All model and time evolution parameters are consistent with those outlined in Fig. 4.8. Note that we employ multiple trajectories solely to mitigate the risk of selecting an outcome influenced by favorable or unfavorable random number combinations. However, this analysis is unrelated to the statistical error defined in Eq. (2.22).

In Fig. 4.8, we present the evolution of $d_{\max} = k_{\max}, \mathrm{b}_{\max}$ required to maintain an overall discarded weight $\delta = 10^{-10}$ throughout the time evolution. Remarkably, despite their conceptual differences, each method exhibits a very similar dependency on g and κ for their required local Hilbert space dimensions, as depicted in the left panel for $k_{\max}$ and the right panel for $\mathrm{b}_{\max}$, across the entire parameter range under investigation. The relationship between these two quantities is explored for other models in [91, 113]. The shapes of the surfaces traced by $k_{\max}$ and $\mathrm{b}_{\max}$ substantiate our earlier observation that, in instances characterized by strong electron-phonon coupling and weak dissipation, numerous highly-excited phononic modes are populated, thereby necessitating extensive Hilbert space dimensions. Note that, in the case of HOPS, the top-left corner of the k_{max} surface is absent. This anomaly arises in a few "extreme" scenarios characterized by exceptionally strong electron-phonon coupling and very feeble dissipation, causing HOPS to become numerically unstable due to the rapid growth in the norm of auxiliary states. As a result, we conclude that the numerical costs for both methods are comparable when enforcing a specific discarded weight.

In all the HOPS calculations conducted on the dissipative Hubbard-Holstein model, we have applied a rescaling of the auxiliary states in accordance with Eq. (2.36). This rescaling operation reduces the norm of the auxiliary states, effectively mitigating numerical errors that may arise during the normalization of the physical state, an operation performed at each time step when computing observables. As illustrated in Fig. 4.9, the significance of this rescaling becomes apparent when considering a scenario with strong electron-phonon coupling ($g = 1$) and weak dissipation ($\kappa = 0.1$). In such cases, when not utilizing auxiliary state rescaling, the HOPS method fails completely when the population of bosonic modes reaches 13. In contrast, with the new definition of auxiliary states (as shown in Fig. 4.8), HOPS is capable of handling up to 55 occupied bosonic modes. It is important to emphasize that this issue is not specific to MPS but also arises in ED calculations.

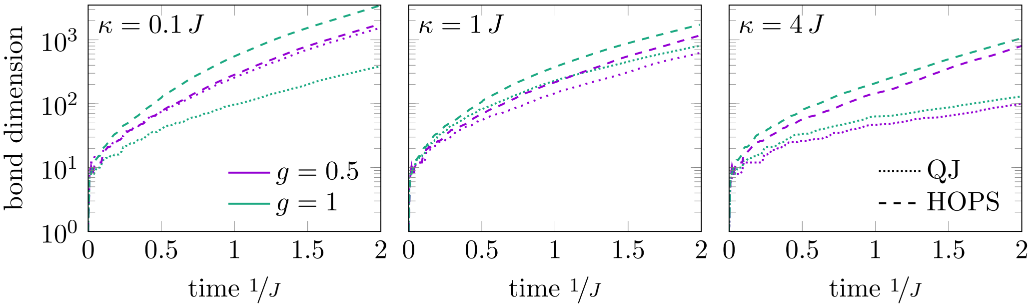

Figure 4.11: The bond dimension for both QJ and HOPS during the time evolution following the global quenches described in the caption of Fig. 4.6.

In Fig. 4.8, we have analyzed the convergence of the time-evolved wave function $|\Psi(t)\rangle$ with respect to the local dimension d_{max}. However, one is often interested in the convergence of specific observables rather than in the accuracy of the wave function. Thus, we select six representative parameter points indicated by circles in Fig. 4.8 to investigate the convergence of the nearest-neighbor pairing correlation function

$$\mathrm{C}_{\mathrm{nn}}^{\mathrm{pa,d_{max}}} = \frac{1}{L-1} \sum_{j=1}^{L-1} \langle \hat{c}_{j,\uparrow}^{\dagger}\, \hat{c}_{j,\downarrow}^{\dagger}\, \hat{c}_{j+1,\downarrow}\, \hat{c}_{j+1,\uparrow} \rangle \ . \tag{4.4}$$

We assess its dependence on the maximally allowed local dimension in comparison to a reference value, denoted as $\mathrm{C}_{\mathrm{nn}}^{\mathrm{pa,k_{max}}}$. This reference value is determined by fixing the discarded weight only and employing the values of k_{max} and b_{max} extracted from Fig. 4.8. We define

$$\text{Err}(j) = \left| \left(\text{C}_{\text{nn}}^{\text{pa,d}_{\text{max}}} - \text{C}_{\text{nn}}^{\text{pa,d}_{\text{max}} \cdot \text{j}} \right) / \text{C}_{\text{nn}}^{\text{pa,d}_{\text{max}}} \right| , \tag{4.5}$$

considering $j \in \{1/4, 1/2, 3/4\}$, thereby reducing the maximally allowed local dimension to as low as a quarter of the optimal value. In Fig. 4.10, we present the achieved convergence for the various fractions j of d_{max} as indicated by the different line styles. Notably, we observe that in most cases, the curves for HOPS lie below those for QJ. This observation can be attributed to the fact that in HOPS, the bosonic degrees of freedom represent auxiliary states with no direct physical interpretation. Consequently, we observe that HOPS is somewhat less affected by truncations in the bosonic Hilbert space compared to QJ.

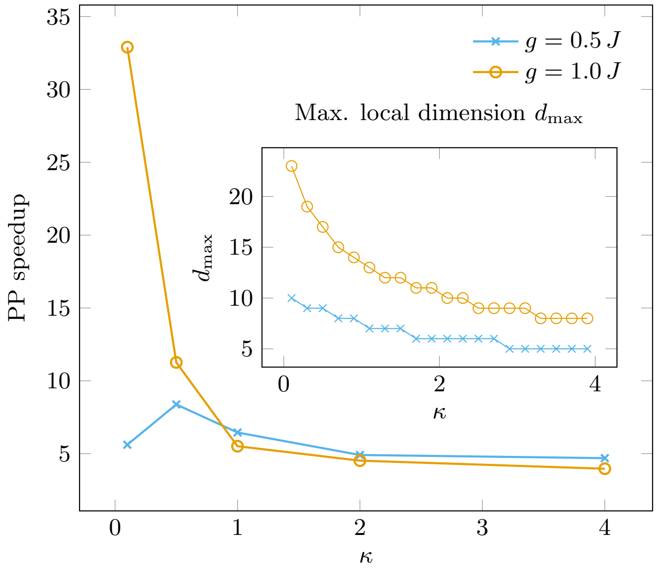

Figure 4.12: PP speedup for intermediate (blue) and strong (orange) electron-phonon couplings across various dissipation strengths. The speedup factor is most prominent for scenarios with large electron-phonon couplings and low dissipation strength, which corresponds to a large bosonic local Hilbert space dimension, as indicated in the inset. These calculations were conducted using the QJ method for systems comprising 20 sites with a single trajectory. All other parameters are consistent with those described in Fig. 4.8.

In addition to examining the bosonic physical local dimension, we also conducted an analysis of the bond dimension denoted as m_{max}. The outcomes of this analysis are presented in Fig. 4.11, using the same model parameters as those used for the benchmark calculation showcased in Figs. 4.6 and 4.7. Similar to the trends observed in local dimensions, the required bond dimensions decrease as the dissipation strength increases. Remarkably, across all six analyzed (g, κ) settings, we note that QJ consistently exhibits a smaller bond dimension compared to HOPS when aiming to maintain a constant discarded weight. One plausible explanation for this phenomenon may be that significant drops in bond dimension occur whenever a jump event occurs, such as when an annihilator is applied to a phononic site. These jumps result in a substantial portion of the local Hilbert space being projected out. Furthermore, for scenarios characterized by low dissipation strengths and high electron-phonon interactions, we also observed a notable increase in the necessary local dimension for HOPS. This tendency is associated with the PP mapping, where the requisite local dimension is directly linked to the decay of the phonon 1RDM diagonal elements. In this parameter regime, HOPS appears to induce more significant fluctuations in the phonon system, consequently elevating the overall bond dimension. However, we cannot determine whether the observed trend in Fig. 4.11 is a specific characteristic of the analyzed systems or a general feature.

We conclude this benchmark by investigating the speedup achieved by combining QJ and HOPS with the PP mapping (see Section 3.1). In Figure 4.12, a system with 20 lattice sites was studied. The runtime is notably reduced when utilizing the PP mapping across various parameter settings. In particular, we observe a substantial speedup, approximately 30-fold, in scenarios with low dissipation and strong electron-phonon coupling, corresponding to larger local Hilbert space dimensions (> 20). The speedup is less pronounced for medium and strong dissipation, approximately 5-fold.

4.4 Summary

In this section, we used the dissipative Hubbard-Holstein model to benchmark various numerical techniques for simulating the dynamics of dissipative quantum systems. ED calculations revealed QJ to be more accurate than QSD (see Fig. 4.3) and thus the former was selected as the Markovian-embedded method of choice to be compared to HOPS (see Fig. 4.1). For HOPS, rescaling the auxiliary states according to Eq. (2.36) turned out to be crucial to be able to describe highly excited environments (see Fig. 4.9). The numerical complexity of HOPS and QJ is surprisingly similar (Fig. 4.8). However, HOPS works best for weak dissipation while QJ works best for strong dissipation, as shown in Fig. 4.2. Moreover, we showed in Fig. 4.12 that the PP representation is greatly beneficial, especially in the numerically most challenging cases of strong electron-phonon coupling and weak dissipation. In Chapter 6, we will extend this benchmark by comparing Markovian-embedded methods to unitary dynamics for exciton dynamics in structured vibrational environments.

Part II

Applications

In part I, we accounted for some remarkable methodological advances in the fields of OQS and MPS algorithms for dissipative and vibrational environments and discussed their numerical properties. Here, we argue that these combined methods constitute a versatile and efficient toolkit for addressing open problems in quantum thermodynamics, condensed matter physics, quantum chemistry, and even biology.

From a methodological point of view, we can categorize the next chapters depending on whether they feature unitary or dissipative dynamics, a few-body or many-body physical subsystem of interest, a featureless or a structured vibrational environment. By featureless environment, we indicate both dissipative Markovian environments and many-body, non-Markovian vibrational environments characterized by a single vibrational frequency. We summarize these aspects in Fig. 4.13.

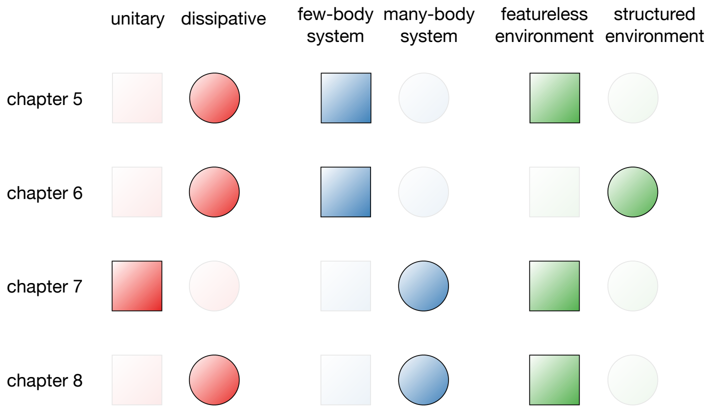

Figure 4.13: Schematic representation of the main characteristics of the systems analyzed in the different chapters of part II.

First, in Chapter 5, we study the quantum version of the Mpemba effect, sometimes stated as “hot water freezes faster than cold water,” from the perspective of non-equilibrium thermodynamics. We investigate the interplay between dissipation and quantum coherence, showing how an exact unitary transformation removing a state’s coherences can exponentially accelerate its thermalization.

In Chapter 6, we demonstrate that dissipation can be leveraged as a valuable resource, as it significantly reduces the numerical complexity of MPS calculations compared to isolated system dynamics. Specifically, studying exciton dynamics in vibrational environments, we show that dissipation presents two key advantages: it decreases the number of vibrational modes needed to fit the environmental spectral density and lowers the occupation of the vibrational modes and the overall entanglement.

Then, in Chapter 7, we study the minimal model for an optically excited metal, considering the unitary dynamics of a non-linearly coupled electron-phonon system. Differently from Chapter 6, at an initial time, an optical pulse excites the phononic degrees of freedom instead of the electronic ones. We use the PST method introduced in Section 3.3 to study the impact of different pulse shapes and the crucial role of the phonon frequency in defining the electrons' dynamics.

Finally, in Chapter 8, we analyze the impact of dissipation on the bipolaronic quasiparticles in a paradigmatic 1D condensed matter model for electron-phonon interactions. We find that dissipation does not affect the stability of the bipolarons but tends to localize them in a process reminiscent of the quantum Zeno effect.

Chapter 5

The thermodynamics of the quantum Mpemba effect

"What is the interplay between quantum coherences and the thermalization speed of an open quantum system?"

This chapter explores a counterintuitive thermalization phenomenon known as the Mpemba effect. It is named after Erasto Mpemba, who, at the age of 13, noticed that a hot ice cream mixture froze faster than a cooler one. In Section 5.1, we summarize the theoretical explanation for the classical Mpemba effect and its experimental realization in colloidal systems. Then, in Section 5.2, we introduce the definition of the genuine quantum Mpemba effect based on non-equilibrium thermodynamics and explore the effect in single- and multi-qubit setups. Finally, in Section 5.3, we present two methods for finding exponential speedups for equilibration processes via stochastic numerical optimization. Overall, we will consider single-and few-qubit systems, performing analytic calculations and employing ED-based numerical methods. The chapter is based on Ref. [2], written in collaboration with Oisín Culhane, Krissia Zawadzki, and John Goold.

5.1 The classical Mpemba effect

The Mpemba effect describes a scenario where a hot system is quenched into a cold bath and achieves equilibrium more rapidly than an initially cooler system. The first systematic inquiries into this phenomenon were conducted by Mpemba, Osborne, and Kell [114, 115] on water cooling in the late sixties. However, the effect had been reported by Aristotle over 2000 years ago [116] and observed by others, such as Descartes [117] and Bacon [118], across history. Since Mpemba and Osborne's original investigation, researchers have explored the effect in a progressively broader spectrum of physical systems such as magnetic alloys [119], carbon nanotube resonators [120], clathrate hydrates [121], granular gases [122], polymers [123], and dilute atomic gases [124], to name a few. However, despite numerous studies, debates persist in the literature regarding the physical explanation and even the phenomenon's existence in water [125, 126].

A pivotal advancement in comprehending this anomalous effect stemmed from the analysis of the stochastic thermodynamics of Markovian systems carried out by Lu and Raz [127, 128], which we will briefly summarize. Consider a classical, discrete system whose state is represented by a probability distribution $|p(t)\rangle$, in contact with a Markovian thermal bath at temperature T_b. The thermalization of $|p(t)\rangle$ is described by a classical Liouvillian operator $\hat{\mathscr{L}}^c$ as

$$\partial_t |p(t)\rangle = \hat{\mathscr{L}}^c |p(t)\rangle \ . \tag{5.1}$$

In general, the classical Liouvillian is a non-Hermitian operator with complex eigenvalues. However, in order to describe a thermalization process, $\hat{\mathscr{L}}^c$ needs to obey thermal detailed balance. If we denote by $\pi(m \to n)$ the transition probability between the $|m\rangle$ and $|n\rangle$ with energy E_m and E_n, respectively, the thermal detailed balance condition reads

$$\frac{\pi(m \to n)}{\pi(n \to m)} = e^{-\beta(E_n - E_m)} \ . \tag{5.2}$$

As we show in Appendix B, enforcing this condition implies that $\hat{\mathscr{L}}^c$ is Hermitian. Thus, the system's initial probability vector can be expanded in the eigenbasis $\{|r_k\rangle\}_k$ of $\hat{\mathscr{L}}^c$:

$$|p(t_0)\rangle = \sum_{k=1}^{D} c_k |r_k\rangle \ , \tag{5.3}$$

where $D = \dim(\hat{\mathscr{L}}^c)$. The (real) spectrum of $\hat{\mathscr{L}}^c$ consists of a single zero eigenvalue $\lambda_1 = 0$ and $D - 1$ negative eigenvalues. The eigenvector $|r_1\rangle$ is the unique steady state which, up to a normalization factor, corresponds to the thermal state of the system at temperature T_b. Let us now reorder the eigenvalues of $\hat{\mathscr{L}}^c$ descendingly according to their absolute value $|\lambda_1| < |\lambda_2| \le |\lambda_3| \cdots \le |\lambda_D|$. With decomposition Eq. (5.3), the time evolution of $|p(t)\rangle$ (i.e. the solution of Eq. (5.1)) can be written as:

$$|p(t)\rangle = |r_1\rangle + \sum_{k=2}^{D} c_k e^{\lambda_k t} |r_k\rangle \ . \tag{5.4}$$

The contribution from each term in the sum will decay exponentially in time with a decay rate given by $|\lambda_k|$.

Eq. (5.4) now allows us to make sense of the Mpemba effect. Assume that the system initially finds itself either in a hot thermal state $|p_{T_h}\rangle$ or a warm thermal state $|p_{T_w}\rangle$ with $T_h > T_w > T_b$. If $|p_{T_h}\rangle$ has a smaller overlap than $|p_{T_w}\rangle$ with the so-called slowest decaying mode $|r_2\rangle$, it will thermalize faster than $|p_{T_w}\rangle$, despite its initial temperature being higher. Moreover, if the overlap of $|p_{T_h}\rangle$ with $|r_2\rangle$ happens to vanish, it will thermalize exponentially faster than $|p_{T_w}\rangle$, namely with rate $|\lambda_3|$ insted of $|\lambda_2|$. The latter case is referred to as the *strong* Mpemba effect.

This theoretical framework inspired recent experimental investigations of the Mpemba effect under controlled conditions. In Ref. [28], Kumar and Bechhoefer studied the thermalization of a colloidal particle diffusing in water (which acts as a cold bath at temperature T_b) under the effect of a potential landscape enforced by optical tweezers. The system's state at time t is described by the probability distribution $p(x,t)$, parametrized by the particle's position x. A particle is drawn from a Boltzmann distribution $\tau(x;T)$ corresponding either to a hot temperature T_h or to a warm temperature T_w, and each experiment is repeated 1000 times. For specific shapes of the potential landscape, on average, particles drawn from an ensemble at T_h thermalized faster than those drawn at T_w, indicating the occurrence of the Mpemba effect (see Fig. 5.1). Since temperature can be defined only in equilibrium, the L_1-distance $|p(x,t) - \tau(x;T_b)|$ was chosen as an instantaneous distance measure from the thermal state at temperature T_b. The inverse effect, namely a cold state heating up faster than a warmer one, has also been demonstrated experimentally in a similar colloidal setup [129].

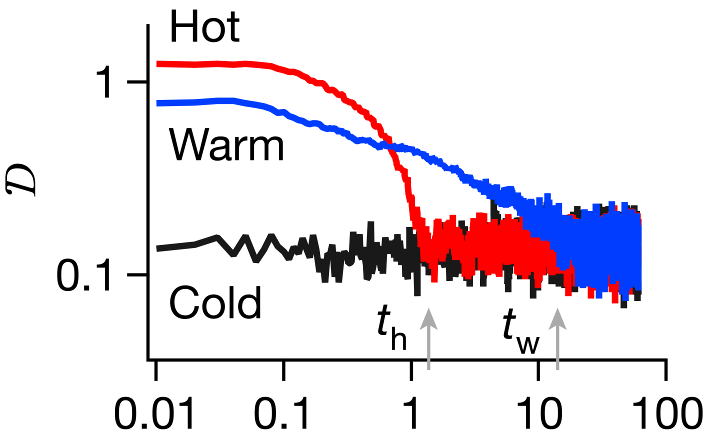

Figure 5.1: Experimental demonstration of the classical Mpemba effect. A single colloidal particle is repeatedly drawn from a thermal ensemble and immersed in water subject to a potential enforced by optical tweezers. For specific shapes of the potential, hot ensembles cool down faster than warm ones, experimentally demonstrating the Mpemba effect. The distance D from the thermal state at bath (water) temperature is measured in terms of the L_1-distance. Adapted from [28].

5.2 The quantum Mpemba effect

In recent years, significant efforts have been directed to investigate the Mpemba effect in quantum systems. The framework introduced in the breakthrough paper [127] was generalized to Lindbladians in Ref. [29], stimulating a variety of theoretical [130–139] and recent experimental [140, 141] studies in open quantum systems. Moreover, a Mpemba-like phenomenon related to symmetry restoration in quenched dynamics starting from states that break the symmetry of the Hamiltonian has been proposed for isolated quantum systems [142–145]. These predictions were experimentally confirmed recently in a trapped-ion quantum simulator [146].

For Markovian open quantum systems, the dynamics are generated by the Lindbladian superoperator $\mathscr{L}$, consisting of a unitary part and a dissipative part such that $\mathscr{L} = i\mathscr{I} + \mathscr{D}$ with $\mathscr{I}(\cdot) = -[\hat{H}_S, \cdot]$, $\hat{H}_S$ being the system Hamiltonian and $\mathscr{D}(\cdot) = \sum_l \hat{L}_l(\cdot)\hat{L}_l^\dagger - \frac{1}{2}\{\hat{L}_l^\dagger \hat{L}_l, (\cdot)\}$, where $\hat{L}_l$ is a jump operator. In analogy to Eq. (5.4), the time evolution of a density matrix $\hat{\rho}$ can be written as

$$\hat{\rho}(t) = e^{\mathscr{L}t}\hat{\rho}_i = \hat{\tau} + \sum_{k=2}^{D^2} \mathrm{Tr}\Big(\hat{l}_k\hat{\rho}_i\Big)\hat{r}_k e^{\lambda_k t} \,, \tag{5.5}$$

where $D = \dim(\hat{H}_S)$. Here, we assume that $\hat{\tau}$ represents the unique steady state, which is directly proportional to the right eigenoperator of the generator $\mathscr{L}$ corresponding to the zero eigenvalue. Moreover, $\hat{l}_k$ and $\hat{r}_k$ are the left and right eigenoperators corresponding to the eigenvalue λ_k such that $\mathscr{L}[\hat{r}_k] = \lambda_k\hat{r}_k$ and $\mathscr{L}^\dagger[\hat{l}_k] = \lambda_k\hat{l}_k$, where $\mathscr{L}^\dagger$ represents the adjoint generator that acts on observables rather than states. The superoperator $\mathscr{L}$ preserves the hermiticity of $\hat{\rho}(t)$, indicating that if λ_k is a complex eigenvalue, then λ_k^* is as well. We arrange the eigenvalues in ascending order based on the modulus of their real part, such that $0 = \lambda_1 < |\Re(\lambda_2)| \leq |\Re(\lambda_3)| \leq \dots$. The spectral gap $|\Re(\lambda_2)|$, represents the longest timescale in the system, implying $|\hat{\rho}(t) - \hat{\tau}| \propto \exp(\Re(\lambda_2)t)$.

In Ref. [29], Carollo, Lasanta and Lesanovsky demonstrated that an exponential acceleration towards the steady state can be obtained via a unitary transformation that removes the overlap of an initial pure state $|\psi_i\rangle$ with the slowest-decaying mode $\hat{l}_2$

$$\mathrm{Tr}\Big(\hat{l}_2\hat{U}\,|\psi_i\rangle\,\langle\psi_i|\,\hat{U}^\dagger\Big) = 0 \,, \tag{5.6}$$

resulting in $|\hat{\rho}(t) - \hat{\tau}| \propto \exp(\Re(\lambda_3)t)$. Apart from being restricted to a pure state, the pivotal assumption outlined in [29] is that the Lindbladian spectral gap needs to be defined by a real eigenvalue. The fact that these conditions exclude thermal states and Lidbladians with a complex λ_2 explains in part why the efforts in open quantum systems [130–141] predominantly considered exponential speedups in generalized equilibration processes instead of thermalization. A thermodynamic understanding of a *genuine* quantum Mpemba effect was still missing.

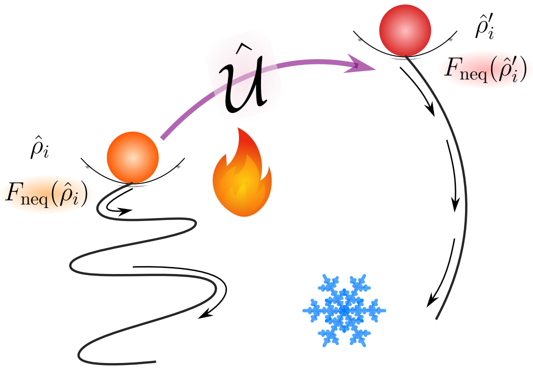

Figure 5.2: For a general quantum state, it is possible to devise a unitary transformation $\hat{U}$ that increases the state's non-equilibrium free energy and eliminates the overlap with a set of slow-decaying modes of the Liouvillian. This leads to exponentially faster thermalization and a genuine quantum Mpemba effect.

Here, we address this issue by investigating the quantum thermalization dynamics induced by a Davies map from the perspective of non-equilibrium thermodynamics. A Davies map is a particular Lindbladian that we denote as $\mathscr{G}$, which describes the thermalization of a quantum system when weakly coupled to a heat bath [147, 148] at inverse temperature β. It is characterized by two main properties: Firstly, the unitary component $\mathscr{I}$ and the dissipative component $\mathscr{D}$ of the generator commute, and secondly, it adheres to quantum detailed balance [149] in relation to the thermal state $\hat{\tau}_\beta = e^{-\beta \hat{H}_S}/Z$, where $Z = \operatorname{Tr}\left(\exp\left(-\hat{H}_S\beta\right)\right)$. Mathematically, quantum detailed balance implies that the unitary and dissipative components of the generator satisfy

$$\begin{aligned} &\langle \hat{A}, \mathscr{D}^\dagger(\hat{B})\rangle_{\hat{\tau}_\beta} = \langle \mathscr{D}^\dagger(\hat{A}), \hat{B}\rangle_{\hat{\tau}_\beta} \\ &\text{and} \quad [\hat{H}_S, \hat{\tau}_\beta] = 0, \end{aligned} \tag{5.7}$$

where $\hat{A}$ and $\hat{B}$ are two arbitrary operators and $\langle \hat{A}, \hat{B}\rangle_{\hat{\tau}_\beta} = \operatorname{Tr}\left(\hat{\tau}_\beta \hat{A}^\dagger \hat{B}\right)$. The eigenmatrices of the unitary part $\mathscr{I}$ are given by the transitions $|n\rangle\langle m|$ between Hamiltonian eigenstates $|m\rangle$ and $|n\rangle$ corresponding to the eigenvalues $\omega_{nm} = E_n - E_m$. Moreover, the dissipative part $\mathscr{D}$ commutes with $\mathscr{I}$, thus sharing a common eigenspace with it. Additionally, if the Hamiltonian is non-degenerate, the Davies map $e^{\mathscr{G}t}$ is block diagonal in the energy eigenbasis. We express $\mathscr{G}$ as $\mathscr{G}_P \oplus \mathscr{G}_C$, where $\mathscr{G}_P = \mathscr{D}_P$ represents the population subblock. Its right eigenmatrices are diagonal in the energy eigenbasis $|n\rangle\langle n|$. $\mathscr{G}_C = i\mathscr{I} + \mathscr{D}_C$ denotes the coherence subblock. Owing to the detailed balance condition, the eigenvalues linked with the off-diagonal eigenmatrices of $\mathscr{D}_C$ are real, while imaginary eigenvalues stem from the unitary part $\mathscr{I}$. All right eigenmatrices except the steady state, i.e., all $\hat{r}_i$ for $i \geq 2$, are off-diagonal matrices in the energy eigenbasis. This ensures that they are traceless, guaranteeing that the dynamics always preserve normalization. However, not only does $\mathscr{I}$ commute with $\mathscr{D}$, but it also commutes with $\mathscr{D}^\dagger$. This implies that the left eigenvectors of $\mathscr{G}_C$ are also purely off-diagonal matrices, as $\mathscr{G}^\dagger[\hat{l}_k] = \lambda_k \hat{l}_k$.

Here we present our first finding: For an initial state $\hat{\rho}_i$ with coherences in the energy eigenbasis, under evolution with a Davies generator featuring a spectral gap defined by the real part of a complex eigenpair, exponential acceleration towards the fixed point is attainable by performing a unitary transformation $\hat{U}_1$ which diagonalizes the state in the energy eigenbasis. As every $\hat{l}_m$ with $\lambda_m \in \mathbb{C}$ is purely off-diagonal in the energy eigenbasis, all corresponding overlaps will be removed $\mathrm{Tr}\left(\hat{l}_m \hat{U}_1 \hat{\rho}_i \hat{U}_1^\dagger\right) = 0$. We want to emphasize that an exponential speedup alone does not qualify as a *genuine* Mpemba effect. In the seminal paper [127], that is centered around thermodynamics, the phenomenon is characterized by states possessing three temperatures $T_b < T_c < T_h$, representing the fixed point, a colder, and a hotter initial state, respectively. A Mpemba effect manifests if there exists a time t_m after which $D[\hat{\rho}^h(t), T_b] < D[\hat{\rho}^c(t), T_b]$. In this context, $D[\hat{\rho}(t), T]$ is a measure of the distance between the evolving state and the fixed point. Given that we are considering non-equilibrium quantum states possibly with coherences in the energy eigenbasis, we lack an initial notion of temperature. There is a single point of equilibrium, i.e. the fixed point $\hat{\tau}_\beta$. In quantum dynamics, we suggest employing instead the non-equilibrium free energy

$$F_{\mathrm{neq}}(\hat{\rho}(t)) = \mathrm{Tr}\left(\hat{H}_S \hat{\rho}(t)\right) + \frac{1}{\beta}\,\mathrm{Tr}(\hat{\rho}(t) \ln \hat{\rho}(t)) \,, \tag{5.8}$$

which is well defined for any state $\hat{\rho}(t)$. We examine the initial scenario $F_{\mathrm{neq}}(\hat{\rho}'(t_0)) > F_{\mathrm{neq}}(\hat{\rho}(t_0)) > F_{\mathrm{eq}}$, where $\hat{\rho}'(t_0) = \hat{U}\hat{\rho}(t_0)\hat{U}^\dagger$ represents the state after a unitary transformation, and $F_{\mathrm{eq}} = -\beta^{-1} \ln Z$ denotes the equilibrium free energy of the fixed point. A quantum Mpemba effect arises if there exists a time t_m such that $F_{\mathrm{neq}}(\hat{\rho}'(t)) < F_{\mathrm{neq}}(\hat{\rho}(t))$ holds for all times $t > t_m$. We refer to this phenomenon as a *genuine* quantum Mpemba effect, distinguishing it from exponential speedups achieved by other transformations. It is important to emphasize that for the speedup to qualify as a quantum Mpemba effect, the non-equilibrium free energy curves must intersect over time. The non-equilibrium free energy exhibits several properties that make it well-suited for defining and analyzing the quantum Mpemba effect. First, it can be expressed in terms of the quantum relative entropy [150–152]

$$D(\hat{\rho}\|\hat{\sigma}) = \mathrm{Tr}[\hat{\rho}(\ln \hat{\rho} - \ln \hat{\sigma})] \,, \tag{5.9}$$

by writing the internal energy E as

$$\begin{aligned}
E(\hat\rho(t)) &= \mathrm{Tr}\Big(\hat H_S \hat\rho(t)\Big) = -\beta^{-1}\,\mathrm{Tr}\Big[\hat\rho(t)\ln e^{-\beta \hat H_S}\Big] \\
&= -\beta^{-1}\,\mathrm{Tr}\left[\hat\rho(t)\ln \frac{e^{-\beta \hat H_S}}{Z}\right] \underbrace{-\,\beta^{-1}\,\mathrm{Tr}(\hat\rho(t)\ln Z)}_{F_{\mathrm{eq}}(\hat\tau_\beta)} \\
&= -\beta^{-1}\,\mathrm{Tr}\Big[\hat\rho(t)\ln \hat\tau_\beta\Big] - \beta^{-1} S(\hat\rho(t)) + \beta^{-1} S(\hat\rho(t)) + F_{\mathrm{eq}}(\hat\tau_\beta) \\
&= \beta^{-1} D(\hat\rho(t)\|\hat\tau_\beta) + \beta^{-1} S(\hat\rho(t)) + F_{\mathrm{eq}}(\hat\tau_\beta)\,.
\end{aligned} \tag{5.10}$$

Plugging this expression into Eq. (5.8) yields

$$F_{\mathrm{neq}}(\hat\rho(t)) = \beta^{-1} D(\hat\rho(t)\|\hat\tau_\beta) + F_{\mathrm{eq}}(\hat\tau_\beta)\,, \tag{5.11}$$

which reduces to the equilibrium free energy $F_{\mathrm{eq}}(\hat\tau_\beta)$ when $\hat\rho(t) = \hat\tau_\beta$. The Klein inequality ensures the positivity of the relative entropy, thereby guaranteeing that $F_{\mathrm{neq}}(\hat\rho(t)) \geq F_{\mathrm{eq}}(\hat\tau_\beta)$ for all t. The quantum relative entropy serves as a stringent measure of the distinguishability between two quantum states. Although it is not a metric, it provides an upper bound on the trace distance through Pinsker's inequality: $D(\hat\rho\|\hat\sigma) \geq \|\hat\rho - \hat\sigma\|_1^2/2$, encapsulating the optimal distinguishability of quantum states with a single measurement. Moreover, the non-equilibrium free energy is directly linked to the Spohn entropy production rate [11, 153, 154] through

$$\Pi = -\beta^{-1}\frac{d}{dt} F_{\mathrm{neq}}(\hat\rho(t))\,. \tag{5.12}$$

Finally, the total irreversible entropy produced can be partitioned into

$$D(\hat\rho(t)\|\hat\tau_\beta) = \mathscr{P}(p(t)\|\hat\tau_\beta) + \mathscr{C}(\hat\rho(t))\,, \tag{5.13}$$

where $\mathscr{P}(p(t)\|t_\beta) = \sum_n p_n(t)\ln\frac{p_n(t)}{t_n^\beta}$ represents the classical relative entropy between the time-dependent population vector and the thermal state. $\mathscr{C}(\hat\rho(t)) = S(\Delta(\hat\rho(t))) - S(\hat\rho(t))$ denotes the relative entropy of coherence, where $\Delta(\hat\rho_s(t))$ represents the state dephased in the system's energy eigenbasis. This is a well-known measure of quantum coherence [155]. The decomposition of the entropy production into a classical and a quantum component has been recently realized experimentally in an optical setup for a single photon [156].

We have discussed above that if the spectral gap is defined by a complex eigenpair, a transformation which exponentially accelerates the thermalization of a state with coherences is a simple unitary $\hat U_1$ which diagonalizes the state in the energy eigenbasis, i.e., $\hat\rho_i \rightarrow \hat\Lambda = \hat U_1 \hat\rho_i \hat U_1^\dagger$ [1]. Now, we want to find a second unitary

---

[1] from here on we are renaming the initial state $\hat\rho(t_0) \equiv \hat\rho_i$ for convenience.

$\hat{U}_2$ that transforms the diagonalized state into a state that has a higher F_{neq} than the initial one. Let us define the combined rotations

$$\hat{U} = \hat{U}_2\hat{U}_1 \, , \tag{5.14}$$

and the transformed state $\hat{\rho}' = \hat{U}\hat{\rho}_i\hat{U}^\dagger$. We consider $\hat{U}_2$ to be the transformation that performs a full population inversion, i.e. it swaps the elements of $\hat{\Lambda}$ arranging them in ascending order, and want to show that $F_{\text{neq}}(\hat{\rho}') \geq F_{\text{neq}}(\hat{\rho}_i)$. Eq. (5.11) tells us that to prove this, we need to show that the rotation increases the relative entropy with respect to the steady state

$$D(\hat{\rho}'||\hat{\tau}_\beta) \geq D(\hat{\rho}_i||\hat{\tau}_\beta) \, . \tag{5.15}$$

Since unitary operations don't change the von Neumann entropy, using the definition Eq. (5.9) this condition reduces to

$$\mathrm{Tr}[\hat{\rho}'\ln(\hat{\tau}_\beta)] \leq \mathrm{Tr}[\hat{\rho}_i\ln(\hat{\tau}_\beta)] \, . \tag{5.16}$$

As the thermal state $\hat{\tau}_\beta$ is diagonal in the energy eigenbasis, only the diagonal part of $\hat{\rho}_i$ gives nonzero contributions in Eq. (5.16), which means that we can simply compare the populations before and after the rotation. Since the entries of the thermal equilibrium state are non-increasing, given $\hat{\Lambda}$, performing a population inversion indeed minimizes the l.h.s. of Eq. (5.16). This, however, still does not prove that Eq. (5.16) holds. For this, we need to compare the population r of $\hat{\rho}_i$ to the population p of $\hat{\rho}'$ using the concept of majorization. Denoting with $p^\downarrow$ the permutation of p so that its elements are non-increasing, we say that $p^\downarrow$ majorizes $r^\downarrow$ if it satisfies

$$\sum_{j=1}^{k} p_j \geq \sum_{j=1}^{k} r_j, \ \forall k \, , \tag{5.17}$$

and indicate this as $p \succ r$. If p majorizes r it means that it is less spread out. Thus, after a population inversion, more weight multiplies the small, high entries of $\hat{\tau}_\beta$ for $\hat{\rho}'$ than for $\hat{\rho}_i$, satisfying Eq. (5.16). Our remaining task is then to prove that $p \succ r$ when r is connected to p via a unitary transformation. We can express the m-th element of r as:

$$r_m = \langle m| \hat{U}^\dagger \hat{\rho}' \hat{U} |m\rangle \tag{5.18}$$

in the energy eigenbasis $|m\rangle$. Moreover, using the fact that $\hat{\rho}'$ is diagonal in the energy eigenbasis we can write

$$r_m = \sum_n \langle m| \hat{U}^\dagger p_n |n\rangle \langle n| \hat{U} |m\rangle = \sum_n |\langle n| \hat{U} |m\rangle|^2 p_n \equiv \sum_n S_{nm} p_n \, . \tag{5.19}$$

The matrix $\hat{S}$ mapping p to r has only non-negative entries, and its rows and columns sum to 1 and is called *doubly stochastic.* The Hardy-Littlewood-Polya inequality [157] tells us that $\hat{S}$ exists if and only if p majorizes r, which concludes the proof.

In summary, if λ_2 is complex, instances of a genuine quantum Mpemba effect for a Markovian thermalization process can be found for any random state $\hat{\rho}_i$. This is achieved by applying the transformation $\hat{U} = \hat{U}_2\hat{U}_1$, where $\hat{U}_1$ removes the coherences in the energy eigenbasis yielding an exponential speedup and $\hat{U}_2$ performs a population inversion increasing the non-equilibrium free energy.

5.2.1 Vectorization and explicit expression of the Davies map

Davies maps are widely used in literature [147, 148, 158, 159]. However, for completeness, here we discuss the jump operators that define them, their explicit form and their structure. The fixed point of Davies maps is the thermal state at inverse temperature β

$$\hat{\tau}_\beta = \frac{e^{-\beta \hat{H}_S}}{\mathrm{Tr}\left(e^{-\beta \hat{H}_S}\right)} . \tag{5.20}$$

Working in the Hamiltonian eigenbasis $\{|n\rangle\}$, we want to show that Davies maps are characterized by the following jump operators

$$\begin{aligned}
\hat{L}^{(1)}_{nm}(\beta) &= \gamma^{1/2} \underbrace{\left(1 \mp f^{\pm}(\beta, h_m - h_n)\right)^{1/2}}_{\alpha^{(1)}_{nm}} |n\rangle\langle m| \\
\hat{L}^{(2)}_{nm}(\beta) &= \gamma^{1/2} \underbrace{\left(f^{\pm}(\beta, h_m - h_n)\right)^{1/2}}_{\alpha^{(2)}_{nm}} |m\rangle\langle n| , \qquad \text{with } m < n ,
\end{aligned} \tag{5.21}$$

where h_n represents the eigenvalues of the Hamiltonian, $f^{\pm}(\beta, h_n) = 1/(\exp(\beta h_n) \pm 1)$ denote the Fermi and the Bose distribution functions and γ is the system-bath coupling strenght. To accomplish this, we need to demonstrate that $\mathcal{G}\left[\hat{\tau}_\beta\right] = 0$, where $\mathcal{G}$ represents the Davies generator obtained by plugging the jump operators Eq. (5.21) into the Lindblad equation Eq. (2.6). Given that $\hat{\tau}_\beta$ commutes with $\hat{H}_S$, we only need to consider the dissipator $\mathcal{D}(\cdot) = \sum_l \hat{L}_l(\cdot)\hat{L}_l^\dagger - \frac{1}{2}\{\hat{L}_l^\dagger \hat{L}_l, (\cdot)\}$. We must demonstrate that $\mathcal{D}(\hat{\tau}_\beta) = \sum_{m<n} \mathcal{D}^{(1)}_{nm}(\hat{\tau}_\beta) + \mathcal{D}^{(2)}_{nm}(\hat{\tau}_\beta) = 0$. Indeed, for every (n, m) pair, the dissipators $\mathcal{D}^{(1)}_{nm}$ and $\mathcal{D}^{(2)}_{nm}$ relative to the jump

operators $\hat{L}^{(1)}_{nm}$ and $\hat{L}^{(2)}_{nm}$ cancel each other out:

$$\begin{aligned}
&\mathscr{D}^{(1)}_{nm}(\hat{\tau}_\beta) + \mathscr{D}^{(2)}_{nm}(\hat{\tau}_\beta) = \\
&\frac{1 \mp f^{\pm}(h_m - h_n)}{\mathcal{N}} e^{-\beta h_m} \left(|n\rangle \langle n| - |m\rangle \langle m| \right) \\
&+ \frac{f^{\pm}(h_m - h_n)}{\mathcal{N}} e^{-\beta h_n} \left(|m\rangle \langle m| - |n\rangle \langle n| \right) = 0 \ ,
\end{aligned}$$

where we used $(1 \mp f^{\pm}(h_m - h_n))e^{-\beta(h_m - h_n)} = f^{\pm}(h_m - h_n)$, which corresponds to the thermal detailed balance condition Eq. (5.2). Hence, the Lindbladian defined by the jump operators Eq. (5.21) possesses the thermal state as its fixed point.

The Davies map can be recast into an operator via the vectorization method introduced in Section 2.2. In this case, it is helpful to use a modified vectorization procedure, sometimes denoted vecdiag() (and implemented, for instance, in the Mathematica package MELT), in which one stacks first the diagonal and then the off-diagonal elements

$$\mathrm{vecdiag}\begin{pmatrix} a & b & c \\ d & e & f \\ g & h & i \end{pmatrix} \rightarrow \begin{pmatrix} a \\ e \\ i \\ d \\ g \\ b \\ h \\ c \\ f \end{pmatrix} . \tag{5.22}$$

In this way, if the Hamiltonian is non-degenerate, $\hat{\mathscr{G}}$ has the block-diagonal form $\hat{\mathscr{G}} = \hat{\mathscr{G}}_p \oplus \hat{\mathscr{G}}_c$, with $\hat{\mathscr{G}}_p$ describing the system's populations and $\hat{\mathscr{G}}_c$ the system's coherences (see Fig. 5.3). Moreover, as explained in the previous section, the left eigenmatrices $\{\hat{l}_k\}$ associated with the system's populations are diagonal and correspond to real eigenvalues $\{\lambda_k\}$. In contrast, those associated with the system's coherences are strictly off-diagonal, and the relative eigenvalues come in complex conjugate pairs.

Rather than inserting the jump operators Eq. (5.21) directly into the general expression for the vectorized Lindbladian Eq. (2.12), an alternative approach involves constructing the two blocks of the Davies map individually. This method can save considerable computational resources. To facilitate this approach, we define the matrix $\hat{J}$ to collect all the jump operators. For concreteness, in the case

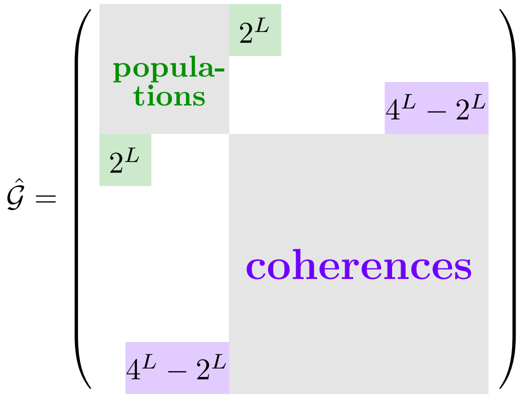

Figure 5.3: Block structure of the vectorized Davies generator $\hat{\mathscr{G}}$, which is specified by the jump operators Eq. (5.21). L indicates the number of fermions, hard-core bosons, or spin-1/2 particles in the system.

of two qubits, it reads

$$\hat{J} = \begin{pmatrix} 0 & \alpha_{01}^{(2)} & \alpha_{02}^{(2)} & \alpha_{03}^{(2)} \\ \alpha_{10}^{(1)} & 0 & \alpha_{12}^{(2)} & \alpha_{13}^{(2)} \\ \alpha_{20}^{(1)} & \alpha_{21}^{(1)} & 0 & \alpha_{23}^{(2)} \\ \alpha_{30}^{(1)} & \alpha_{31}^{(1)} & \alpha_{32}^{(1)} & 0 \end{pmatrix} . \tag{5.23}$$

The coefficients $\alpha_{nm}^{(1)}$ and $\alpha_{nm}^{(2)}$ are defined in Eq. (5.21). It can be demonstrated that the populations block $\hat{\mathscr{G}}_p$ is given by

$$\hat{\mathscr{G}}_p = \hat{J}_2 + \hat{J}_s \,, \tag{5.24}$$

where $\hat{J}_2$ is obtained by squaring $\hat{J}$ elementwise, and $\hat{J}_s$ represents a diagonal matrix with $\hat{J}_s[k,k] = -\sum_{i=0}^{2^L-1} \left(\hat{J}[i,k]\right)^2$.

To construct the coherences block $\hat{\mathscr{G}}_c$, which is diagonal in the energy eigenbasis, one must select all possible pairs of columns $\hat{J}[:,n]$ and $\hat{J}[:,m]$ with $n = 0, 1, \ldots 2^L$ and $m > n$. Every pair of columns (n,m) corresponds to two elements $\hat{\mathscr{G}}_c[k,k]$ and $\hat{\mathscr{G}}_c[l,l]$, which are complex conjugates of each other. The indices of these two elements are $k = m \cdot 2^L - m + n - 1$ and $l = n \cdot 2^L + m - n$. Their real part is

$$\begin{aligned} &\Re(\hat{\mathscr{G}}_c[k,k]) = \Re(\hat{\mathscr{G}}_c[l,l]) = \\ &- \sum_{i=0}^{2^L-1} \left(\frac{(\hat{J}[i,n])^2}{2} + \frac{(\hat{J}[i,m])^2}{2} \right) \,, \end{aligned} \tag{5.25}$$

and their imaginary part reads

$$\Im(\hat{\mathscr{G}}_c[k,k]) = \Im(\hat{\mathscr{G}}_c^*[l,l]) = i(h_n - h_m) \,. \tag{5.26}$$

Equipped with an explicit description of Davies maps and the speedup transformation $\hat{U}$ (see Eq. (5.14)), in the upcoming sections we will explore the thermalization of single-and multi-qubit systems.

5.2.2 Example 1: Single Qubit

Let us consider a qubit prepared in a random state $\hat{\rho}_i = \frac{1}{2}(\mathbb{1} + \mathbf{r} \cdot \hat{\boldsymbol{\sigma}})$, where $\mathbf{r}$ represents the Bloch vector and $\hat{\boldsymbol{\sigma}}$ is the vector comprising the three Pauli matrices. The characteristic energy scale is denoted as J, and we will adopt $k_B = 1$ and the dissipation strength $\gamma = 1$. The thermalization is characterized by a unitary component, governed by the Hamiltonian $\hat{H}_S = \omega/2\,\hat{\sigma}_z$, and a dissipative component $\mathscr{D}$, which is defined according to the Davies map for a bosonic particle and a bath at temperature T_b. We apply the unitary transformation $\hat{U}$ defined in Eq. (5.14) to $\hat{\rho}_i$, rotating the Bloch vector to $\mathbf{r}_i'$ and obtaining a new state $\hat{\rho}_i'$ diagonal in the energy eigenbasis, with eigenvalues arranged in ascending order.

The dynamics of both states are depicted on the Bloch sphere in Fig. 5.4(a). The color bar illustrates the non-equilibrium free energy F_{neq}, as also depicted in panel (b). We emphasize that the intersection of the two lines demonstrates the occurrence of a genuine quantum Mpemba effect. The inset displays the L_1-distance from the steady state

$$D_{L_1}[\hat{\rho}(t), T_b] = \sum_{i,j} \left| \hat{\rho}^{ij}(t) - \hat{\tau}_\beta^{ij} \right| . \tag{5.27}$$

This measure, extensively studied in many experimental investigations of both the classical [28, 129] and quantum [140, 141] Mpemba effects, demonstrates that the thermalization for the transformed state $\hat{\rho}_i'$ is exponentially accelerated. In Fig. 5.4(c), we examine the partition of the entropy production defined by Eq. (5.13). For the transformed state $\hat{\rho}_i'$, it is evident that the coherent contribution (which slows down the thermalization of $\hat{\rho}_i'$) is zero, as the overlap with the coherent modes has been eliminated. The inset displays the spectrum of the Davies map. Note that for a single qubit, the spectral gap is *always* defined by a complex eigenpair, while for multiple-qubit setups, whether λ_2 is real or complex depends on the system's details and the bath's temperature.

5.2.3 Example 2: Many Qubits

We now focus our attention on a more complex system and consider a transverse-field Ising model (TFIM) with open boundary conditions

$$\hat{H}_S = -J \sum_{j=1}^{L-1} \hat{\sigma}_j^z \hat{\sigma}_{j+1}^z + h \sum_{j=1}^{L} \hat{\sigma}_j^x . \tag{5.28}$$

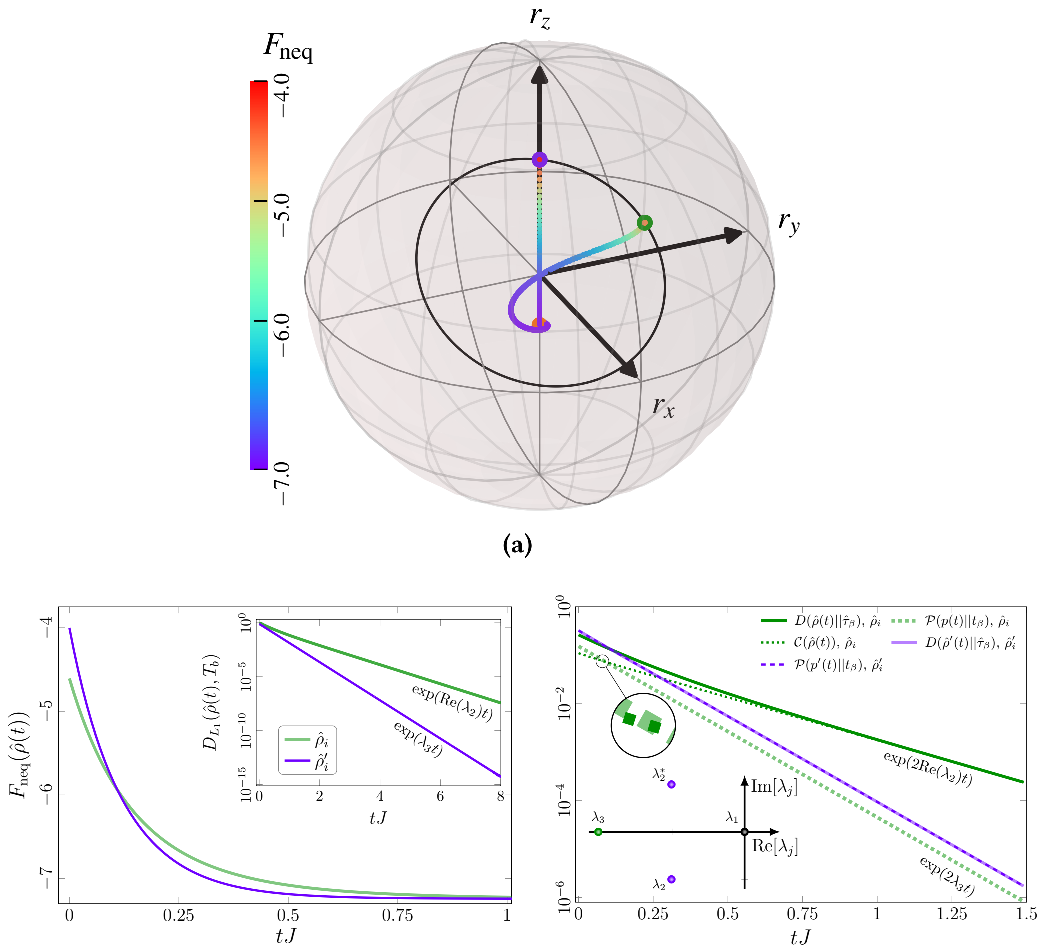

(a)

(b) **(c)**

Figure 5.4: The quantum Mpemba effect in a single-qubit system. a) The equilibration process of a random state $\hat{\rho}_i$ (green dot) and the transformed state $\hat{\rho}'_i = \hat{U}\hat{\rho}_i\hat{U}^\dagger$ (purple dot) towards the thermal steady state (orange dot) is illustrated on the Bloch sphere. The color scheme represents the non-equilibrium free energy $F_{\rm neq}$ for the two thermalization processes. b) Initially, the non-equilibrium free energy $F_{\rm neq}$ is higher for the optimized state (purple line), but it decreases below the random state's $F_{\rm neq}$ (green line) at a later time. This crossing shows the occurrence of a genuine quantum Mpemba effect. *Inset*: The L_1-distances from the steady state illustrate that $\hat{\rho}_i$ undergoes thermalization exponentially faster than $\hat{\rho}'_i$. c) The dynamics of the total entropy production D and its classical $\mathscr{P}$ and coherent $\mathscr{C}$ contributions are displayed. The rotation $\hat{U}$ leads to an exponential speedup. *Inset*: Spectrum of the Davies generator $\mathscr{G}$ for a single qubit. Here $\omega = 5J$, $\mathrm{r}_i = (0.276, 0.359, 0.303)$, $\mathrm{r}'_i = (0., 0., 0.545)$, and $T_b = 10J$.

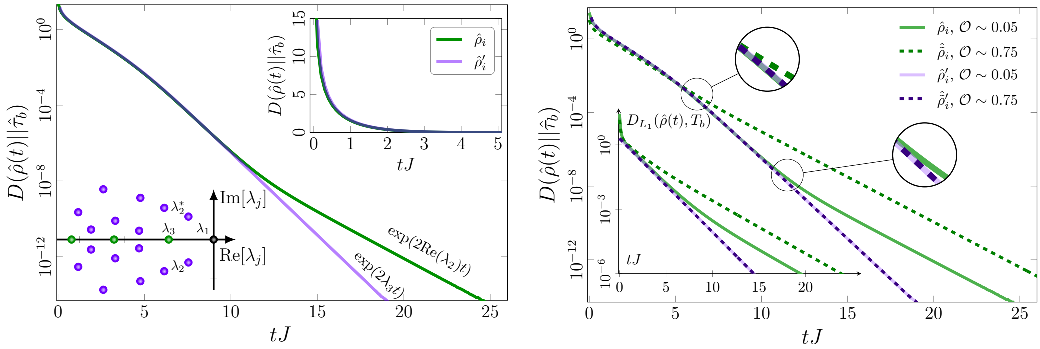

(a) **(b)**

Figure 5.5: The quantum Mpemba effect in a many-qubit system manifests at different timescales. We consider the transverse field Ising model at $h = J/2$, comprising $L = 5$ spins, and a bath temperature $T_b = 0.1\,J$ and study the total entropy production D. (a) The rotation $\hat{U}$ promotes an exponential speedup governed by λ_3, appearing at significantly larger timescales compared to the single-qubit case. The upper inset shows D in a linear scale up to a time $t/J = 5$, while in the lower inset the first 20 eigenvalues of the Davies generator $\mathscr{G}$ are displayed. (b) An initial state exhibiting a substantial overlap with the two slowest decaying modes $\mathcal{O} = \left|\text{Tr}\left(\hat{l}_2^{\dagger}\hat{\rho}_i\right)\right| + \left|\text{Tr}\left(\hat{l}_2\hat{\rho}_i\right)\right|$ attains the speedup earlier than a state with a smaller overlap. For $\mathcal{O} \sim 0.05$ (full green line), the curves for the total entropy production depart around $t/J \sim 10$, whereas with $\mathcal{O} \sim 0.75$ (dashed green line), they do so at half this time.

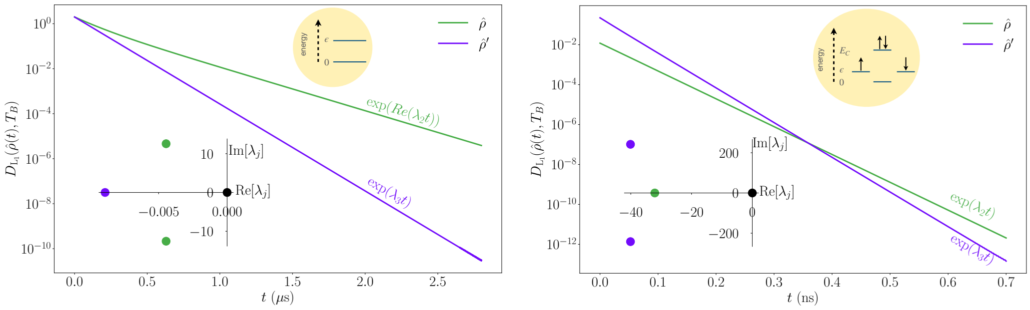

(a) **(b)**

Figure 5.6: The thermalization of a two-level atom in a photonic environment [160] and of a spinful fermionic quantum dot [161] can be accelerated exponentially by exploiting the properties of the Davies map. (a) We initialize the two-level atom in the state $\hat{\rho}(t = 0) = |+\rangle\langle+|$ with $|+\rangle = 1/\sqrt{2}(|0\rangle + |1\rangle)$. *Inset*: the eigenvalues of the Davies generator. The eigenvalue λ_2 is complex. Thus we can obtain the state $\hat{\rho}'(t = 0)$ having zero overlap with the slowest-decaying mode $\hat{l}_2$ via the exact transformation $\hat{U}$ described in Section 5.2. (b) The spinful fermionic quantum dot is initialized in the thermal state at $T_i = 0.1$K. *Inset*: the four eigenvalues of the Davies generator with the smallest module of the real part. Since for this system the eigenvalue λ_2 of the vectorized Davies map is real, a transformed state $\hat{\rho}'(t = 0)$ with overlap $\mathcal{O} = \left|\mathrm{Tr}\left(\hat{l}_2\hat{\rho}'\right)\right| + \left|\mathrm{Tr}\left(\hat{l}_2^{\dagger}\hat{\rho}'\right)\right| < 2 \cdot 10^{-5}$ is obtained using the Metropolis-based algorithm that will be introduced in Section 5.3. In both panels, we show the systems' energy levels in the yellow circles.

We build a random mixed state $\hat{\rho}_i$ by averaging over 1000 random pure states and obtain the transformed state $\hat{\rho}_i'$ by applying $\hat{U}$ (see Eq. (5.14)), as done for the single qubit case. In panel (a) of Fig. 5.5, we compute the irreversible entropy production. The primary distinction from the single qubit scenario is that due to the small overlap of the random state $\hat{\rho}_i$ with the slowest mode $\hat{l}_2$, the difference with the transformed state becomes apparent only at a later time. The scenario shifts when considering an initial state $\hat{\tilde{\rho}}_i$ with greater overlap with $\hat{l}_2$. We obtain such a state by employing a Metropolis-based transformation, that will be introduced in Section 5.3. The dashed green line in panel (b) indicates that, akin to the single qubit case, the exponential difference in the thermalization speed between $\hat{\tilde{\rho}}_i$ and $\hat{\tilde{\rho}}_i'$ becomes apparent even at short times.

5.2.4 Example 3: Physical realization of Davies maps

To derive a unitary transformation revealing the Mpemba effect in quantum thermalization processes, we solely made use of the abstract mathematical properties of the Davies map. Moreover, in the previous two examples, we considered toy models and arbitrary parameters. Here, we consider two realistic physical scenarios described by a Davies map and show that exponential speedups can be obtained for experimentally relevant parameters. Besides the examples considered below, we mention that Davies maps have recently been used also to accurately estimate the impact of noise on single-qubit and two-qubit operations in superconducting transmon architectures [162].

A two-level atom in a photonic environment We start by studying a two-level atom interacting with a photonic environment. This system is characterized by the Jaynes-Cummings Hamiltonian that, in the rotating wave approximation, reads [160]

$$\hat{H} = \underbrace{\epsilon\hat{\sigma}^+\hat{\sigma}^-}_{\hat{H}_S} + \underbrace{\sum_k \omega_k \hat{a}_k^\dagger \hat{a}_k}_{\hat{H}_E} + \underbrace{\sum_k g\left(\hat{\sigma}^-\hat{a}_k^\dagger e^{-i(\epsilon-\omega_k)t} + \hat{\sigma}^+\hat{a}_k e^{+i(\epsilon-\omega_k)t}\right)}_{\hat{H}_I}, \tag{5.29}$$

where we have set $\hbar = 1$. Here ϵ is the energy difference between the two states of the atom, $\hat{\sigma}^+$ and $\hat{\sigma}^-$ are the ladder operators for the two-level atom, $\hat{a}^\dagger$ and $\hat{a}$ are the bosonic creation and annihilation operators, respectively, and the homogeneous coupling g describes the interaction strength between the two-level atom and the bosonic modes. We assume that the photons represented by $\hat{H}_E$ are in thermal equilibrium at inverse temperature β. Then, following the usual steps for the derivation of a Lindblad master equation [163] (Born, Markov, and rotating wave approximation, see Section 2.1), one obtains the Davies map [160]

$$\begin{aligned}\frac{\mathrm{d}\hat{\rho}(t)}{\mathrm{d}t} &= -i[\hat{H}_S, \hat{\rho}(t)] + \gamma n_\beta(\hat{\sigma}^+\hat{\rho}(t)\hat{\sigma}^- - \frac{1}{2}\{\hat{\sigma}^-\hat{\sigma}^+, \hat{\rho}(t)\}) \\ &+ \gamma(n_\beta + 1)(\hat{\sigma}^-\hat{\rho}(t)\hat{\sigma}^+ - \frac{1}{2}\{\hat{\sigma}^+\hat{\sigma}^-, \hat{\rho}(t)\}),\end{aligned} \tag{5.30}$$

where $\gamma \propto g$ is the damping coefficient, and n_β is the occupation of the two-level atom at the inverse temperature β. In Ref. [161], a similar setup including a resonator was applied for modeling a transmon qubit, considering the parameters $\epsilon = 2\pi \times 4\mathrm{GHz}$, $\gamma = 2\pi \times 1.41\mathrm{MHz}$, and $T_b = 0.1\mathrm{K} = 2.08\mathrm{GHz} \gg \gamma$. Fig. 5.6a shows that for such parameters, the thermalization of the two-level atom in a photonic environment can be exponentially accelerated by applying the exact unitary transformation $\hat{U}$ introduced in Eq. (5.14).

A spinful fermionic quantum dot Next, we consider a spinful fermionic quantum dot interacting with a fermionic reservoir. This setup has been studied for instance in [164] and can be described microscopically by

$$\hat{H} = \underbrace{\sum_{\sigma=\uparrow,\downarrow} \epsilon\hat{n}_\sigma + E_C\hat{n}_\uparrow\hat{n}_\downarrow}_{\hat{H}_S} + \underbrace{\sum_{k,\sigma} \omega_k \hat{c}_{k,\sigma}^\dagger \hat{c}_{k,\sigma}}_{\hat{H}_E} + \underbrace{\sum_{k,\sigma} g\hat{d}_\sigma^\dagger \hat{c}_{k,\sigma} + \mathrm{h.c.}}_{\hat{H}_I}\ . \tag{5.31}$$

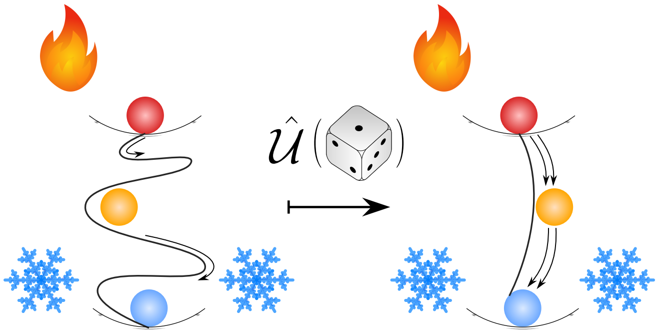

Figure 5.7: A unitary optimization based on a stochastic Metropolis algorithm can exponentially accelerate relaxation.

Here, ϵ is the dot's single particle energy, E_c is the Coulomb repulsion, ω_k is the energy of the reservoir-fermions, g describes the coupling between the dot and the reservoir-fermions, $\hat{d}$ ($\hat{d}^\dagger$) and $\hat{c}$ ($\hat{c}^\dagger$) are the annihilation (creation) operators for the quantum dot and the reservoir, respectively and $\hat{n}_{\uparrow(\downarrow)} = \hat{d}^\dagger_{\uparrow(\downarrow)}\hat{d}_{\uparrow(\downarrow)}$. If we consider a weak coupling g and a reservoir in thermal equilibrium, precisely as for Eq. (5.31), we obtain the Davies map for the quantum dot [61]

$$\begin{aligned}\frac{\mathrm{d}\hat{\rho}(t)}{\mathrm{d}t} = -i[\hat{H}_S, \hat{\rho}(t)] + \gamma n_\beta \sum_{\sigma=\uparrow,\downarrow} (\hat{d}^\dagger_\sigma \hat{\rho}(t) \hat{d}_\sigma - \frac{1}{2}\{\hat{d}_\sigma \hat{d}^\dagger_\sigma, \hat{\rho}(t)\}) \\ + \gamma(1-n_\beta) \sum_{\sigma=\uparrow,\downarrow} (\hat{d}_\sigma \hat{\rho}(t) \hat{d}^\dagger_\sigma - \frac{1}{2}\{\hat{d}^\dagger_\sigma \hat{d}_\sigma, \hat{\rho}(t)\}) \,.\end{aligned} \tag{5.32}$$

In accordance with the experimental parameters in Ref. [161], we consider $E_c = 1189\text{GHz}$, $\gamma = 1\text{GHz}$, $T_b = 2\text{K} = 41.67\text{GHz} \gg \gamma$. The dot's energy can be tuned by applying a voltage and we set it to $\epsilon = 242\text{GHz}$. In Fig. 5.6b, we illustrate the exponential acceleration of the thermalizing spinful quantum dot. Since the eigenvalue λ_2 is real, in this case, the speedup is obtained via a stochastic numerical transformation that will be introduced in Section 5.3. Furthermore, given that $\Re(\lambda_2) - \Re(\lambda_3)$ is small, the speedup is more modest than the one obtained for the two-level atom (Fig. 5.6a).

5.3 Exponential speedups via stochastic numerical optimization

In the preceding section, focusing on Davies maps, we demonstrated how exponential speedups related to a genuine quantum Mpemba effect can be achieved in thermalization processes. However, transformations of initial states that result in anomalous relaxations for *general Lindbladians* are of considerable interest, as highlighted by a plethora of recent literature [29, 130–141]. Here, we introduce a numerical method that generalizes [29, 133] to find (possibly multiple) exponential speedups for *mixed* states evolving with general Lindbladians.

5.3.1 The unitary Metropolis algorithm: quantum dynamics

For an initial state $\hat{\rho}$ and K left eigenmodes of a Lindbladian $\mathscr{L}$, the goal is to find the unitary transformation $\hat{U} : \quad \hat{\rho} \to \hat{\rho}'$, such that the cost function

$$C = \sum_{k=2}^{K+1} \left|\mathrm{Tr}\left(\hat{l}_k \hat{\rho}'\right)\right| \tag{5.33}$$

is minimized. A general global unitary transformation acting on L qubits is specified by 4^L real parameters. To handle large systems, we decompose the global unitary in terms of single-qubit unitaries as

$$\begin{aligned} &\hat{U} = \prod_{j=1}^{L} \hat{U}_j \quad \text{with} \\ &\hat{U}_j(\alpha_j, \beta_j, \gamma_j, \delta_j) = \exp\left(i\alpha_j\right)\hat{R}_z(\beta_j)\hat{R}_x(\gamma_j)\hat{R}_z(\delta_j)\,, \end{aligned} \tag{5.34}$$

where $\alpha, \beta, \gamma, \delta \in [0, 2\pi]$. With this ansatz, an optimal $\hat{U}$ can be obtained by performing a Metropolis search [165, 166]. This comprises the following steps:

1. Initialize a random $\hat{U}$ and an effective temperature $T_{\text{eff}} = 1$, rotate $\hat{\rho}$ with $\hat{U}$ and compute the cost function C.

2. Pick randomly which qubit j to optimize.

3. For the selected qubit, choose stochastically which parameter $x_j \in \{\alpha_j, \beta_j, \gamma_j, \delta_j\}$ of $\hat{U}_j$ to optimize.

4. Vary the selected parameter $x_j \to x_j' = x_j + \delta x_j$ by a random increment $\delta x_j \in [0, 2\pi]$, update $\hat{U}$ and $\hat{\rho}' \equiv \hat{U}\hat{\rho}\hat{U}^\dagger$ and reevaluate the cost function Eq. (5.33) with $\hat{\rho}'$.

5. If $C' < C$, accept the new unitary $\hat{U}' \to \hat{U}$ and update $C' \to C$. Otherwise, accept the new unitary with probability $p = \exp\left(-\frac{C'-C}{T_{\text{eff}}}\right)$.

6. If the new unitary is accepted, decrease the effective temperature by a cooling constant τ as $T_{\text{eff}} \to \tau T_{\text{eff}}$.

7. Repeat steps 4-6 n times (nano iterations: optimizing over one parameter).
8. Repeat steps 3-6 m times (micro iterations: optimizing over all parameters of a single qubit j).
9. Repeat steps 2-6 LM times (macro iterations: optimizing over all qubits).

The algorithm is terminated once the cost function has decreased below a threshold ϵ. We dub this algorithm *unitary Metropolis.* The extension to fermionic systems is straightforward and involves accounting for the fermionic anticommutation relations. This can be accomplished, for instance, by replacing the single-qubit unitary $\mathbb{1} \otimes \mathbb{1}_2 \cdots \otimes \hat{U}_j \otimes \mathbb{1}_{j+1} \ldots \mathbb{1}_L$ in Eq. (5.34) with $\mathbb{1}_1 \otimes \mathbb{1}_2 \cdots \otimes \hat{U}_j \otimes \sigma^z_{j+1} \ldots \sigma^z_L$, resulting in

$$\hat{U}^{\mathrm{f}} = \prod_{j=1}^{L} \hat{U}_j \left(\hat{\sigma}^z_j\right)^{\mathrm{mod(L\text{-}j,2)}} . \tag{5.35}$$

Furthermore, the same technique can be extended to bosonic systems with a local dimension d by decomposing single-site d-dimensional unitary operators $\hat{U}(d)$ into two-level rotations, as detailed in Algorithm 1 in Ref. [167]. The effect of $\hat{U}$ is pictorially represented in Fig. 5.7.

5.3.2 The swap Metropolis algorithm: classical dynamics

The algorithm outlined above can be streamlined when considering the special class of Lindbladians known as Davies maps. As discussed in the previous section, Davies maps exhibit a block diagonal structure, indicating that the populations and coherences of an initial state evolve independently. Hence, if the initial state is diagonal (incoherent) in the energy eigenbasis, the unitary optimization can be substituted by a simpler swap of the state's populations. Since for a D-dimensional system the number of swaps is $D!$, we resort again to a Metropolis algorithm implemented as follows:

1. Recast the diagonal part of the incoherent $(2^L \times 2^L)$ initial state $\hat{\rho}$ into a 2^L-dimensional vector and do the same for the targeted diagonal left eigenmatrices $\{\hat{l}_k\}_{k=2}^{K+1}$. Following Section 2.2, we indicate vectorized matrices with double brackets $\hat{\cdot} \rightarrow |\cdot\rangle\!\rangle$.
2. Evaluate the cost function $C \equiv \sum_{k=2}^{K+1} |\langle\!\langle l_k|\rho\rangle\!\rangle|$ and initialize an effective temperature $T_{\mathrm{eff}} = 1$.
3. Randomly select four integers $n_1, n_2, n_3, n_4 \in [0, D]$ representing the indices of four entries of $|\rho\rangle\!\rangle$ and perform a random permutation

$P(n_1, n_2, n_3, n_4) = (\tilde{n}_1, \tilde{n}_2, \tilde{n}_3, \tilde{n}_4)$, excluding the trivial permutation $(\tilde{n}_1, \tilde{n}_2, \tilde{n}_3, \tilde{n}_4) = (n_1, n_2, n_3, n_4)$.

4. Compute $|\rho'\rangle\rangle$ by swapping the four randomly selected elements of $|\rho\rangle\rangle$ according to the random permutation P and compute the cost function C' with the updated state.

5. If $C' < C$, accept the new state $|\rho'\rangle\rangle \to |\rho\rangle\rangle$ and update $C' \to C$. Otherwise accept the new state with probability $p = \exp\left(-\frac{C'-C}{T_{\text{eff}}}\right)$.

6. If the new state is accepted, decrease the effective temperature by a cooling constant τ: $T_{\text{eff}} \to \tau T_{\text{eff}}$.

7. Repeat steps $3-6$ until the cost function is reduced below a threshold ϵ.

We denote this technique as the *swap Metropolis* method. The same approach can be employed for a classical Markovian equilibration process (see Section 5.1), with the only distinction being that the eigenmodes and initial states are already vectors, rendering step 1 unnecessary. We mention that a swap minimization method (which we did not utilize in this work) was implemented in Mathematica [168].

5.3.3 Example 4: Applications of the swap and unitary Metropolis algorithms

We will now utilize the two Metropolis algorithms to investigate the thermalization of a TFIM with open boundary conditions, as described by Eq. (5.28), employing the Davies map. We set $h = J/2$ and $L = 5$. Initially, we investigate the heating process of a thermal state from $T_i = 1, J$ to $T_b = 4\,J$, utilizing the swap Metropolis algorithm to minimize the overlap of the initial state with a single incoherent eigenmode $\hat{l}_2$. Subsequently, we examine the thermalization of a random mixed state (obtained by averaging over 1000 random pure states) with $T_b = 0.1\,J$, applying the unitary Metropolis to target two coherent modes, $\hat{l}_2$ and $\hat{l}_3$. As illustrated in Fig. 5.8, the swap Metropolis achieves a reduction in C below $\epsilon = 10^{-6}$ after approximately 5300 iterations, whereas the unitary Metropolis surpasses the convergence threshold after about 60500 iterations. It is worth emphasizing that despite the relatively high number of iterations, both methods have low computational costs. The bottleneck for investigating the Mpemba effect lies in the diagonalization of the quantum or classical Liouvillian (which is needed to obtain the left eigenmodes), rather than the minimization algorithms themselves. In Fig. 5.9, we depict the dynamics of the L_1-distance (Eq. (5.27)) from the steady state before and after applying the swap Metropolis and the unitary Metropolis optimizations. In both scenarios, exponential speedups are found.

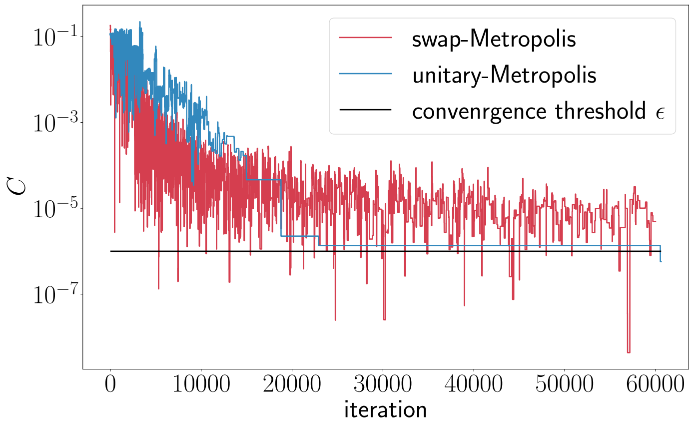

Figure 5.8: The swap Metropolis and the unitary Metropolis methods are applied to the thermalization process of a TFIM with $L = 5$ and $h = J/2$. In the swap Metropolis approach (red line), the goal is to diminish the overlap of a thermal state with a single diagonal eigenmode, employing a cooling constant $\tau = 0.998$. Conversely, the unitary Metropolis technique aims to reduce the overlap of a random state with two off-diagonal eigenmodes, utilizing a cooling constant $\tau = 0.999$. We set the maximum allowed number of nano iterations to $n = 200$, micro iterations to $m = 20$, and macro iterations to $M = 20$.

Specifically, panel (a) illustrates that as the swap Metropolis algorithm conserves the diagonal structure of the thermal initial state, the transformed state continues to remain orthogonal to the off-diagonal modes, thereby enhancing the thermalization rate from λ_2 to λ_5.

5.4 Summary and outlook

This chapter explored the quantum Mpemba effect from the perspective of non-equilibrium thermodynamics. We first summarized the classical Markovian Mpemba effect and its experimental verification in colloidal systems in Section 5.1. Then, in Section 5.2, we studied the spectral properties of Davis maps and showed that the thermalization of a state with coherences in the energy eigenbasis can always be exponentially accelerated if the spectral gap is defined by a complex eigenpair. Moreover, inspired by the stochastic thermodynamics approach to the classical Mpemba effect, we argued that an accelerated equilibration process is not by itself an instance of the quantum Mpemba effect; a genuine quantum Mpemba effect occurs when the non-equilibrium free energies F_{neq} of the original and the transformed state cross in time. We applied our exact unitary transformation to study the Mpempa effect in a single-qubit Fig. 5.4 and a multiple-qubit setup Fig. 5.5. This provides the thermodynamic foundations for a research field

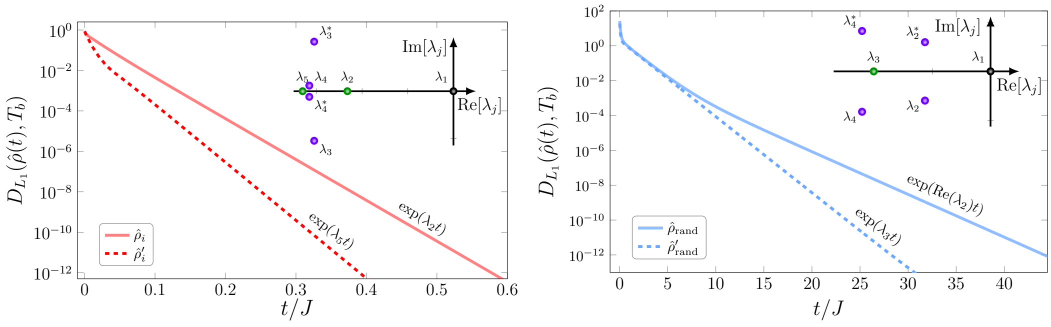

(a) **(b)**

Figure 5.9: Exponentially accelerated thermalizations are observed after the Metropolis optimization (see Fig. 5.8). Panel (a): the L_1-distance from the thermal steady state before (solid line) and after (dashed line) applying the swap metropolis optimization during the heating process of a thermal state. Panel (b): the L_1-distance from the thermal steady state before (solid line) and after (dashed line) applying the unitary metropolis optimization during the thermalization process of a random mixed state. In both cases, the Metropolis algorithms result in exponential speedups.

that is rapidly expanding and can help establishing new avenues of exploration. We also discussed the physical realization of Davies maps, which are used for instance in quantum computing and quantum optics, and presented two concrete examples in Fig. 5.6.

In Section 5.3, we introduced two numerical methods, based on the Metropolis algorithm, that stochastically minimize the overlap between a (possibly mixed) initial state and one or multiple Lindbladian left eigenmatrices. These can exponentially speed up thermalization processes, as shown in Fig. 5.9. In particular, the swap Metropolis algorithm succeeds in accelerating thermalization processes for incoherent (diagonal) initial states and Davies maps with $\lambda_2 \in \mathbb{R}$, thus complementing the analytic transformation introduced in Section 5.2. Moreover, since the dynamics generated by the Davies map for an incoherent initial state are effectively classical, swap Metropolis can be used to investigate the connection between the quantum and the classical Mpemba effect. The unitary Metropolis algorithm should, in principle, apply to general quantum Markovian equilibration processes, as it does not rely on any assumption of the spectral structure of the Liouvillian. Exploring its application to general Lindbladians different from the Davies maps considered here will be the subject of future work.

The experimental investigation of the quantum Mpemba effect is in its infancy [140, 141], but its potential application to dissipative state preparation [169–171] and cooling protocols [172, 173] appears to be promising. Furthermore, conceptual questions concerning, for instance, the relation between the quantum Mpemba effect and thermodynamic geodesics [174] as well as the asymmetry between heating and cooling processes [175] remain unanswered. Due to its deep fundamental and practical implications, we believe that the Mpemba effect will continue to inspire fundamental and applied research in the years to come.

Chapter 6

Photoexciting electrons: Exciton dynamics in structured vibrational environments

“Can dissipation be leveraged as a resource for simulating quantum dynamics?”

In this chapter, we transition from the single- and few qubit systems studied in Chapter 5 to many-body systems. For numerical calculations, we thus adopt MPS methods instead of ED for most of the remainder of this thesis. We investigate the dynamics of single photo-induced electronic excitation in contact with large, structured vibrational environments, which are challenging to simulate. We first introduce the systems of interest and discuss the limitations of current numerical methods in Section 6.1. We argue that we can overcome these limitations by combining the mesoscopic leads approach with a pure-state unraveling and state-of-the-art MPS techniques and label the resulting method PS-HyB-MPS for convenience. Then, in Section 6.2, we apply PS-HyB-MPS to study a minimal model for singlet fission (SF). Next, we simulate the exciton dynamics of the FMO light-harvesting complex at finite temperature in Section 6.3. Comparisons to literature results obtained with unitary dynamics clearly show the advantage of our PS-HyB-MPS approach. Finally, we summarize our results and discuss potential developments and applications of the introduced method. This chapter is based on Ref. [4], written in collaboration with Zhaoxuan Xie, Ulrich Schollwöck, and Sebastian Paeckel.

6.1 Overcoming current limitations in the simulations of exciton dynamics

Accurately describing light-matter interactions represents a major effort in theoretical condensed matter physics. Here, we will focus on the photo-excitation of electronic degrees of freedom, which can result, for instance, in the formation of excitonic quasiparticles (i.e. bound electron-hole pairs). In many physical setups, excited electronic states interact with vibrational degrees of freedom that strongly influence their dynamics. Two important examples of such photophysical processes are i) singlet fission (SF), i.e., creating two triplet excitations from one singlet excitation in molecular crystals and ii) the exciton dynamics in light-harvesting complexes. Despite being very different, the two phenomena can be modeled similarly for the following reasons: First, the electronic excitations are long-lived compared to the timescales on which the relevant dynamics take place [176, 177]. Second, the scattering amplitude between electronic excitations is typically much smaller than the one between electronic excitations and vibrational modes and is usually omitted (even though exciton-exciton interactions can play a role in light-harvesting complexes [178]). Thus, the electronic dynamics can be modeled by considering a single excitation hopping on a lattice

$$\hat{H}_{\mathrm{ex}} = \sum_{i,j} t_{ij} \hat{c}_i^\dagger \hat{c}_j + \mathrm{h.c.}\,, \tag{6.1}$$

where $\hat{c}_j^\dagger$ ($\hat{c}_j$) creates (annihilates) a fermionic excitation on site j. Note that the lattice represents spatially-separated photosynthetic pigments for FMO (see Section 6.3) while in the case of SF they indicate different many-body electronic states (see Section 6.2). For every electronic degree of freedom j, we will consider an independent vibrational bath represented by a collection of harmonic oscillators $\hat{H}^j_{\mathrm{vib}} = \sum_p \omega_{jp} \hat{a}^\dagger_{jp} \hat{a}_{jp}$, that couple linearly to the electron density

$$\hat{H}^j_{\mathrm{ex-vib}} = \sum_p g_{jp} \hat{c}_j^\dagger \hat{c}_j \frac{1}{\sqrt{2}} \left(\hat{a}^\dagger_{jp} + \hat{a}_{jp} \right) \,, \tag{6.2}$$

where $\hat{a}_p^\dagger$ ($\hat{a}_p$) creates (annihilates) a vibrational excitation with frequency ω_{jp}. The interaction strength g_{jp} between the electronic excitation j and the vibrational mode p is described by the spectral density $J_j(\omega) = \pi/2 \sum_p |g_{jp}|^2 \delta(\omega - \omega_{jp})$.

In some instances, the excitons couple strongly to a discrete number of vibrational modes. This situation, represented by a spectral density $J(\omega)$ displaying sharp peaks (Fig. 6.1, upper-right panel), can occur for instance when the exciton's dynamics are affected by the normal vibrational modes of organic molecules as tetracene [84]. Such scenarios can be efficiently described by associating the highest peaks of $J(\omega)$ to a harmonic oscillator and evolving the combined

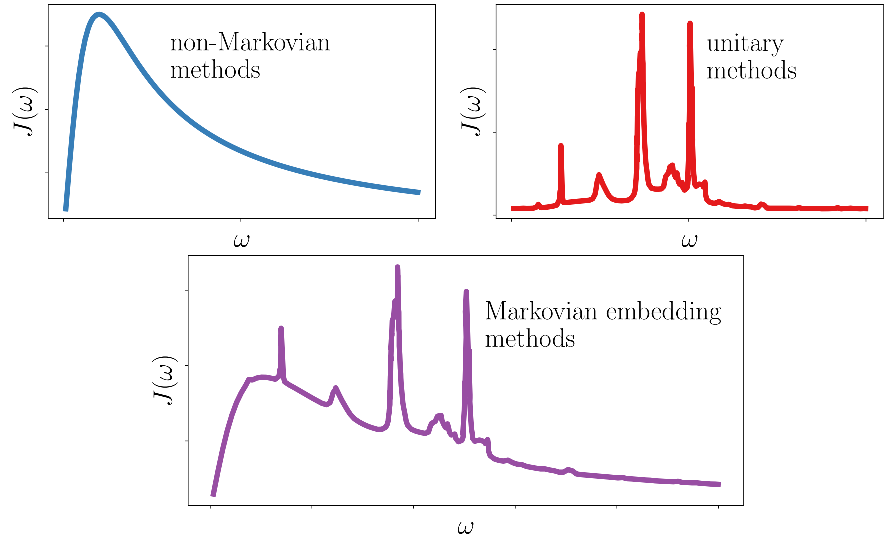

Figure 6.1: Spectral densities describing electronic-vibrational interactions. The influence of smooth spectral densities, denoting the coupling of electronic excitations to a continuum of vibrational frequencies (upper-left panel) is well described by non-Markovian methods, while the impact of spectral densities displaying sharp peaks (upper-right panel) can be efficiently simulated with unitary dynamics. Both these features (lower panel) are efficiently captured by Markovian-embedding methods (see Sections 6.2 and 6.3).

excitonic and vibrational system unitarily. Well-established numerical methods in this context are multilayer multiconfiguration time-dependent Hartree (ML-MCTDH) [31, 179] and TDVP [84, 180]. Instead, when the excitons interact with a continuum of vibrational modes, represented by a smooth $J(\omega)$ (Fig. 6.1, upper-left panel), the unitary description becomes very expensive, as a large number of vibrational modes needs to be used to approximate the continuous features of $J(\omega)$. In such cases, it is beneficial to trace out the vibrational degrees of freedom and use a non-Markovian method to simulate the dynamics of the excitonic system exactly. Suitable methods include HOPS (see Section 2.5) [26, 66], HEOM [69, 181] and the quasi-adiabatic path integral (QUAPI) approach [65, 182]. In non-Markovian methods, each vibrational mode is damped by coupling it dissipatively to its own thermal bath, and $J(\omega)$ is fitted with Lorentzians. This allows us to approximate a smooth $J(\omega)$ with fewer vibrational modes than needed by unitary methods. In turn, however, non-Markovian methods struggle to describe discrete features of $J(\omega)$, as sharp peaks represent long memory effects of the bath, which can render the complexity of, for instance, HOPS unmanageable in practice (see Section 4.3).

A way to combine the best features of the unitary and the non-Markovian evolution is to adopt a Markovian-embedding method, i.e. to consider the unitary evolution of the combined excitonic and vibrational systems and to couple the vibrational modes to a thermal bath additionally. This can be achieved using

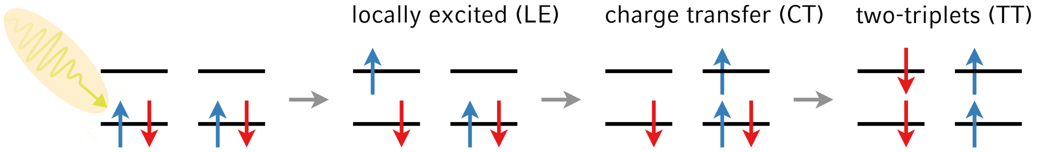

Figure 6.2: Schematics of singlet fission. From left to right: an incoming photon excites the spin-up electron from the ground state to the first excited state of the left molecular orbital, forming one singlet excitation (locally excited (LE) state). The excited electron hops from the left to right molecular orbital (charge transfer (CT) state). Finally, the spin-down electron from the ground state of the right molecular orbital gets excited to the left molecular orbital (two-triplet (TT) state).

the mesoscopic leads methods outlined in Section 2.6. In short, this approach amounts to solving a Lindblad equation for the joint excitonic and vibrational systems

$$\frac{\mathrm{d}\hat{\rho}}{\mathrm{d}t} = \mathscr{L}(\hat{\rho}) = -i\left[\hat{H}, \hat{\rho}\right] + \sum_{j,p} \mathscr{D}_{jp}(\hat{\rho}) \,, \tag{6.3}$$

where the dissipator $\mathscr{D}$ describes the thermalization of each vibrational mode (see Eq. (2.44)). To solve Eq. (6.3) for large systems, we use the QJ method (see Section 2.3) to replace the deterministic evolution of $\hat{\rho}(t)$ with the propagation of many stochastic pure states. This quadratically reduces the dimension of the considered Hilbert space and avoids the numerical problems that arise when representing $\hat{\rho}$ as an MPO and solving Eq. (6.3) directly (see Section 3.2.1). Then, for every so-called trajectory we represent $|\Psi(t)_q\rangle$ as an MPS [21] and use PP to efficiently treat the vibrational modes (see Section 3.1).

We propagate each trajectory in time using LSE-TDVP, which is very efficient for bosonic degrees of freedom [37, 86]. For convenience, we will label the QJ-unraveled mesoscopic leads method combined with state-of-the-art tensor network techniques for vibrational environments *pure-state unraveled hybrid-bath based on matrix product states (PS-HyB-MPS)*. As we will show in the next section, PS-HyB-MPS allows us to efficiently simulate exciton dynamics interacting with vibrational environments characterized by spectral densities with both continuous and discrete features (Fig. 6.1, lower panel). We note that a similar approach, based however on a discretization of the bath in the time domain and the propagation of $\hat{\rho}$ as an MPO was introduced by Somoza et al. [24].

6.2 A dissipative approach to singlet fission

Singlet fission (SF) is a photophysical process in which a singlet excitation (labeled locally excited (LE) state) induced by an incoming photon is split into two triplet excitations (referred to as the TT state). The detailed mechanism behind SF and the timescales on which it occurs are material-specific. In organic semiconductors such as tetracene [84] and rubrane [64], the process is believed to be mediated by an intermediate charge transfer (CT) state (see Fig. 6.2 for a schematic representation). Moreover, in such materials, the excited electronic states typically interact with many molecular vibrational modes, rendering the dynamics computationally costly to simulate. SF is of great interest for technological applications, such as designing novel solar cells with efficiencies above the Shockley-Queisser limit [183, 184].

Here, we apply PS-HyB-MPS to study a minimal model for singlet fission at zero temperature. Following Ref. [31] we couple each electronic state (LE, CT and TT) linearly to its own vibrational bath (see Eq. (6.2)), where the couplings are defined by a Debye spectral density

$$J^D(\omega) = \frac{2\lambda\omega\omega_c}{(\omega^2 + \omega_c^2)} , \tag{6.4}$$

with $\lambda = 807\text{cm}^{-1}$ and $\omega_c = 1452\text{cm}^{-1}$. We draw the parameters for the excitonic Hamiltonian Eq. (6.1) from [31] and fit $J^D(\omega)$ with $P = 10$ Lorentzians. The system is initialized with one excitation on the LE state and a vacuum state for the vibrational degrees of freedom. In Fig. 6.3a, we show the dynamics of the populations of the three electronic states, employing 1000 trajectories, a time step $dt = 5\text{fs}$ and a cutoff dimension $d = 16$ for the vibrational modes. Our sample-averaged PS-HyB-MPS results (crosses) agree very well with the reference ML-MCTDH data from [31].

Having tested the accuracy of PS-HyB-MPS, we proceed by analyzing its efficiency compared to unitary time evolution methods. In [31], a careful analysis found that $P = 61$ vibrational modes per electronic site were necessary for converging the calculations. Indeed, in Fig. 6.3b, comparison between $P = 61$ (dotted black line) and $P = 30$ (dashed red line) reveals that the latter number is insufficient to converge the dynamics of the LE state's population with a unitary time evolution. Instead, with PS-HyB-MPS, we find that $P = 10$ modes are enough for obtaining converged results. This is because fitting the spectral density $J^D(\omega)$ with Lorentzians with width κ (which corresponds to the strength of the dissipatively damping of the vibrational modes, see Section 2.6), allows us to efficiently capture the continuous features of $J^D(\omega)$. The small deviations from the reference data can be attributed to the stochastic unraveling of the master equation and can be reduced by increasing the number of applied trajectories. By comparing the slowest PS-HyB-MPS trajectory to a unitary time evolution, we found that reducing P from 61 to 10 results in a $\sim$ 7.5-fold speedup. For both approaches, we used LSE-TDVP with the same parameters, and all calculations were run on an Intel Xeon Gold 6130 CPU (2.10GHz) with 16 threads. In the next section, we will see that the reduction of the required number of vibrational modes is not the only advantage of PS-HyB-MPS.

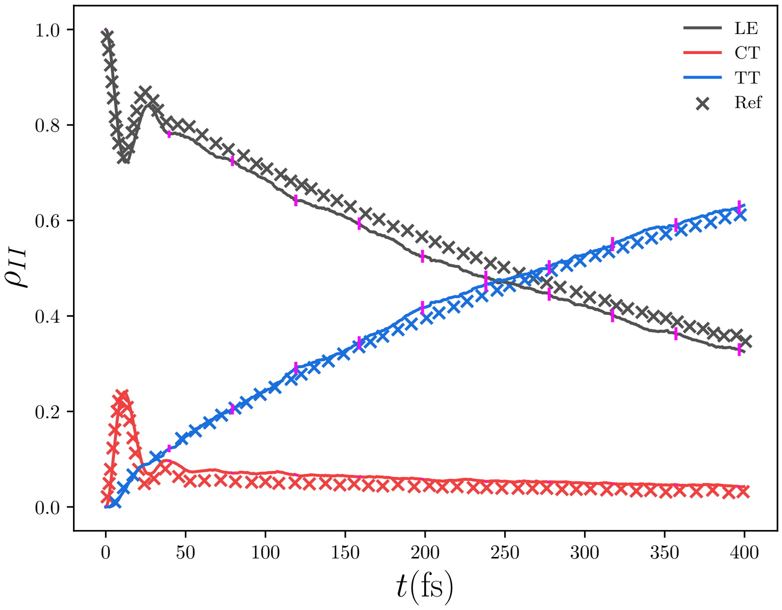

(a)

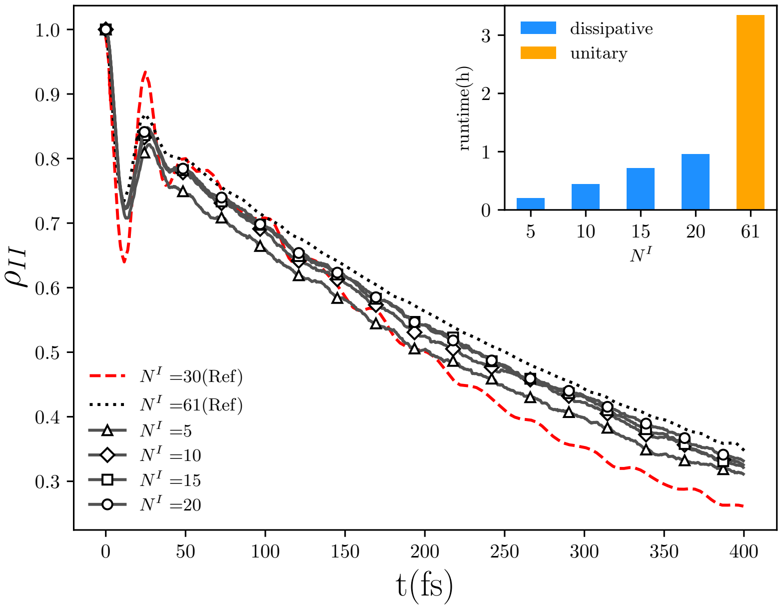

(b)

Figure 6.3: Singlet fission dynamics. Fig. 6.3a: Dynamics of the populations of the LE, the CT and the TT states. We compared our PS-HyB-MPS results (solid lines) to the reference data (crosses) from [31], finding good agreement. Fig. 6.3b: Convergence of the LE dynamics with the number of vibrational modes per excitonic site. Compared to unitary dynamics, the damping of the vibrational modes in the mesoscopic leads approach (see the discussion in the main text) allows to reduce the number of vibrational modes per electronic site from 61 to 10, resulting in a ~ 7.5-fold speedup, as shown in the inset.

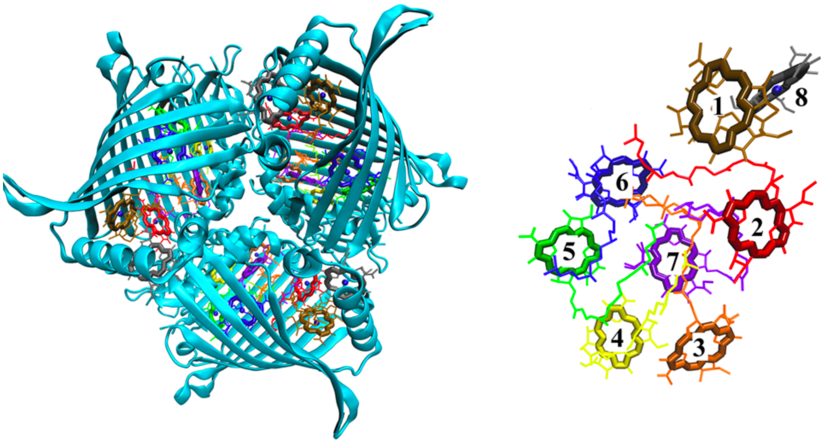

Figure 6.4: The Fenna-Matthews-Olson (FMO) light-harvesting complex. Left: The FMO complex consists of three identical subunits, each made up of eight chlorophyll pigments surrounded by a protein scaffold (light blue strands). Right: the eight chlorophyll pigments of one subunit. Typically, the exciton energy is conveyed from pigment 1 to pigment 3 via hopping over all pigments except for pigment 8, which does not contribute significantly to the dynamics. Taken from Ref. [32].

6.3 Exciton transport in the FMO complex at finite temperature

Light-harvesting complexes are pigment-protein compounds found in plants and some bacteria that are involved in the early stage of photosynthesis [185]. The pigments absorb photons from the sun, exciting excitons that are transported to the reaction center, where their energy is used to produce carbohydrates. In the case of oxygenic photosynthesis, this hugely complex process can be summarized as $H_2O + CO_2 + \text{photons} \longrightarrow CH_2O + O_2$. The best studied light-harvesting complex (together with light-harvesting complex II (LHC-II) [33]) is the Fenna-Matthews-Olson (FMO) complex, resposible for anoxygenic photosynthesis in green sulfur bacteria [32]. As shown in Fig. 6.4, it consists of three identical subunits made up of eight chlorophyll pigments embedded in a protein scaffold. The most significant exciton energy transport happens from pigment 1 to pigment 3 and encompasses all pigments except unit 8, which does not contribute significantly to the dynamics. One of the primary exciton transport mechanisms is Förster resonance energy transfer, describing a dipole-dipole coupling between pigments [186]. The vibration of the protein scaffold can lead to fluctuations in the pigment's position and orientation, altering the dipole couplings and thus strongly affecting the excitonic energy transport. Beyond acting as a classical heat bath, the role of vibrational modes in long-lived quantum coherence in the exciton transport has been widely debated [187, 188], with the current consensus

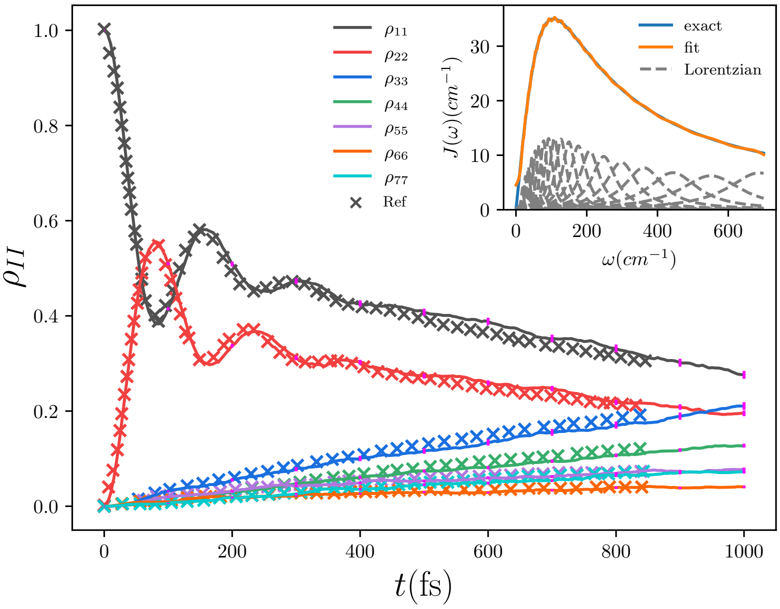

(a)

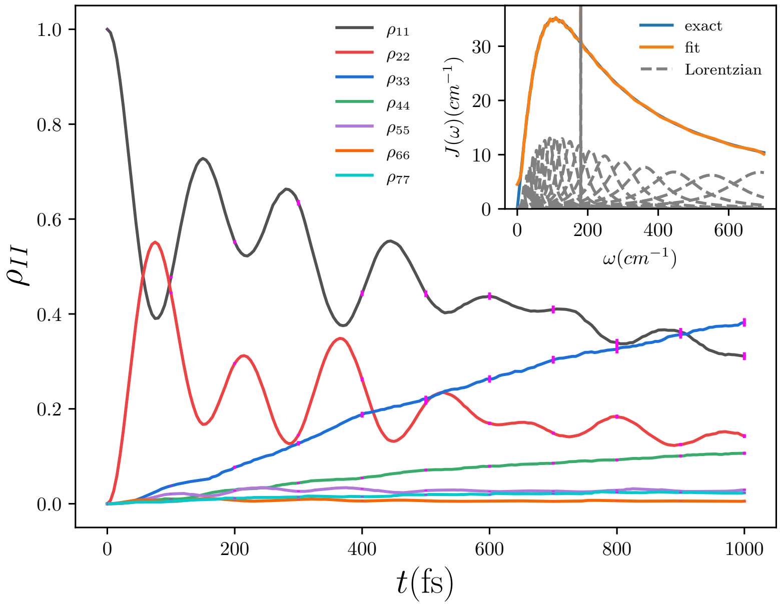

(b)

Figure 6.5: Exciton dynamics in the FMO light-harvesting complex at finite temperature. (a): Time-dependent exciton populations following the initial excitation of pigment 1 at $T = 300\text{K}$ with a Debye bath spectral density (see Eq. (6.4)). The PS-HyB-MPS data (solid lines) agrees well with the QUAPI reference data from [65] (crosses) and indicates that at long times the excitonic population is monotonically decreasing on pigments 1 and 2 and steadily increasing on 3. (b): Same as (a) but with an additional δ-peak at the frequency $\omega_0 = 29\text{cm}^{-1}$ on top of the Debye spectral density at $T = 77\text{K}$. The insets show the exact (blue) and approximated (orange) spectral densities, as well as the Lorentzians used for the fitting (gray). For both panels, we used a time step $dt = 5\text{fs}$, a local dimension for the vibrational modes $d = 16$, a maximal bond dimension $m = 50$, $P = 19$ modes to discretize $J^D(\omega)$ and averaged the results over 1000 trajectories.

being that they likely play no relevant role at room temperatures [189, 190].

Here, we consider the exciton dynamics in a 7-pigment subunit of the FMO complex to further test the efficacy of the PS-HyB-MPS method. We adopt the Hamiltonian parameters from [65], considering again a Debye spectral density Eq. (6.4) which describes the vibrations of the protein scaffold and initialize the excitonic system with one excitation on pigment 1 and the vibrational bath in a thermal state at temperature T. In Fig. 6.5a, we show the exciton dynamics on every pigment at ambient temperature $T = 300\text{K}$. Our PS-HyB-MPS results agree well with the reference data from [65], which was obtained using the exact, non-Markovian QUAPI method [182] and show that at long times a steady increase in the exciton population on pigment 3 is observed. We found that $P = 19$ vibrational modes per excitonic site were needed to fit the spectral density accurately (inset of Fig. 6.5a) and averaged our results over 1000 trajectories. Next, we modify the Debye spectral density by adding a δ-peak at a frequency $\omega_0 = 29\text{cm}^{-1}$, representing the vibration of the pigments [65]. This leads to long-time memory effects in the vibrational bath. Such an undamped mode cannot be studied with non-Markovian methods such as QUAPI, where a broadening of the peak needs to be considered. We display the exciton dynamics for such a vibrational bath in Fig. 6.5b, considering a temperature $T = 77\text{K}$. Compared to the bare Debye spectral density [65], the additional delta peak modifies the exciton dynamics, enhancing the population's oscillation at times $t \sim 200\text{fs}$. This indicates the flexibility of PS-HyB-MPS in describing baths with both continuous and discrete features.

The (mixed) thermal state for the vibrational modes $\hat{\rho}^{\beta}_{\text{vib}}$, which is uncorrelated with the pure excitonic state $|\psi(0)\rangle_{\text{ex}}$ at initial times

$$\hat{\rho}(0) = |\psi(0)\rangle_{\text{ex}} \langle\psi(0)|_{\text{ex}} \otimes \hat{\rho}^{\beta}_{\text{vib}} , \tag{6.5}$$

can be represented as an MPS using different methods. One possible strategy is to sample from the Boltzmann distribution, initializing each QJ trajectory with a different pure state. When considering independent harmonic oscillators, the probability of finding n vibrational excitations on the p-th mode relative to the excitonic site j is simply

$$p_{jp}(n) = \frac{e^{-\beta\omega_{jp}n}}{\text{Tr}\left(e^{-\beta\omega_{jp}n}\right)} . \tag{6.6}$$

We use this approach to compute the exciton population on pigment 1 in Fig. 6.6a, considering a temperature of 77K. The results are completely off for a time step $dt = 5\text{fs}$ and are still unconverged for the smallest considered time step of $dt = 0.5\text{fs}$. This is because many "jumps" on the vibrational are required to thermalize the system, and given that only one jump per time step can occur in a system with 133 modes, the required time step becomes exceedingly small.

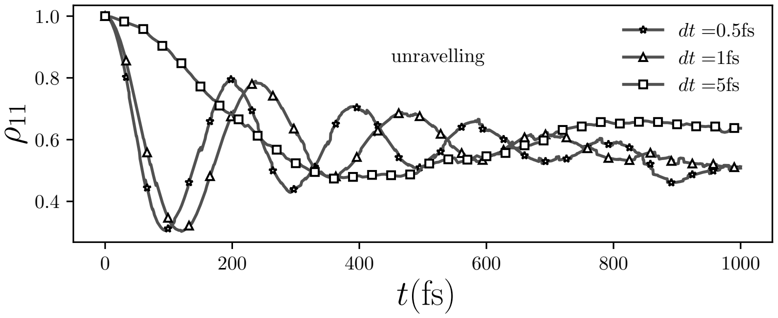

(a)

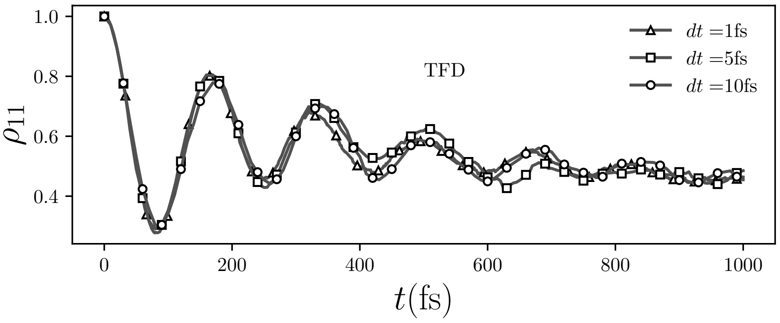

(b)

Figure 6.6: Finite-temperature: unraveling vs. thermofield doubling. (a): We sample the initial thermal state for the vibrational modes, thus initializing each QJ trajectory with a different pure state. The large number of jumps needed to thermalize the vibrational modes at $T = 77$K leads to an unconverged time-dependent excitonic occupation of pigment 1 even when utilizing a small time step $dt = 0.5$fs. (b) A thermofield doubling combined with a Bogoliubov transformation allows us to map the thermal state to a vacuum state, thus significantly reducing the number of jumps and leading to well-converged QJ results with $dt = 5$fs. We considered a Debye spectral density, set $m = 50$ and $d = 16$, and averaged over 50 trajectories.

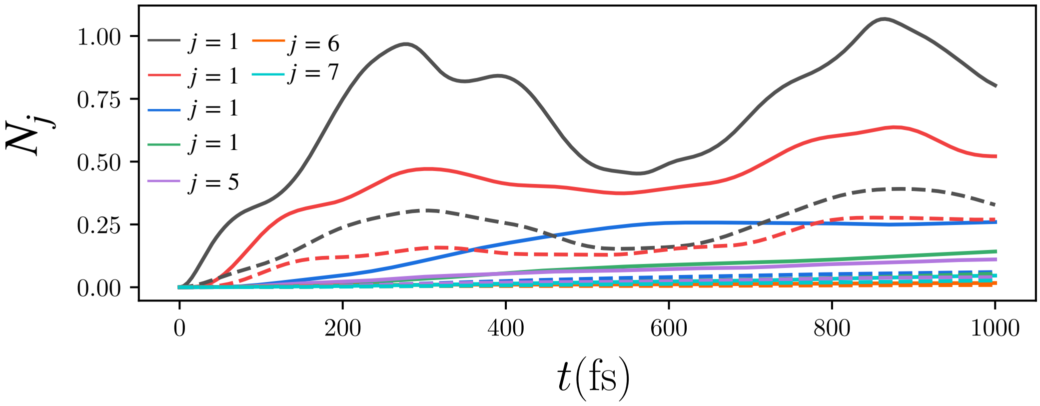

(a)

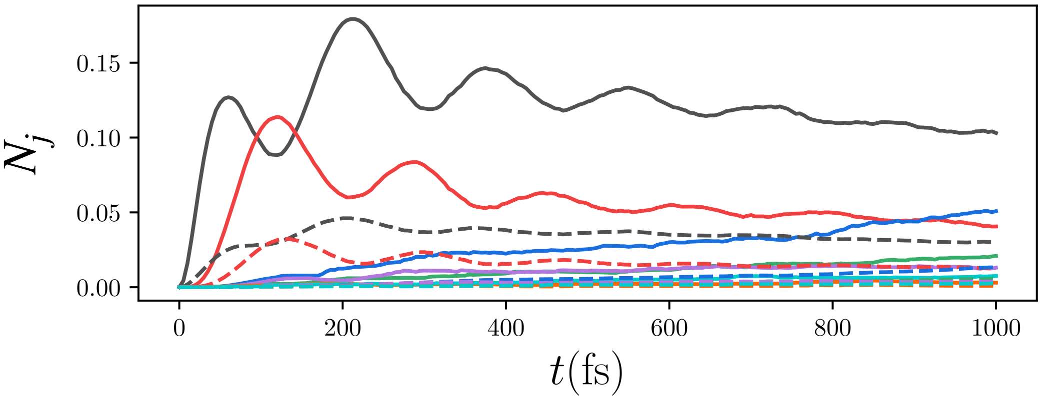

(b)

Figure 6.7: Total occupation of the vibrational modes for unitary and dissipative dynamics at 77K. The bosonic annihilation operators, which act as jump operators in the PS-HyB-MPS method, lead to an approximately sixfold decrease of the total occupation of the vibrational modes $N_j(t) \equiv \sum_p \langle\Psi(t)|\, \hat{n}_{jp}\, |\Psi(t)\rangle$ for each excitonic site j (panel (b)) compared to the unitary dynamics (panel (a)). We considered $P = 6$ vibrational modes per exciton and set all other parameters to the same values as in Fig. 6.6.

An alternative strategy is to double the vibrational Hilbert space, performing a purification. For an arbitrary mixed state $\hat{\rho}_A$ defined on a Hilbert space $\mathscr{H}_A$, it is always possible to find a (non-unique) pure state $|\psi\rangle_{AB}$ defined on the doubled Hilbert space $\mathscr{H}_A \otimes \mathscr{H}_B$ (with $\mathscr{H}_A \cong \mathscr{H}_B$) such that $\mathrm{Tr}_B(|\psi\rangle_{AB} \langle\psi|_{AB}) = \hat{\rho}_A$ [14]. This avoids the sampling of the initial state (at the cost of doubling the number of vibrational sites), but does not solve the time step issue shown in Fig. 6.6a, which can be addressed with the technique presented in Ref. [191]. The idea outlined by de Vega and Bañuls is to identify every purified site with a harmonic oscillator with negative frequency $-\omega_{jp}$ and then to perform a (unitary) thermal Bogoliubov transformation which maps the thermal state $\hat{\rho}^{\beta}_{\mathrm{vib}}$ to a vacuum state [191]. In this way, working in the new basis, the number of quantum jumps on the vibrational modes is drastically reduced, and as Fig. 6.6b shows, the QJ calculations are well converged for a time step $dt = 5$fs.

Together with the bond dimension m, the most important parameter dictating the simulation's complexity is the physical local dimension d of the vibrational sites. To assess the efficiency of PS-HyB-MPS compared to a unitary evolution, we study the total occupation of the vibrational baths of each excitonic site $N_j(t) \equiv \sum_p \langle\Psi(t)|\, \hat{n}_{jp}\, |\Psi(t)\rangle$. For a unitary evolution, $N_j(t)$ (see Fig. 6.7a) is approximately 6 times higher than for PS-HyB-MPS (see Fig. 6.7b). This follows in part from the fact that thanks to the Bogoliubov transformation mapping the thermal initial state to a vacuum [191], all jump operators are annihilation operators (see Eq. (2.45)), which lower the occupation of the vibrational modes. Importantly, this implies that oscillators with smaller local dimensions are required (see the discussion on PP in Section 3.1).

As a further check, we compare the convergence of the dynamics of the exciton population on the first pigment w.r.t. the bond dimension m during unitary and PS-HyB-MPS dissipative dynamics. Fig. 6.8a shows that while a bond dimension for at least $m = 50$ is needed for unitary dynamics, dissipative PS-HyB-MPS dynamics yield converged results for $m = 10$ (see Fig. 6.8b). This can be attributed in part to the lower local dimension for the vibrational modes and in part to the "measuring" effect of dissipation, which can suppress the entanglement propagation in the system [1, 192] (see Chapter 8). Note also that to first order in dt, the non-Hermitian time evolution in the QJ algorithm (see Section 2.3)

$$|\Psi(t + dt)\rangle \approx e^{-idt\hat{H}} e^{-dt/2 \sum_l \hat{L}_l \hat{L}_l} |\Psi(t)\rangle \tag{6.7}$$

is formally similar to the recently proposed complex contour time evolution scheme [193], which has been shown to significantly suppress the entanglement growth w.r.t. a standard real-time evolution. Exploring the connection between the two would be an interesting research topic for the future.

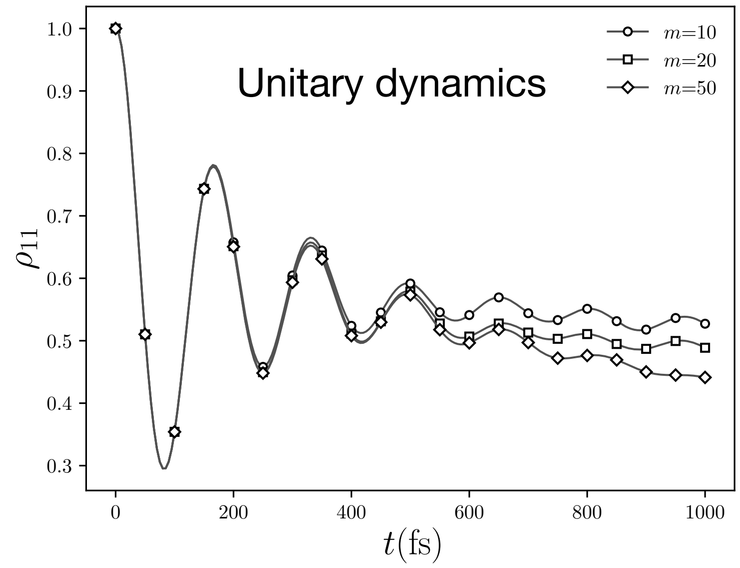

(a)

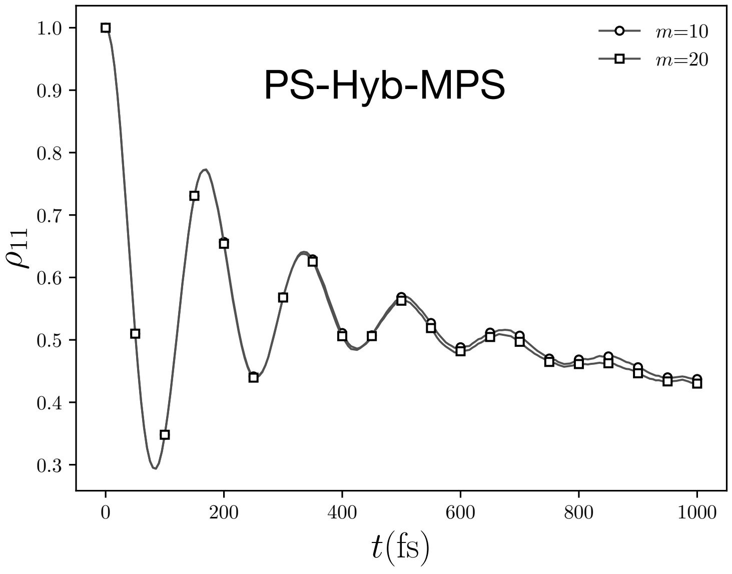

(b)

Figure 6.8: Bond dimension convergence for unitary and dissipative dynamics at $T = 77$K. Dissipation suppresses the occupation of the vibrational modes as well as the spread of correlations in time (see the discussion in the main text) and thus PS-HyB-MPS calculations (right panel) converge for a smaller bond dimension m than unitary dynamics (left panel). We considered $P = 30$ vibrational modes per exciton and set all other parameters to the same values as in Fig. 6.6.

6.4 Summary and outlook

Photophysical processes in which incoming photons excite electronic degrees of freedom are of great interest both from a fundamental and an applied point of view. When the excited electrons interact strongly with vibrational degrees of freedom, these processes become very challenging to simulate. In Section 6.1, we argued that while well-established methods excel either at describing electronic interactions with smooth, continuous vibrational baths (non-Markovian methods) or with selected, undamped modes (unitary methods), the mesoscopic leads method (see Section 2.6) captures both types of interactions equally well. Leveraging the flexibility of the mesoscopic leads method, we combined it with an efficient solution method for the Lindblad equation (QJ) and state-of-the-art MPS techniques for vibrational degrees of freedom (LSE-TDVP and PP) and labeled the resulting method PS-HyB-MPS. We applied PS-HyB-MPS to the study of SF at zero temperature for a smooth Debye spectral density in Section 6.2. We found that compared to unitary dynamics, PS-HyB-MPS requires far fewer vibrational modes to accurately represent the spectral density, which results in a large computational speedup. Next, we studied the finite-temperature exciton dynamics of the FMO complex in Section 6.3. In this context, we demonstrated that PS-HyB-MPS can describe undamped modes, which are in practice out of reach for non-Markovian methods. We also showed that, compared to unitary dynamics, dissipative calculations require a significantly lower bond dimension (Fig. 6.8) and physical local dimension for the vibrational modes (Fig. 6.7).

We argue that this last point is the most significant result presented in this chapter. That a notable modification of the dynamics of the vibrational modes (Fig. 6.7) does not appreciably alter the electronic dynamics (Fig. 6.5) is a remarkable observation. While in simple electronic systems like the ones considered here, for which only small bond dimensions are required, this does not lead to huge computational speedups, the advantage of PS-HyB-MPS can become more evident for interacting, strongly-correlated systems (see for instance Chapter 8). In this context, it would be interesting to extend the mesoscopic leads method from diagonal to off-diagonal electronic-vibrational couplings, which play a prominent role in SF in tetracene [84] rubrane [64], and appear in the Su-Schrieffer-Heeger (SSH) model [37]. Furthermore, replacing the MPS with a tree tensor network (TTN) [194], which can mirror the topology of large vibrational baths interacting locally with electronic sites, could prove beneficial in further reducing the numerical costs of the simulations.

Chapter 7

Photoexciting phonons: Analyzing light-induced phenomena with PST

"How do phonon excitations affect non-equilibrium properties of electrons in photo-excited metals?"

This chapter analyzes the impact of excited vibrational modes on the photo-induced electron dynamics in a metal. In contrast to Chapter 6, we do not consider the direct photo-excitation of the electrons but instead of the vibrational system. Furthermore, we move from a single electronic excitation to a many-body electron system at half-filling. At the same time, we simplify the vibrational system by considering a single vibrational mode for every electronic site. Crucially, we also adopt a non-linear electron-phonon coupling. This is the only chapter in which we consider unitary rather than dissipative dynamics.

Optical driving is an important tool for manipulating quantum materials and studying novel non-equilibrium phenomena. In this context, one notable type of experiment consists in using optical excitations to target specific infrared-active phonons that strongly affect the electronic properties of the material [99, 100, 195]. The photo-excited phonons obey dipole selection rules, implying that they couple non-linearly to electrons [196, 197]. This contrasts strikingly with equilibrium scenarios, in which lattice nonlinearities are subdominant and electron properties are well-described by linear electron-phonon interactions [198]. Compounds in which optically-excited phonons strongly affect the electrons' properties are, for instance, copper oxides [199] and organic materials [41]. These exhibit signatures of structural distortions due to nonlinearities [200, 201] and phonon resonances in the optical response [42, 202]. Pump-probe experiments provide direct access to the response functions defining the charge transport [41, 102], but accurate simulations of these phenomena are extremely challenging [45, 46, 203, 204].

Here, we apply phonon state tomography (PST) (see Section 3.3) and state-of-

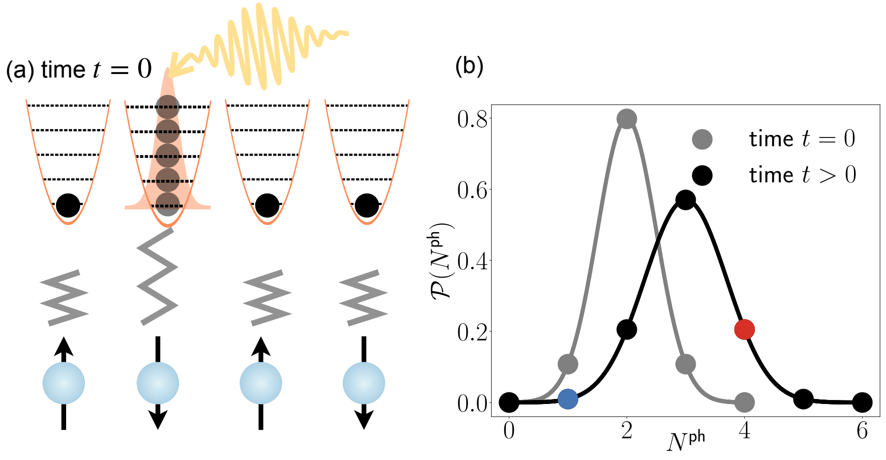

(a) time $t = 0$

(b)

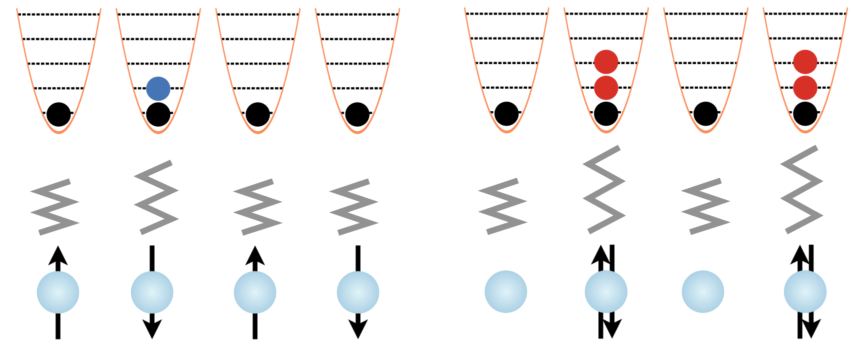

(c) time $t > 0$, $N^{\mathrm{ph}} = 1$

(d) time $t > 0$, $N^{\mathrm{ph}} = 4$

Figure 7.1: Sketch of phonon state tomography (PST) for a photo-excited metal. (a) The electrons (blue spheres) in a 1D metal couple locally to phonons (parabolas), which are excited by an optical pulse at $t = 0$. (b) The probability $\mathscr{P}(N^{\mathrm{ph}})$ to find a total of N^{ph} phonons in the system at initial and later times. (c) and (d) The tomographic decomposition of the wavefunction for one (blue dot) and four (red dots) phonon excitations, respectively.

the-art tensor network methods to obtain numerically-exact descriptions of 1D optically-excited metals in which the electrons are non-linearly coupled to phonons. In Section 7.1, we show that PST allows us to accurately reconstruct electronic observables, phonon occupations, and the global phonon probability distribution function. PST can also correctly simulate x-ray and electron diffuse scattering experiments, which measure phonon occupations. Moreover, PST enables us to reveal the impact of an optical pulse's strength and shape on the long-time electron dynamics. In Section 7.2, we report evidence of a light-induced charge-density wave (CDW) tendency at long simulation times, indicating an enhancement of long-range electron correlations. We focus on the crucial role of small phonon frequencies and the relation between global phonon probability distributions and disorder. Finally, we summarize our results in Section 7.3, pointing towards potential future applications of PST.

This chapter is based on Refs. [3, 5], written in collaboration with Matteo Mitrano, Ulrich Schollwöck, Sebastian Paeckel, and John Sous.

7.1 Pulse shapes, phonon probes and electron correlations

In Section 3.3, we introduced phonon state tomography (PST) as a theoretical tool for decomposing the electronic wavefunction into the contributions from all different phonon sectors

$$|\Psi\rangle = \sum_{\{\mathbf{n}^{\mathrm{ph}}\}} \varphi(\mathbf{n}^{\mathrm{ph}}) \, |\psi^{\mathrm{el}}(\mathbf{n}^{\mathrm{ph}})\rangle \otimes |\mathbf{n}^{\mathrm{ph}}\rangle \ . \tag{7.1}$$

This decomposition enables a precise reconstruction of electron correlation functions by sampling contributions associated with the statistically typical phononic configurations, which are inferred from the phononic 1RDM. PST also allows us to compute phonon occupations in momentum space and to estimate the complicated global phonon probability distribution function $\mathscr{P}(N^{\mathrm{ph}})$. This is not a mere theoretical exercise, as the occupation of individual phonon branches in momentum spaces can be directly measured. In diffuse x-ray [205, 206] and electron [207] scattering experiments, for instance, the scattering intensity I_{S} is proportional to the phonon occupation. Applying the first-order kinematical approximation [208] one obtains

$$I_{\mathrm{S}} \sim \sum_i \frac{1}{\omega_i(\mathbf{k})} \left(n_i^{\mathrm{ph}}(\mathbf{k}) + \frac{1}{2} \right) |F_i(\mathbf{k})|^2 . \tag{7.2}$$

Here $\omega_i(\mathbf{k})$, $n_i^{\mathrm{ph}}(\mathbf{k})$ and $F_i(\mathbf{k})$ are the frequency, the occupation of the i^{th} phonon branch at momentum $\mathbf{k}$ and the structure factor, respectively. If the Hamiltonian governing the electronic and phononic dynamics is known, PST enables simulating I_{S} and reconstructing the associated electronic correlations. This means that PST can be used as a diagnostic tool to relate the measured phonon response following various time delays to the dynamics of electronic correlation functions, as sketched in Fig. 7.1. PST can thus provide insights into the physics of materials probed in experiments such as multiple time-resolved infrared and Raman spectroscopy, x-ray and electron scattering, that access the frequency, damping, occupation number, and couplings (to electrons) of the optically excited phonons.

7.1.1 Model and main results

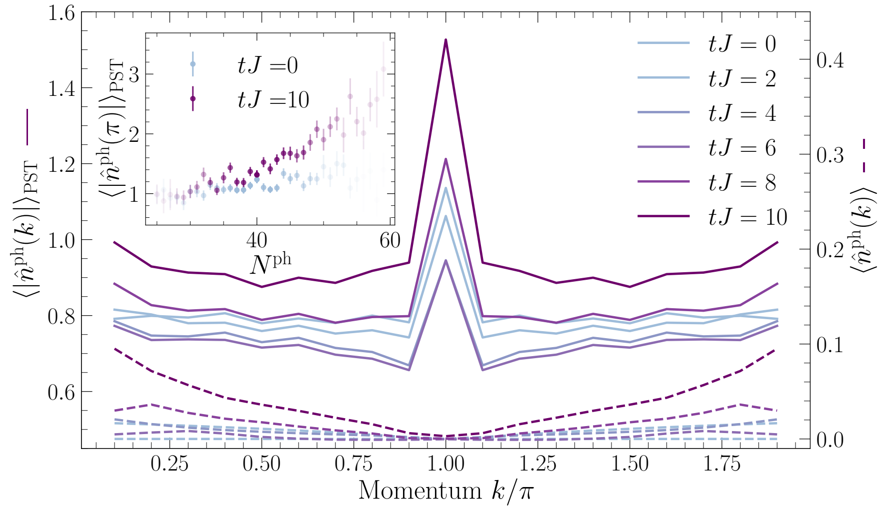

Figure 7.2: Momentum-dependent phonon occupation for different time delays. Using PST (left axis, solid lines), we first take the absolute value of every sample and then compute an ensemble average. This mimics x-ray diffuse scattering experiments, in which the phase of $n^{\text{ph}}(k)$ is inaccessible. Computing the conventional expectation value of $\hat{n}^{\text{ph}}(k)$ (right axis, dashed lines) yields completely different results (see the discussion in the main text). In the inset, we decompose $\langle|\hat{n}^{\text{ph}}(\pi)|\rangle_{\text{PST}}$ into the contributions from the phonon number sectors N^{ph}. The color intensity indicates the statistical incidence of a specific N^{ph}. We used 3000 samples for the PST calculations.

Modeling an optically pumped metal A minimal model describing metal whose phonons are coherently excited by a light pulse at initial time in 1D is [45, 198]

$$\begin{aligned}\hat{H} = \hat{H}_{\text{el}} + \hat{H}_{\text{ph}} + \hat{H}_{\text{el-ph}} &= -J \sum_{j=1}^{L} \sum_{\sigma=\uparrow,\downarrow} \left(\hat{c}^{\dagger}_{j,\sigma}\hat{c}_{j+1,\sigma} + \text{h.c.}\right) \\ &+ \omega \sum_{j=1}^{L} \left(\hat{a}_j^{\dagger}\hat{a}_j + \frac{1}{2}\right) + g \sum_{j=1}^{L} \left(\hat{n}_j - 1\right)\left(\hat{a}_j^{\dagger} + \hat{a}_j\right)^2 ,\end{aligned} \tag{7.3}$$

where the first term represents electrons hopping with amplitude J, the second Einstein phonons with frequency ω, and the third a local, quadratic electron-phonon interaction with coupling strength g. Here, $\hat{c}^{\dagger}_{\sigma}$ ($\hat{c}_{\sigma}$) and $\hat{a}^{\dagger}$ ($\hat{a}$) create (annihilate) an electron with spin σ and a phonon excitation, respectively and $\hat{n}_j = \hat{n}_{j,\uparrow} + \hat{n}_{j,\downarrow}$ counts the number of electrons. We consider a chain with L lattice sites. The reason we employ a coupling that is quadratic in the phonon displacement is that optically accessible phonons are dipole-active modes, and thus, selection rules do not allow for a linear coupling in the presence of inversion symmetry [196, 197, 209]. In the following calculations, we set J as the unit of energy and consider the small phonon frequency $\omega = \pi/10\,J$ as well as $g = 0.07\,J$. Note that for the nonlinear model Eq. (7.3), in order to preserve a positive oscillator stiffness [198], the allowed values of g need to be restricted to $g < |\omega/4|$. In equilibrium, the value of $g = 0.07\,J$ is so small that the ground state of Eq. (7.3) is well approximated by a tensor product between the Fermi sea at half filling for the electrons and a phononic vacuum

$$|\psi(t=0)\rangle = |\mathrm{FS}\rangle^{\mathrm{el}} \otimes |0\rangle^{\mathrm{ph}} = \prod_{k\in\left([0,\frac{\pi}{2}]\cup[\frac{3\pi}{2},2\pi]\right)} \hat{c}^{\dagger}_{k,\uparrow}\hat{c}^{\dagger}_{k,\downarrow}\,|0\rangle^{\mathrm{el}} \otimes |0\rangle^{\mathrm{ph}} \;. \tag{7.4}$$

Instead, we will show that out of equilibrium, this small coupling leads to a large correlation between electrons and phonons.

We globally quench the system by applying a homogeneous, coherent pump pulse

$$\hat{A}^{\mathrm{c}} \equiv \hat{\mathscr{D}}(\alpha) = \prod_j \hat{d}_j(\alpha) \equiv \prod_j e^{\alpha\hat{a}^{\dagger}_j - \alpha^*\hat{a}_j} \;, \tag{7.5}$$

which generates a coherent state on every phonon site j. The intensity of the optical pulse α, usually labeled *pump fluence*, determines the number of excited phonons $|\alpha|^2 = n_j^{\mathrm{ph}}$ on every site. We compute the dynamics induced by Eq. (7.5) using LSE-TDVP and the PP representation for the phononic degrees of freedom (see Section 3.1). Unless specified otherwise, we consider a system composed of $L = 20$ lattice sites, initially excite two phonons per site $\alpha = \sqrt{2}$, and allow for up to $\mathrm{d}^{\mathrm{ph}} = 40$ phonon excitation during the time evolution.

Sampling the phonon occupation in momentum space Time-resolved phonon probes like diffuse x-ray and electron scattering can determine the phonon occupation at momentum k by repeatedly measuring I_{S} (see Eq. (7.2)) and averaging the outcomes for a large number of samples. For every sample, these experiments resolve $\left|n^{\mathrm{ph}}(k)\right|$, as the associated phase is inaccessible. Thus, when simulating $\left|n^{\mathrm{ph}}(k)\right|$ by Fourier-transforming the phonon occupation in real space, the absolute value needs to be taken *before* sample-averaging. We do this by generating samples of phonon occupations in real space with PST and indicate the sample-averaged absolute value of the Fourier-transformed phonon occupation as $\langle|\hat{n}^{\mathrm{ph}}(k)|\rangle_{\mathrm{PST}}$. Fig. 7.2 shows $\langle|\hat{n}^{\mathrm{ph}}(k)|\rangle_{\mathrm{PST}}$ (left axis) and the expectation value of the phonon occupation in the exact electron-phonon wavefunction $\langle\hat{n}^{\mathrm{ph}}(k)\rangle$ (right axis). It can be seen that the latter yields completely different outcomes than the PST simulation of the experimental protocol. This is a significant result because it means that the access to the full electron-phonon wavefunction alone is not sufficient to compute the experimentally-measured $\langle|\hat{n}^{\mathrm{ph}}(k)|\rangle_{\mathrm{PST}}$. Instead, it is crucial to be able to generate phonon configurations by sampling $\mathscr{P}(N^{\mathrm{ph}})$, which is exactly what PST provides.

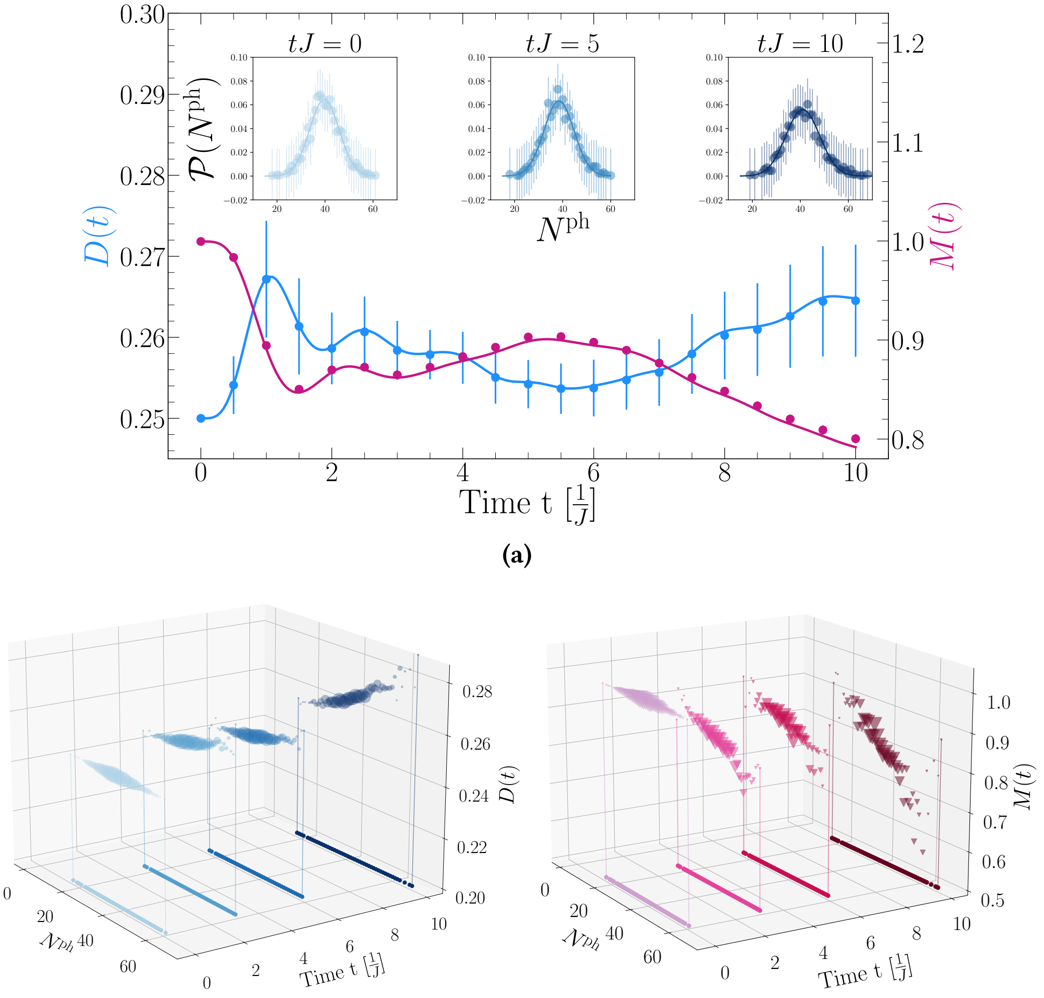

(a)

(b) **(c)**

Figure 7.3: Reconstructing time-dependent electronic correlations with PST. (a) The exact charge double occupancy $D(t)$ (left axis) and staggered magnetic correlation $M(t)$ (right axis), represented by solid lines, are compared to the PST-reconstructed observables indicated by symbols with error bars. The three insets show the sampled global phonon distribution function $\mathscr{P}(N^{\mathrm{ph}})$ at the initial, intermediate, and final time. (b) and (c) show the PST decomposition of $D(t)$ and $M(t)$, respectively, into the contributions from the total phonon number sectors N^{ph}. The size of the symbols indicates the fraction of all drawn samples found to have the corresponding value of N^{ph}. The small dots at the bottom of the two lower panels simply serve as a guide to the eye. We use 2000 samples, and the error bars correspond to the statistical error defined in Eq. (2.22).

In the inset of Fig. 7.2, the peak $\langle|\hat{n}^{\mathrm{ph}}(\pi)|\rangle_{\mathrm{PST}}$ is decomposed into contributions from sectors with total phonon number $N^{\mathrm{ph}} \equiv \sum_j n_j^{\mathrm{ph}}$ both at initial and late times. We find that at late times, the peak is enhanced in the large N^{ph} sectors.

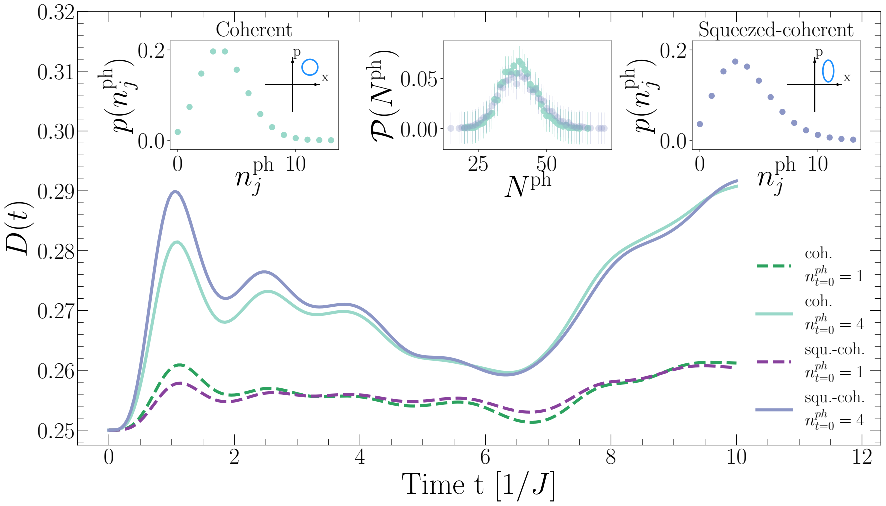

Figure 7.4: Impact of the local shape of the pulse on the electron dynamics. We compare the effect of a coherent pulse $\hat{A}^{\mathrm{c}}$ defined in Eq. (7.5) (green lines) with that of a squeezed-coherent pulse $\hat{A}^{\mathrm{sc}}$ introduced in Eq. (7.8) (purple lines). For both pulses, we consider an initial phonon occupation of 1 (dashed lines) and 4 (solid lines), corresponding to pump fluences $\alpha = 1$ and $\alpha = 2$, respectively. For the squeezed-coherent pulse, we set the squeezing parameter $z = +1/4 \ln 2$ for the dashed curve and $z = -1/4 \ln 2$ for the solid curve. In the left and right insets, we display the local phonon probability distribution function following a coherent and a squeezed-coherent excitation, respectively. The central inset shows the global phonon distribution function $\mathscr{P}(N^{\mathrm{ph}})$ for both pulses computed with PST. We set $L = 10$.

Tomographically reconstructed electronic observables Given the tomographic representation of the wavefunction Eq. (7.1), we reconstruct the electronic double occupancy

$$D(t) = \frac{1}{L} \sum_{j=0}^{L-1} \langle \Psi(t) | \, \hat{n}_{j,\uparrow} \hat{n}_{j,\downarrow} \, | \Psi(t) \rangle \ , \tag{7.6}$$

and the staggered magnetic correlation

$$M(t) = \frac{1}{L} \sum_{r=0}^{L-1} (-1)^r \langle \Psi(t) | \, \hat{s}_j^z \hat{s}_{j+r}^z \, | \Psi(t) \rangle \ , \tag{7.7}$$

where $\hat{s}_j^z = \hat{n}_{j,\uparrow} - \hat{n}_{j,\downarrow}$. The time evolution of these two observables is displayed in Fig. 7.3a. At late times, the electronic double occupancy slightly increases while the staggered magnetic correlation is suppressed. Note that the tomographically-reconstructed data (symbols with error bars) agrees very well with the exact results (solid lines), which indicates that PST can faithfully reconstruct electronic correlations. We see that as few as 1000 samples are enough to obtain converged electronic observables (see Section 7.1.2). This is remarkable given that the phononic Hilbert space is 40^L dimensional and hints towards the conclusion that only a few phonon configurations contribute considerably to the electrons' dynamics.

Most importantly, PST also allows us to decompose $D(t)$ and $M(t)$ into contributions from sectors with different total phonon numbers N^{ph} (see Section 3.3). We show these decompositions at different time instants in Fig. 7.3b and Fig. 7.3c. At time $t = 0$, electrons and phonons are uncorrelated, and thus, both displayed electron observables are independent of N^{ph}, as indicated by the flat lines at $t = 0$. Since electrons and phonons become entangled during the dynamics, the electronic observables become dependent on N^{ph} at $t > 0$. Remarkably, the electronic double occupancy correlates with N^{ph}, while the staggered magnetic correlation and N^{ph} anticorrelate. This is analogous to what we observed for $\langle|\hat{n}^{\mathrm{ph}}(\pi)|\rangle_{\mathrm{PST}}$ in the inset of Fig. 7.2. Moreover, the insets of Fig. 7.3a show a slight increase in the width of the global phonon distribution function $\mathscr{P}(N^{\mathrm{ph}})$, indicating that a larger number of phonon sectors becomes relevant for the late-time dynamics.

The role of the pulse intensities and shapes Fig. 7.3 shows that at late times, the electronic double occupancy is increased while the staggered magnetic correlation is suppressed in large phonon number sectors N^{ph}. The conjunction of this effect with a widening of the global phonon distribution function $\mathscr{P}(N^{\mathrm{ph}})$ suggests that by using tailored optical pulses, it might be possible to enhance/suppress specific electronic correlations.

We investigate this by studying the squeezed-coherent pulse

$$\hat{A}^{\mathrm{sc}} = \prod_j \hat{d}_j(\alpha) \mathrm{e}^{\frac{1}{2}\left(z^* \hat{a}_j^2 - z \hat{a}_j^{\dagger 2}\right)} \,. \tag{7.8}$$

This generates squeezed-coherent phonon states, where the squeezing parameter z controls $\Delta x / \Delta p$, i.e., the ratio between the standard deviation of the position and momentum operators. Thus, z allows tuning the width of the onsite local phonon distribution created by the pump, as indicated in the left and right insets of Fig. 7.4.

We analyze the post-pump dynamics generated by the application of a coherent pulse $\hat{A}^{\mathrm{c}}$ with that obtained following the application of a squeezed-coherent pulse $\hat{A}^{\mathrm{sc}}$ in Fig. 7.4. We consider the pump fluences $\alpha = 1, 2$ for each pulse, corresponding to $n^{\mathrm{ph}} = 1, 4$ excited phonons on each site. Notably, the electron dynamics induced by the two different pulse shapes are nearly identical. Computing $\mathscr{P}(N^{\mathrm{ph}})$ with PST for the two pulses (middle inset of Fig. 7.4), we find that the two different local phonon distributions induce the same (within the error bars) global phonon distribution. This seems to imply that the local phonon distribution does not affect the electronic dynamics, while tuning the global phonon distribution $\mathscr{P}(N^{\mathrm{ph}})$ may allow for better control.

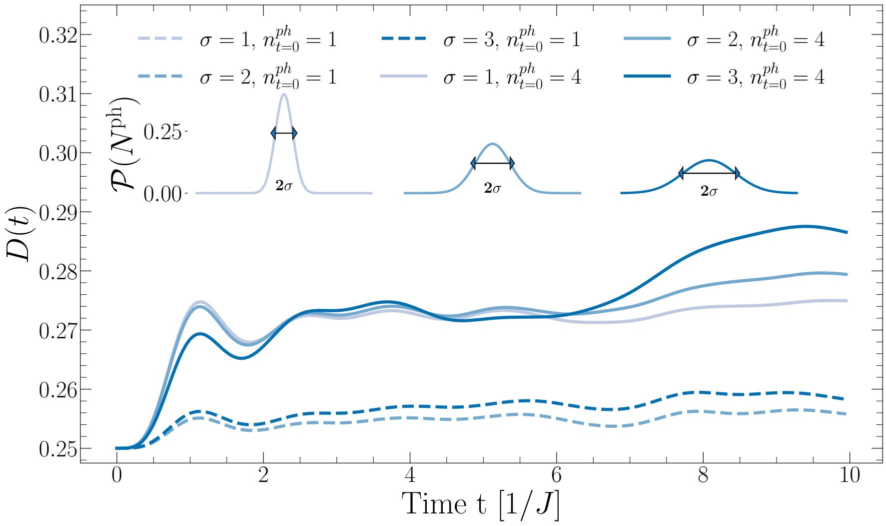

Figure 7.5: Impact of the global shape of the pulse on the electron dynamics. We consider the simple β-pulse $\hat{A}^\beta$ (see Eq. (7.10)), where the single parameter β tunes the width σ of the global phonon distribution function $\mathscr{P}(N^{\rm ph})$. It can be seen that increasing σ systematically enhances the double occupancy at late times. We set $L = 10$.

The complexity of the coherent and squeezed-coherent states considered above implies that we have to resort to PST to numerically compute the associated global phonon distribution function $\mathscr{P}(N^{\rm ph})$ for a many-body state. Here, we seek to find a state simple enough to allow an exact analytic treatment. Thus, we make the following homogeneous ansatz

$$|\psi\rangle = \bigotimes_{j=0}^{L-1} \left(\frac{\alpha\,|n\rangle_j + \beta\,|n+1\rangle_j + \beta\,|n-1\rangle_j}{\sqrt{\alpha^2+\beta^2}} \right) , \tag{7.9}$$

where $|n\rangle_j$ is the n-th phononic Fock state of the j-th phononic site, while α and β are real constants satisfying $\alpha^2 + 2\beta^2 = 1$. This state is generated by acting on the phononic vacuum with

$$\hat{A}^\beta = \prod_{j=0}^{L-1} \left[\hat{a}_j^\dagger\right]^{n^{\rm ph}} \left(\frac{\alpha}{\sqrt{n^{\rm ph}!}} + \frac{\beta \hat{a}_j^\dagger}{\sqrt{n^{\rm ph}+1!}} + \frac{\beta \hat{a}_j}{\sqrt{n^{\rm ph}-1!}} \right) . \tag{7.10}$$

The simplicity of Eq. (7.9) lies in the fact that, since normalization implies $\alpha = \pm\sqrt{1-2\beta^2}$, the single parameter β controls the global phonon probability distribution $\mathscr{P}(N^{\rm ph})$. Thus, we label Eq. (7.10) *β-pulse*. The state Eq. (7.9), has contributions from the phonon sectors $N^{\rm ph}_m = Ln + m$, with $m = -L, -L+1, \dots, +L-1, +L$ and its associated $\mathscr{P}(N^{\rm ph}_m)$ can be determined as follows. We start by introducing an index i that labels all non-permutationally equivalent states corresponding to the same $N^{\rm ph}_m$. For example, for $L = 2$ sites and $m = 0$, we have $|L = 2, m = 0, i = 0\rangle \equiv \{|n, n\rangle\}$ and $|L = 2, m = 0, i = 1\rangle \equiv \{|n+1, n-1\rangle, |n-1, n+1\rangle\}$. A simple algebraic calculation shows that all permutationally-equivalent states have the same probability amplitude $\alpha^{L-m-2i}\beta^{m+2i}$. The square of this probability amplitude, giving the i-th contribution to $\mathscr{P}(N_m^{\mathrm{ph}})$, has to be multiplied by $L!/(L-m-2i)!(m+1)!i!$, which accounts for the multiplicity associated to each i. Note also that the sum over the non-permutationally-equivalent contributions for a sector fixed by m runs from 0 to $L - m - 2i \geq 0$. Combining these elements, we obtain

$$\mathscr{P}(N_m^{\mathrm{ph}}) = \sum_{i=0}^{L-m-2i\geq 0} \frac{\left(\alpha^{L-m-2i}\beta^{m+2i}\right)^2 L!}{(L-m-2i)!(m+2i)!}\,, \tag{7.11}$$

which is the exact probability of finding N_m^{ph} phonons in the state Eq. (7.9). The standard deviation $\sigma(\beta)$ of $\mathscr{P}(N_m^{\mathrm{ph}})$ for a given β can be extrapolated with a Gaussian fit.

In Fig. 7.5, we show the electron dynamics following the application of β-pulses $\hat{A}^{\beta}$ corresponding to induced global phonon distributions with different widths $\sigma(\beta)$. We observe that increasing σ (while keeping the number of excited phonons fixed) systematically enhances the light-induced electron double occupancy. Together with Fig. 7.3, this gives us a first hint of how PST can be employed to analyze and design different pulse shapes tailored to enhance or suppress specific electronic correlations, potentially aiding the experimental control of light-matter interactions.

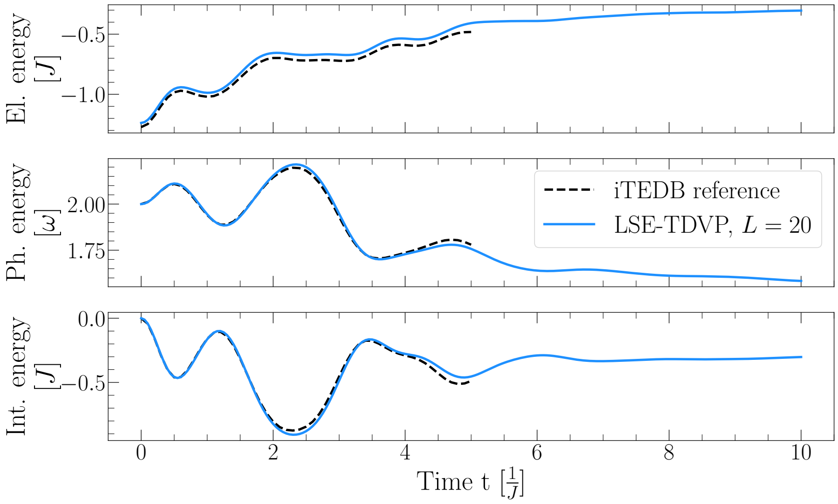

Figure 7.6: Comparing the photo-excited dynamics to infinite time-evolving block decimation (iTEBD) reference data from Ref. [198]. We compute the electron (upper panel), phonon (middle panel), and interaction (lower panel) energies using LSE-TDVP for $g = 0.25\,J$, $\omega = \pi/2\,J$, and $\alpha = \sqrt{2}$. We consider a system with $L = 20$ sites, allowing for a maximum of $d = 12$ phonons on each site (to match [198]), and employ a time step of $dt = 0.05\,1/J$ and a bond dimension of $m = 2000$. Overall, we observed an excellent agreement and can double the simulation time.

7.1.2 Numerical analysis

Here, we discuss the accuracy of the PST and the time evolution algorithms used to produce the results presented in Section 7.1.1. We once again use LSE-TDVP [36, 37] to compute the time evolution and PP [35] to represent bosonic sites with large local dimensions efficiently. Since at $t = 0$ the electronic and the phononic systems are uncorrelated, we utilize GSE-TDVP for the first four timesteps in order to avoid the potentially large projection error of LSE-TDVP (see Chapter 3).

We first test our implementation by reproducing the results presented in Fig. (1) of Ref. [198]. We compute the time evolution of the electron, phonon, and interaction energy with Eq. (7.3) and consider the same parameters as in Ref. [198], i.e. $\omega = \pi/2\,J$ and $g = 0.25\,J$. Fig. 7.6 shows that our LSE-TDVP results for a system with $L = 20$ sites agree very well with the iTEBD calculations from [198]. The small deviations in the electron energy at initial times (upper panel) are due to the fact that we consider open boundary conditions (OBC) while periodic boundary conditions (PBC) were used in [198]. Note also that we could double the simulation time compared to the reference data.

Compared to Ref. [198], LSE-TDVP combined with PP allows us to consider larger pump fluences and larger g/ω ratios (i.e. greater phonon occupations). The upper panel of Fig. 7.7, shows the electron double occupancy $D(t)$ for $\omega =$

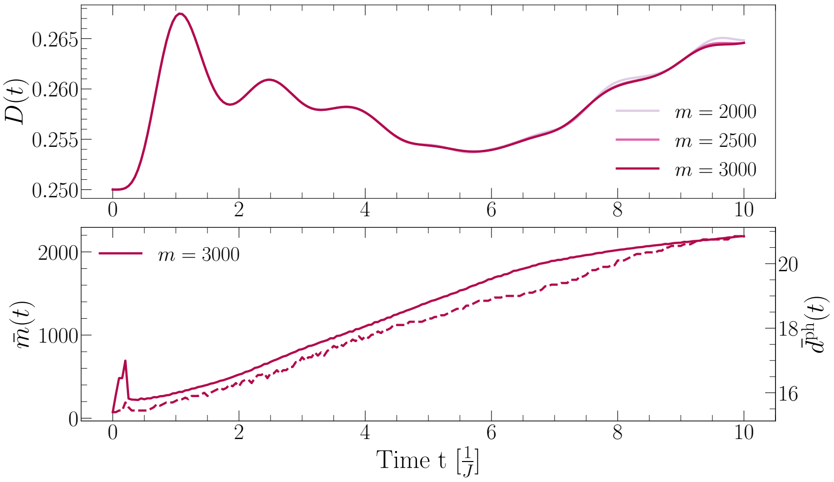

Figure 7.7: Numerical accuracy of the time evolution. Upper panel: The electronic double occupation $D(t)$, with the same parameters as in Fig. 7.3. Increasing the maximally allowed bond dimension from $m = 2000$ to $m = 3000$ does not significantly alter the results. Lower panel: evolution of the average bond dimension $\bar{m}$ (on the left axis, indicated by solid lines) and the average phonon physical dimension $\bar{d}^{\text{ph}}$ (on the right axis, represented by dashed lines). The small spikes in $\bar{m}$ are typical for the GSE-TDVP method [36] and are present only for the first four timesteps, i.e., up to the point when we switch to LSE-TDVP.

$\pi/10\,J$ and $g = 0.07$ (as in Fig. 7.3), and we vary the bond dimension from $m = 2000$ to $m = 3000$. Increasing m has a very small impact on $D(t)$, indicating that the calculations are well-converged. In the lower panel of Fig. 7.7, we plot the evolution of the site-averaged bond dimension (left axis) and physical dimension (right axis).

Next, we study the convergence of PST with respect to the number of generated samples by considering the same parameters as in Fig. 7.7. As in Section 7.1.1, we compute the electron double occupation $D(t)$ (Eq. (7.6)) and the staggered magnetic correlation $M(t)$ (Eq. (7.7)), finding that as few as 1000 samples yield well-converged results. The lower panel displays the global phonon distribution function $\mathscr{P}(\mathbf{n}^{\text{ph}})$ computed with 3000 samples. The noisy result shows that phonon observables converge slower than electron observables in the PST approach.

We construct the squeezed-coherent states $|z,\alpha\rangle_j \equiv \hat{D}_j(\alpha)\hat{S}_j(z)\,|\text{vac}\rangle$ used in Fig. 7.4 by Taylor-expandig the squeezing and the displacement operator

$$\begin{aligned} \hat{S}^{(M)}_{\text{taylor}}(z) &\equiv \sum_{m=0}^{M} \frac{1}{m!}\left(\frac{1}{2}\left(z^*\hat{a}^2 - z\hat{a}^{\dagger 2}\right)\right)^m \\ \hat{D}^{(M)}_{\text{taylor}}(\alpha) &\equiv \sum_{m=0}^{M} \frac{1}{m!}\left(\alpha\hat{a}^\dagger - \alpha^*\hat{a}\right)^m \ , \end{aligned} \tag{7.12}$$

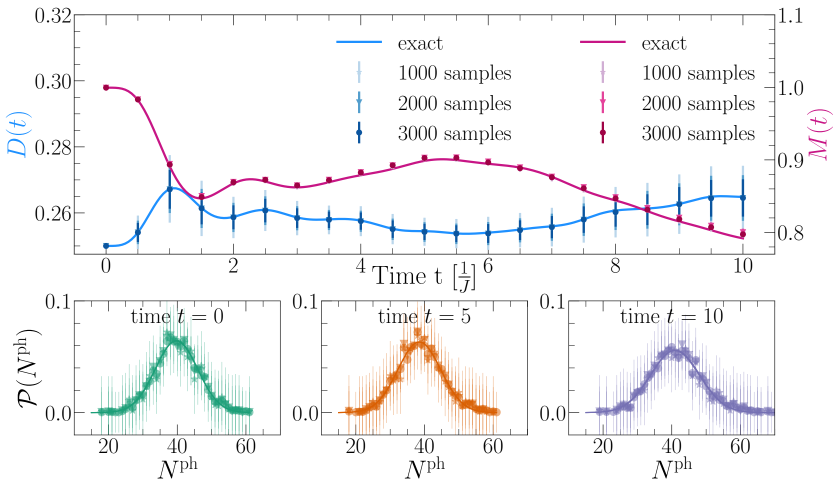

Figure 7.8: Convergence of electronic observables obtained with PST with the number of computed samples. Upper panel: Electronic double occupation $D(t)$ (left axis, pink points) and the staggered magnetic correlation $M(t)$ (right axis, blue points). A comparison with the exact observables (represented by solid lines) illustrates that as few as $|\Omega| = 1000$ samples yield converged results. Lower panel: PST-sampled global phonon probability distribution $\mathscr{P}(N^{\mathrm{ph}})$ at different time delays $t = 0,\ 5,\ 10$ for 3000 trajectories. It can be seen that the convergence of $\mathscr{P}(N^{\mathrm{ph}})$ w.r.t. the number of samples is significantly worse than that of electronic observables.

where M indicates the order of the Taylor expansion. In Eq. (7.12), we omitted the site index j since the operators are identical on every site. We assess the convergence of the state of order M, $|\tilde{\Phi}^{(M)}\rangle \equiv \hat{D}^{(M)}_{\mathrm{taylor}}(\alpha)\hat{S}^{(M)}_{\mathrm{taylor}}(z)\,|\mathrm{vac}\rangle$, by computing its overlap with $|\tilde{\Phi}^{(M+1)}\rangle \equiv \hat{D}^{(M+1)}_{\mathrm{taylor}}(\alpha)\hat{S}^{(M+1)}_{\mathrm{taylor}}(z)\,|\mathrm{vac}\rangle$. As shown in Fig. 7.9, for both $z = \pm 1/4 \log 2$ (corresponding to $\Delta x/\Delta p = 1/2, 2$, respectively), the error steadily decreases with M increases and becomes zero at $M = 19$. Additionally, at $M = 19$, the local phonon dimension (right axis) stabilizes at $d^{\mathrm{ph}} = 47$.

As an additional validation, we compute the convergence in M of the local phonon probability distribution $p\left(n^{\mathrm{ph}}\right)$ for the two squeezed-coherent states considered in Fig. 7.9. In Fig. 7.10, it can be observed that when 4 phonons per site are excited, $p\left(n^{\mathrm{ph}}\right)$ exhibits a smooth behavior and converges well with increasing Taylor order M. On the other hand, for $\bar{n}^{\mathrm{ph}} = 1$ (lower panel), we notice that $p\left(n^{\mathrm{ph}}\right)$ decays more rapidly and displays a spiked pattern. These artifacts are likely due to numerical instabilities, indicating that in this instance, $p\left(n^{\mathrm{ph}}\right)$ is accurate only up to approximately 10^{-6}.

We conclude this section by considering the global phonon distribution function $\mathscr{P}(N^{\mathrm{ph}})$ for the $\beta-$pulse Eq. (7.10). In particular, we aim to inspect which values of β (which can, in principle, vary between 0 and $\sqrt{1/2}$) yield a Gaussian $\mathscr{P}(N^{\mathrm{ph}})$ when the system size L is moderate. In Fig. 7.11 we compute $\mathscr{P}(N^{\mathrm{ph}})$

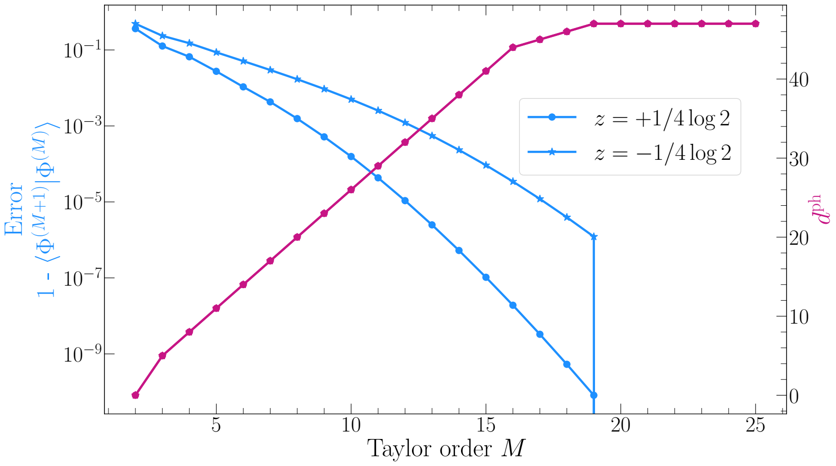

Figure 7.9: Convergence of the Taylor-expanded squeezed-coherent state. Left axis: Error $\epsilon \equiv 1 - \langle \tilde{\Phi}^{(M+1)} | \tilde{\Phi}^{(M)} \rangle$ as a function of the Taylor order M for squeezing $z = +1/4 \log 2$ (corresponding to $\bar{n}^{\text{ph}} = 1$) and $z = -1/4 \log 2$ (corresponding to $\bar{n}^{\text{ph}} = 4$). Right axis: The local phonon dimension d^{ph} as a function of M.

using Eq. (7.11) for different system sizes $L = 10,\ 40$ and different β (note that we have omitted the m index). We see that for $L = 10$ (Fig. 7.11a), the global phonon distribution $\mathscr{P}(N^{\text{ph}})$ shows some deviations from the Gaussian fits when either a very small or a very large β is considered. This implies that for this system size, β should be restricted to approximately the range of $[0.25, 0.66]$. Instead, for $L = 40$ both narrow and wide β-pulse-generated $\mathscr{P}(N^{\text{ph}})$ agree very well with the Gaussian fits.

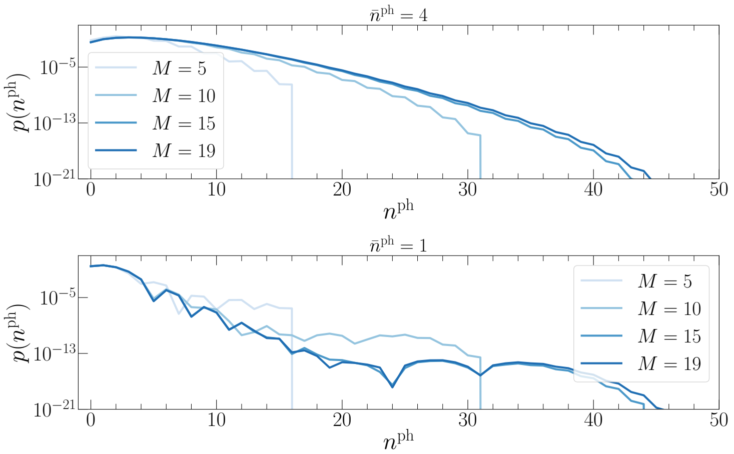

Figure 7.10: Convergence of the local phonon probability distribution $p\left(n^{\mathrm{ph}}\right)$ for the Taylor-expanded squeezed-coherent state (see Eq. (7.12)). Upper panel: $p\left(n^{\mathrm{ph}}\right)$ for $\bar{n}^{\mathrm{ph}} = 4$ excited phonons per site as a function of the Taylor order M. Lower panel: $p\left(n^{\mathrm{ph}}\right)$ for the case with $\bar{n}^{\mathrm{ph}} = 1$ phonon per site, also as a function of the Taylor order M.

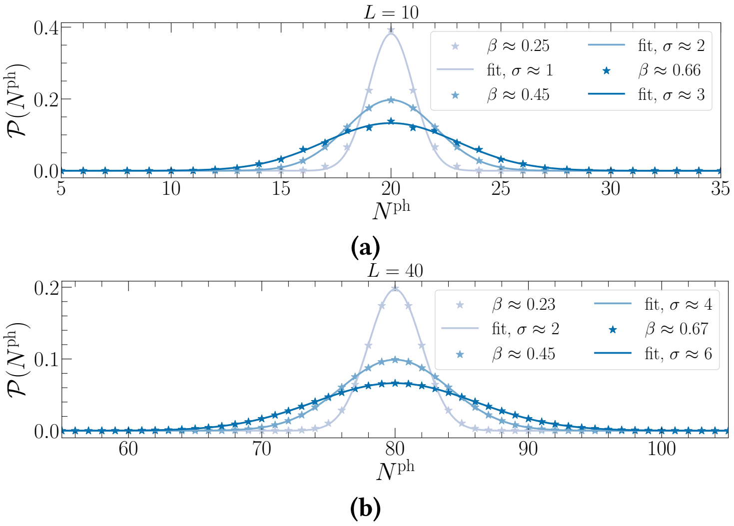

Figure 7.11: Global phonon distribution function $\mathscr{P}(N^{\mathrm{ph}})$ induced by the β–pulse Eq. (7.10), which allows to tune the width σ of $\mathscr{P}(N^{\mathrm{ph}})$ via the parameter β. We obtained the data points by evaluating Eq. (7.11) for $L = 10$ sites (upper panel) and $L = 40$ sites (lower panels). The solid lines represent Gaussian fits.

7.2 Photo-induced enhancement of long-range electron correlation

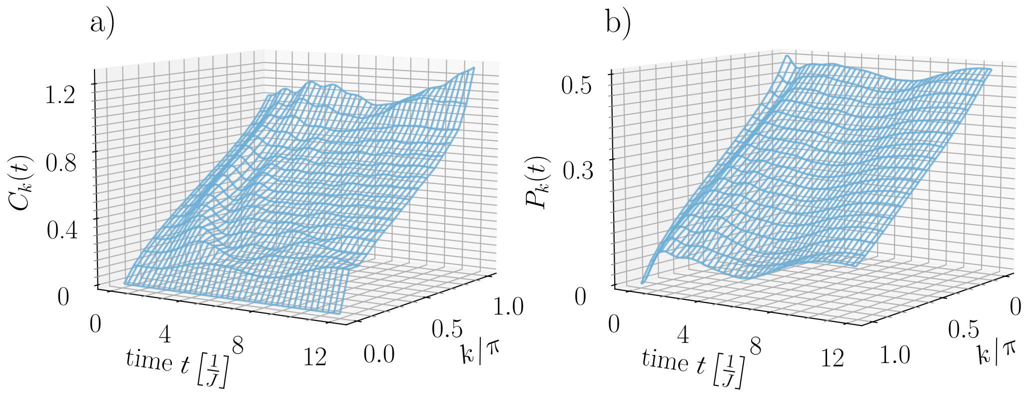

Figure 7.12: Dynamics of momentum-dependent charge and pairing correlations at small phonon frequency. a) The charge correlation $C_k(t)$ Eq. (7.13) at momentum $k = \pi$ increases by $\sim$ 20% in the scope of the time evolution. b) The pairing correlation $P_k(t)$ Eq. (7.14) at momentum $k = \pi$ does not vary significantly, while at $k = \pi$ it grows from zero to $\sim$ 0.1. We consider the small phonon frequency $\omega = \pi/10\,J$, the electron-phonon interaction strength $g = 0.07\,J$ and utilize the system size $L = 32$, the maximal bond dimension $m = 2000$ and the maximal physical local dimension for the phonons $d = 40$.

In the last section, we used PST to study the effect of different optical pulses on the electron's dynamics in a metal following a photoexcitation. We found that the phonons excited by the optical pulse can have the opposite effect on different electronic observables. Moreover, we discovered that broad pulses (of the same intensity) enhance the electron double occupancy at late times. Here, we ask a different question: What role does the *phonon frequency* play in the non-equilibrium electronic properties following an optical pulse? To address this question and directly connect to Ref. [198], we will study momentum-resolved electronic correlation functions.

We repeat the same protocol as in Section 7.1.1, i.e., we initialize the electron system in a Fermi sea (Eq. (7.4)) and the phonon system in a homogeneous coherent state (see Eq. (7.5)) with an average of two phonon excitations per site. Then, we time evolve the system with the Hamiltonian introduced in Eq. (7.3). First, we consider the same parameters as in Section 7.1.1, i.e. $\omega = \pi/10J$ and $g = 0.07J$ and compute the time-dependent momentum-resolved charge $C_k(t)$ and pairing $P_k(t)$ correlations. These are obtained by Fourier-transforming the real space correlations

$$C_r(t) \equiv \langle\Psi(t)|\, \hat{n}_j \hat{n}_{j+r}\, |\Psi(t)\rangle - \langle\Psi(t)|\, \hat{n}_j\, |\Psi(t)\rangle \langle\Psi(t)|\, \hat{n}_{j+r}\, |\Psi(t)\rangle \ , \tag{7.13}$$

and

$$P_r(t) \equiv \langle\Psi(t)|\, \hat{c}^\dagger_{j,\uparrow}\hat{c}^\dagger_{j,\downarrow}\hat{c}_{j+r,\downarrow}\hat{c}_{j+r,\uparrow}\, |\Psi(t)\rangle \ , \tag{7.14}$$

respectively. In Fig. 7.12 we display $C_k(t)$ and $P_k(t)$ for a system of $L = 32$ sites up to a time $tJ = 12$. At every timestep, $C_k(t)$ increases monotonically with k. Moreover, at late times $C_\pi(t)$ is enhanced. In fact, $C_\pi(t)$ increases by about 20% in the scope of the time evolution. Remarkably, this indicates a light-induced enhancement of the spatial modulation of the charge density, i.e. the tendency towards the formation of an out-of-equilibrium charge density wave with a period of two lattice sites. Let us now examine the pairing correlation $P_k(t)$ (note that the k-axis is inverted w.r.t. panel a). Pairing at zero momentum $P_0(t)$ does not vary significantly over time, indicating no enhancement of Cooper pairs uniformly distributed in real space. Instead, $P_\pi(t)$ grows from 0 to ≈ 0.1, indicating a (weak) signal of spatial modulation in electron pairs. This modest change in the pairing behavior is no surprise in a 1D model at half filling where the electron-electron attraction is only indirect, i.e. phonon-mediated.

Note that a more direct way of investigating the formation of quasi-long-range order in a 1D quantum system is to study the decay of correlations such as $C_r(t)$ and $P_r(t)$ in real space. In this context, the onset of quasi-long-range order is signaled by the transition from exponentially-to-algebraically decaying correlations [210]. Due to the presence of highly-excited (and thus high-dimensional) phonon modes and the fact that we are considering non-equilibrium setups in which entanglement area laws are generally violated [80], we are limited to moderate system sizes (at most $L = 32$). In such cases, distinguishing between an exponential and an algebraic decay in real space is challenging. For this reason, we resort to studying momentum-resolved correlation functions. Specifically, the significant enhancement of C_π at long times, accompanied by essentially no change in C_k at other momenta, serves as a strong indicator of a periodic modulation of the charge density in real space and an enhancement of long-range correlations.

As mentioned in Section 7.1, the model considered here had previously been studied at large phonon frequencies $\omega = \pi/2J$ for an electron-phonon coupling of $g = 0.25$ with iTEBD for short timescales in [198]. The authors reported a flattening tendency of correlations in momentum space, which indicates a loss of spatial coherence. This was attributed to the interaction with the phonons and labeled phonon-induced disorder.

To connect to these results, we increase the phonon frequency from $\omega = \pi/10J$ to $\omega = \pi/5J$ and $\omega = \pi/2J$, while keeping the ratio g/ω constant, resulting in $g = 0.14J, 0.35J$, respectively. We display $C_k(t)$ for increasing frequency from left to right in the upper row of Fig. 7.13. Considering stronger couplings g and longer timescales than [198] we confirm a substantial flattening of the charge correlations in momentum space for the large phonon frequency (left panel). For the intermediate phonon frequency (central panel), the flattening of $C_k(t)$ is sup-

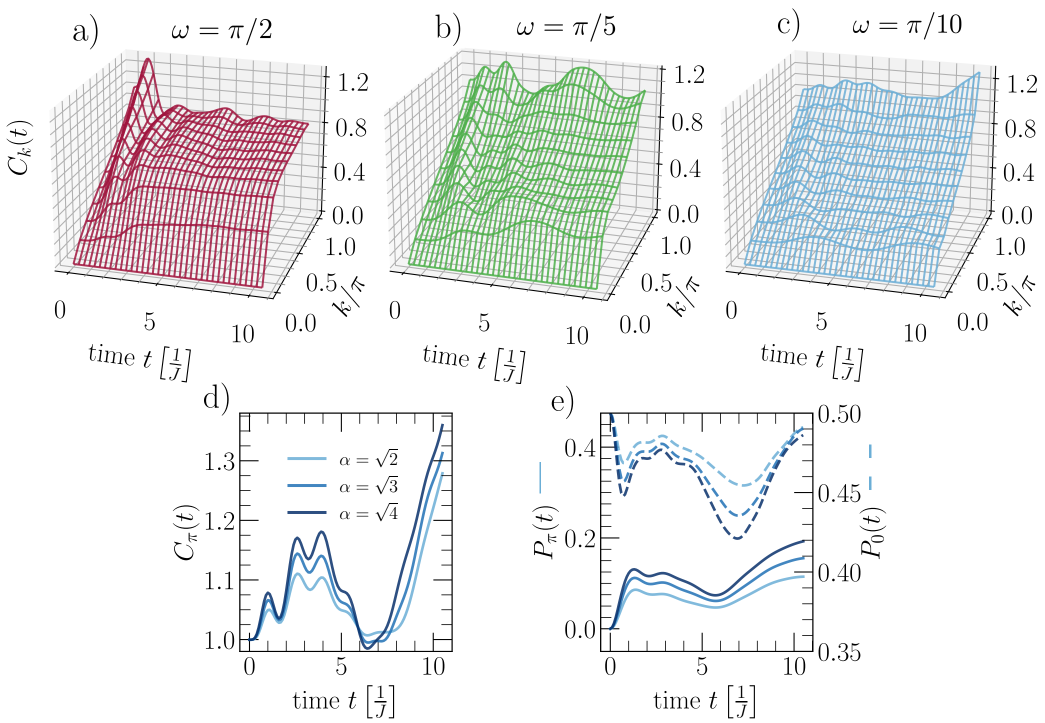

Figure 7.13: Impact of the phonon frequency and the pump fluence on the electron correlations. Upper row: In panels a), b), and c), we show the momentum-dependent charge correlation $C_k(t)$ (Eq. (7.6)) for the phonon frequencies $\omega = \pi/2J$, $\omega = \pi/5J$, and $\omega = \pi/10J$, respectively. We kept the ratio g/ω fixed utilizing $g/J = 0.35, 0.14, 0.07$, from left to right. At large phonon frequency (panel a), $C_k(t)$ flattens out in momentum space at late times, while at small phonon frequency (panel c), it increases monotonically with k and C_π is enhanced at late times. Lower row: charge correlation (panel d) and pairing correlation (panel e) at small phonon frequency for different pump fluences α. Increasing α only slightly enhances C_π and P_π. We consider the system size $L = 20$, the maximal bond dimension $m = 2000$, and the maximal physical local dimension for the phonons $d = 40$.

pressed, and strong oscillations are present. Finally, for the smallest phonon frequency (as we previously shown in Fig. 7.12), the flattening is absent and $C_\pi(t)$ increases significantly at late times. These results show that when decreasing ω the phonon-induced disorder is progressively suppressed in favor of an enhancement of long-range electron correlation, indicating a CDW tendency. In the lower row, we investigate the impact of the pump fluence α on the charge and pairing correlation for the smallest phonon frequency $\omega = \pi/10J$. Specifically, we consider $\alpha = \sqrt{2}, \sqrt{3}, \sqrt{4}$, corresponding to the excitation of $2, 3, 4$ phonons at initial time, respectively. Panel d) shows that $C_\pi(t)$ is slightly increased for larger pump fluences. At the same time, panel e) shows that $P_\pi(t)$ is slightly suppressed (left axis) while $P_0(t)$ is moderately increased (right axis). Overall, the impact of the pump fluence is moderate, and the phonon frequency seems to play a more relevant role.

The complicated dynamics induced by Eq. (7.3) can be approximately described by an effective model introduced by Kennes et al. [45] and further analyzed by Sous et al. [198]. This approach involves rotating the Hamiltonian into the squeezed phonon basis, in which the dynamics of electrons and phonons approximately decouple. This is achieved by transforming $\hat{H} \rightarrow \hat{H}' = \hat{U}\hat{H}\hat{U}^\dagger$, where $\hat{U} = e^{\hat{S}}$ with $\hat{S} = -\sum_j \frac{1}{2}\hat{\zeta}_j(\hat{a}_j^\dagger \hat{a}_j^\dagger - \hat{a}_j\hat{a}_j)$ where the squeezing parameter is $\hat{\zeta}_j = -\frac{1}{4}\ln\Big(1 + 4\frac{g}{\omega}(\hat{n}_j - 1)\Big)$. Unfortunately, $\hat{H}'$ cannot be computed exactly. However, when g/ω is small, one can Taylor-expand $\hat{U}$ and approximate $\hat{H}' \approx \hat{H}_{\text{eff}} + \mathcal{O}((g/\omega)^2)$, where a lenghty calculation shows that

$$\begin{aligned}
\hat{H}_{\text{eff}} = & - J_{\text{eff}} \sum_{j=1}^{L} \sum_{\sigma=\uparrow,\downarrow} \left(\hat{c}_{j,\sigma}^\dagger \hat{c}_{j+1,\sigma} + \text{h.c.}\right) \\
& + U_{\text{eff}} \sum_{j=1}^{L} \left(\hat{n}_{j,\uparrow} - \frac{1}{2}\right)\left(\hat{n}_{j,\downarrow} - \frac{1}{2}\right)\left(\hat{\beta}_j^\dagger \hat{\beta}_j + \frac{1}{2}\right) \\
& + \epsilon_{\text{eff}} \sum_{j=1}^{L} (\hat{n}_j - 1)\left(\hat{\beta}_j^\dagger \hat{\beta}_j + \frac{1}{2}\right) + \omega_{\text{eff}} \sum_{j=1}^{L} \left(\hat{\beta}_j^\dagger \hat{\beta}_j + \frac{1}{2}\right) .
\end{aligned} \tag{7.15}$$

Here, the first term indicates electron hopping with a renormalized amplitude $J_{\text{eff}} = Je^{-\frac{1}{2}(\frac{g}{\omega})^2(\alpha^4+2\alpha^2+1)}$, the second term represents an onsite electron attraction with $U_{\text{eff}} = -4g^2/2\omega$, the third expression describes an onsite electron potential with $\epsilon_{\text{eff}} = 2g$ and finally in the last term the phonon frequency has been modified to $\omega_{\text{eff}} = \omega - g^2/\omega$. One of the crucial features of Eq. (7.15) is that the electronic and phononic degrees of freedom decouple: the terms $\hat{\beta}_j^\dagger \hat{\beta}_j$ in the second and third line simply count the number of squeezed phonon excitations on site j, which do not change in time. The squeezed phonon operators are related to original operators as $\hat{\beta}_j^\dagger \equiv e^{\hat{S}}\hat{a}_j^\dagger e^{-\hat{S}} = \cosh\big(\hat{\zeta}_j\big)\hat{a}_j^\dagger + \sinh\big(\hat{\zeta}_j\big)\hat{a}_j$ and $\hat{\beta}_j \equiv e^{\hat{S}}\hat{a}_j e^{-\hat{S}} = \cosh\big(\hat{\zeta}_j\big)\hat{a}_j + \sinh\big(\hat{\zeta}_j\big)\hat{a}_j^\dagger$. Since for the small $g/\omega \approx 0.22$ that we consider the squeezing parameter $\hat{\zeta}_j$ is very small, we have that $\hat{\beta}_j^{(\dagger)} \approx \hat{a}_j^{(\dagger)}$. Thus, we simplify Eq. (7.15), substituting the squeezed operators with the original ones.

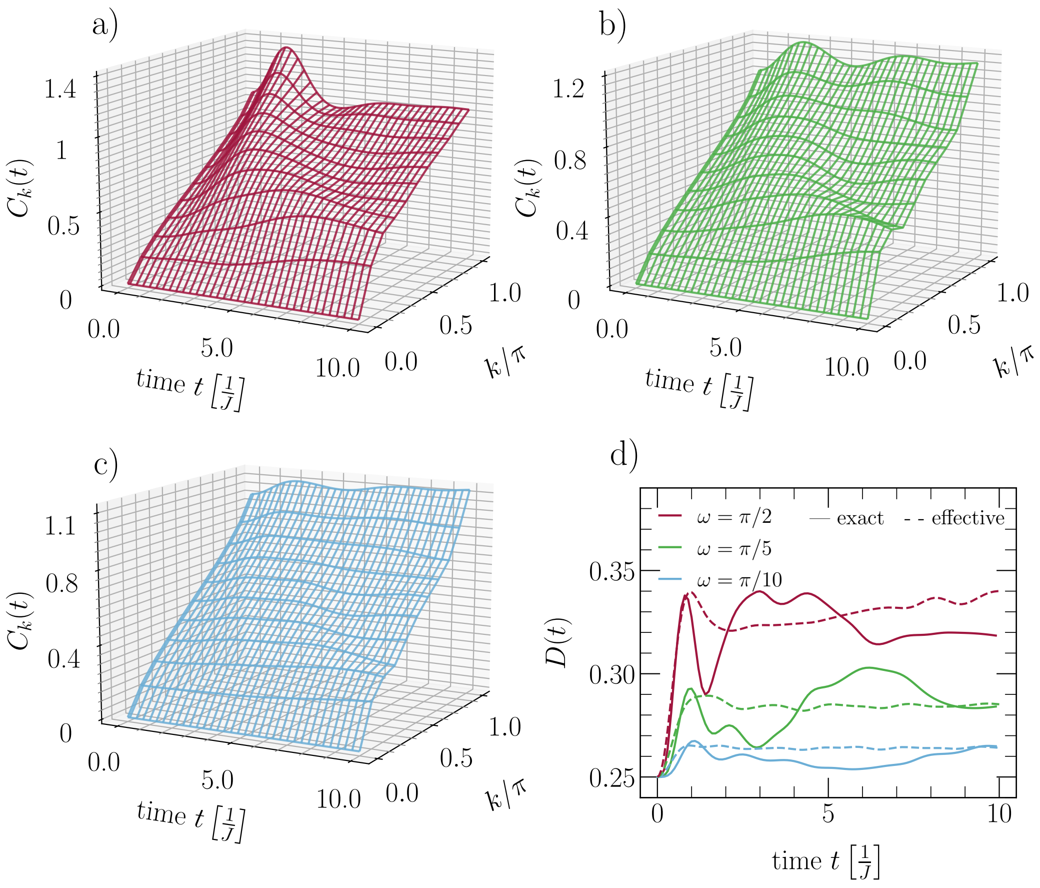

Figure 7.14: Comparing exact and effective results. In panels a), b), and c), we show the momentum-dependent charge correlation $C_k(t)$ for the same parameters as in Fig. 7.13, obtained using the effective model Eq. (7.15). While there is no precise quantitative agreement with the exact results (see Fig. 7.13), the effective model qualitatively captures the tendency of $C_k(t)$ to flatten at high phonon frequency. For the double occupancy $D(t)$, defined in Eq. (7.6), the effective results agree reasonably well with the exact ones, indicating that the effective model captures onsite observables better than long-range correlations. We consider the system size $L = 20$, the maximal bond dimension $m = 2000$, and the maximal physical local dimension for the phonons $d = 40$.

To investigate the accuracy of the effective model, we again consider a system with two phononic excitations per site at initial time and time-evolve the Fermi sea state Eq. (7.4). The results for the charge correlation function $C_k(t)$ for the same parameters as in Fig. 7.13 are shown in Fig. 7.14. It can be seen that overall the effective model captures the qualitative behavior that we found in Fig. 7.13. In particular, $C_k(t)$ tends to flatten for the largest phonon frequency (panel a) oscillates at the intermediate phonon frequency (panel b) and monotonically increases with k for the smallest phonon frequency (panel c). However, these features are somewhat underestimated compared to the exact results. Specifically, the flattening is only partial in panel (a), the oscillations are underestimated in panel b), and the enhancement of C_π at long times is small in panel c). We also compute the site-averaged double occupancy defined in Eq. (7.6), which is displayed in panel d). The agreement to the exact data (solid lines) is better than for $C_k(t)$, indicating that the effective model captures local observables better than long-range correlations.

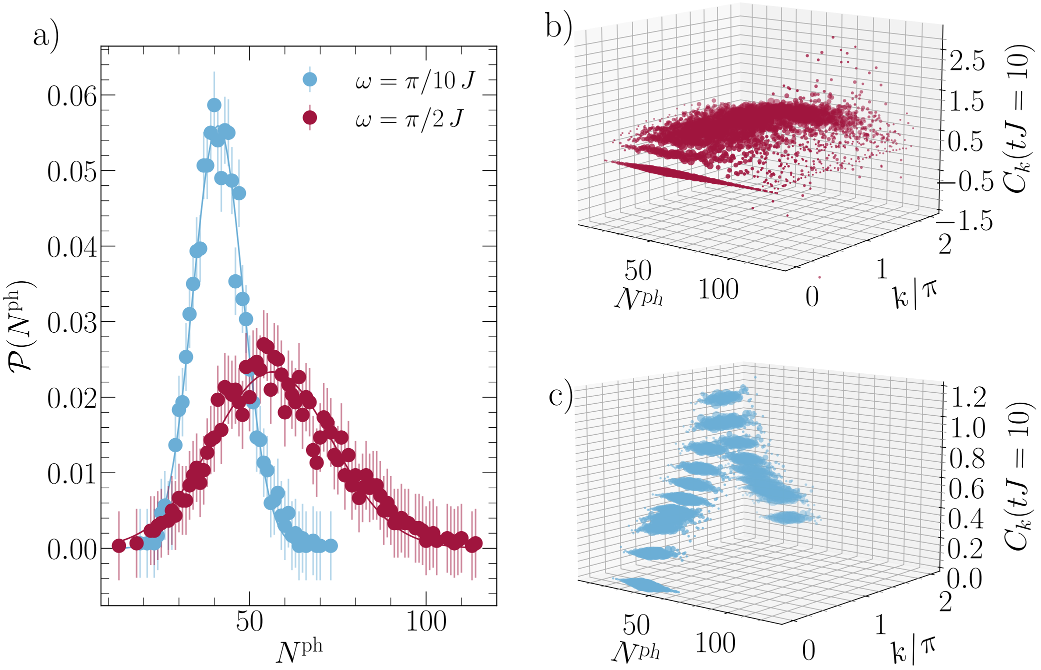

Figure 7.15: Phonon state tomography at different phonon frequencies. Left: The global phonon distribution function $\mathscr{P}(N^{\text{ph}})$ is significantly wider at large phonon frequency (red dots) than at small phonon frequency (blue dots). The solid lines are Gaussian fits, and the error bars represent the statistical error defined in Eq. (2.22) divided by 4 to improve the readability of the plot. Right: The PST-decomposed momentum-dependent charge correlation C_k at time $tJ = 10$ for large phonon frequency (panel b) and small phonon frequency (panel c). As indicated already by panel a), at large phonon frequency, for every momentum k the charge correlation spreads over many phonon sectors, while at small phonon frequency, it covers significantly fewer N^{ph} sectors. We consider the system size $L = 20$, the maximal bond dimension $m = 2000$, the maximal physical local dimension for the phonons $d = 40$ and used 3000 PST samples.

The most significant simplification of the effective model is that it ignores the time evolution of the phononic system. To assess the severity of this limitation, we apply PST to the full model Eq. (7.3) to compute the global phonon probability distribution $\mathscr{P}(N^{\text{ph}})$ for the smallest and the largest phonon frequencies at the late time $tJ = 10$. Panel a) of Fig. 7.15 shows that for the large phonon frequency $\omega = \pi/2\,J$ (red), $\mathscr{P}(N^{\text{ph}})$ is substantially broader than for $\omega = \pi/10\,J$ (blue). This is accompanied by a moderate shift of the maximum of $\mathscr{P}(N^{\text{ph}})$ to a larger N^{ph}, indicating that more phonons are excited in the scope of the time evolution. Next, we use PST to decompose the momentum-resolved charge correlation at $tJ = 10$ for $\omega = \pi/2J$ (panel b) and $\omega = \pi/10J$ (panel c). As suggested by panel a), we find many more phonon sectors N^{ph} contributing to $C_k(tJ = 10)$ for the large than for the small phonon frequency. Even more clearly than in Fig. 7.13, we can appreciate the well-defined structure of the charge correlation in momentum space at small phonon frequencies contrasting the flat C_k at large phonon frequencies. Furthermore, for a specific momentum k, the oscillations in $C_k(tJ = 10)$ at different N^{ph} are much stronger for $\omega = \pi/2J$ than for $\omega = \pi/10J$ (note the different scales of the z-axis in panels b and c). Thus, PST suggests that phonon-induced disorder is enhanced at large frequencies where many phonon sectors (as indicated by the broad $\mathscr{P}(N^{\text{ph}})$) contribute to C_k with different values.

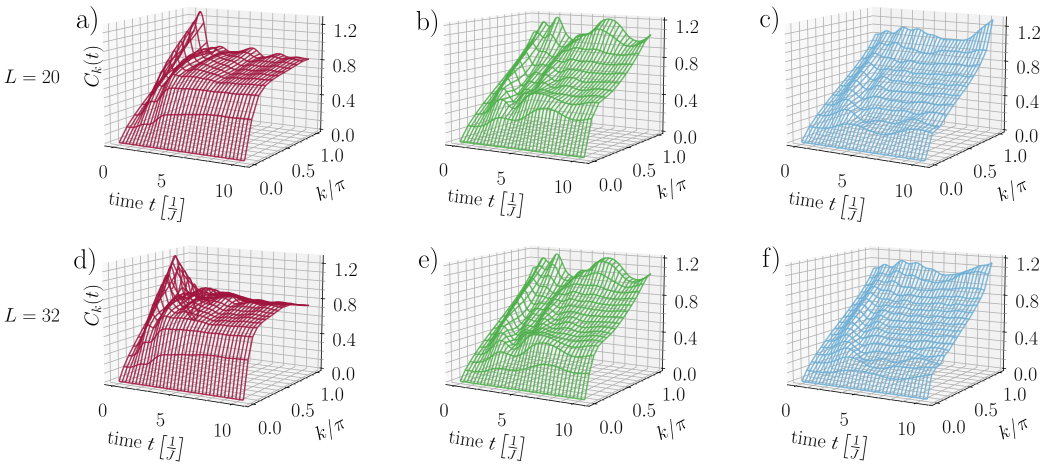

Figure 7.16: Momentum-dependent charge correlation for different system sizes. For all examined phonon frequencies $C_k(t)$ undergoes very similar dynamics for $L = 20$ (upper row) and $L = 32$ (lower row). We employed the same physical and numerical parameters as in Fig. 7.13.

7.2.1 Numerical analysis

In this section, we explore the numerical accuracy of the results presented in Section 7.2. We will focus, in particular, on the role of the phonon frequency and the effective model. Unless otherwise specified, we used the maximal bond dimension $m = 2000$, the maximal physical local dimension for the phonons $d = 40$, the discarded weight $\delta = 10^{-10}$ and the timestep $dt = 0.05J^{-1}$. For further implementation details and convergence analyses, we refer to Section 7.1.2.

As previously discussed, we are limited in system size by the large local Hilbert space dimension d of the phononic modes and by the rapid increase of entanglement during the time evolution. In Fig. 7.16, we show the momentum-resolved charge correlation $C_k(t)$ for systems with $L = 20$ and $L = 32$ sites at the phonon frequencies $\omega = \pi/2J$ (left panel), $\omega = \pi/5J$ (central panel) and $\omega = \pi/10J$ (right panel). While finite-size effects are clearly present in our results, the qualitative behavior of $C_k(t)$ is the same for both system sizes at all considered frequencies.

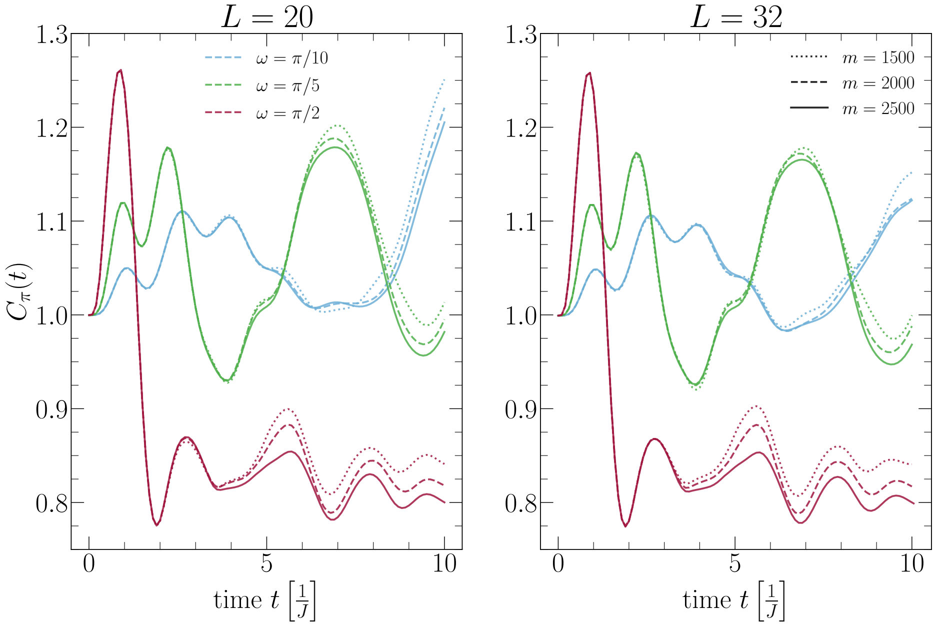

Figure 7.17: Bond dimension scaling for the momentum-dependent charge correlation function at different frequencies. We used the same parameters as in Fig. 7.13 and compute $C_k(t)$ for a system composed of 20 sites (left) and 32 sites (right), varying the bond dimension $m = 1500, 2000, 2500$.

Next, we study the convergence of $C_\pi(t)$ at the three different considered phonon frequencies w.r.t. the bond dimension, employing $m = 1500, 2000, 2500$. While for both $L = 20$ sites (left) and $L = 32$ sites (right), $C_k(t)$ is well-converged at small (blue lines) and intermediate frequencies (green lines), for large frequencies, some deviations are present at late times. These can be attributed to the fact that for $\omega = \pi/2J$, a slightly higher number of phonons is excited during the dynamics (see panel a in Fig. 7.15) and a significantly large number of phonon sectors contribute to $C_k(t)$ (see panels b and c in Fig. 7.15).

Subsequently, we compare the PST-sampled $C_k(t)$, which we considered in Fig. 7.15, to the exact value at different times for $\omega = \pi/2J$ and $\omega = \pi/10J$. Overall PST is quite precise, but slightly larger deviations are seen for the large phonon frequency (red dots) than for the small one (blue dots). This can be attributed to the significantly wider global phonon distribution function $\mathscr{P}(N^{\mathrm{ph}})$ in the former case (see Fig. 7.15), which makes it harder to sample. The errorbars correspond to the statistical error (see Eq. (2.22)) and slightly underestimate the deviation from the exact results.

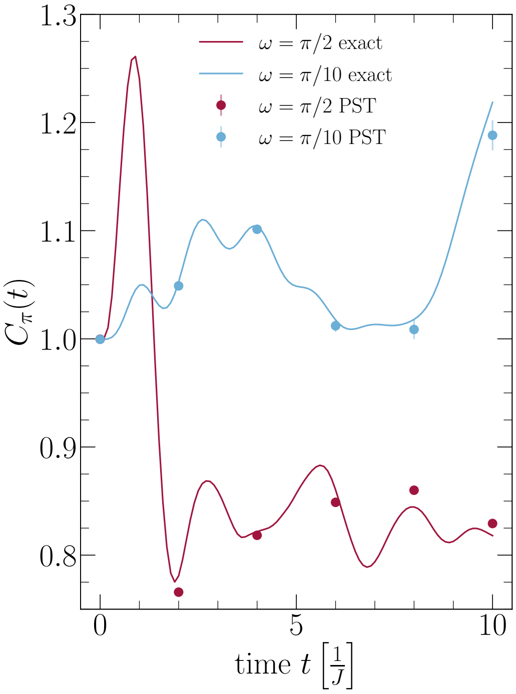

Figure 7.18: Accuracy of PST at different phonon frequencies. For the same physical and numerical parameters as in Fig. 7.15, we compare the exact time-dependent charge correlation at $k = \pi$ with the PST sampled one.

Finally, we compare the dynamics of the exact momentum-dependent pairing correlations $P_k(t)$ (Eq. (7.14)) to those obtained with the effective model Eq. (7.15). As for the charge correlations (see Fig. 7.14), the effective model captures well the qualitative behavior of $P_k(t)$. In particular, $P_k(t)$ is flattened in momentum space at a large phonon frequency (left panel). The oscillations displayed by the exact model are, however, underestimated in the effective description.

7.3 Summary and outlook

In this chapter, we demonstrated the utility of phonon state tomography (PST) (see Section 3.3) by studying the non-equilibrium properties of a metal whose phonons are excited by a pump pulse at an initial time.

In Section 7.1, we showed that, by decomposing electronic observables into contributions from different phonon sectors N^{ph}, PST allowed us to determine that the electron double occupancy $D(t)$ correlates with the number of phonon excitations present. In contrast, the staggered magnetic correlation $M(t)$ anticorrelates with it (see Fig. 7.3). Moreover, by modeling different optical pulses, we found that while the long-electron dynamics are insensitive to the local phonon

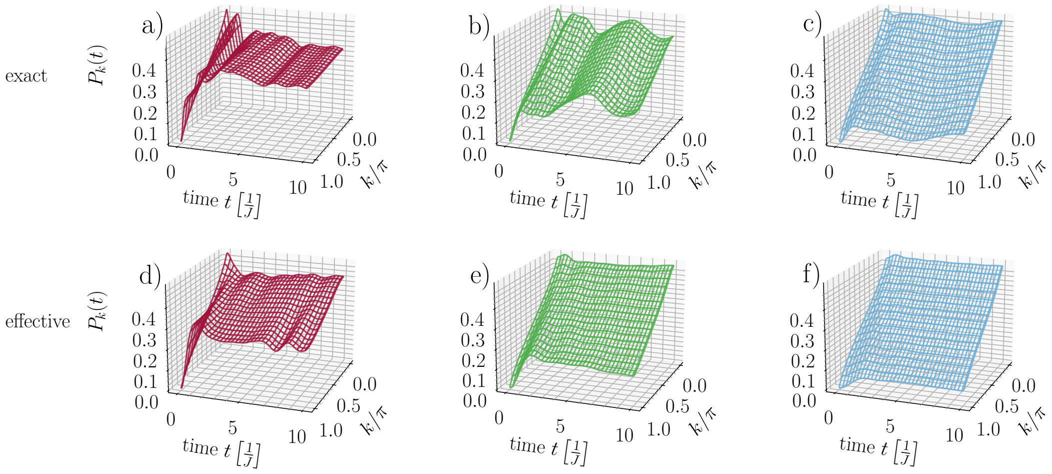

Figure 7.19: Momentum-dependent pairing correlations in the exact and in the effective model. We employed the same physical and numerical parameters as in Fig. 7.13.

probability distributions induced by these pulses (Fig. 7.4), the shapes of the global phonon distribution can be controlled to increase specific electronic correlations (Fig. 7.5). PST thus allows us to make a connection between the underlying electronic correlations and phononic observables measured in direct phonon probes (Fig. 7.2), which are potentially relevant to experiments based on diffuse x-ray and electron scattering [205, 207]. This could help interpret the ultrafast electron diffraction and x-ray diffuse scattering on cuprate superconductors (e.g. $Bi_2Sr_2CaCu_2O_{8+\delta}$ and $YBa_2Cu_3O_{6+\delta}$) under resonant excitation of the c-axis apical oxygen distortions [42].

In Section 7.2, we studied the role of the phonon frequency on the long-time dynamics of a photoexcited metal analyzing momentum-resolved correlation functions. At large phonon frequencies, a quick flattening of the charge correlation $C_k(t)$ and a PST decomposition corroborated the picture of phonon-induced disorder proposed in Ref. [198]. Instead, surprisingly, at small phonon frequencies, we found a significant enhancement of $C_\pi(t)$, indicating a light-induced CDW tendency. The decrease of the impact of phonon-induced disorder at small phonon frequencies was accompanied by a narrowing of the global phonon distribution function $\mathscr{P}(N^{\mathrm{ph}})$. This observation raises the question of whether a narrow $\mathscr{P}(N^{\mathrm{ph}})$ is a *necessary* condition for the emergence of long-range order, as broad phonon distributions favor the onset of disorder. It would be interesting to apply PST to compute the global phonon distribution in ordered and disordered equilibrium phases of well-studied models (such as, for instance, the CDW phase and the metallic Luther-Emery phase in the 1D Hubbard-Holstein model [211]) to address this question.

In another context, it would be interesting to apply PST to the setups considered in Chapter 6, i.e. the dynamics of excitons in structured environments [31, 65]. Accessing $\mathscr{P}(N^{\mathrm{ph}})$ could enable us to estimate the temperature-dependence of the two-triples yields in the singlet fission process from a single simulation. PST could also straightforwardly be adapted to open quantum systems dynamics via pure-state unravelings [1, 18].

Chapter 8

Dissipation-induced bipolaron localization

"How does dissipation affect quasiparticles in the Hubbard-Holstein model?"

This chapter investigates the physics of electrons coupled to dissipative phonons, i.e., phonons interacting with an external environment. Differently from Chapter 7, we consider linear electron-phonon coupling and study the Hubbard-Holstein model, that we utilized in Chapter 4 to compare the numerical accuracy and complexity of Markovian and non-Markovian methods. After introducing the model in Section 8.1, we study global quenches in the electron-phonon coupling and dissipation strength in Section 8.2. Then, we transform the Hubbard-Holstein Hamiltonian into a polaronic representation using a Lang-Firsov transformation and separate the single polaron and bipolaron contributions to the dynamics in Section 8.3. Equipped with these tools, in Section 8.4, we analyze the impact of the dissipation on the bipolaronic quasiparticles. Surprisingly, we find that strong dissipation does not affect the bipolarons' stability, but it tends to localize them. Finally, we conclude by discussing the interpretation of the effect of dissipation in terms of non-projective measurements in Section 8.5. This chapter is based on Ref. [1], written in collaboration with Martin Grundner, François Damanet, Ulrich Schollwöck, Sam Mardazad, Stuart Flannigan, Thomas Köhler, and Sebastian Paeckel.

8.1 The Hubbard-Holstein model

A minimal model for studying the complex interplay between electrons and lattice vibrations is provided by the Hubbard-Holstein model [111], which describes spinful fermions locally coupled to Einstein phonons and in 1D reads

$$\begin{aligned}\hat{H}_{\mathrm{HH}} = &- J \sum_{j=1}^{L} \sum_{\sigma=\uparrow,\downarrow} \left(\hat{c}^{\dagger}_{j,\sigma} \hat{c}_{j+1,\sigma} + \mathrm{h.c.} \right) + U \sum_{j=1}^{L} \hat{n}_{j,\uparrow} \hat{n}_{j,\downarrow} \\ &+ \omega \sum_{j=1}^{L} \hat{a}^{\dagger}_{j} \hat{a}_{j} + g \sum_{j=1}^{L} \left(\hat{a}_{j} + \hat{a}^{\dagger}_{j} \right) \hat{n}_{j} \, . \end{aligned} \tag{8.1}$$

Here, U indicates the onsite electron-electron interaction, ω is the phonon frequency, and g denotes the electron-phonon coupling. The operator $\hat{c}^{\dagger}_{j,\sigma}$ ($\hat{c}_{j,\sigma}$) creates (annihilates) a fermionic particle with spin σ on site j while $\hat{a}^{\dagger}_{j}$ ($\hat{a}_{j}$) creates (annihilates) a phonon on site j. The first two terms represent the electron's hopping and Hubbard repulsion, respectively. The third term describes dispersionless phonons, and the last term represents the linear coupling of the electron density to the phonon displacement. As in Chapter 4, we consider OBCs, set J to represent the energy unit and J^{-1} to denote the unit of time.

Eq. (8.1) offers a conceptually straightforward model for studying the interaction between lattice vibrations and electronic degrees of freedom in the regime of strong coupling. However, grasping the intricacies of the regime marked by the competition between (spinless) fermion-phonon interactions and onsite Hubbard interactions presents a challenging numerical endeavor, even in equilibrium. Over the past decade, significant numerical work has been undertaken to tackle this challenge [34, 63, 212–216]. The phase diagram of the Hubbard-Holstein model at half-filling sketched in Fig. 8.1 has been investigated comprehensively. In the regime of large phonon frequencies, the picture of three different phases has been established [63, 88, 211, 212, 217–219]. As the electron-phonon coupling g/U approaches zero, a correlated spin-density wave (SDW) phase emerges, reminiscent of a Hubbard Mott phase. Conversely, in the limit $g/U \gg 1$, strong phonon fluctuations push the system towards a Peierls state, also identified as charge-density wave (CDW) phase. This limit becomes particularly clear when the Hubbard-Holstein model is transformed into a polaronic representation using a Lang-Firsov transformation [220]. The onsite Hubbard interaction experiences a phonon-induced renormalization in this transformation, leading to $U \to U - \frac{2g^2}{\omega}$. When the electron-phonon coupling is sufficiently strong, an attractive interaction between the polarons becomes predominant, resulting in the spontaneous breaking of the system's translational symmetry. In the range of intermediate couplings, where $U \sim \frac{2g^2}{\omega}$, the system's behavior is influenced by the interplay between two opposing forces: attractive phonon-mediated interactions between polarons and repulsive electron-electron interactions. This pushes the system towards a metallic Luther-Emery phase [211].

A significant debate has revolved around whether this metallic regime might also exhibit superconductivity. Presently, the consensus is that superconduct-

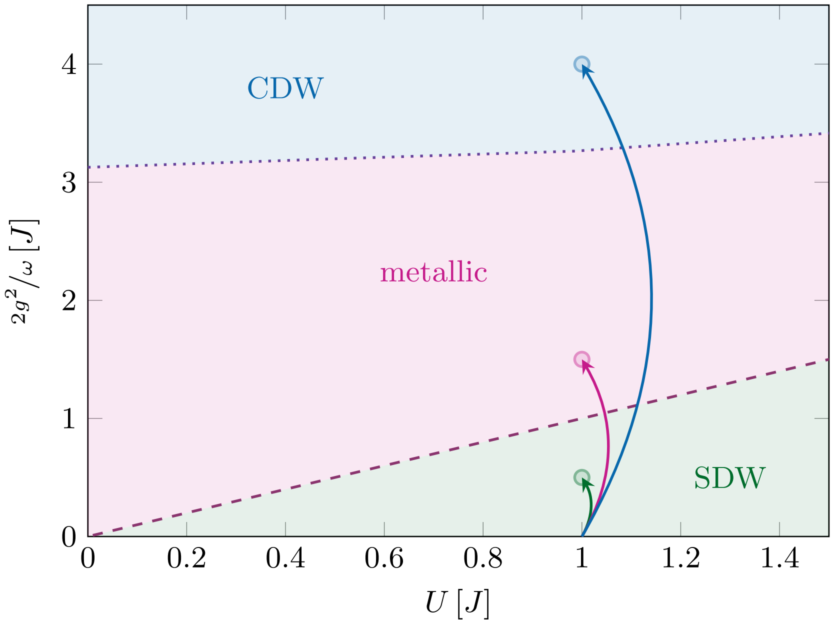

Figure 8.1: Phase diagram of the Hubbard-Holstein model at a constant phonon oscillation frequency $\omega = 2\,J$ adapted from Ref. [63]. The colored arrows indicate quenches from the Hubbard ground state at $U = J$ into the SDW, the metallic, and the CDW phase.

ing correlations in this regime are overshadowed by charge correlations [63]. However, upon incorporating Gaussian or quartic anharmonicities in the phonon potentials, a reinforcement of the metallic characteristics has been noted. This prompts the question of whether anharmonic phonons could potentially promote the metallic phase to a superconducting one [47, 48, 221].

Here, our focus lies in investigating the impact of a specific origin of anharmonicity: the dissipative coupling of phonons to an environment. We compute the dissipative dynamics using both the Markovian-embedded QJ (see Section 2.3) and the non-Markovian HOPS (see Section 2.5) methods. As outlined in Chapter 4, in the QJ approach, the dissipative dynamics are simulated by unraveling the Lindblad equation 2.6, where $\hat{H}_s$ is the Hubbard-Holstein Hamiltonian (Eq. (8.1)) and one jump operator $\hat{L}_j = \sqrt{\kappa}\hat{a}_j$ acts on every site j. Instead, for HOPS the effective Hamiltonian in Eq. (2.39) is constructed setting $\hat{H}_s$ equal to the Hubbard Hamiltonian (i.e. the upper line in Eq. (8.1)) and again $\hat{L}_j = \sqrt{\kappa}\hat{a}_j$. Note that the dissipative Hubbard-Holstein model examined here can be derived from a broader perspective, where electronic degrees of freedom are coupled to a global bosonic environment (see Section 2.7).

8.2 Dissipation and double occupancy

In a previous study [67], the influence of dissipation in the Hubbard-Holstein model has been explored using the HOPS technique. Investigating global quenches from a Neel state, the authors observed amplified superconducting correlations. We connect to this work by studying the dynamics of the double occupancy $\langle \hat{n}_{j,\uparrow}\hat{n}_{j,\downarrow} \rangle$ in the presence of phonon dissipation. We initialize the system in the ground state of the Hubbard model ($g = 0$, $\kappa = 0$) at $U = J$, and quench to the SDW phase ($2g^2/\omega = 0.5\,J$), the metallic phase ($2g^2/\omega = 1.5\,J$), and the CDW phase ($2g^2/\omega = 4\,J$), as indicated by the arrows in Fig. 8.1. Moreover, we turn on to either intermediate ($\kappa = J$) or strong ($\kappa = 4J$) dissipation and compute the dynamics using the HOPS method. In Fig. 8.2, we present the time evolution of the double occupancy, focusing on the central site within a system containing 20 electrons. Upon quenching into the SDW region of the Hubbard-Holstein phase diagram (illustrated by the green curves), we observe only a minimal dependence on the strength of dissipation. This outcome aligns with the notion of predominant spin-spin correlations prevailing within the SDW phase, which remain relatively unperturbed by phonon occupations. Conversely, upon performing a quench into the CDW region (depicted by the blue curve), dissipation has a significant impact. This can be understood as follows: For an isolated system, large phonon fluctuations trigger charge correlations and promote the emergence of double occupations within the Peierls phase. When strong dissipation is turned on, the phonons' occupations are reduced, attenuating charge correlations. Interestingly, the quenches to the metallic region (illustrated by the purple curve) share resemblances with the behaviors witnessed in SDW quenches. The limited dependence on the dissipation strength indicates a strong suppression of charge correlations, even in the presence of moderate dissipation.

8.3 Polarons and bipolarons

The quenches from the Hubbard ground state into the Hubbard-Holstein model's different phases shown in Section 8.2 provide a first glimpse into the interplay between dissipation and electron-phonon coupling. Now, we want to disentangle the effect of dissipation from that of the electron-phonon coupling g. To do so, we initialize the system in the ground state of the full Hubbard-Holstein model and perform *dissipative quenches* by suddenly turning on κ.

To study bipolaronic quasiparticles, we decompose the electronic annihilation (creation) operators into distinct single-particle and two-particle operators,

$$\hat{c}_{j,\sigma} = \hat{s}_{j,\sigma} + \mathrm{sgn}(\sigma)\hat{s}^{\dagger}_{j,\bar{\sigma}}\hat{d}_j \,, \tag{8.2}$$

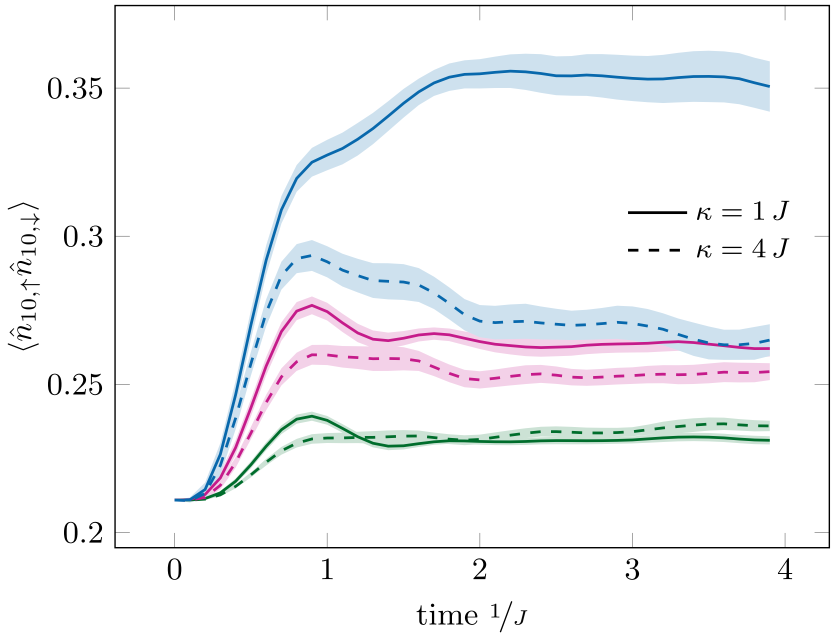

Figure 8.2: Double occupancy dynamics after global quenches from the Hubbard ground state (lines with arrows in Fig. 8.1). We used HOPS and considered intermediate dissipation $\kappa = J$ (solid line) and strong dissipation $\kappa = 4\,J$ (dashed line). The double occupancy dynamics in the electron systems depend more strongly on the phonon loss rate for large electron-phonon coupling g. We simulate a system with $L = 20$ sites, a time step $dt = 0.01\,J^{-1}$ and compute $|\mathcal{Q}| = 200$ trajectories, using $k_{\max} = 40$ local basis states and a max. bond dimension of $m = 2000$ fixing the discarded weight to $\delta = 10^{-10}$.

where $\hat{s}_{j,\sigma} = \hat{c}_{j,\sigma}(1-\hat{n}_{j,\bar{\sigma}})$ and $\hat{d}_j = \hat{c}_{j,\downarrow}\hat{c}_{j,\uparrow}$ and we indicate spin conjugation with $\bar{\sigma}$ [37]. After implementing a Lang-Firsov transformation [220], the Hubbard-Holstein Hamiltonian becomes

$$\begin{aligned}\hat{H}_{\mathrm{LF}} &= -J\sum_{j,\sigma}\left(\hat{D}_j^\dagger\left(\frac{g}{\omega}\right)\hat{c}_{j,\sigma}^\dagger\hat{c}_{j+1,\sigma}\hat{D}_{j+1}\left(\frac{g}{\omega}\right)+\text{h.c.}\right)+U_{\text{eff}}\sum_j \hat{n}_{j,\uparrow}\hat{n}_{j,\downarrow}+\omega\sum_j\hat{a}_j^\dagger\hat{a}_j\\ &= \sum_j \hat{U}_j^{bp} - J\sum_j\left(\hat{T}^{bp}_{j,j+1}+\sum_\sigma \hat{T}^{p}_{j,j+1,\sigma}\right)+\omega\sum_j \hat{a}_j^\dagger\hat{a}_j\,,\end{aligned} \tag{8.3}$$

where $U_{\text{eff}} = \left(U - \frac{2g^2}{\omega}\right)$ and we introduced the bipolaron potential energy $\hat{U}_j^{bp} = U_{\text{eff}}\hat{d}_j^\dagger\hat{d}_j$, the displacement operator $\hat{D}_j^\dagger\left(\frac{g}{\omega}\right) = e^{g/\omega(\hat{a}_j^\dagger-\hat{a}_j)}$, and the polaronic and bipolaronic hopping operators, $T^{p}_{i,j,\sigma}$ and $T^{bp}_{i,j}$, respectively:

$$\hat{T}^{p}_{i,j,\sigma} = \hat{D}_i^\dagger\left(\frac{g}{\omega}\right)\hat{s}_{i,\sigma}^\dagger\hat{s}_{j,\sigma}\hat{D}_j\left(\frac{g}{\omega}\right)+\text{h.c.}\,, \tag{8.4}$$

$$\hat{T}^{bp}_{i,j} = \hat{D}^{\dagger}_{i}\left(\frac{g}{\omega}\right)\hat{d}^{\dagger}_{i}\left(\sum_{\sigma}\hat{s}_{i,\sigma}\hat{s}^{\dagger}_{j,\sigma}\right)\hat{d}_{j}\hat{D}_{j}\left(\frac{g}{\omega}\right) + \text{h.c.}\,. \tag{8.5}$$

By evaluating the complete hopping matrix $\hat{T}^{bp}_{i,j}$, we can examine the kinetic energies t_k of bipolaronic quasiparticles. This analysis involves the diagonalization of the matrix $\langle\hat{T}^{bp}_{i,j}\rangle \equiv t^{bp}_{ij}$, where the eigenstates are denoted by quasi-momenta $k_n \equiv \frac{2\pi}{L}n$ and correspond to eigenvalues t_k[1]. Using the kinetic energies, we compute the maximum effective quasiparticles' velocity v_{eff} by discretely differentiating at $k_{\text{eff}} = \pi$. Within the quasiparticles' perspective, we introduce a mass estimation for the bipolaronic quasiparticles through the following relation:

$$m_{\text{eff}} = \frac{k_{\text{eff}}}{v_{\text{eff}}} = k_{\text{eff}}\left(\left.\frac{\Delta t_k}{\Delta k}\right|_{k_{\text{eff}}}\right)^{-1}\,. \tag{8.6}$$

In scenarios where stable bipolaronic quasiparticles exist within the system, the value of m_{eff} indicates the smallest quasiparticle mass. Consequently, this parameter serves as an indicator of their degree of mobility.

This interpretation becomes readily apparent when examining the dissipative quenches within the CDW phase depicted in Fig. 8.3 (right column). We notice an almost constant energy band throughout the entire simulation time. This constancy displays the insulating nature of the CDW phase, arising from localized bipolarons. Conversely, within the SDW phase, we identify a single-particle gap, indicating a small bipolaron effective mass. Within the metallic phase, the response to dissipation strength is most pronounced: A robust initial metallicity wanes as the system evolves in time, especially for $\kappa = 4\,J$. In this case, the closure of the single-particle gap implies the localization of bipolaronic quasiparticles.

8.4 Bipolarons' stability and localization length

To assess the stability of bipolaronic quasiparticles, we further computed the averaged bipolaronic binding energy [222]. Using Eqs. (8.4) and (8.5) this quantity can be expressed as the difference between the site-averaged bipolaronic and polaronic energies

$$\Delta E = \frac{1}{L}\sum_{j}\left(\langle\hat{U}^{bp}_{j}\rangle + \langle\hat{T}^{bp}_{j,j+1}\rangle - \langle\hat{T}^{p}_{j,j+1,\uparrow}\rangle - \langle\hat{T}^{p}_{j,j+1,\downarrow}\rangle\right)\,. \tag{8.7}$$

---

[1] In the thermodynamic limit, this is equivalent to Fourier-transforming the hopping matrix. However, for our $L = 20$-sites-system, we found that the diagonalization procedure is less affected by finite-size effects.

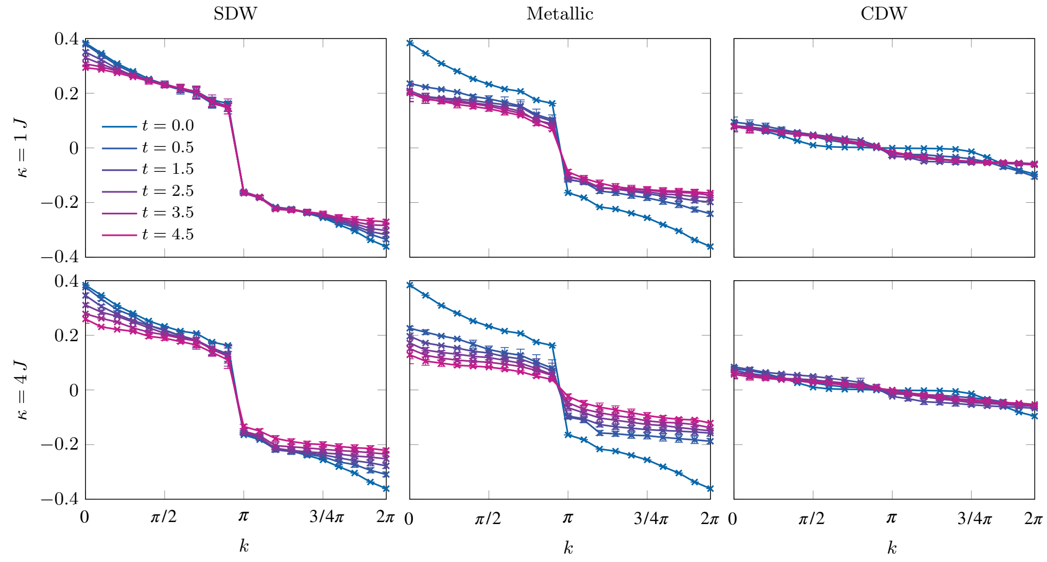

Figure 8.3: Eigenvalues t_k of the bipolaronic hopping matrix $\hat{T}^{bp}_{i,j,\sigma}$ (see Eq. (8.5)) as a function of time, after turning on dissipation to $\kappa = 1\,J$ and $\kappa = 4\,J$ in the three different regions of the Hubbard-Holstein ground state phase diagram (indicated by the three circles in Fig. 8.1). In the SDW phase, a large single-particle gap indicates a small bipolaronic effective mass (but, as we will display in Fig. 8.4, no stable bipolarons are present in this phase). In contrast, the flat band in the CDW phase represents heavy bipolarons. Both phases are basically insensitive to dissipation. In the metallic phase, the gap closing shows that strong dissipation $\kappa = 4$ significantly increases the bipolarons' effective mass. We use the QJ method and the same parameters as in Fig. 8.2.

Here, $\Delta E > 0$ implies unstable bipolarons, which tend to decay into two polarons. Conversely, $\Delta E < 0$ indicates stable bipolaronic quasiparticles.

In Fig. 8.4, the dashed lines (right axis) depict the bipolarons' binding energies in the large-dissipation scenario. When turning on dissipation in the SDW, ΔE remains constant and positive, indicating that bipolarons are unstable. This is consistent with the insulating character of the antiferromagnetic Hubbard ground state. For the quench in the CDW phase, we find $\Delta E < 0$, which, however, decreases by roughly a factor of two during the time evolution on a time scale comparable to one phonon oscillation period ω. Nonetheless, the bipolaronic binding energy remains relatively high throughout the entire time evolution, suggesting the presence of stable bipolaronic quasiparticles. In the metallic regime, we also observe a negative ΔE which, surprisingly, is nearly time-independent. Therefore, in the metallic phase, even when strong dissipation is present, most phonons that are bound into bipolaronic quasiparticles do not escape into the environment. Note that these results are in good agreement with the time-dependent double occupations shown in Fig. 8.2. In the metallic regime, the double occupation remains nearly unaffected by the dissipation strength, while the drop in the

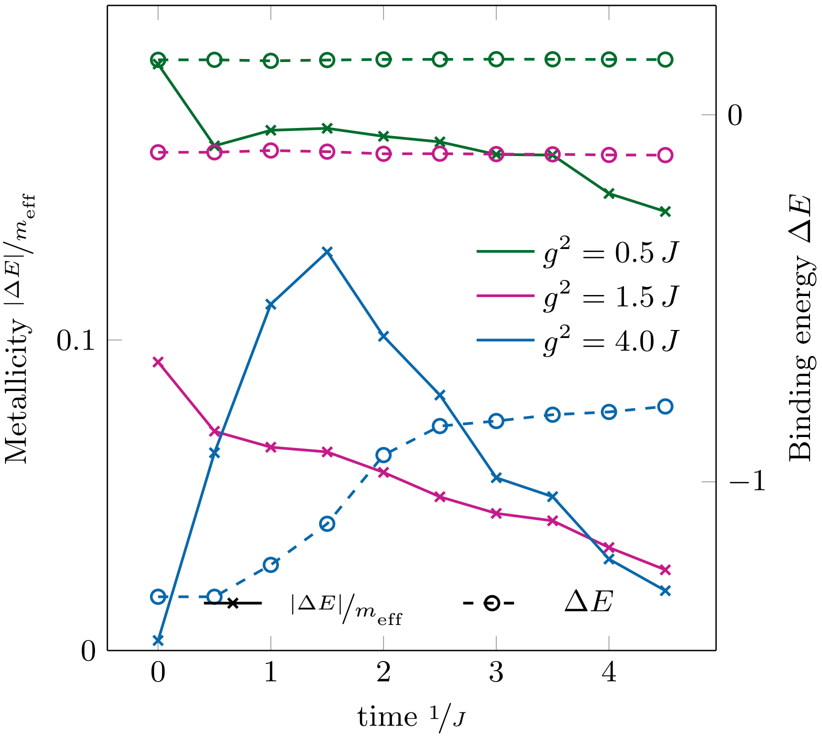

Figure 8.4: Binding energy (circles, right axis) and metallicity (crosses, left axis), after the dissipative quenches at $\kappa = 4\,J$ from the three points in the Hubbard-Holstein phase diagram considered in Fig. 8.1. Analyzing the sign of the binding energy ΔE, we observe the formation of stable bipolarons in the metallic and in the CDW phase, but not in the SDW phase. Most interestingly, in the metallic phase, strong dissipation localizes the bipolarons (the metallicity decreases) without disrupting their stability (ΔE is constant).

double occupancy during the dynamics within the CDW phase at $\kappa = 4, J$ occurs on a similar time scale as the decrease in bipolaronic binding energy in Fig. 8.4.

The solid lines in Fig. 8.4 (left axis) depict the ratio between the absolute value of the binding energy and the effective bipolaron mass. This serves as an indicator of bipolaronic metallicity, where, with constant binding energies, larger ratios indicate highly mobile bipolarons. The curves presented here offer a concise summary of our analysis, demonstrating the enduring insulating nature of both the SDW and CDW phases, even when dissipation is introduced. Furthermore, we observe a substantial reduction in metallicity within the metallic regime, attributable to the augmented quasiparticle mass of the bipolarons.

We delve deeper into the remarkable effect of strong dissipation on the metallic phase by examining the bipolaron's localization length ξ^2. This parameter can be derived from the connected correlation functions of the bipolaronic density-density correlation matrix, as described in [223]. First we define the time-dependent bipolaronic center of mass operator as $\langle \hat{X}_t \rangle \equiv \sum_j j \langle \hat{n}_j^d(t) \rangle / L$, where

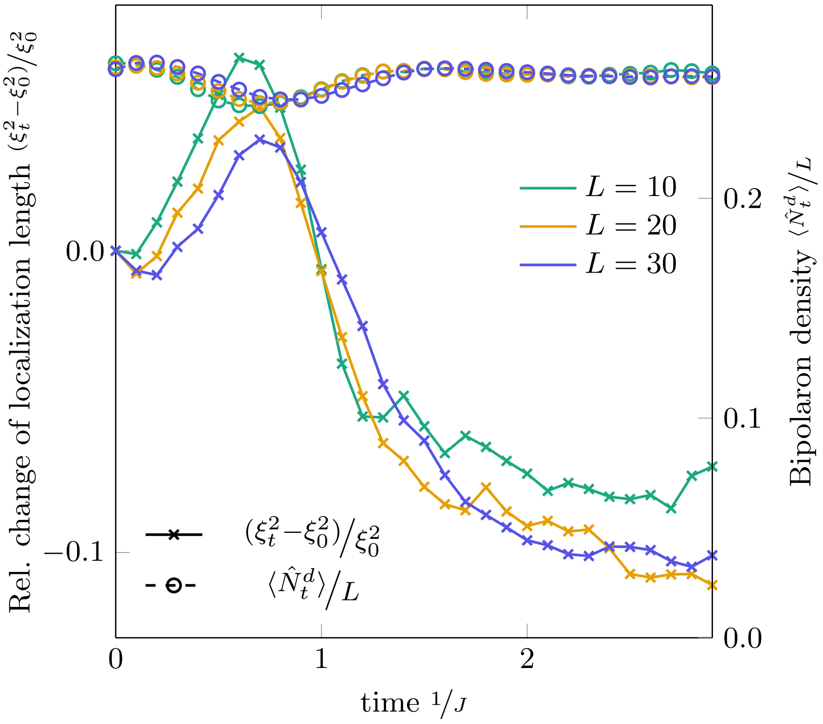

Figure 8.5: Dissipation-induced bipolaron localization. Left y-axis (crosses): Relative change of the bipolaron's localization length ξ_t^2 after the dissipative quenches for $\kappa = 4\,J$ from the metallic region in the Hubbard-Holstein phase diagram considered in Fig. 8.1, for various system sizes. After a small increase at short timescales, the localization length decreases for all considered system sizes. Right y-axis (circles): The time-dependent bipolaron densities, apart from a small initial dip, are almost constant in time. This is consistent with the constant binding energy found in Fig. 8.4.

$\hat{n}_j^d \equiv \hat{d}_j^\dagger \hat{d}_j$. Then, the localization length at time t can be expressed as

$$\xi_t^2 \equiv \frac{\langle \hat{X}_t^2 \rangle - \langle \hat{X}_t \rangle^2}{N_t^d}, \tag{8.8}$$

with $N_t^d \equiv \langle \sum_j \hat{n}_j^d(t) \rangle$. In Fig. 8.5, we illustrate the evolution of the relative change $(\xi_t^2 - \xi_0^2)/\xi_0^2$ when introducing dissipation in the metallic phase for various system sizes L (solid lines, left y-axis). After an initial rise, primarily driven by the short-term behavior of the bipolaron density, we notice a quick drop in the metallic phase, implying the localization of bipolaronic quasiparticles. We have verified that this localization is not an artifact of a diminished bipolaron population by monitoring the bipolaron density $\langle \hat{N}_t^d \rangle / L$ (right y-axis in Fig. 8.5).

Two key observations can be made: firstly, excluding the very short-term dynamics, the bipolaron density remains unaffected by the system size. Secondly, there is no substantial decrease in the bipolaron density at later stages, align-ing with the constant binding energy observed (see Fig. 8.4). As a result, the bipolaronic localization length is an additional quantity that, when considered alongside binding energy and metallicity, indicates that dissipation localizes the bipolaronic quasiparticles.

8.5 Summary and outlook

In this chapter, we studied the Hubbard-Holstein model, examining the role of phonon anharmonicities originating from a dissipative interaction between the phonons and an environment. This was motivated in part by the fact that recent (semi-)analytical studies had indicated the potential enhancement of the metallic phase when anharmonic phonons are considered (see Appendix C for a comparison between the effect of dissipation and Gaussian anharmonicities on the occupation of the phonon modes). Leveraging the PP-enhanced HOPS and QJ methods (see Chapter 4), we investigated the effect of dissipation on metallicity in the Hubbard-Holstein model. For that purpose, we performed a series of quenches, studying the formation of bipolarons, i.e., phonon-mediated bound two-electron quasiparticles, and their metallicity. In this context, we defined metallicity as the ratio between the bipolaronic binding energy and their effective mass. In the metallic regime of the Hubbard-Holstein groundstate phase diagram, we found that the time-dependent bipolaronic binding energy remains mainly unchanged, i.e., the phonons that contribute to bound electron pairs do not tend to escape the system. When studying the dynamics of bipolaronic kinetic energy, we noticed the melting of the bipolaron's single-particle gap for strong dissipation. Thus, dissipation augments the bipolaronic effective mass, leading to an overall decrease in bipolaronic metallicity. We complemented this analysis by computing the bipolaronic localization length, explicitly revealing the localization of bipolarons in the presence of dissipation within the metallic regime. Additionally, we observed that the bipolaronic binding energy exhibits significant stability against dissipation. This observation is particularly noteworthy, especially considering that the calculated binding energies are on the order of $0.15\,J$, which is substantially smaller than the investigated dissipation strengths of $\kappa = 1J$ and $4J$.

In a recent investigation, it was demonstrated that interactions with an environment can be represented through measurements, which inhibit transport by promoting the formation of decoupled clusters [224]. In the regime of strong dissipation, this behavior bears a resemblance to the quantum Zeno effect [192]. In particular, the observation that intermediate levels of dissipation have little to no significant influence on the dynamics (see Fig. 8.3), whereas strong dissipation induces pronounced localization of the bipolarons, hints at the existence of a transition between a phase characterized by volume law entanglement and a quantum Zeno phase, as described in [225]. Furthermore, it is important to emphasize

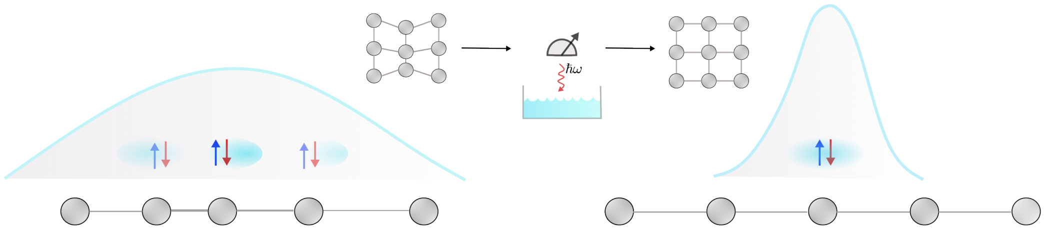

Figure 8.6: Pictorial representation of dissipation-induced bipolaron localization. Dissipation can be interpreted as repeated, non-projective measurements on the phononic system. In the metallic phase (see Fig. 8.1), the coupling of the phononic degrees of freedom to a dissipative bath tends to localize the bipolarons. However, the binding energy of bipolarons remains mostly unchanged, implying that bipolarons remain stable even under strong dissipation.

that the non-projective measurements are exclusively conducted on the phononic system, making the observed localization of bipolarons a potential manifestation of an indirect quantum Zeno effect [226, 227]. The dissipation-induced bipolaron localization is shown pictorially in Fig. 8.6.

Chapter 9

Conclusion and Outlook

In this thesis, we investigated the impact of quantum dissipative and vibrational environments on various systems, ranging from qubits to excitons and electrons. In recent years, the methodological advances in OQS were boosted by the development of digital quantum computers, but their applicability ranges much beyond that, as we have shown here. In particular, OQS methods combined with efficient MPS algorithms are ripe for studying many-body condensed matter models. Nevertheless, there is still much room for improvement.

Dissipative dynamics can be efficiently described using the complementary approaches of vectorization or pure state unravelings. In Chapter 2, we discussed such methods for Markovian, non-Markovian, and Markovian-embedded setups. Importantly, pure state OQS methods can be easily combined with MPS algorithms, with the only potentially critical point being the application of TDVP to non-Hermitian Hamiltonians, as we outlined in Chapter 3. As future methodological improvements, using tree tensor networks [194] rather than MPS, especially when dealing with structured environments, could be beneficial. Moreover, it would be intriguing to explore whether pure state unravelings could be used to target steady states directly, avoiding the need to extract the zero-energy eigenstate of the highly-dimensional vectorized Lindbaldian [25, 53].

The physics of OQS are so rich that, even in the simplest case of few-body systems weakly interacting with Markovian (i.e., memoryless) environments, there are still numerous exciting phenomena to study. In Chapter 5, we considered the anomalous thermalization phenomenon known as the Mpemba effect. We defined a thermodynamically consistent Mpemba effect based on the non-equilibrium free energy and went beyond Ref. [29] by providing a unitary transformation $\hat{U}$ that always exponentially accelerates the thermalization of any mixed state. The transformation is based on the block structure of the Lindbladians describing thermalization processes, known as Davies maps, which implies that a state's coherences and populations evolve independently. The spectrum of the Davies maps allows us to identify two cases: in one, an exact $\hat{U}$ exists, and in the other, we obtain an approximated $\hat{U}$ via a stochastic method based on the Metropolis algorithm. Our results suggest that it would be interesting to study in which dissipative quantum systems the Mpemba effect occurs *typically* (like for colloidal particles for asymmetric potentials [28]) rather than only following the application of a special unitary transformation. Moreover, we explored the Mpemba effect in few-body systems using ED. To handle many-body systems, we would need a more efficient method to obtain at least some of the lowest-lying eigenvalues and eigenvectors of the (non-Hermitian) Lindbladian superoperator. Building upon recent work which employs an Arnoldi scheme for the Lindbladian [228], this could be achieved with MPS techniques.

When moving on to the methodologically more challenging setups of electrons interacting with vibrational environments, we typically need to account for the environment explicitly. In practical numerical calculations, it is then necessary to determine whether the best strategy is to adopt the non-Markovian description (i.e. a small system and a complicated environment) such as HOPS [26], HEOM [229] or QUAPI [182], or a Markovian-embedded description (i.e. a large the system and a simpler, Markovian environment). In Chapter 4, we studied the Hubbard-Holstein model, which describes interacting electrons coupled locally to dispersionless phonons, comparing the performance of HOPS to the Markovian-embedded QJ approach. We found that despite displaying a remarkably similar numerical complexity in a vast parameter regime, QJ works best for weak dissipation (for which the non-Hermitian part of the dynamics can be considered a small perturbation), while HOPS excels for strong dissipation, where the short memory effects in the environments allow adopting a shallow hierarchy. Moreover, while HOPS allows for larger truncations of the hierarchy depth, corresponding to the physical local dimension of the phonons for QJ, a smaller bond dimension is required for QJ.

In Chapter 6, we investigated the performance of different numerical approaches for the description of exciton dynamics in structured vibrational environments, which can model, for instance, light-harvesting complexes [32] and singlet fission in molecular crystals [31]. We argued that for these setups, Markovian embedding schemes are the most flexible; non-Markovian approaches are efficient only when considering smooth spectral densities and unitary descriptions only for spectral densities characterized by few sharp peaks. In particular, studying singlet fission, we found that the dissipation-enabled efficient fitting of the spectral density yields a speedup of almost one order of magnitude compared to the isolated-system description. Furthermore, studying the exciton dynamics in the FMO complex, we showed that dissipation reduces both the occupation of the vibrational modes and the overall system's entanglement without affecting the accuracy of the dynamics. These results point towards an important role of dissipation as a resource for MPS calculations [24].

Studying the effect of vibrational environments on many body electron systems out of equilibrium is an arduous task, but the recent advances in representation [35] and time evolution [36, 37] constitute an important step forward. However, the huge dimensionality of bosonic degrees of freedom does not complicate only the description of vibrational environments but also the *analysis* of their impact on the electrons. To address this challenge, we introduced phonon state tomography (PST), a numerical method that enables decomposing an electron wave function into contributions corresponding to different numbers of vibrational excitations. In Chapter 7, we studied the dynamics of electrons in a 1D metal following the photoexcitation of non-linearly coupled phonons and showed that PST can help interpret the impact of phonon excitations on the electron system. Specifically, we found that the electron double occupancy correlates with the number of phonon excitations, while the staggered magnetization anticorrelates with it. Moreover, broad optical pulses cause a stronger enhancement of the electron double occupancy than narrow pulses with the same intensity. Crucially, PST also allowed us to directly explore phonon-induced disorder, which tends to localize the electrons at large phonon frequencies. For small phonon frequencies, instead, we found a light-induced enhancement of long-range electron correlation in the numerically-exact study of a many-body system. While the calculations presented here were purely explorative, it would be interesting to perform them with the parameters of a real material (for instance, a 1D cuprate, including a Hubbard electron repulsion U), which would enable a direct experimental comparison. We have focused on equal-time correlations functions because precise calculations of two-time correlation functions such as the optical conductivity [41] require long simulation times following global quenches, which are currently out of reach for electron-phonon systems. However, PST could enable the determination of an effective Hamiltonian for the electrons only, rendering the time evolution much cheaper. Furthermore, while here we demonstrated the utility of PST to interpret the impact of an environment characterized by a single vibrational frequency, it would be interesting to apply PST to more challenging structured environments. Finally, it would be highly desirable to move to higher-dimensional systems, where one could potentially observe true light-induced long-range order.

In conclusion, we considered the indirect effect of dissipation on electron systems interacting with vibrational environments. In recent years, many approaches have been proposed to go beyond the toy-model of Einstein phonons, i.e. harmonic oscillators. These include for instance dissipative phonons [49, 50] and anharmonic phonons [47, 48]. Here, we used dissipation as an alternative way to model more realistic phonons, implicitly accounting for phenomena like phonon-phonon or phonon-impurity scattering. Studying the phase diagram of the Hubbard-Holstein model, we found that strong dissipation has no significant impact on the SDW and CDW insulating phases. Instead, in the metallic phase, the mobility of bipolarons (i.e. Cooper pairs dressed by phonons) is strongly suppressed. However, they remain stable rather than decaying into two single polarons, as one would naively expect. We also showed that this corresponds to a localization of the bipolarons in real space. Viewing dissipation as non-projective measurements on the phonons, this is reminiscent of an (indirect) quantum Zeno effect [225], in which the measurement rate dictates the transition from a localized, area-law-entangled phase to a delocalized, volume-law-entangled phase. Therefore, we believe that the dissipative Hubbard-Holstein model represents a good example of a condensed matter model that can be investigated from the perspective of quantum information theory.

Almost a hundred years have passed since the discovery of quantum mechanics. While usually predictions on the *end of physics* are disproved in a spectacular way (Philipp von Jolly [230] and Albert Michelson [231] are some of the most famous examples in this regard), Paul A. M. Dirac might have been right in 1929 when he claimed that *"the underlying physical laws necessary for the mathematical theory of a large part of physics and the whole of chemistry are thus completely known"* [232]. However, the ability to essentially solve the Schrödinger equation for increasingly complex systems has not only tremendously advanced our understanding of solids and molecules but also led to crucial new insights in fundamental topics regarding the connection between quantum mechanics and classicality [12], computation [14], information [233], and topology [234], to mention just a few. Much more modestly, in this thesis, we have explored some specific open questions from some of the subfields initiated by quantum mechanics, such as condensed matter physics, quantum thermodynamics, and quantum chemistry, from the perspective of OQS. While much remains to be done, we believe that OQS methods combined with MPS algorithms provide a versatile framework in which many methodological and conceptual problems from the different fields above can be addressed.

Bibliography

6 M. Schlosshauer:
Decoherence: And the Quantum-To-Classical Transition,
The Frontiers Collection. Springer, 2007. isbn: 9783540357735.

7 M. Schlosshauer:
'Decoherence, the measurement problem, and interpretations of quantum mechanics',
in: *Reviews of Modern Physics* 76.4 (2005), pp. 1267–1305. issn: 1539-0756.

8 D. Chruściński and S. Pascazio:
'A Brief History of the GKLS Equation',
in: *Open Systems & Information Dynamics* 24.03 (2017), p. 1740001. eprint: `https://doi.org/10.1142/S1230161217400017`.

9 V. Gorini, A. Kossakowski and E. C. G. Sudarshan:
'Completely positive dynamical semigroups of N-level systems',
in: *Journal of Mathematical Physics* 17.5 (May 1976), pp. 821–825. issn: 0022-2488. eprint: `https://pubs.aip.org/aip/jmp/article-pdf/17/5/821/19090720/821\_1\_online.pdf`.

10 G Lindblad:
'On the generators of quantum dynamical semigroups',
in: *Communications in Mathematical Physics* 48.2 (June 1976), pp. 119–130.

11 H. Spohn:
'Entropy production for quantum dynamical semigroups',
in: *J. Math. Phys.* 19.5 (May 1978), pp. 1227–1230. issn: 0022-2488.

12 W. H. Zurek:
'Pointer basis of quantum apparatus: Into what mixture does the wave packet collapse?',
in: *Phys. Rev. D* 24 (6 1981), pp. 1516–1525.

13 H. J. Carmichael:
An open systems approach to quantum optics,
Berlin Heidelberg: Springer-Verlag, 1993.

14 M. A. Nielsen and I. L. Chuang:
Quantum Computation and Quantum Information: 10th Anniversary Edition,
Cambridge University Press, 2011. isbn: 9781107002173.

15 Q. Xu, J. P. Bonilla Ataides, C. A. Pattison, N. Raveendran, D. Bluvstein, J. Wurtz, B. Vasić, M. D. Lukin, L. Jiang and H. Zhou:
'Constant-overhead fault-tolerant quantum computation with reconfigurable atom arrays',
in: *Nature Physics* 20.7 (2024), pp. 1084–1090.

16 C. Portmann and R. Renner:
'Security in quantum cryptography',
in: *Rev. Mod. Phys.* 94 (2 2022), p. 025008.

17 V. Giovannetti, S. Lloyd and L. Maccone:
'Advances in quantum metrology',
in: *Nature Photonics* 5.4 (2011), pp. 222–229.

18 A. J. Daley:
'Quantum trajectories and open many-body quantum systems',
in: *Advances in Physics* 63.2 (2014), pp. 77–149. issn: 1460-6976.

19 S. Ajisaka, F. Barra, C. Mejía-Monasterio and T. Prosen:
'Nonequlibrium particle and energy currents in quantum chains connected to mesoscopic Fermi reservoirs',
in: *Phys. Rev. B* 86 (12 2012), p. 125111.

20 S. R. White:
'Density matrix formulation for quantum renormalization groups',
in: *Phys. Rev. Lett.* 69 (19 1992), pp. 2863–2866.

21 U. Schollwöck:
'The density-matrix renormalization group in the age of matrix product states',
in: *Annals of Physics* 326.1 (2011), pp. 96–192. issn: 0003-4916.

22 D. Jaschke, S. Montangero and L. D. Carr:
'One-dimensional many-body entangled open quantum systems with tensor network methods',
in: *Quantum Science and Technology* 4.1 (2018), p. 013001.

23 S. Wolff, A. Sheikhan and C. Kollath:
'Numerical evaluation of two-time correlation functions in open quantum systems with matrix product state methods: a comparison',
in: *SciPost Phys. Core* 3 (2020), p. 010.

24 A. D. Somoza, O. Marty, J. Lim, S. F. Huelga and M. B. Plenio:
'Dissipation-Assisted Matrix Product Factorization',
in: *Phys. Rev. Lett.* 123 (10 2019), p. 100502.

25 J. Cui, J. I. Cirac and M. C. Bañuls:
'Variational Matrix Product Operators for the Steady State of Dissipative Quantum Systems',
in: *Phys. Rev. Lett.* 114 (22 2015), p. 220601.

26 D. Suess, A. Eisfeld and W. T. Strunz:
'Hierarchy of Stochastic Pure States for Open Quantum System Dynamics',
in: *Phys. Rev. Lett.* 113 (15 2014), p. 150403.

27 J. Smith:
'Viewpoint: Exploring Quantum Mpemba Effects',
in: *Phys. Rev. Lett.* Physics 17, 105 (2024).

28 A. Kumar and J. Bechhoefer:
'Exponentially faster cooling in a colloidal system',
in: *Nature* 584.7819 (Aug. 2020), pp. 64–68.

29 F. Carollo, A. Lasanta and I. Lesanovsky:
'Exponentially Accelerated Approach to Stationarity in Markovian Open Quantum Systems through the Mpemba Effect',
in: *Phys. Rev. Lett.* 127 (6 2021), p. 060401.

30 J. Neugebauer, M. Reiher, C. Kind and B. A. Hess:
'Quantum chemical calculation of vibrational spectra of large molecules—Raman and IR spectra for Buckminsterfullerene',
in: *Journal of Computational Chemistry* 23.9 (2002), pp. 895–910. eprint: `https://onlinelibrary.wiley.com/doi/pdf/10.1002/jcc.10089`.

31 J. Zheng, Y. Xie, S. Jiang and Z. Lan:
'Ultrafast Nonadiabatic Dynamics of Singlet Fission: Quantum Dynamics with the Multilayer Multiconfigurational Time-Dependent Hartree (ML-MCTDH) Method',
in: *J. Phys. Chem. C* 120.3 (2016), pp. 1375–1389.

32 S. Kihara, D. A. Hartzler, G. S. Orf, R. E. Blankenship and S. Savikhin:
'The Fate of the Triplet Excitations in the Fenna-Matthews-Olson Complex',
in: *The Journal of Physical Chemistry B* 119.18 (2015). PMID: 25856694, pp. 5765–5772. eprint: `https://doi.org/10.1021/jp512222c`.

33 S. Tretiak, C. Middleton, V. Chernyak and S. Mukamel:
'Bacteriochlorophyll and Carotenoid Excitonic Couplings in the LH2 System of Purple Bacteria',
in: *The Journal of Physical Chemistry B* 104.40 (2000), pp. 9540–9553. eprint: `https://doi.org/10.1021/jp001585m`.

34 C. Brockt, F. Dorfner, L. Vidmar, F. Heidrich-Meisner and E. Jeckelmann:
'Matrix-product-state method with a dynamical local basis optimization for bosonic systems out of equilibrium',
in: *Phys. Rev. B* 92 (24 2015), p. 241106.

35 T. Köhler, J. Stolpp and S. Paeckel:
'Efficient and flexible approach to simulate low-dimensional quantum lattice models with large local Hilbert spaces',
in: *SciPost Physics* 10.3 (2021). issn: 2542-4653.

36 M. Yang and S. R. White:
'Time-dependent variational principle with ancillary Krylov subspace',
in: *Phys. Rev. B* 102 (9 2020), p. 094315.

37 M. Grundner, T. Blatz, J. Sous, U. Schollwöck and S. Paeckel:
Cooper-Paired Bipolaronic Superconductors,
2023. arXiv: `2308.13427 [cond-mat.supr-con]`.

38 A. M. Lacerda, A. Purkayastha, M. Kewming, G. T. Landi and J. Goold:
'Quantum thermodynamics with fast driving and strong coupling via the mesoscopic leads approach',
in: *Phys. Rev. B* 107 (19 2023), p. 195117.

39 N. W. Ashcroft and N. D. Mermin:
Solid state physics,
New York, NY: Holt, Rinehart and Winston, 1976.

40 J. Bardeen, L. N. Cooper and J. R. Schrieffer:
'Theory of Superconductivity',
in: *Phys. Rev.* 108 (5 1957), pp. 1175–1204.

41 M. Mitrano et al.:
'Possible light-induced superconductivity in K3C60 at high temperature',
in: *Nature* 530.7591 (2016), pp. 461–464. issn: 1476-4687.

42 B. Liu, M. Först, M. Fechner, D. Nicoletti, J. Porras, T. Loew, B. Keimer and A. Cavalleri:
'Pump Frequency Resonances for Light-Induced Incipient Superconductivity in $YBa_2Cu_3O_{6.5}$',
in: *Phys. Rev. X* 10 (1 2020), p. 011053.

43 M. A. Sentef, A. F. Kemper, A. Georges and C. Kollath:
'Theory of light-enhanced phonon-mediated superconductivity',
in: *Phys. Rev. B* 93 (14 2016), p. 144506.

44 M. Babadi, M. Knap, I. Martin, G. Refael and E. Demler:
'Theory of parametrically amplified electron-phonon superconductivity',
in: *Phys. Rev. B* 96 (1 2017), p. 014512.

45 D. M. Kennes, E. Y. Wilner, D. R. Reichman and A. J. Millis:
'Transient superconductivity from electronic squeezing of optically pumped phonons',
in: *Nature Physics* 13.5 (2017), pp. 479–483. issn: 1745-2481.

46 C. J. Eckhardt, S. Chattopadhyay, D. M. Kennes, E. A. Demler, M. A. Sentef and M. H. Michael:
Theory of resonantly enhanced photo-induced superconductivity,
2023. arXiv: `2303.02176 [cond-mat.supr-con]`.

47 A. Chatterjee and Y. Takada:
'The Hubbard–Holstein Model with Anharmonic Phonons in One Dimension',
in: *Journal of the Physical Society of Japan* 73.4 (2004), pp. 964–969. eprint: `https://doi.org/10.1143/JPSJ.73.964`.

48 C. U. Lavanya, I. V. Sankar and A. Chatterjee:
'Metallicity in a Holstein-Hubbard Chain at Half Filling with Gaussian Anharmonicity',
in: *Scientific Reports* 7.1 (2017), p. 3774. issn: 2045-2322.

49 N. C. Costa, T. Blommel, W.-T. Chiu, G. Batrouni and R. T. Scalettar:
'Phonon Dispersion and the Competition between Pairing and Charge Order',
in: *Phys. Rev. Lett.* 120 (18 2018), p. 187003.

50 D. Jansen, J. Bonča and F. Heidrich-Meisner:
Finite-temperature optical conductivity with density-matrix renormalization group methods for the Holstein polaron and bipolaron with dispersive phonons,
2022.

51 C. Hubig, F. Lachenmaier, N.-O. Linden, T. Reinhard, L. Stenzel, A. Swoboda, M. Grundner and S. Mardazad:
The SyTen Toolkit.

52 C. Hubig:
'Symmetry-Protected Tensor Networks',
PhD thesis. LMU München, 2017.

53 D. Manzano:
'A short introduction to the Lindblad master equation',
in: *AIP Advances* 10.2 (2020).

54 P. Pearle:
'Simple derivation of the Lindblad equation',
in: *European Journal of Physics* 33.4 (2012), p. 805.

55 A. Peres:
'Separability Criterion for Density Matrices',
in: *Phys. Rev. Lett.* 77 (8 1996), pp. 1413–1415.

56 E.-M. Laine, J. Piilo and H.-P. Breuer:
'Measure for the non-Markovianity of quantum processes',
in: *Phys. Rev. A* 81 (6 2010), p. 062115.

57 G. T. Landi, D. Poletti and G. Schaller:
'Nonequilibrium boundary-driven quantum systems: Models, methods, and properties',
in: *Rev. Mod. Phys.* 94 (4 2022), p. 045006.

58 M. Am-Shallem, A. Levy, I. Schaefer and R. Kosloff:
Three approaches for representing Lindblad dynamics by a matrix-vector notation,
2015. arXiv: `1510.08634`.

59 V. V. Albert and L. Jiang:
'Symmetries and conserved quantities in Lindblad master equations',
in: *Phys. Rev. A* 89 (2 2014), p. 022118.

60 I. de Vega and D. Alonso:
'Dynamics of non-Markovian open quantum systems',
in: *Rev. Mod. Phys.* 89 (1 2017), p. 015001.

61 H. M. Wiseman and G. J. Milburn:
Quantum Measurement and Control,
Cambridge University Press, 2009.

62 D Suess, W. T. Strunz and A Eisfeld:
'Hierarchical Equations for Open System Dynamics in Fermionic and Bosonic Environments',
in: *Journal of Statistical Physics* 159.6 (June 2015), pp. 1408–1423.

63 M. Tezuka, R. Arita and H. Aoki:
'Phase diagram for the one-dimensional Hubbard-Holstein model: A density-matrix renormalization group study',
in: *Phys. Rev. B* 76 (15 2007), p. 155114.

64 Y. Xu, C. Liu and H. Ma:
'Hierarchical Mapping for Efficient Simulation of Strong System-Environment Interactions',
in: *J. Chem. Theory Comput.* 19.2 (Jan. 2023), pp. 426–435.

65 P. Nalbach, D. Braun and M. Thorwart:
'Exciton transfer dynamics and quantumness of energy transfer in the Fenna-Matthews-Olson complex',
in: *Phys. Rev. E* 84 (4 2011), p. 041926.

66 R. Hartmann and W. T. Strunz:
'Exact Open Quantum System Dynamics Using the Hierarchy of Pure States (HOPS)',
in: *Journal of Chemical Theory and Computation* 13.12 (2017), pp. 5834–5845. issn: 1549-9626.

67 S. Flannigan, F. Damanet and A. J. Daley:
'Many-Body Quantum State Diffusion for Non-Markovian Dynamics in Strongly Interacting Systems',
in: *Phys. Rev. Lett.* 128 (6 2022), p. 063601.

68 I. de Vega, D. Alonso and P. Gaspard:
'Two-level system immersed in a photonic band-gap material: A non-Markovian stochastic Schrödinger-equation approach',
in: *Phys. Rev. A* 71 (2 2005), p. 023812.

69 X. Gao, J. Ren, A. Eisfeld and Z. Shuai:
'Non-Markovian stochastic Schrödinger equation: Matrix-product-state approach to the hierarchy of pure states',
in: *Physical Review A* 105.3 (2022).

70 S. Shams Es-haghi and D. J. Gardner:
'A Critical Evaluation and Modification of the Padé–Laplace Method for Deconvolution of Viscoelastic Spectra',
in: *Molecules* 26.16 (2021). issn: 1420-3049.

71 A. Imamoglu:
'Stochastic wave-function approach to non-Markovian systems',
in: *Phys. Rev. A* 50 (5 1994), pp. 3650–3653.

72 B. M. Garraway:
'Nonperturbative decay of an atomic system in a cavity',
in: *Phys. Rev. A* 55 (3 1997), pp. 2290–2303.

73 J. E. Elenewski, D. Gruss and M. Zwolak:
'Communication: Master equations for electron transport: The limits of the Markovian limit',
in: *The Journal of Chemical Physics* 147.15 (Oct. 2017), p. 151101. issn: 0021-9606. eprint: `https://pubs.aip.org/aip/jcp/article-pdf/doi/10.1063/1.5000747/15534440/151101\_1\_online.pdf`.

74 G. Wojtowicz, J. E. Elenewski, M. M. Rams and M. Zwolak:
'Open-system tensor networks and Kramers' crossover for quantum transport',
in: *Phys. Rev. A* 101 (5 2020), p. 050301.

75 M. Brenes, J. J. Mendoza-Arenas, A. Purkayastha, M. T. Mitchison, S. R. Clark and J. Goold:
'Tensor-Network Method to Simulate Strongly Interacting Quantum Thermal Machines',
in: *Phys. Rev. X* 10 (3 2020), p. 031040.

76 S. Flannigan:
'The application of quantum simulation to topological and open many-body systems',
dissertation. University of Strathclyde, 2020.

77 U. Schollwöck:
'The density-matrix renormalization group',
in: *Rev. Mod. Phys.* 77 (1 2005), pp. 259–315.

78 S. Östlund and S. Rommer:
'Thermodynamic Limit of Density Matrix Renormalization',
in: *Phys. Rev. Lett.* 75 (19 1995), pp. 3537–3540.

79 U. Schollwöck:
'DMRG: Ground States, Time Evolution, and Spectral Functions',
in: *Emergent Phenomena in Correlated Matter.* Forschungszentrum Jülich GmbH Institute for Advanced Simulation, 2013. Chap. 16.

80 J. Eisert, M. Cramer and M. B. Plenio:
'Colloquium: Area laws for the entanglement entropy',
in: *Rev. Mod. Phys.* 82 (1 2010), pp. 277–306.

81 J. Haegeman, C. Lubich, I. Oseledets, B. Vandereycken and F. Verstraete:
'Unifying time evolution and optimization with matrix product states',
in: *Phys. Rev. B* 94 (16 2016), p. 165116.

82 S. Paeckel, T. Köhler, A. Swoboda, S. R. Manmana, U. Schollwöck and C. Hubig:
'Time-evolution methods for matrix-product states',
in: *Annals of Physics* 411 (2019), p. 167998. issn: 0003-4916.

83 Y. Xu, Z. Xie, X. Xie, U. Schollwöck and H. Ma:
'Stochastic Adaptive Single-Site Time-Dependent Variational Principle',
in: *JACS Au* 2.2 (2022), pp. 335–340. eprint: `https://doi.org/10.1021/jacsau.1c00474`.

84 S. Mardazad, Y. Xu, X. Yang, M. Grundner, U. Schollwöck, H. Ma and S. Paeckel:
'Quantum dynamics simulation of intramolecular singlet fission in covalently linked tetracene dimer',
in: *The Journal of Chemical Physics* 155.19 (2021), p. 194101. issn: 1089-7690.

85 C. Hubig, I. P. McCulloch, U. Schollwöck and F. A. Wolf:
'Strictly single-site DMRG algorithm with subspace expansion',
in: *Phys. Rev. B* 91 (15 2015), p. 155115.

86 M. Yang and S. R. White:
Time-dependent variational principle with ancillary Krylov subspace,
Sept. 2020. arXiv: `2005.08821 [cond-mat.str-el]`.

87 S. Singh, R. N. C. Pfeifer and G. Vidal:
'Tensor network states and algorithms in the presence of a global U(1) symmetry',
in: *Phys. Rev. B* 83 (11 2011), p. 115125.

88 S. Mardazad:
Simulating real molecules with tensor network techniques,
2022.

89 J. Hauschild, E. Leviatan, J. H. Bardarson, E. Altman, M. P. Zaletel and F. Pollmann:
'Finding purifications with minimal entanglement',
in: *Phys. Rev. B* 98 (23 2018), p. 235163.

90 H. P. Casagrande, D. Poletti and G. T. Landi:
'Analysis of a density matrix renormalization group approach for transport in open quantum systems',
in: *Computer Physics Communications* 267 (2021), p. 108060. issn: 0010-4655.

91 B. Debecker, J. Martin and F. Damanet:
Spectral Theory of Non-Markovian Dissipative Phase Transitions,
2023. arXiv: `2307.01119 [quant-ph]`.

92 M. Kliesch, D. Gross and J. Eisert:
'Matrix-Product Operators and States: NP-Hardness and Undecidability',
in: *Phys. Rev. Lett.* 113 (16 2014), p. 160503.

93 A. H. Werner, D. Jaschke, P. Silvi, M. Kliesch, T. Calarco, J. Eisert and S. Montangero:
'Positive Tensor Network Approach for Simulating Open Quantum Many-Body Systems',
in: *Phys. Rev. Lett.* 116 (23 2016), p. 237201.

94 S. Paeckel, T. Köhler and S. R. Manmana:
'Automated construction of $U(1)$-invariant matrix-product operators from graph representations',
in: *SciPost Phys.* 3 (2017), p. 035.

95 M. Kornyik and A. Vukics:
'The Monte Carlo wave-function method: A robust adaptive algorithm and a study in convergence',
in: *Computer Physics Communications* 238 (2019), pp. 88–101. issn: 0010-4655.

96 S. Mardazad:
'Private Communications',
Unpublished results. 2021.

97 R. V. Dyukin, G. A. Martsinovskiy, O. N. Sergaeva, G. D. Shandybina, V. V. Svirina and E. B. Yakovlev:
'Interaction of Femtosecond Laser Pulses with Solids: Electron/Phonon/Plasmon Dynamics',
in: *Laser Pulses.* Ed. by I. Peshko. Rijeka: IntechOpen, 2012. Chap. 7.

98 O. Busch, F. Ziolkowski, I. Mertig and J. Henk:
'Ultrafast dynamics of electrons excited by femtosecond laser pulses: Spin polarization and spin-polarized currents',
in: *Phys. Rev. B* 108 (18 2023), p. 184401.

99 T. F. Nova, A Cartella, A Cantaluppi, M Först, D Bossini, R. V. Mikhaylovskiy, A. V. Kimel, R Merlin and A Cavalleri:
'An effective magnetic field from optically driven phonons',
in: *Nat. Phys.* 13.2 (2017), pp. 132–136.

100 G. Khalsa, N. A. Benedek and J. Moses:
'Ultrafast Control of Material Optical Properties via the Infrared Resonant Raman Effect',
in: *Phys. Rev. X* 11 (2 2021), p. 021067.

101 D. Fausti, R. I. Tobey, N. Dean, S. Kaiser, A. Dienst, M. C. Hoffmann, S. Pyon, T. Takayama, H. Takagi and A. Cavalleri:
'Light-Induced Superconductivity in a Stripe-Ordered Cuprate',
in: *Science* 331.6014 (2011), pp. 189–191. eprint: `https://www.science.org/doi/pdf/10.1126/science.1197294`.

102 M. Budden et al.:
'Evidence for metastable photo-induced superconductivity in K3C60',
in: *Nature Physics* 17.5 (2021), pp. 611–618. issn: 1745-2481.

103 A. Bohrdt, C. S. Chiu, G. Ji, M. Xu, D. Greif, M. Greiner, E. Demler, F. Grusdt and M. Knap:
'Classifying snapshots of the doped Hubbard model with machine learning',
in: *Nature Physics* 15.9 (2019), pp. 921–924.

104 A. Bohrdt, S. Kim, A. Lukin, M. Rispoli, R. Schittko, M. Knap, M. Greiner and J. Léonard:
'Analyzing Nonequilibrium Quantum States through Snapshots with Artificial Neural Networks',
in: *Phys. Rev. Lett.* 127 (15 2021), p. 150504.

105 A. Bohrdt, L. Homeier, C. Reinmoser, E. Demler and F. Grusdt:
'Exploration of doped quantum magnets with ultracold atoms',
in: *Annals of Physics* 435 (2021). Special issue on Philip W. Anderson, p. 168651. issn: 0003-4916.

106 M. Buser, U. Schollwöck and F. Grusdt:
'Snapshot-based characterization of particle currents and the Hall response in synthetic flux lattices',
in: *Physical Review A* 105.3 (2022).

107 F. A. Palm, S. Mardazad, A. Bohrdt, U. Schollwöck and F. Grusdt:
'Snapshot-based detection of $\nu = \frac{1}{2}$ Laughlin states: Coupled chains and central charge',
in: *Physical Review B* 106.8 (Aug. 2022), p. L081108.

108 F. J. Pauw, F. A. Palm, U. Schollwöck, A. Bohrdt, S. Paeckel and F. Grusdt:
Detecting Hidden Order in Fractional Chern Insulators,
2023. arXiv: `2309.03666 [cond-mat.quant-gas]`.

109 S. Hirthe, T. Chalopin, D. Bourgund, P. Bojović, A. Bohrdt, E. Demler, F. Grusdt, I. Bloch and T. A. Hilker:
'Magnetically mediated hole pairing in fermionic ladders of ultracold atoms',
in: *Nature* 613.7944 (2023), pp. 463–467.

110 A. J. Ferris and G. Vidal:
'Perfect sampling with unitary tensor networks',
in: *Physical Review B* 85.16 (2012).

111 T Holstein:
'Studies of polaron motion: Part I. The molecular-crystal model',
in: *Ann. Phys.* 8.3 (1959), pp. 325–342. issn: 0003-4916.

112 X. Li:
Markovian Embedding Procedures for Non-Markovian Stochastic Schrödinger Equations,
2020. arXiv: `2005.00103 [physics.comp-ph]`.

113 V. Link, K. Müller, R. G. Lena, K. Luoma, F. m. c. Damanet, W. T. Strunz and A. J. Daley:
'Non-Markovian Quantum Dynamics in Strongly Coupled Multimode Cavities Conditioned on Continuous Measurement',
in: *PRX Quantum* 3 (2 2022), p. 020348.

114 E. B. Mpemba and D. G. Osborne:
'Cool?',
in: *Phys. Educ.* 4.3 (1969), p. 172.

115 G. S. Kell:
'The Freezing of Hot and Cold Water',
in: *Am. J. Phys.* 37.5 (May 1969), pp. 564–565. issn: 0002-9505.

116 Aristotle and H. D. L. P.:
'Book I Chapter XII',
in: *Meteorologica. with an English translation.* Harvard University Press, 1952, pp. 79–86.

117 Descartes, René and 1596-:
Discourse on method,
New York : Macmillan ; London : Collier Macmillan, 1986., 1986.

118 F. Bacon:
Novum Organum,
ed. by M. Joseph Devey. New York: P.F. Collier, 1902.

119 P. Chaddah, S. Dash, K. Kumar and A. Banerjee:
Overtaking while approaching equilibrium,
2010. arXiv: `1011.3598`.

120 P. A. Greaney, G. Lani, G. Cicero and J. C. Grossman:
'Mpemba-Like Behavior in Carbon Nanotube Resonators',
in: *Metall. Mater. Trans. A* 42.13 (Dec. 2011), pp. 3907–3912.

121 Y.-H. Ahn, H. Kang, D.-Y. Koh and H. Lee:
'Experimental verifications of Mpemba-like behaviors of clathrate hydrates',
in: *Korean J. Chem. Eng.* 33.6 (2016), pp. 1903–1907.

122 A. Lasanta, F. Vega Reyes, A. Prados and A. Santos:
'When the Hotter Cools More Quickly: Mpemba Effect in Granular Fluids',
in: *Phys. Rev. Lett.* 119 (14 2017), p. 148001.

123 C. Hu, J. Li, S. Huang, H. Li, C. Luo, J. Chen, S. Jiang and L. An:
'Conformation Directed Mpemba Effect on Polylactide Crystallization',
in: *Cryst. Growth Des.* 18.10 (2018), pp. 5757–5762.

124 T. Keller, V. Torggler, S. B. Jäger, S. Schütz, H. Ritsch and G. Morigi:
'Quenches across the self-organization transition in multimode cavities',
in: *New J. Phys.* 20.2 (2018), p. 025004.

125 H. C. Burridge and P. F. Linden:
'Questioning the Mpemba effect: hot water does not cool more quickly than cold',
in: *Sci. Rep.* 6.1 (Nov. 2016), p. 37665.

126 J. Bechhoefer, A. Kumar and R. Chétrite:
'A fresh understanding of the Mpemba effect',
in: *Nat. Rev. Phys.* 3.8 (Aug. 2021), pp. 534–535.

127 Z. Lu and O. Raz:
'Nonequilibrium thermodynamics of the Markovian Mpemba effect and its inverse',
in: *Proceedings of the National Academy of Sciences* 114.20 (2017), pp. 5083–5088.

128 I. Klich, O. Raz, O. Hirschberg and M. Vucelja:
'Mpemba Index and Anomalous Relaxation',
in: *Phys. Rev. X* 9 (2 2019), p. 021060.

129 A. Kumar, R. Chétrite and J. Bechhoefer:
'Anomalous heating in a colloidal system',
in: *PNAS* 119.5 (2022), e2118484119.

130 A. Nava and M. Fabrizio:
'Lindblad dissipative dynamics in the presence of phase coexistence',
in: *Phys. Rev. B* 100 (12 2019), p. 125102.

131 R. Bao and Z. Hou:
Accelerating relaxation in Markovian open quantum systems through quantum reset processes,
2022. arXiv: `2212.11170`.

132 S. K. Manikandan:
'Equidistant quenches in few-level quantum systems',
in: *Phys. Rev. Res.* 3 (4 2021), p. 043108.

133 S. Kochsiek, F. Carollo and I. Lesanovsky:
'Accelerating the approach of dissipative quantum spin systems towards stationarity through global spin rotations',
in: *Phys. Rev. A* 106 (1 2022), p. 012207.

134 F. Ivander, N. Anto-Sztrikacs and D. Segal:
'Hyperacceleration of quantum thermalization dynamics by bypassing long-lived coherences: An analytical treatment',
in: *Phys. Rev. E* 108 (1 2023), p. 014130.

135 A. K. Chatterjee, S. Takada and H. Hayakawa:
'Quantum Mpemba Effect in a Quantum Dot with Reservoirs',
in: *Phys. Rev. Lett.* 131 (8 2023), p. 080402.

136 A. K. Chatterjee, S. Takada and H. Hayakawa:
Multiple quantum Mpemba effect: exceptional points and oscillations,
2023. arXiv: `2311.01347`.

137 X. Wang and J. Wang:
Mpemba effects in nonequilibrium open quantum systems,
2024. arXiv: `2401.14259`.

138 F. Caceffo, S. Murciano and V. Alba:
Entangled multiplets, asymmetry, and quantum Mpemba effect in dissipative systems,
2024. arXiv: `2402.02918`.

139 D. J. Strachan, A. Purkayastha and S. R. Clark:
Non-Markovian Quantum Mpemba effect,
2024. arXiv: `2402.05756`.

140 S. A. Shapira, Y. Shapira, J. Markov, G. Teza, N. Akerman, O. Raz and R. Ozeri:
The Mpemba effect demonstrated on a single trapped ion qubit,
2024. arXiv: `2401.05830`.

141 J. Zhang et al.:
Observation of quantum strong Mpemba effect,
2024. arXiv: `2401.15951`.

142 F. Ares, S. Murciano and P. Calabrese:
'Entanglement asymmetry as a probe of symmetry breaking',
in: *Nat. Commun.* 14.1 (Apr. 2023), p. 2036.

143 S. Murciano, F. Ares, I. Klich and P. Calabrese:
'Entanglement asymmetry and quantum Mpemba effect in the XY spin chain',
in: *J. Stat. Mech.* 2024.1 (Jan. 2024), p. 013103. issn: 1742-5468.

144 S. Yamashika, F. Ares and P. Calabrese:
Entanglement asymmetry and quantum Mpemba effect in two-dimensional free-fermion systems,
2024. arXiv: `2403.04486`.

145 S. Liu, H.-K. Zhang, S. Yin and S.-X. Zhang:
Symmetry restoration and quantum Mpemba effect in symmetric random circuits,
2024. arXiv: `2403.08459 [quant-ph]`.

146 L. K. Joshi et al.:
Observing the quantum Mpemba effect in quantum simulations,
2024. arXiv: `2401.04270`.

147 E. Davies:
'Generators of dynamical semigroups',
in: *J. Funct. Anal.* 34.3 (1979), pp. 421–432. issn: 0022-1236.

148 W. Roga, M. Fannes and K. Życzkowski:
'Davies maps for qubits and qutrits',
in: *Rep. Math. Phys.* 66.3 (2010), pp. 311–329. issn: 0034-4877.

149 R. Alicki:
'On the detailed balance condition for non-Hamiltonian systems',
in: *Rep. Math. Phys.* 10.2 (1976), pp. 249–258.

150 M. J. Donald:
'Free energy and the relative entropy',
in: *J. Stat. Phys.* 49 (1987), pp. 81–87.

151 M. Esposito and C. Van den Broeck:
'Second law and Landauer principle far from equilibrium',
in: *EPL* 95.4 (2011), p. 40004.

152 J. M. Parrondo, J. M. Horowitz and T. Sagawa:
'Thermodynamics of information',
in: *Nat. Phys.* 11.2 (2015), pp. 131–139.

153 J. P. Santos, L. C. Céleri, G. T. Landi and M. Paternostro:
'The role of quantum coherence in non-equilibrium entropy production',
in: *npj Quantum Inf* 5.1 (Mar. 2019), p. 23.

154 G. Francica, J. Goold and F. Plastina:
'Role of coherence in the nonequilibrium thermodynamics of quantum systems',
in: *Phys. Rev. E* 99 (4 2019), p. 042105.

155 A. Streltsov, G. Adesso and M. B. Plenio:
'Colloquium: Quantum coherence as a resource',
in: *Rev. Mod. Phys.* 89 (4 2017), p. 041003.

156 Q.-F. Xue, X.-C. Zhuang, D.-Y. Duan, Y.-J. Zhang, W.-B. Yan, Y.-J. Xia, R. L. Franco and Z.-X. Man:
Evidence of genuine quantum effects in nonequilibrium entropy production,
2024. arXiv: `2402.06858 [quant-ph]`.

157 G. Hardy, J. Littlewood and G. Pólya:
Inequalities,
2nd. Reviewed in The Mathematical Gazette, 1953;37(321):236-236. doi:10.1017/S0025557200027455. Cambridge University Press, 1952.

158 G. Deçordi and A. Vidiella-Barranco:
'Two coupled qubits interacting with a thermal bath: A comparative study of different models',
in: *Optics Communications* 387 (2017), pp. 366–376. issn: 0030-4018.

159 R. Dann and R. Kosloff:
'Open system dynamics from thermodynamic compatibility',
in: *Phys. Rev. Res.* 3 (2 2021), p. 023006.

160 G. Paule:
Thermodynamics and Synchronization in Open Quantum Systems,
Springer Theses. Springer International Publishing, 2018. isbn: 9783319939636.

161 A. Vaaranta, M. Cattaneo and R. E. Lake:
'Dynamics of a dispersively coupled transmon qubit in the presence of a noise source embedded in the control line',
in: *Phys. Rev. A* 106 (4 2022), p. 042605.

162 M. Papič, A. Auer and I. de Vega:
Fast Estimation of Physical Error Contributions of Quantum Gates,
2023. arXiv: `2305.08916 [quant-ph]`.

163 H. P. Breuer and F. Petruccione:
The theory of open quantum systems,
Great Clarendon Street: Oxford University Press, 2002.

164 M. Josefsson, A. Svilans, A. M. Burke, E. A. Hoffmann, S. Fahlvik, C. Thelander, M. Leijnse and H. Linke:
‘A quantum-dot heat engine operating close to the thermodynamic efficiency limits’,
in: *Nature Nanotechnology* 13.10 (Oct. 2018), pp. 920–924.

165 N. Metropolis, A. W. Rosenbluth, M. N. Rosenbluth, A. H. Teller and E. Teller:
‘Equation of State Calculations by Fast Computing Machines’,
in: *jcp* 21.6 (June 1953), pp. 1087–1092.

166 W. H. Press, S. A. Teukolsky, W. T. Vetterling and B. P. Flannery:
Numerical recipes in C (2nd ed.): the art of scientific computing,
USA: Cambridge University Press, 1992. isbn: 0521431085.

167 M. Ringbauer, M. Meth, L. Postler, R. Stricker, R. Blatt, P. Schindler and T. Monz:
‘A universal qudit quantum processor with trapped ions’,
in: *Nat. Phys.* 18.9 (Sept. 2022), pp. 1053–1057.

168 R. Schmied:
Maximize Over Permutations,
Wolfram Function Repository. `https://resources.wolframcloud.com/FunctionRepository/resources/MaximizeOverPermutations`. 2019.

169 F. Verstraete, M. M. Wolf and J. Ignacio Cirac:
‘Quantum computation and quantum-state engineering driven by dissipation’,
in: *Nature Physics* 5.9 (2009), pp. 633–636. issn: 1745-2481.

170 P. M. Harrington, E. J. Mueller and K. W. Murch:
‘Engineered dissipation for quantum information science’,
in: *Nat. Rev. Phys.* 4.10 (Aug. 2022), pp. 660–671. issn: 2522-5820.

171 M. E. Edo and L.-A. Wu:
Study on quantum thermalization from thermal initial states in a superconducting quantum computer,
2024. arXiv: `2403.14630`.

172 F. Schreck and K. van Druten:
‘Laser cooling for quantum gases’,
in: *Nature Physics* 17.12 (Dec. 2021), pp. 1296–1304.

173 S. D. Fallek, V. S. Sandhu, R. A. McGill, J. M. Gray, H. N. Tinkey, C. R. Clark and K. R. Brown:
‘Rapid exchange cooling with trapped ions’,
in: *Nature Communications* 15.1 (Feb. 2024), p. 1089.

174 M. Scandi and M. Perarnau-Llobet:
‘Thermodynamic length in open quantum systems’,
in: *Quantum* 3 (Oct. 2019), p. 197. issn: 2521-327X.

175 M Ibáñez, C Dieball, A Lasanta, A Godec and R. A. Rica:
‘Heating and cooling are fundamentally asymmetric and evolve along distinct pathways’,
in: *Nature Physics* 20.1 (Jan. 2024), pp. 135–141.

176 T. Reinot, A. Khmelnitskiy, A. Kell, M. Jassas and R. Jankowiak:
'Exciton Lifetime Distributions and Population Dynamics in the FMO Protein Complex from Prosthecochloris aestuarii',
in: *ACS Omega* 6.8 (2021), pp. 5990–6008. eprint: `https://doi.org/10.1021/acsomega.1c00286`.

177 W. Ni, L. Sun and G. G. Gurzadyan:
'Ultrafast spectroscopy reveals singlet fission, ionization and excimer formation in perylene film',
in: *Scientific Reports* 11.1 (2021), p. 5220.

178 J. Dostál, F. Fennel, F. Koch, S. Herbst, F. Würthner and T. Brixner:
'Direct observation of exciton–exciton interactions',
in: *Nature Communications* 9.1 (2018), p. 2466.

179 H.-D. Meyer, U. Manthe and L. Cederbaum:
'The multi-configurational time-dependent Hartree approach',
in: *Chemical Physics Letters* 165.1 (1990), pp. 73–78. issn: 0009-2614.

180 X. Xie, Y. Liu, Y. Yao, U. Schollwöck, C. Liu and H. Ma:
'Time-dependent density matrix renormalization group quantum dynamics for realistic chemical systems',
in: *The Journal of Chemical Physics* 151.22 (Dec. 2019), p. 224101. issn: 0021-9606. eprint: `https://pubs.aip.org/aip/jcp/article-pdf/doi/10.1063/1.5125945/13331146/224101\_1\_online.pdf`.

181 Q. Shi, Y. Xu, Y. Yan and M. Xu:
'Efficient propagation of the hierarchical equations of motion using the matrix product state method',
in: *The Journal of Chemical Physics* 148.17 (May 2018), p. 174102. issn: 0021-9606. eprint: `https://pubs.aip.org/aip/jcp/article-pdf/doi/10.1063/1.5026753/15539991/174102\_1\_online.pdf`.

182 N. Makri and D. E. Makarov:
'Tensor propagator for iterative quantum time evolution of reduced density matrices. II. Numerical methodology',
in: *The Journal of Chemical Physics* 102.11 (Mar. 1995), pp. 4611–4618. issn: 0021-9606. eprint: `https://pubs.aip.org/aip/jcp/article-pdf/102/11/4611/8103115/4611\_1\_online.pdf`.

183 M. C. Hanna and A. J. Nozik:
'Solar conversion efficiency of photovoltaic and photoelectrolysis cells with carrier multiplication absorbers',
in: *Journal of Applied Physics* 100.7 (Oct. 2006), p. 074510. issn: 0021-8979. eprint: `https://pubs.aip.org/aip/jap/article-pdf/doi/10.1063/1.2356795/14977645/074510\_1\_online.pdf`.

184 D. N. Congreve, J. Lee, N. J. Thompson, E. Hontz, S. R. Yost, P. D. Reusswig, M. E. Bahlke, S. Reineke, T. V. Voorhis and M. A. Baldo:
'External Quantum Efficiency Above 100% in a Singlet-Exciton-Fission-Based Organic Photovoltaic Cell',
in: *Science* 340.6130 (2013), pp. 334–337. eprint: `https://www.science.org/doi/pdf/10.1126/science.1232994`.

185 F. Fassioli, R. Dinshaw, P. C. Arpin and G. D. Scholes:
'Photosynthetic light harvesting: excitons and coherence',
in: *Journal of the Royal Society Interface* 11.92 (2014), p. 20130901.

186 R. M. Clegg, M. Sener and. Govindjee:
'From Förster resonance energy transfer to coherent resonance energy transfer and back', in: *Optical Biopsy VII.* Ed. by R. R. Alfano. Vol. 7561. International Society for Optics and Photonics. SPIE, 2010, p. 75610C.

187 G. S. Engel, T. R. Calhoun, E. L. Read, T.-K. Ahn, T. Mančal, Y.-C. Cheng, R. E. Blankenship and G. R. Fleming:
'Evidence for wavelike energy transfer through quantum coherence in photosynthetic systems',
in: *Nature* 446.7137 (2007), pp. 782–786.

188 E. Collini, C. Y. Wong, K. E. Wilk, P. M. G. Curmi, P. Brumer and G. D. Scholes:
'Coherently wired light-harvesting in photosynthetic marine algae at ambient temperature',
in: *Nature* 463.7281 (2010), pp. 644–647.

189 D. M. Wilkins and N. S. Dattani:
'Why Quantum Coherence Is Not Important in the Fenna-Matthews-Olsen Complex',
in: *Journal of Chemical Theory and Computation* 11.7 (2015), pp. 3411–3419. eprint: `https://doi.org/10.1021/ct501066k`.

190 H.-G. Duan, V. I. Prokhorenko, R. J. Cogdell, K. Ashraf, A. L. Stevens, M. Thorwart and R. J. D. Miller:
'Nature does not rely on long-lived electronic quantum coherence for photosynthetic energy transfer',
in: *Proceedings of the National Academy of Sciences* 114.32 (2017), pp. 8493–8498. eprint: `1610.08425`.

191 I. de Vega and M.-C. Bañuls:
'Thermofield-based chain-mapping approach for open quantum systems',
in: *Phys. Rev. A* 92 (5 2015), p. 052116.

192 B. Yan, S. A. Moses, B. Gadway, J. P. Covey, K. R. A. Hazzard, A. M. Rey, D. S. Jin and J. Ye:
'Observation of dipolar spin-exchange interactions with lattice-confined polar molecules',
in: *Nature* 501.7468 (Sept. 2013), pp. 521–525. issn: 1476-4687.

193 M. Grundner, P. Westhoff, F. B. Kugler, O. Parcollet and U. Schollwöck:
'Complex time evolution in tensor networks and time-dependent Green's functions',
in: *Phys. Rev. B* 109 (15 2024), p. 155124.

194 K. Gunst, F. Verstraete, S. Wouters, O. Legeza and D. Van Neck:
'T3NS: Three-Legged Tree Tensor Network States',
in: *Journal of Chemical Theory and Computation* 14.4 (2018), pp. 2026–2033. issn: 1549-9626.

195 M. Rini, R. Tobey, N. Dean, J. Itatani, Y. Tomioka, Y. Tokura, R. W. Schoenlein and A. Cavalleri:
'Control of the electronic phase of a manganite by mode-selective vibrational excitation',
in: *Nature* 449.7158 (2007), pp. 72–74.

196 M. Först, C. Manzoni, S. Kaiser, Y. Tomioka, Y. Tokura, R. Merlin and A. Cavalleri:
'Nonlinear phononics as an ultrafast route to lattice control',
in: *Nature Physics* 7.11 (2011), pp. 854–856.

197 A. Subedi, A. Cavalleri and A. Georges:
'Theory of nonlinear phononics for coherent light control of solids',
in: *Phys. Rev. B* 89 (22 2014), p. 220301.

198 J. Sous, B. Kloss, D. M. Kennes, D. R. Reichman and A. J. Millis:
'Phonon-induced disorder in dynamics of optically pumped metals from nonlinear electron-phonon coupling',
in: *Nature Communications* 12.1 (2021).

199 W Hu, S Kaiser, D Nicoletti, C. R. Hunt, I Gierz, M. C. Hoffmann, M Le Tacon, T Loew, B Keimer and A Cavalleri:
'Optically enhanced coherent transport in $YBa_2Cu_3O_{6.5}$ by ultrafast redistribution of interlayer coupling',
in: *Nat. Mater.* 13 (May 2014), pp. 705–711.

200 R. Mankowsky et al.:
'Nonlinear lattice dynamics as a basis for enhanced superconductivity in $YBa_2Cu_3O_6$.5',
in: *Nature* 516.7529 (2014), pp. 71–73. issn: 1476-4687.

201 R Mankowsky, M Först, T Loew, J Porras, B Keimer and A Cavalleri:
'Coherent modulation of the $YBa_2Cu_3O_{6+x}$ atomic structure by displacive stimulated ionic Raman scattering',
in: *Phys. Rev. B* 91.9 (2015), p. 094308.

202 E. Rowe et al.:
'Resonant enhancement of photo-induced superconductivity in K_3C_{60}',
in: *Nat. Phys.* (2023). issn: 1745-2481.

203 M. Knap, M. Babadi, G. Refael, I. Martin and E. Demler:
'Dynamical Cooper pairing in nonequilibrium electron-phonon systems',
in: *Phys. Rev. B* 94 (21 2016), p. 214504.

204 S. Paeckel, B. Fauseweh, A. Osterkorn, T. Köhler, D. Manske and S. R. Manmana:
'Detecting superconductivity out of equilibrium',
in: *Phys. Rev. B* 101 (18 2020), p. 180507.

205 M. Trigo, J. Chen, V. H. Vishwanath, Y. M. Sheu, T. Graber, R. Henning and D. A. Reis:
'Imaging nonequilibrium atomic vibrations with x-ray diffuse scattering',
in: *Phys. Rev. B* 82 (23 2010), p. 235205.

206 M Trigo et al.:
'Fourier-transform inelastic X-ray scattering from time- and momentum-dependent phonon–phonon correlations',
in: *Nat. Phys.* 9.12 (Dec. 2013), pp. 790–794.

207 T. Konstantinova et al.:
'Nonequilibrium electron and lattice dynamics of strongly correlated Bi2Sr2CaCu2O8+δ single crystals',
in: *Sci. Adv.* 4.4 (Apr. 2018), eaap7427.

208 R. Xu and T. C. Chiang:
'Determination of phonon dispersion relations by X-ray thermal diffuse scattering',
in: *Z. Kristallogr. - Cryst. Mater.* 220.12 (2005), pp. 1009–1016.

209 R. Mankowsky, M. Först and A. Cavalleri:
'Non-equilibrium control of complex solids by nonlinear phononics',
in: *Reports on Progress in Physics* 79.6 (2016), p. 064503.

210 T. Giamarchi:
Quantum Physics in One Dimension,
Oxford University Press, Dec. 2003. isbn: 9780198525004.

211 J. Greitemann, S. Hesselmann, S. Wessel, F. F. Assaad and M. Hohenadler:
'Finite-size effects in Luther-Emery phases of Holstein and Hubbard models',
in: *Phys. Rev. B* 92 (24 2015), p. 245132.

212 R. T. Clay and R. P. Hardikar:
'Intermediate Phase of the One Dimensional Half-Filled Hubbard-Holstein Model',
in: *Phys. Rev. Lett.* 95 (9 2005), p. 096401.

213 M. Weber, F. F. Assaad and M. Hohenadler:
'Phonon spectral function of the one-dimensional Holstein-Hubbard model',
in: *Phys. Rev. B* 91 (23 2015), p. 235150.

214 T. E. Reinhard, U. Mordovina, C. Hubig, J. S. Kretchmer, U. Schollwöck, H. Appel, M. A. Sentef and A. Rubio:
'Density-Matrix Embedding Theory Study of the One-Dimensional Hubbard–Holstein Model',
in: *Journal of Chemical Theory and Computation* 15.4 (2019), pp. 2221–2232.

215 D. Jansen, C. Jooss and F. Heidrich-Meisner:
'Charge density wave breakdown in a heterostructure with electron-phonon coupling',
in: *Physical Review B* 104.19 (2021).

216 M. ten Brink, S. Gräber, M. Hopjan, D. Jansen, J. Stolpp, F. Heidrich-Meisner and P. E. Blöchl:
'Real-time non-adiabatic dynamics in the one-dimensional Holstein model: Trajectory-based vs exact methods',
in: *The Journal of Chemical Physics* 156.23 (June 2022), p. 234109. issn: 0021-9606.

217 Y. Takada and A. Chatterjee:
'Possibility of a metallic phase in the charge-density-wave–spin-density-wave crossover region in the one-dimensional Hubbard-Holstein model at half filling',
in: *Phys. Rev. B* 67 (8 2003), p. 081102.

218 W. Koller, D. Meyer, A. Hewson and Y. Ōno:
'Phase diagram and dynamic response functions of the Holstein–Hubbard model',
in: *Physica B: Condensed Matter* 359-361 (2005), pp. 795–797.

219 R. P. Hardikar and R. T. Clay:
'Phase diagram of the one-dimensional Hubbard-Holstein model at half and quarter filling',
in: *Phys. Rev. B* 75 (24 2007), p. 245103.

220 I. Lang and Y. A. Firsov:
'Kinetic theory of semiconductors with low mobility',
in: *Sov. Phys. JETP* 16.5 (1963), p. 1301.

221 M. Frick, I. Morgenstern and W. von der Linden:
'High-temperature superconductivity in the apex-oxygen model: a quantum Monte Carlo study',
in: *Zeitschrift für Physik B Condensed Matter* 82 (1991), pp. 339–345.

222 O. S. Barišić and S. Barišić:
'Bipolarons and polarons in the Holstein-Hubbard model: analogies and differences',
in: *The European Physical Journal B* 85.3 (2012).

223 I. Souza, T. Wilkens and R. M. Martin:
'Polarization and localization in insulators: Generating function approach',
in: *Phys. Rev. B* 62 (3 2000), pp. 1666–1683.

224 E. V. H. Doggen, Y. Gefen, I. V. Gornyi, A. D. Mirlin and D. G. Polyakov:
'Generalized quantum measurements with matrix product states: Entanglement phase transition and clusterization',
in: *Phys. Rev. Research* 4 (2 2022), p. 023146.

225 Y. Li, X. Chen and M. P. A. Fisher:
'Quantum Zeno effect and the many-body entanglement transition',
in: *Phys. Rev. B* 98 (20 2018), p. 205136.

226 M. G. Makris and P. Lambropoulos:
'Quantum Zeno effect by indirect measurement: The effect of the detector',
in: *Phys. Rev. A* 70 (4 2004), p. 044101.

227 S. Wallentowitz and P. E. Toschek:
'Comment on "Impossibility of distant indirect measurement of the quantum Zeno effect"',
in: *Phys. Rev. A* 72 (4 2005), p. 046101.

228 F. Minganti and D. Huybrechts:
'Arnoldi-Lindblad time evolution: Faster-than-the-clock algorithm for the spectrum of time-independent and Floquet open quantum systems',
in: *Quantum* 6 (2022), p. 649. issn: 2521-327X.

229 Y. Tanimura and R. Kubo:
'Time Evolution of a Quantum System in Contact with a Nearly Gaussian-Markoffian Noise Bath',
in: *Journal of the Physical Society of Japan* 58.1 (1989), pp. 101–114. eprint: `https://doi.org/10.1143/JPSJ.58.101`.

230 M. Planck:
'Vom Relativen zum Absoluten',
in: *Naturwissenschaften* 13.3 (Jan. 1925), pp. 53–59.

231 *Dedication of Ryerson Physical Laboratory*,
Quoted in Annual Register 1896, p. 159. 1894.

232 P. A. M. Dirac:
'Quantum Mechanics of Many-Electron Systems',
in: *Proceedings of The Royal Society A: Mathematical, Physical and Engineering Sciences* 123 (1929), pp. 714–733.

233 F. Benatti:
Dynamics, information and complexity in quantum systems,
vol. 2009. Jan. 2009. isbn: 978-1-4020-9305-0.

234 S. H. Simon:
Topological Quantum,
Oxford University Press, Sept. 2023. isbn: 978-0-19-888672-3.

235 B. C. Hall:
Lie Groups, Lie Algebras, and Representations,
Springer, 2015. isbn: 978-3-319-13467-3.

236 M. Manhart:
Markov Processes,
Rutgers University. 2016.

237 D. Debnath, M. Z. Malik and A. Chatterjee:
'A semi exact solution for a metallic phase in a Holstein-Hubbard chain at half filling with Gaussian anharmonic phonons',
in: *Scientific Reports* 11.1 (2021), p. 12305. issn: 2045-2322.

238 J. Sous, M. Chakraborty, R. V. Krems and M. Berciu:
'Light Bipolarons Stabilized by Peierls Electron-Phonon Coupling',
in: *Phys. Rev. Lett.* 121 (24 2018), p. 247001.

239 A. Nocera, J. Sous, A. E. Feiguin and M. Berciu:
'Bipolaron liquids at strong Peierls electron-phonon couplings',
in: *Phys. Rev. B* 104 (20 2021), p. L201109.

240 C. Zhang, J. Sous, D. R. Reichman, M. Berciu, A. J. Millis, N. V. Prokof'ev and B. V. Svistunov:
'Bipolaronic High-Temperature Superconductivity',
in: *Phys. Rev. X* 13 (1 2023), p. 011010.

Appendix

A Exact factorization of the Hubbard-Holstein time evolution operator

When considering the dissipative Hubbard-Holstein model, both for lQSD and nlQSD (see Section 2.4), the matrix elements of the non-Hermitian part of the effective Hamiltonian can be computed exactly. Here, we examine the linear case as given in Eq. (4.2) defining

$$\hat{B} = \sum_{j=1}^{L} \left[Z_l(t)\hat{a}_l - \frac{\kappa}{2}\hat{a}_l^\dagger \hat{a}_l \right] \tag{1}$$

and start by decomposing the exponential of the effective Hamiltonian using a second-order Trotter decomposition:

$$e^{-i(\hat{H}_{\mathrm{HH}}+i\hat{B})\delta t} \approx e^{\hat{B}\delta t/2} e^{-i\hat{H}_{\mathrm{HH}}\delta t} e^{\hat{B}\delta t/2} + \mathcal{O}(\delta t^3)\,. \tag{2}$$

Next, we focus on the computation of the exponential $e^{B\delta t}$. Since the terms acting on each site commute, the expression

$$e^{\sum_{j=1}^{L}\left[Z_j(t)\hat{a}_j - \frac{\kappa}{2}\hat{a}_j^\dagger \hat{a}_j\right]\delta t} = e^{\left[Z_1(t)\hat{a}_1 - \frac{\kappa}{2}\hat{a}_1^\dagger \hat{a}_1\right]\delta t} e^{\left[Z_2(t)\hat{a}_2 - \frac{\kappa}{2}\hat{a}_2^\dagger \hat{a}_2\right]\delta t} \dots e^{\left[Z_L(t)\hat{a}_L - \frac{\kappa}{2}\hat{a}_L^\dagger \hat{a}_L\right]\delta t}$$

is exact. We thus examine the expression for a single site, omitting the site subscript and the explicit time dependence of Z and define

$$F \equiv e^{\left[Z\hat{a} - \frac{\kappa}{2}\hat{a}^\dagger \hat{a}\right]\delta t}\,. \tag{3}$$

Our objective now is to express this exponential as the product of two exponentials. To achieve this, we apply the following theorem from Ref. [235]:

Given two operators $\hat{X}$ *and* $\hat{Y}$*, if* $[\hat{X},\hat{Y}] = s\hat{Y}$ *with* $s \in \mathbb{C}, s \neq 2\pi i n, n \in \mathbb{N}$*, then* $e^{\hat{X}}e^{\hat{Y}} = \exp\left\{(\hat{X} + \frac{s}{1-e^{-s}}\hat{Y})\right\}$.

Applied to Eq. (3), this theorem implies that

$$e^{\left[Z\hat{a} - \frac{\kappa}{2}\hat{a}^\dagger \hat{a}\right]\delta t} = e^{\left[-\frac{\kappa}{2}\hat{a}^\dagger \hat{a} + \frac{s}{1-e^{-s}}\tilde{Z}\hat{a}\right]\delta t} = e^{-\frac{\kappa}{2}\hat{a}^\dagger \hat{a}\delta t} e^{\tilde{Z}\hat{a}\delta t}\,, \tag{4}$$

where $\tilde{Z} = Z\frac{1-e^{-s}}{s}$ and $s = \frac{\kappa}{2}\delta t$. With this, the factorized operator reads

$$e^{\left[Z\hat{a} - \frac{\kappa}{2}\hat{a}^\dagger \hat{a}\right]\delta t} = e^{-\frac{\kappa}{2}\hat{a}^\dagger \hat{a}\delta t} e^{Z\frac{1-e^{-\kappa\delta t/2}}{\kappa\delta t/2}\hat{a}\delta t} = e^{-\frac{\kappa}{2}\hat{a}^\dagger \hat{a}\delta t} e^{Z\frac{1-e^{-\kappa\delta t/2}}{\kappa/2}\hat{a}}\,. \tag{5}$$

The operator $e^{Z\frac{1-e^{-K\delta t/2}}{\kappa/2}\hat{a}}$ does not conserve the bosonic particle number. To restore the $U(1)$ symmetry, we employ the PP mapping (see Eq. (7.3)), where we substitute the annihilation operator $\hat{a}$ with $\hat{a}\otimes\hat{b}^\dagger$, with $\hat{b}^\dagger$ representing the balancing operator acting on the bath site. We define the prefactor as $\gamma(Z)$ obtaining

$$F = e^{-\frac{\kappa}{2}\hat{a}^\dagger\hat{a}\delta t} e^{\gamma(Z)\hat{a}\otimes\hat{b}^\dagger} \ .$$

Our next objective is to determine the MPO representation of the dissipative operator. To achieve this, we proceed by calculating the matrix elements:

$$\begin{aligned}
&\langle n, n'|\, e^{-\frac{\kappa}{2}\hat{a}^\dagger\hat{a}\delta t} e^{\gamma(Z)\hat{a}\otimes\hat{b}^\dagger} \,|m, m'\rangle = \\
&e^{-\frac{\kappa}{2}n\delta t} \sum_{l=0}^{\infty} \frac{\gamma(z)^l}{l!} \langle n|\, \hat{a}^l \,|m\rangle \langle n'|\, (\hat{b}^\dagger)^l \,|m'\rangle = \\
&e^{-\frac{\kappa}{2}n\delta t} \sum_{l=0} \frac{\gamma(z)^l}{l!} \sqrt{\frac{(l+n)!}{n!}} \delta_{n+l,m}\delta_{n',m'+l} = \\
&\begin{cases} 0, & n > m \\ \frac{e^{-\frac{\kappa}{2}n\delta t}}{(m-n)!}\gamma(Z)^{m-n}\sqrt{\frac{m!}{n!}}\delta_{n'-m',m-n}, & \text{otherwise.} \end{cases}
\end{aligned} \tag{6}$$

We can express the rank-4 tensor $\delta_{n'-m',m-n}$ as

$$\delta_{n'-m',m-n} = \sum_{a=0}^{d-1} \delta_{n'-m',a}\delta_{m-n,a} \ .$$

Hence, we obtain the exact MPO representation

$$\begin{aligned}
&e^{-\frac{\kappa}{2}\hat{a}^\dagger\hat{a}\delta t} e^{\gamma(Z)\hat{a}\otimes\hat{b}^\dagger} = \\
&\sum_{n,m,n',m',a} \frac{e^{-\frac{\kappa}{2}n\delta t}}{(m-n)!}\gamma(Z)^{m-n}\sqrt{\frac{m!}{n!}}\, W_{1,a}^{(p)n,m} W_{a,1}^{(pp)n',m'} \,|n\rangle\langle m| \otimes |n'\rangle\langle m'| \ ,
\end{aligned} \tag{7}$$

where

$$\begin{cases} W_{1,a}^{(p)n,m} = \delta_{m-n,a} \\ W_{a,1}^{(pp)n',m'} = \tilde{W}_{a,1}^{(pp)n',m'} = \delta_{n'-m',a} \ . \end{cases} \tag{8}$$

At this stage, getting the exact factorization of the effective Hamiltonian for nlQSD is straightforward. We begin by introducing $\kappa\langle\Psi(t)|\,(\hat{a}_j^\dagger + \hat{a}_j)\,|\Psi(t)\rangle \equiv f$, focusing on a single site, and omitting the subscript j, resulting in:

$$e^{(Z+f)\delta t\hat{a} - \frac{\kappa}{2}\delta t\hat{a}^\dagger\hat{a}} \ . \tag{9}$$

The operator takes on the same form as Eq. (3), but with $Z + f$ in place of f.

Consequently, the factorized operator reads:

$$e^{(Z+f)\delta t\hat{a} - \frac{\kappa}{2}\delta t\hat{a}^\dagger\hat{a}} = e^{-\frac{\kappa}{2}\hat{a}^\dagger\hat{a}\delta t} e^{(Z+f)\frac{1-e^{-\kappa\delta t/2}}{\kappa/2}\hat{a}} \ . \tag{10}$$

The MPO representation of this operator is provided by Eqs. (7) and (8), where we set $\gamma(Z) = (Z+f)\frac{1-e^{-\kappa\delta t/2}}{\kappa/2}$.

B Classical Liouvillians with detailed balance have real spectra

The analysis presented here was developed together with Oisín Culhane as part of the project on the quantum Mpemba effect [2]. Following [236], we start by defining the so-called Markovian inner product relative to the steady-state probability distribution $|\tau\rangle$ of the Liouvillian $\hat{\mathscr{L}}^c$

$$(|\pi_1(t)\rangle, |\pi_2(t)\rangle)_M = \sum_x \frac{p_1(x,t)p_2(x,t)}{p_\tau(x)} , \tag{11}$$

where $|\pi_1(t)\rangle$ and $|\pi_2(t)\rangle$ are arbitrary probability distributions and p_1, p_2, and p_τ are the elements of $|\pi_1(t)\rangle$, $|\pi_2(t)\rangle$, and $|\tau\rangle$, respectively. For the Liouvillian this inner product is

$$\begin{aligned} \left(|\pi_1(t)\rangle, \hat{\mathscr{L}}^c |\pi_2(t)\rangle\right)_M &= \sum_x \frac{p_1(x,t)}{p_\tau(x)} \sum_y \langle x| \hat{\mathscr{L}}^c |y\rangle\, p_2(y,t) && (12) \\ &= \sum_{x,y} \frac{p_1(x,t)}{p_\tau(x)} \langle x| \hat{\mathscr{L}}^c |y\rangle\, p_2(y,t) \,. && (13) \end{aligned}$$

The detailed balance condition reads

$$\frac{\langle x| \hat{\mathscr{L}}^c |y\rangle}{p_\tau(x)} = \frac{\langle y| \hat{\mathscr{L}}^c |x\rangle}{p_\tau(y)} \,. \tag{14}$$

Plugging this condition into Eq. (13) gives

$$\begin{aligned} \left(|\pi_1(t)\rangle, \hat{\mathscr{L}}^c |\pi_2(t)\rangle\right)_M &= \sum_{x,y} \frac{p_1(x,t)}{p_\tau(y)} \langle y| \hat{\mathscr{L}}^c |x\rangle\, p_2(y,t) && (15) \\ &= \left(\hat{\mathscr{L}}^c |\pi_1(t)\rangle, |\pi_2(t)\rangle\right)_M , && (16) \end{aligned}$$

Thus, the operator $\hat{\mathscr{L}}^c$ is a self-adjoint operator under this inner product, which implies that its spectrum is real.

C Comparing Gaussian anharmonicities and dissipation

Recent theoretical investigations have explored the impact of anharmonicities on the characteristics of the metallic phase within the Hubbard-Holstein model. These studies have suggested a propensity to stabilize light bipolarons, even at higher electron-phonon couplings [48, 237]. This stabilization is a critical prerequisite for achieving high critical temperatures for bipolaronic, superconducting states [198, 222, 238–240].

In order to establish a link between our findings and the observed enhancement of the metallic phase through Gaussian and quartic anharmonic alterations of the phononic modes, we conducted a comparative analysis of the effects of dissipation and the anharmonicities explored in previous studies [47, 48] on the excitation probabilities of a single phonon mode. The thermal state for a single harmonic oscillator $\hat{\rho}_\beta^{eq} = e^{-\beta\omega\hat{n}} / \operatorname{Tr}\left(e^{-\beta\omega\hat{n}}\right)$, is the steady-state solution to a Lindblad master equation characterized by the jump operators $\hat{L}_1 = e^{-\beta\omega/2}\hat{a}^\dagger$ and $\hat{L}_2 = \hat{a}$, satisfying thermal detailed balance[1]. Combining these operators with the jump operator for dissipation, denoted as $\hat{L}_3 = \sqrt{\kappa}\hat{a}$, we obtain the following equation:

$$\begin{aligned}\partial_t\hat{\rho} = &- e^{-\beta\omega}\left(\frac{1}{2}\{\hat{a}\hat{a}^\dagger, \hat{\rho}\} - \hat{a}^\dagger\hat{\rho}\hat{a}\right)\\ &- (1+\kappa)\left(\frac{1}{2}\{\hat{a}^\dagger\hat{a}, \hat{\rho}\} - \hat{a}\hat{\rho}\hat{a}^\dagger\right) ,\end{aligned} \tag{17}$$

which is easily solved numerically for a finite-dimensional system. In Fig. C.1, we present the excitation probabilities of three distinct systems: a harmonic oscillator $\hat{H}_{\mathrm{HO}} = \omega\hat{a}^\dagger\hat{a}$, an anharmonic oscillator with Gaussian anharmonicity $\hat{H}_{\mathrm{G}}(\lambda,\gamma) = \hat{H}_{\mathrm{HO}} + \lambda \mathrm{e}^{-\gamma(\hat{a}^\dagger+\hat{a})^2}$, and a harmonic oscillator subject to dissipation as described in Eq. (17). Dissipation has the opposite effect of Gaussian anharmonicities on the population of the excited phonon states. While the decay of the excitation probability is reduced by Gaussian anharmonicities, it is enhanced when considering dissipation. These observations can be linked to our examination of metallicity and the localization length: dissipation has a minimal impact on the binding energy within the metallic phase (see Fig. 8.4). This suggests that metallicity is primarily dependent on the mean free path length of bipolaronic quasi-particles, which appears to be diminished by dissipation.

---

[1] This is the simplest instance of the more general Davies map [147] that we discuss in Section 5.2.1.

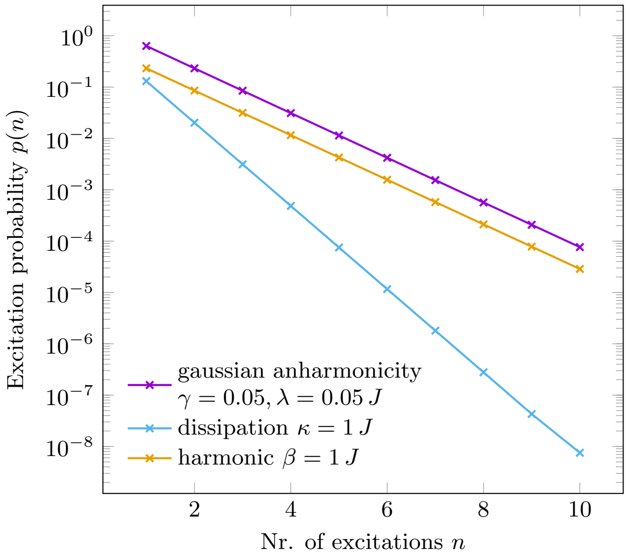

Figure C.1: Impact of dissipation and anharmonicities on the probability of exciting bosonic modes. The yellow curve shows the excitation probabilities of a harmonic oscillator $\hat{H}_{\mathrm{HO}}$ at an inverse temperature of $\beta = 1$. We compare these probabilities to those obtained by introducing a Gaussian, quadratic anharmonicity $\hat{H}_{\mathrm{HO}} + \lambda e^{-\gamma(\hat{a}^\dagger + \hat{a})^2}$ with $\lambda = 0.05\,J, \gamma = 0.05$ (represented by the purple line), and by including dissipation $\kappa = 1\,J$ (illustrated by the blue data). Gaussian anharmonicities diminish the energy level spacing, boosting the likelihood of populating highly excited states. On the other hand, the effect of dissipation is to leak phonons into the environment, increasing the ground state occupation while higher excitations are suppressed.

Glossary

1D one-dimensional. iv, 4, 26–28, 36, 39, 40, 45, 57, 94, 95, 97, 109, 118, 121, 133

1RDM single-site reduced density-matrix. 31, 38, 39, 54, 96

1TDVP single-site time-dependent variational principle. 29, 30

2TDVP two-site time-dependent variational principle. 29, 30, 35, 48, 50

CDW charge-density wave. 95, 110, 118, 121–123, 125–127, 133

CT charge transfer. 83–85

DMRG density-matrix renormalization group. 26, 27, 29, 31, 33, 34

ED exact diagonalization. 7, 12, 25, 32, 42–48, 52, 54, 58, 80, 132

FMO Fenna-Matthews-Olson. 80, 81, 86–93, 132

FSM finite-states machine. 34

GSE-TDVP global subspace expansion time-dependent variational principle. 29, 30, 48, 104

HEOM hierarchy of equations of motion. 32, 82, 132

HOPS hierarchy of pure states. 17–21, 30, 34, 35, 41–54, 82, 122–124, 129, 132

iTEBD infinite time-evolving block decimation. 103, 104, 110

LE locally excited. 83–85

LHC-II light-harvesting complex II. 86

lQSD linear quantum state diffusion. 15, 16, 45, 155

LSE-TDVP local subspace expansion time-dependent variational principle. 7, 30, 48, 83, 84, 93, 98, 103, 104

ME master equation. 42–45

ML-MCTDH multilayer multiconfiguration time-dependent Hartree. 82, 84

MPO matrix-product operator. 28, 29, 32–34, 46, 83, 156

MPS matrix-product state. iv, 3, 4, 7, 13, 25–38, 45, 46, 48, 49, 52, 56, 80, 83, 88, 93, 131, 132, 134

nlQSD non-linear quantum state diffusion. 16, 20, 155, 156

NMQSD non-Markovian quantum state diffusion. 18

OBC open boundary conditions. 104, 121

OQS open quantum system. 2–4, 7–11, 13, 26, 31–35, 40, 56, 131, 134, 164, 165

PBC periodic boundary conditions. 104

PP projected purification. 7, 20, 30, 31, 38, 39, 41, 45, 48, 49, 53, 54, 83, 91, 93, 98, 104, 129, 155

PS-HyB-MPS pure-state unraveled hybrid-bath based on matrix product states. 83–85, 87, 88, 90–93

PST phonon state tomography. iv, 4, 7, 26, 36–39, 57, 94–101, 103–105, 108, 114–119, 133

QJ quantum jumps. 13–15, 18, 34, 35, 41–50, 52–54, 83, 88, 89, 91, 93, 122, 126, 129, 132

QSD quantum state diffusion. 15–17, 34, 35, 43, 45, 54

QUAPI quasi-adiabatic path integral. 82, 87, 88, 132

SDW spin-density wave. 121–123, 125–127, 133

SF singlet fission. 80, 81, 83, 84, 93

SSH Su-Schrieffer-Heeger. 93

SVD singular value decomposition. 27, 28, 33, 39

TDVP time-dependent variational principle. 29, 33–36, 46, 82, 131

TEBD time-evolving block decimation. 33

TFIM transverse-field Ising model. 70, 77, 78

TT two-triplet. 83–85

TTN tree tensor network. 93

List of Figures

2.1 Algorithmic sketch of the quantum jumps (QJ) method. 14
2.2 Algorithmic sketch of the hierarchy of pure states method. 19
2.3 Schematic representation of the transition from a global to local environments. 22
2.4 Bath correlation function Eq. (2.55) approximated with one and three complex exponentials 24

3.1 Graphical representation of an MPS. 27
3.2 Graphical representation of an MPO. 28
3.3 Application of an MPO to an MPS. 29
3.4 The projected purification (PP) mapping. 31
3.5 Depiction of the phonon state tomography (PST) method. 39

4.1 Two possible system-environment partitionings for dissipative electron-phonon models. 41
4.2 Comparison of HOPS and QJ to the exact ME. 42
4.3 Comparing linear and nonlinear QSD to the exact ME. 43
4.4 Comparison between a master equation for the ”electron + phonon” system and a master equation for the electron system alone. 44
4.5 MPS for a 1D electron-phonon system with the PP mapping. . . . 45
4.6 Spin-density correlations $\langle \hat{\sigma}^z_{20} \, \hat{\sigma}^z_{20+j} \rangle$ computed for a system consisting of $L = 40$ sites at half-filling, following a quench from a Neel state. 46
4.7 Charge-density correlations $\langle \hat{n}^{\mathrm{f}}_{20} \, \hat{n}^{\mathrm{f}}_{20+j} \rangle$ computed using both HOPS and QJ 47
4.8 Left: Hierarchy depth k_{max} for HOPS as a function of g and κ. . . . 49
4.9 Improved stability of HOPS is achieved by employing auxiliary states transformed according to Eq. (2.36). 50
4.10 Convergence analysis of the nearest neighbor pairing correlation, as described in Eq. (4.4), with respect to the local Hilbert space dimension d_{max}. 51

4.11 The bond dimension for both QJ and HOPS during the time evolution following the global quenches described in the caption of Fig. 4.6. 52
4.12 PP speedup for intermediate (blue) and strong (orange) electron-phonon couplings across various dissipation strengths. 53
4.13 Dissipation-induced bipolaron localization 56

5.1 Experimental demonstration of the classical Mpemba effect. . . . 60
5.2 Schematic representation of the quantum Mpemba effect. 62
5.3 Block structure of the vectorized Davies generator $\hat{\mathscr{G}}$. 68
5.4 The quantum Mpemba effect in a single-qubit system. 70
5.5 The quantum Mpemba effect in a many-qubit system manifests at different timescales. 71
5.6 The Davies map for two experimental scenarios 72
5.7 A unitary optimization based on a stochastic Metropolis algorithm can exponentially accelerate relaxation. 74
5.8 The swap Metropolis and the unitary Metropolis methods are applied to the thermalization process of a TFIM. 78
5.9 Exponentially accelerated thermalizations are observed after the Metropolis optimization. 79

6.1 Spectral densities describing electronic-vibriational interactions. . 83
6.2 Schematics of singlet fission 84
6.3 Singlet fission dynamics. 86
6.4 The FMO light-harvesting complex. 87
6.5 Exciton dynamics in the FMO light-harvesting complex at finite temperature. 88
6.6 Finite-temperature: unraveling vs. thermofield doubling. 90
6.7 Total occupation of the vibrational modes for unitary and dissipative dynamics. 91
6.8 Bond dimension convergence for unitary and dissipative dynamics. 93

7.1 Phonon state tomography (PST) for a photo-excited metal. 96
7.2 Momentum-dependent phonon occupation for different time delays. 98
7.3 Reconstructing time-dependent electronic correlations with PST. . 100
7.4 Impact of the local shape of the pulse on the electron dynamics. . 101
7.5 Impact of the global shape of the pulse on the electron dynamics. 103
7.6 Comparing the photo-excited dynamics to iTEBD reference data from [198]. 105
7.7 Numerical accuracy of the time evolution. 106
7.8 Convergence of electronic observables obtained with PST with the number of computed samples. 107
7.9 Convergence of the Taylor-expanded squeezed-coherent state. . . 108

7.10 Convergence of the local phonon probability distribution $p\left(n^{\mathrm{ph}}\right)$ for the Taylor-expanded squeezed-coherent state. 109
7.11 Global phonon distribution function $\mathscr{P}(N^{\mathrm{ph}})$ induced by the β−pulse Eq. (7.10). 109
7.12 Dynamics of momentum-dependent charge and pairing correlations at small phonon frequency. 110
7.13 Impact of the phonon frequency and the pump fluence on the electron correlations. 112
7.14 Comparing exact and effective results. 114
7.15 Phonon state tomography at different phonon frequencies. 115
7.16 Momentum-dependent charge correlation for different system sizes. 116
7.17 Bond dimension scaling for the momentum-dependent charge correlation function at different frequencies. 117
7.18 Accuracy of PST at different phonon frequencies. 118
7.19 Momentum-dependent pairing correlations in the exact and in the effective model. 119

8.1 Phase diagram of the Hubbard-Holstein model at a constant phonon oscillation frequency $\omega = 2\,J$ 123
8.2 Double occupancy dynamics after global quenches from the Hubbard ground state. 125
8.3 Eigenvalues t_k of the bipolaronic hopping matrix $\hat{T}^{bp}_{i,j,\sigma}$ following dissipative quenches. 127
8.4 Dynamics of the bipolaronic binding energy and metallicity induced by dissipative quenches. 128
8.5 Relative change of localization length ξ_t^2 following dissipative quenches. 129
8.6 Pictorial representation of dissipation-induced bipolaron localization 131

C.1 The impact of dissipation and anharmonicities on the probability of exciting bosonic modes. 160

Acknowledgements

Somedays, I felt stupid, comparing myself to brighter and more successful colleagues. Somedays I felt frustrated, not being able to sort out what was wrong with my calculations or my code. Somedays, I felt useless, reading about a new horrible conflict breaking out while I was sitting in my office trying to diagonalize a Hamiltonian. But most days, I felt grateful to be able to spend so much time doing what I love (and even getting paid for it!), excited to learn something new, and blessed to work with so many extraordinary people to whom I owe a lot. In particular, I want to thank:

Uli Schollwöck, my supervisor, for giving me the great previlige of spending the last four years doing research in his group, for always supporting me and for understanding my strengths and weaknesses.

Sebastian Peckel, my co-supervisor, for his incredible support, patience and teachings. The hours spent at the blackboard with him, trying to tell whether his scribbles were genius (usually) or madness (sometimes), are the best memories of my PhD.

Christian Mendl, Steffen Rulands, **Alexander Urban** and **Ilka Brunner** for taking the time to be part of my doctoral committee.

John Goold for hosting me in Dublin and sharing his great positive energy and his vast knowledge about physics. I am extremely happy to join his group this autumn.

Martin Grundner for being my mentor in the first phase of my PhD, for always leading me in the right direction, and for persuading me not to quit after a tough first year.

John Sous for the enriching collaborations over the last two years, introducing me to the exciting field of optically driven quantum systems, and hosting me in San Diego.

Matteo Mitrano for being a great collaborator, hosting me in Harvard, and literally enlightning teaching on optically-induced phenomena.

Stuart Flannigan for supporting me during the first period of my PhD and teaching me everything I know about pure-state unravelings of OQS.

Max Bramberger for patiently sharing his brilliant knowledge about open quantum systems and numerics with me during the first phase of my PhD.

Mari Carmen Bañuls for being an exceptional IMPRS-QST supervisor, particu-

larly for sharing her immense knowledge about tensor network methods for OQS.
Sam Mardazad, **Héloïse Albot**, **Zhaoxuan Xie**, **Fabian Pauw**, **Pit Bermes**, **Ke Liao** for being exceptional colleagues, office mates and collaborators.
Damiano Aliverti-Piuri, **Annabelle Bohrdt**, **Tizian Blatz**, **Giovanni Canossa**, **Lexin Ding**, **Fabian Grusdt**, **Jad Halimeh**, **Tim Harris**, **Lukas Homeier**, **Matjaz Kebric**, **Hannah Lange**, **Julia Liebert**, **Lode Pollet**, **Felix Palm**, **Nihal Rao**, **Nader Mostaan**, **Rajah Nutakki**, **Nico Sadoune**, **Henning Schlömer**, **Reja Wilke** for all the and funny moments interesting discussions that make up so many of my good memories at LMU.
Oisín Culhane and **Krissia Zawadzki** for being fantastic friends and collaborators and for all the time spent together obsessing over the Mpemba effect.
François Damanet and **Thomas Köhler** for being great collaborators from whom I learned a lot when writing my first paper.
Alessandro Summer, **Laetitia Bettman**, **Artur Lacerda**, **Leonard Logaric**, **Nathan Keenan**, **Felix Binder**, **Michael Kewming**, **Shane Dooley**, **Alex Nico-Katz** for welcoming me in Dublin last spring and after.
Mark Mitchison for always finding time to discuss with me and sharing some of his encyclopedic knowledge on open quantum systems and physics in general.
Ines de Vega, whose work on OQS has inspired me since my Master's studies for her advice, especially recommending John Goold as a PostDoc supervisor.
Sonya Gzyl for her fantastic support for all IMPRS-QST activities, which I recommend to all PhD students in Munich.
Tobias Kiermeyer, **Yudong Sun**, **Réka Schwengelbeck**, **Leonard Werner-Pingen**, **Jonas Egle**, for the enriching experiences as co-supervisor and for being fantastic students.
Miha Papic for teaching me about noisy superconducting qubits and **Erika Kiel** and **Erling Thyrhaug** for teaching me about light-harvesting complexes, and I apologize to all three of them for not having managed to finish the projects we started together.
Taissa, my wife, my inseparable companion for the last eleven years, for believing in me even when I don't and for filling my life with joy.
my mum **Franca**, my dad **Helmuth** my syster **Elena** for all their love and support which helped a dyslexic child becoming a physicist.
Gabriele Degano, my good friend, for helping me during the first challenging phase of my PhD.